

3D printing of nanoparticle-based aerogels

Dissertation

zur Erlangung des Doktorgrades
an der Fakultät für Mathematik, Informatik und
Naturwissenschaften
Fachbereich Physik
der Universität Hamburg

vorgelegt von
Matthias Nils Rebber

Hamburg
2022

Gutachter/in der Dissertation:	Prof. Dr. Dorota Koziej Prof. Dr. Andreas Stierle
Zusammensetzung der Prüfungskommission:	Prof. Dr. Dorota Koziej Prof. Dr. Andreas Stierle Prof. Dr. Arwen Pearson Prof. Dr. Daniela Pfannkuche Dr. Robert Zierold
Vorsitzende der Prüfungskommission:	Prof. Dr. Arwen Pearson
Datum der Disputation:	13.12.2022
Vorsitzender Fach-Promotionsausschuss PHYSIK:	Prof. Dr. Wolfgang J. Parak
Leiter des Fachbereichs PHYSIK:	Prof. Dr. Günter H. W. Sigl
Dekan der Fakultät MIN:	Prof. Dr.-Ing. Norbert Ritter

Abstract

Multiscale nanoparticle processing is essential for the integration of colloidal nanomaterials into macroscopic, functional devices. In this regard, aerogels are especially promising as they preserve the nanoscopic characteristic of colloidal nanomaterials in a highly porous, macroscopic solid. However, the restricted range of molds in the gel casting process prevents sophisticated aerogel geometries that are tailor-made for their application. In this thesis we explore 3D printing as a fabrication method for functional, hierarchically structured nanoparticle-based aerogels with full control of the nano-, micro-, and macroscopic length scales.

We develop a 3D printing scheme for TiO_2 nanoparticle-based aerogels by introducing the concept of *gelled nanoinks* as a new design scheme for aerogel inks. Here, additive-free inks are formulated by destabilizing a liquid nanoparticle dispersion into a volume-filling colloidal gel. The print is performed in an alkaline liquid bath to solidify the soft ink after extrusion and to enable subsequent processing into aerogels via supercritical drying. The 3D printing method sustains key structural characteristics of conventionally casted aerogels such as a large specific surface area of up to $539 \text{ m}^2 \text{ g}^{-1}$ and pore sizes of 20 nm while offering an unparalleled designability on the micrometer scale. In general, various nanomaterials can be processed into inks and 3D-printed giving access to multifunctional aerogels. To exemplify, we load the TiO_2 inks with plasmonic, photothermal Au nanorods prior to gelation. Here, 3D printing enables the fabrication of 3D microstructures with a spatially controlled heating characteristic.

Moreover, we combine the aerogel 3D printing method with digital design tools such as computational fluid dynamics and Monte Carlo light transport simulations to create a 3D geometry optimized for photocatalysis in the gas phase. To this end, we introduce a unit cell based microstructuring approach and identify the face-centered cubic (fcc) structure as an ideal photocatalyst architecture since it lowers the resistance to gas flow by five orders of magnitude compared to an unstructured aerogel without compromising the light utilization efficiency. To evaluate the photocatalytic performance of the fcc microstructure, we take the hydrogen evolution from a water/methanol saturated gas stream as an example. We show that the fcc structured TiO_2 aerogel raises the mass normalized hydrogen evolution rate by a factor of five relative to the commonly utilized TiO_2 powder. Moreover, we indicate that the benefits of fcc microstructuring are not limited to TiO_2 and that similar improvements of the mass normalized production rate can be achieved for Au/ TiO_2 aerogels.

Zusammenfassung

Die Prozessierung von Nanopartikeln auf mehreren Längenskalen ist für ihre Integration in ein makroskopisches, funktionales Material unerlässlich. In diesem Zusammenhang sind Aerogele besonders vielversprechend, da sie die nanoskopischen Eigenschaften von kolloidalen Nanomaterialien in einem hochporösen makroskopischen Festkörper beibehalten. Hierbei verhindert jedoch die Auswahl an Formen im notwendigen Gießverfahren die Anfertigung anspruchsvoller, für die Anwendung maßgeschneiderte Aerogel-Geometrien. In dieser Arbeit untersuchen wir den 3D-Druck als Herstellungsmethode für funktionale, hierarchisch strukturierte Aerogele auf Nanopartikelbasis mit voller Kontrolle über die nano-, mikro- und makroskopischen Größenordnung.

Wir entwickeln eine 3D-Druckmethode zur Herstellung von Aerogelen auf Basis von TiO_2 Nanopartikeln, indem wir das Konzept der „*gelierten Nanotinten*“ als ein neues Verfahren zur Formulierung von Aerogeltinten einführen. Hierzu werden additivfreie Tinten formuliert, indem eine flüssige Nanopartikeldispersion durch Destabilisierung in ein volumenfüllendes kolloidales Gel überführt wird. Der 3D-Druck erfolgt in einem alkalischen Flüssigkeitsbad, um die weiche Tinte nach der Extrusion zu verfestigen und die anschließende Verarbeitung zu Aerogelen durch superkritische Trocknung zu ermöglichen. Das Druckverfahren behält wichtige strukturelle Merkmale herkömmlich gegossener Aerogele bei, wie etwa eine große spezifische Oberfläche von bis zu $539 \text{ m}^2 \text{ g}^{-1}$ und eine Porengröße von 20 nm, und bietet zusätzlich eine unvergleichliche geometrische Kontrolle im Mikrometermaßstab. Generell können verschiedene Nanomaterialien zu Tinten verarbeitet und 3D-gedruckt werden, welches die Herstellung multifunktionaler Aerogele ermöglicht. Auf dieser Grundlage beladen wir die TiO_2 -Tinten vor der Gelierung mit plasmonischen, photothermischen Au-Nanostäbchen. Wir veranschaulichen, dass der 3D-Druck eine 3D Mikrostrukturierung mit einer räumlich kontrollierten Heizcharakteristik ermöglicht.

Darüber hinaus kombinieren wir die digitale Herstellungsmethode des 3D-Drucks mit computergestützten Methoden wie der numerischen Strömungsmechanik und der Simulation des Lichttransports über die Monte Carlo Methode, um eine optimale 3D-Geometrie für die Photokatalyse in der Gasphase zu entwerfen. Zu diesem Zweck führen wir eine Mikrostrukturierung basierend auf Einheitszellen ein und leiten her, dass eine flächenzentrierte (fcc) Struktur ideal für die Photokatalyse ist, da diese einen um fünf Größenordnungen geringeren Widerstand für den Gasfluss im Vergleich zu einem unstrukturierten Aerogel aufweist ohne die Lichtnutzungseffizienz zu beeinträchtigen. Wir bewerten die photokatalytische Leistung der fcc Mikrostruktur am Beispiel der Wasserstoffentwicklung in einem mit Wasser/Methanol gesättigten Gasstrom. Wir zeigen, dass das fcc-strukturierte TiO_2 -Aerogel die massennormierte Wasserstoffproduktionsrate im Vergleich zur typischen TiO_2 -Pulverform um den Faktor fünf erhöht. Außerdem deuten wir

an, dass die Vorteile der fcc-Mikrostrukturierung nicht auf TiO_2 beschränkt sind, da eine ähnliche Steigerung in der massennormalisierten Produktionsrate auch für Au/ TiO_2 -Aerogele erzielt werden kann.

Contents

Abstract	V
Zusammenfassung	VII
1 Introduction	1
2 From Individual Building Blocks to Nanostructured Bulk Aerogels	7
2.1 Introduction to Aerogels	7
2.2 Gelation - General Guidelines for Colloidal Nanomaterials	8
2.3 Solvent Extraction – Conversion of Wet Gels to Aerogels	12
2.4 Literature Review – State of the Art Nanoparticle-Based Aerogels	13
3 Geometric Control during Aerogel Processing	17
3.1 Traditional Shaping Methods	17
3.2 3D Printing – A Novel Shaping Method	18
3.3 3D Printed Aerogels	20
3.3.1 Ink Formulation Guidelines	21
3.3.2 State of the Art Aerogel Inks	21
3.3.3 The Next Generation - Gelled Nanoinks	25
4 Experimental Methods and Computational Modeling Tools	31
4.1 3D Printing Setup	31
4.2 Basics of Rheology	32
4.3 Photocatalysis Setup	34
4.4 Computational Fluid Dynamics	39
4.5 Monte Carlo Method	40
5 Gelled Nanoinks: A 3D Printing Toolbox for Hierarchically Structured Aerogels	45
5.1 Abstract	46
5.2 Introduction	47
5.3 Results and Discussion	48
5.4 Conclusion	59
5.5 Experimental Section	60
5.6 Supporting Information	64
5.7 Acknowledgment	79
5.8 Appendix	80

6	Form Follows Function: A 3D Printed, Nature-Inspired Aerogel Photocatalyst	91
6.1	Abstract	92
6.2	Introduction	92
6.3	Results and Discussion	93
6.4	Conclusion	102
6.5	Experimental Section	102
6.6	Supporting Information	106
6.6.1	Optical Characterization	114
6.6.2	Mass Transport Considerations	122
6.6.3	Computational Fluid Dynamics	126
6.7	Acknowledgment	128
6.8	Data Availability	128
7	Further Prospects of 3D Printed Aerogels	133
7.1	3D Printing in a Supportive Gel	133
7.2	Alignment of Au Nanorods	136
7.3	Photocatalytic CO ₂ Reduction	138
8	Conclusion and Outlook	143
9	Organic–Inorganic Hybrids for CO₂ Sensing, Separation, and Conversion	147
9.1	Abstract	148
9.2	Introduction	148
9.3	Individual Organic and Inorganic Building Blocks	149
9.4	Organic-Inorganic Hybrids for Sensing of CO ₂	154
9.5	Organic-Inorganic Hybrids for Separation of CO ₂	162
9.6	Organic-Inorganic Hybrids for Catalytic Conversion of CO ₂	169
9.7	Conclusion	178
9.8	Acknowledgment	179
	List of Figures	193
	List of Tables	195
	List of Abbreviations	197
	Declaration	199
	Acknowledgments	203
	Curriculum Vitae	205
	Eidesstattliche Versicherung / Declaration on oath	207

1 Introduction

Material processing is a fundamental human endeavor to improve the overall quality of life and closely linked to human history. In retrospect, we even named entire eras after the most dominant material such as the stone age, the iron age, and beyond. While in the past human beings reshaped natural resources into a product, we nowadays established sophisticated technologies to produce artificial materials that are engineered for a specific application. This enormous material revolution has enabled and defined our present technological era and material science expanded from traditional use cases such as tools, weapons, or jewelry to new areas such as electronics, biomedical implants, energy storage or conversion.^[1] Besides expanding applications, material science nowadays takes on a greater responsibility for the future of our planet by facing unprecedented, existential challenges such as the finite amount of resources, or the anthropogenic climate change.^[2] At the same time, we also have greater access than ever before to highly developed processing tools, and to high-performance materials to set up a sustainable production and energy system. Two of the recent advances in material science are the use of 3D printing, which precisely fabricates objects in a layer-by-layer fashion with less generation of waste than already established subtractive manufacturing methods,^[3] and the synthesis of nanomaterials, which allows to manipulate material properties on an atomic level and enables more effective renewable energy applications.^[4] Combining both aspects enables the hierarchical design of functional materials using nanoscale building blocks and might define the next material era.^[5-7]

We refer to materials as nano when they feature length scales in a range of 1 to 100 nm on at least one dimension. The resulting high surface to volume ratio of nanomaterials leads to many unusual material properties in comparison to their bulk counterpart. Whether it is the red color of spherical gold nanoparticles,^[8] the size-tunable band gap of semiconductor quantum dots,^[9] or the melting point depression by hundreds of degrees:^[10] controlling the size and shape on the nanometer scale opened another dimension to tailor material properties. Considering the variety of nanomaterials that can be synthesized with different sizes, shapes, and compositions, it becomes apparent that such a toolbox opens many fascinating options to combine nanomaterials into macroscopic functional objects with distinct properties. Therefore, research attention has now shifted from the synthesis of nanomaterials to the construction of functional materials based on nanoscale building blocks.^[11] So far, nano building blocks are either arranged in well-defined ordered superstructures in the form of 2D monolayers and 3D supercrystals,^[12] or in complex, disordered assemblies such as colloidal gels and aerogels. While order and symmetry are aesthetically more pleasing than disordered colloidal gels, a high order within nanoparticle assemblies is often not required for the later application.^[13] In fact, disorder can even be beneficial for catalytic applications due to improved mass transport in the percolating 3D pore

network.^[14] Independent on the type of arrangement, property and function of the final material are not only defined through the choice of nanoscopic building blocks, but also through the 3D architecture on the nano, micro and macroscopic length scales.^[15] While the nanoarchitecture is well controlled via rational shape-engineering and compositional modulation during synthesis,^[16] a simultaneous geometric control of the micro- and macroarchitecture via direct patterning of nanomaterials still remains a scientific challenge and hinders facile integration of nanoscale building blocks in advanced functional devices.^[7,17]

Promising functional materials that might play a key role in establishing a sustainable energy system are photocatalysts. These materials convert the energy of light into chemical energy and can be used to produce solar fuels such as hydrogen, which is a key component of the 21st century energy transition.^[2] In this regard, nanoparticle-based aerogels have a huge potential since they combine the intrinsic catalytic activity of the employed nanoparticles with the nanoscale 3D structure of the aerogel featuring a large surface area and open porosity. However, not only the development of an efficient nanomaterial is still ongoing, but recent efforts have also shown that a geometric shape control along all length scales is needed to unlock the full potential of aerogel photocatalysts.^[18]

In this Ph.D. thesis, we aim at the processing of hierarchically structured aerogels via 3D printing to fabricate a tailor-made photocatalyst architecture. Since TiO_2 is one of the most studied photoactive materials and considered as a benchmark catalyst,^[19] we employ TiO_2 nanoparticles as the primary aerogel building block. The use of 3D printing overcomes the geometric limitations of traditional shaping methods and enables a rational, data-driven design when coupled with computational methods.

Chapter 2 introduces the class of aerogels and discusses the general preparation routes. In the course of this chapter, we present universal strategies to induce the gelation of a liquid nanomaterial dispersion and challenges in the subsequent transformation of the wet gel into an aerogel. We end the chapter with a state-of-the-art literature overview of accessible aerogel materials.

Chapter 3 covers the geometrical length scales during aerogel processing. We discuss the limitations of traditional shaping techniques such as gel casting or wet spinning and highlight the potential benefits of novel methods such as 3D printing. We identify potential 3D printing techniques applicable to aerogels and discuss the drawbacks of already reported aerogel printing methods. Based on that, we derive guidelines for the development of a new class of aerogel inks, so-called *gelled nanoinks*.

Chapter 4 summarizes the main experimental and computational methods established in part of this thesis. These include the 3D printing and photocatalysis setup, a rheometer, computational fluid dynamics, and the Monte Carlo method for the modeling of photon transport. Combining the unprecedented geometric freedom of 3D printing with computational tools allows to optimize the 3D architecture of the aerogel for the application as a photocatalyst.

Chapter 5 presents a 3D printing methodology for the fabrication of hierarchically structured TiO_2 nanoparticle-based aerogels by formulating additive-free *gelled nanoinks*. This approach provides a modular platform for multicomponent, functional inks via the cogelation of TiO_2 with other nanomaterials such as photothermal Au-nanorods. The content of this chapter was

published in *Advanced Functional Materials* (*Adv. Funct. Mater.* **2022**, 32, 2112914).

In chapter 6, we use the same printing technology but focus on the photocatalytic activity of the TiO₂ aerogel backbone. We combine the Monte Carlo method and computational fluid dynamics to derive an ideal 3D geometry with efficient illumination, facile mass transport and highest photocatalytic production rates. As an example of a photocatalytic reaction, we use the hydrogen evolution from a water/methanol saturated gas stream. The content of the chapter was submitted in August 2022.

Chapter 7 summarizes preliminary results of ongoing research projects. These include modification on the 3D printing process, the alignment of anisotropic nanomaterials during ink extrusion, and the photocatalytic reduction of CO₂.

Chapter 8 presents the conclusion of the Ph.D. thesis and an outlook for potential future research directions.

Chapter 9 is not directly related to nanoparticle-based aerogels. We review how organic and inorganic nanoscale building blocks can be combined into a hybrid material to improve the affinity to CO₂ in the context of sensing, separation, and conversion. The presented strategies can be applied to formulate inks incorporating functional additives and might control the selectivity of the photocatalytic CO₂ reduction process in the future. The chapter was published in *Nanoscale Horizon* (*Nanoscale Horiz.* **2020**, 5, 431-453).

Comment on the use of the term *we* throughout this thesis: In chapters 5, 6 and 9, the term *we* means all authors of the respective work. In all other chapters, *we* refers to the reader and the author of the thesis and is used to guide the reader through the text.

Bibliography

- [1] R. E. Hummel, *Understanding materials science history, properties, applications*, Springer, 1998.
- [2] J. Cook, N. Oreskes, P. T. Doran, W. R. L. Anderegg, B. Verheggen, E. W. Maibach, J. S. Carlton, S. Lewandowsky, A. G. Skuce, S. A. Green, D. Nuccitelli, P. Jacobs, M. Richardson, B. Winkler, R. Painting and K. Rice, *Environ. Res. Lett.*, 2016, **11**, 048002.
- [3] K. Taylor-Smith, *How is 3D Printing a Sustainable Manufacturing Method?*, 2021, <https://www.azom.com/article.aspx?ArticleID=20017>, accessed on 18.07.2022.
- [4] X. Chen, C. Li, M. Grätzel, R. Kostecki and S. S. Mao, *Chem. Soc. Rev.*, 2012, **41**, 7909–7937.
- [5] K. Ariga, *Nanoscale Horiz.*, 2021, **6**, 364–378.
- [6] K. Ariga, *Nanoscale*, 2022, **14**, 10610–10629.
- [7] M. S. Lee, D. W. Yee, M. Ye and R. J. Macfarlane, *J. Am. Chem. Soc.*, 2022, **144**, 3330–3346.
- [8] J. Turkevich, P. C. Stevenson and J. Hillier, *J. Phys. Chem.*, 1953, **57**, 670–673.
- [9] C. B. Murray, D. J. Norris and M. G. Bawendi, *J. Am. Chem. Soc.*, 1993, **115**, 8706–8715.
- [10] F. Gao and Z. Gu, in *Melting Temperature of Metallic Nanoparticles*, ed. M. Aliofkhazraei, Springer International Publishing, Cham, 2016, pp. 661–690.
- [11] D. Koziej, A. Lauria and M. Niederberger, *Adv. Mater.*, 2014, **26**, 235–257.
- [12] M. A. Boles, M. Engel and D. V. Talapin, *Chem. Rev.*, 2016, **116**, 11220–11289.
- [13] M. Niederberger, *Adv. Funct. Mater.*, 2017, **27**, 1703647.
- [14] D. R. Rolison, *Science*, 2003, **299**, 1698–1701.
- [15] Y. Zhang, F. Zhang, Z. Yan, Q. Ma, X. Li, Y. Huang and J. A. Rogers, *Nat. Rev. Mater.*, 2017, **2**, 17019.
- [16] M. V. Kovalenko, L. Manna, A. Cabot, Z. Hens, D. V. Talapin, C. R. Kagan, V. I. Klimov, A. L. Rogach, P. Reiss, D. J. Milliron, P. Guyot-Sionnest, G. Konstantatos, W. J. Parak, T. Hyeon, B. A. Korgel, C. B. Murray and W. Heiss, *ACS Nano*, 2015, **9**, 1012–1057.
- [17] M. R. Begley, D. S. Gianola and T. R. Ray, *Science*, 2019, **364**, eaav4299.
- [18] F. Matter and M. Niederberger, *Adv. Sci.*, 2022, **9**, 2105363.
- [19] H. Xu, S. Ouyang, L. Liu, P. Reunchan, N. Umezawa and J. Ye, *J. Mater. Chem. A*, 2014, **2**, 12642–12661.

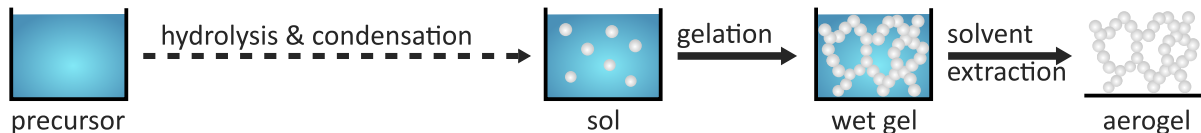
2 From Individual Building Blocks to Nanostructured Bulk Aerogels

This chapter introduces the fundamental steps to process colloidal nanomaterials into bulk, nanostructured aerogels, and reviews state-of-the-art materials from literature.

2.1 Introduction to Aerogels

The term aerogel describes a macroscopic solid derived from a gel with a three-dimensional, interconnected pore network in which the dispersed phase is a gas. Aerogels are neither limited to any type of material nor to any synthesis procedure and mostly consists of pores in the 1 to 100 nm range, which results in unique macroscopic properties such as extremely low thermal conductivity, ultralow refractive index, a large specific surface area and a high porosity.^[1-7] The scientific story of aerogels started in 1931 with an experiment by Samuel Stephens Kistler who demonstrated that the liquid in silica gel can be replaced by air with little or no shrinkage.^[8] Since then many preparation routes for a variety of aerogels were developed. While aerogels are traditionally formed by the so-called molecular route, nanoparticle-based aerogels became a viable alternative to widen the accessible range of functional materials. Figure 2.1 illustrates the key difference between both approaches. The molecular approach is a continuous process based on aqueous sol-gel chemistry and is mainly used to prepare metal oxide aerogels, in which the ongoing hydrolysis and condensation of a molecular metal alkoxide precursor leads to the formation of an amorphous sol and eventually to a wet gel. For the nanoparticle-based approach, sol and gel formation are separated to enable the preparation of functional, often crystalline building blocks with atomically defined properties. First, the nanoscopic building blocks are synthesized, washed, and processed into a highly concentrated dispersion, which is followed by the transformation into a gel as a second step. For both processing schemes, a three-dimensional sponge-like network is formed where the solid network is completely soaked with the initial solvent.^[6] By dedicated drying techniques, the solvent is replaced with air while retaining the three-dimensional nanoscopic structure in a macroscopic aerogel. In this thesis, we focus on nanoparticle-based aerogels. In section 2.2 we discuss the fundamental principle to transform a liquid nanoparticle dispersion into a wet gel. In section 2.3 we briefly present commonly applied procedures to remove the solvent from the pores via supercritical drying and freeze-drying, respectively. We end this chapter with an overview of reported nanoparticle-based aerogels to illustrate the versatility of this processing scheme.

a) Molecular sol-gel approach



b) Nanoparticle-based approach

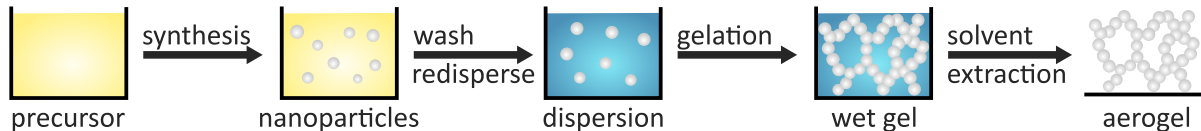


Figure 2.1: General scheme of aerogel processing. a) The molecular approach involves the formulation of a sol and a subsequent gelation from a molecular precursor via hydrolysis and condensation reactions. b) The nanoparticle-based approach separates formulation of a dispersion and gelation. The dispersion is prepared via wet colloidal chemistry. Both approaches require subsequent solvent extraction to transform the wet gel into aerogel.

2.2 Gelation - General Guidelines for Colloidal Nanomaterials

Surface chemistry plays a decisive role to prevent an uncontrolled agglomeration of colloidal nanomaterials and the loss of their nanospecific properties.^[9–12] Thus, formulating stable dispersions with a well-defined surface chemistry is essential to process nanomaterials into gels with is essential to process nanomaterials into gels with features than can be designed based on the characteristics of the nanoscopic building blocks.^[6,13,14] We first explain the fundamental principles of stabilizing nanomaterials in polar and nonpolar solvents, followed by a discussion of gelation strategies which require an alteration of the repulsive, stabilizing forces.

In polar solvents nanomaterials can be charge-stabilized. The most common stabilizers are organic acids which can be deprotonated to create a negative charge on the nanoparticle’s surface. For metal nanoparticles typical examples are sodium citrate or mercaptopropionic acid.^[6] For quantum dots inorganic ligands such as halogen ions, or transition metal complexes can be employed.^[15] For metal oxides electrostatic stabilization can be achieved by protonating or deprotonating OH groups on the ligand-free surface. Independent of nanomaterial type, charges lead to the attraction of oppositely charged ions and the formation of an electric double layer. The surrounding counter-ions shield the nanoparticle surface and creates a strong electrostatic repulsion once the ion clouds of two particles overlap.^[16] The electrostatic interaction potential can be written for two spherical particles in a simplified form as:

$$V_{\text{elec}} \approx 2\pi\epsilon\epsilon_0 \cdot r \cdot \Psi_0^2 \cdot \exp\left(-\frac{d}{\lambda_D}\right) \quad (2.1)$$

with particle radius r , surface potential Ψ_0 , interparticle distance d and Debye length λ_D , which depends on temperature, ionic strength, and dielectric constant ϵ of the solvent and counteracts the attractive Van-der-Waals potential. The different distance-scaling behavior of the opposing force fields results in a secondary energetic minimum emerges which defines the average interparticle distance in the dispersion, as illustrated in Figure 2.2a-c.

In nonpolar solvents, nanoparticles are sterically stabilized. Here long-chained organic ligands

are anchored on the particle surface and form a protective, hydrophobic shell that prevents touching of inorganic surfaces and an accompanied agglomeration of particles, as depicted in Figure 2.2d. The repulsive force is short-ranged and is generally caused by osmotic and elastic interaction of the ligand shell.^[16] Some prominent steric stabilizers involved in nanoparticle synthesis are trioctylphosphine, oleic acid, oleylamine or polymers such as polyvinyl alcohol or polyvinylpyrrolidone.^[6]

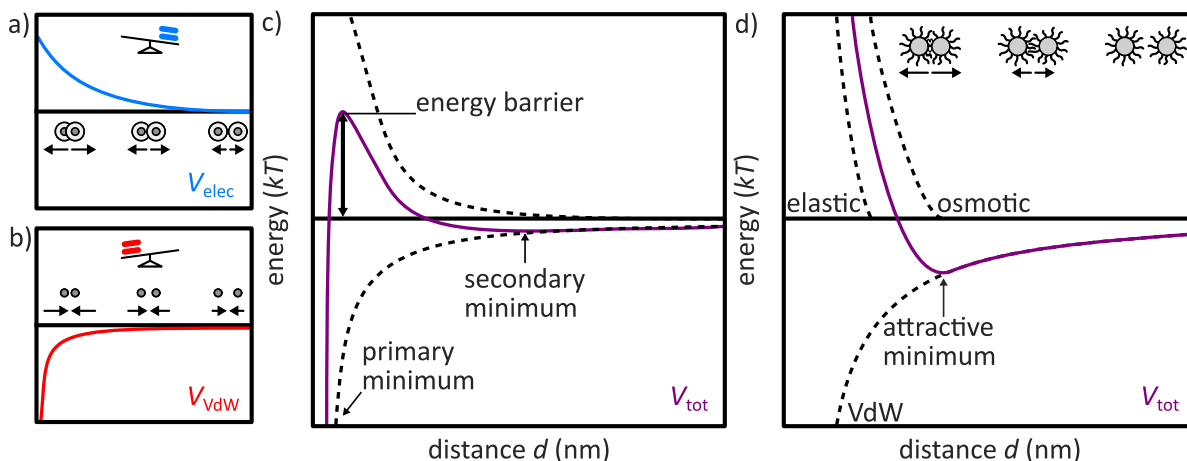


Figure 2.2: Schematic energy diagram for a-c) electrostatically and d) sterically stabilized spherical particles as a function of the interparticle distance d . a) The electrostatic repulsion and b) van-der-Waals attraction add up to c) a total interaction profile featuring two minima and an energy barrier. The barrier caused by the electrostatic repulsion defines the stability of the dispersion and prevents particle agglomeration. d) The elastic and osmotic repulsive ligand interaction of two sterically stabilized particles overcome the attractive Van-der-Waals attraction at short interparticle distances and prevents agglomeration. Adapted with permission from reference [16].

To induce gelation, the interparticle distances must be shortened. Depending on the stabilizer of the nanoparticles, different strategies can be employed. For electrostatically stabilized particles, the long-ranged electrostatic repulsion must be reduced by the addition of destabilizers so that individual particles overcome the repulsive energetic barrier and stick to one another upon collision, as depicted in Figure 2.3a. From equation 2.1 it becomes apparent that the electrostatic interaction potential V_{elec} can be altered by changing the surface potential Ψ_0 , the dielectric constant ϵ or the Debye length λ_D . The surface potential can be altered by changing the pH of the dispersion, by the addition of salts or by replacing charged with neutral ligands.^[16,17] However, tuning the surface charge via pH is challenging since small changes in pH close to the isoelectric point result in drastic changes of the surface charge.^[18] A better control on destabilization can be achieved by first creating a stable dispersion at high or low pH, followed by a precise reduction of the electrostatic repulsion via the addition of a cosolvent with smaller dielectric constant ϵ .^[19] This can be combined with gentle heating of the destabilized nanoparticle dispersion to accelerate the kinetics by thermally overcoming the energetic barrier of the total interaction profile V_{tot} (Figure 2.2a).^[16]

For sterically stabilized particles, the removal of ligands via the addition of a destabilizer leads to a successive destabilization and gelation of particles, as depicted in Figure 2.3b. Ligands

are typically removed by washing, dialysis or oxidative ligand removal.^[6,20] By selective ligand removal from certain crystallographic facets an orientated attachment of nanoparticles can be achieved.^[21] Besides controlled destabilization, enhancement of interparticle attraction is also a viable approach to induce nanoparticle gelation which can be achieved by the addition of secondary compounds that act as bridging molecules between individual nanoparticles, as illustrated in Figure 2.3c. The type of molecule is selected in consideration of the material-specific surface chemistry. For metal oxide nanoparticles, macromolecules based on polyethylene glycol are commonly used.^[22,23] However, depending on concentration the same macromolecule can induce different phase behaviors where the bridging gel might become fluid when exceeding a certain concentration threshold (Figure 2.3c).^[13] Instead of bridging particles by the aid of macromolecules, gelation can also be induced by the addition of linkers such as metal ions that form coordinated bonds between ligands of neighboring nanoparticles (Figure 2.3d). This approach can be applied to a broad material library as long as the organic ligands are terminated with a complexing group. Examples include CdSe, PbS, PbSe, ZnO nanospheres, CdSe nanoplatelets, and ZnO nanorods covered with different inorganic ligands such as S^{2-} , I^- , Cl^- , F^- , Ga/I, and In/Cl complexes or CdS and CdSe quantum dots functionalized with carboxylate-terminated ligands. Here gelation was induced by adding optimal amounts of Cd^{2+} , Pb^{2+} , Zn^{2+} , Ni^{2+} , Co^{2+} , Ag^+ ions.^[24,25] An intrinsic benefit of coordinated bonding as a gelation strategy is the formed metal coordination complex which can induce further functionality in the gel compared to the individual nanoscopic building blocks.^[13]

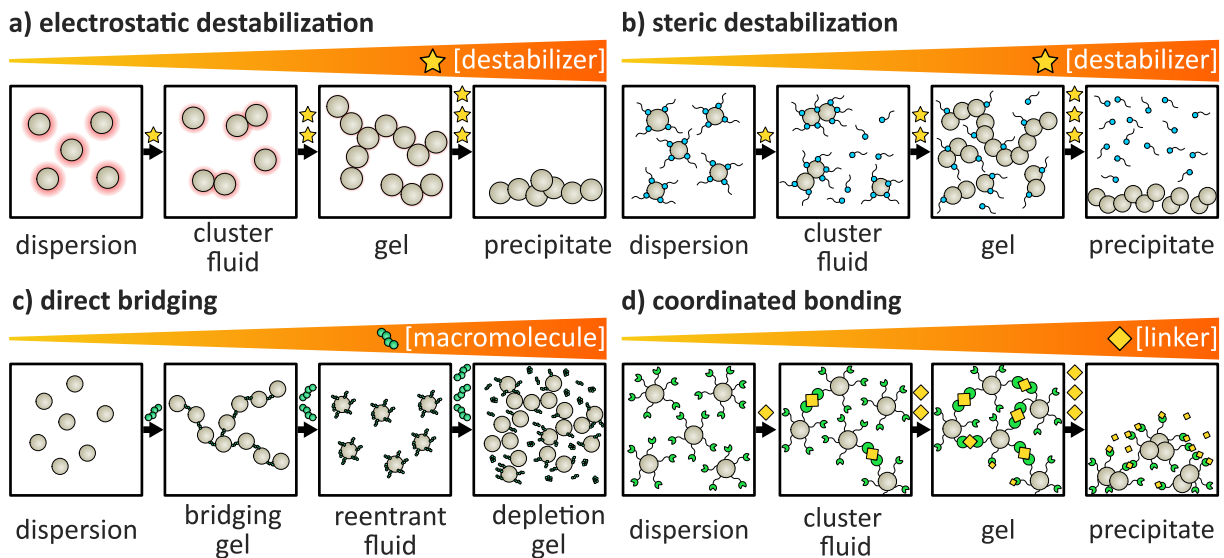


Figure 2.3: Schematic overview of potential nanoparticle gelation strategies including a) electrostatic destabilization, b) steric destabilization, c) direct bridging, and d) coordinated bonding. b-d) adapted with permission from reference [13]. a) Own creation following similar format.

Generally, multiple strategies for the gelation of colloidal nanomaterials emerged that preserve the inherent nanoscale properties in macroscopic objects. However, if not well controlled, the destabilization will lead to the irreversible precipitation of nanoparticle aggregates which goes along with a loss of properties of the original nanoscopic building blocks.^[13] Moreover, each approach has its own strengths and weaknesses that have to be evaluated for the application

of the final material. For example, controlled destabilization always leads to a direct linkage of nanoparticles, which prevents the realization of aerogels that preserve the excitation of plasmonic resonances in individual building blocks. Here, attractive gelation approaches such as direct bridging or coordinated bonding are a better option and even allow to control the optical properties by controlling the spacer distance.^[22] In contrast, nanoparticle linkage via electrostatic or steric destabilization is beneficial for photocatalytic application. Here, photoexcited charge carriers can diffuse over micrometer-scale distances along the nanoparticle chains which leads to improved electron hole separation.^[26] Moreover, the high-surface area architecture will not be covered by less organic material than for attractive gelation which enables a good interaction of the reactant with the nanomaterial. Besides, gels formed via direct bridging or coordinated bonding can be reversible. For example, it was demonstrated that the gel character of terpyridine-terminated indium tin oxide nanocrystals gelled with Co^{2+} ions is lost upon heating.^[27] Other linking chemistries could be responsive to alternative stimuli, such as light, magnetic field or pH changes, which needs to be considered when designing an aerogel processing scheme that relies on direct bridging or coordinated bonding.

2.3 Solvent Extraction – Conversion of Wet Gels to Aerogels

The final step in the aerogel processing scheme is the extraction of solvent from the wet gel. To avoid a collapse of the 3D nanoporous network and the formation of a dense xerogel due to high capillary tension at the liquid-gas interface, special drying techniques such as freeze and supercritical drying instead of simple evaporation are commonly applied with phase changes being liquid-solid-gas and liquid-supercritical fluid-gas, respectively (Figure 2.4).^[28] Supercritical drying involves the heating of the wet gel in a closed vessel so that the pressure and temperature exceed the critical point of the liquid. By releasing the pressure at constant temperature, a transition from the supercritical to the gas phase can be performed. Due to the relatively low supercritical temperature of 31 °C and supercritical pressure of 7.37 MPa, the solvent of the wet gel is typically replaced with liquid carbon dioxide for supercritical drying.^[2] In freeze drying water is commonly the solvent of choice. Here, the freezing of the wet gel below the triple point is followed by a sublimation at reduced pressure to perform a transition from the solid to the gas phase. Nevertheless, the use of freeze-drying remains limited because the volume expansion of the solvent during freezing results in cracking.^[29] However, in recent years freeze drying gained usage for the preparation of aerogels from 2D nanomaterials such as graphene, which can endure the expansion of ice during freezing due to the high flexibility of the atomically thin 2D building blocks.^[30] Since supercritical drying does not have this limitation to a certain type of nanomaterial, it is still the more versatile technique for the production of high-quality aerogels.^[31]

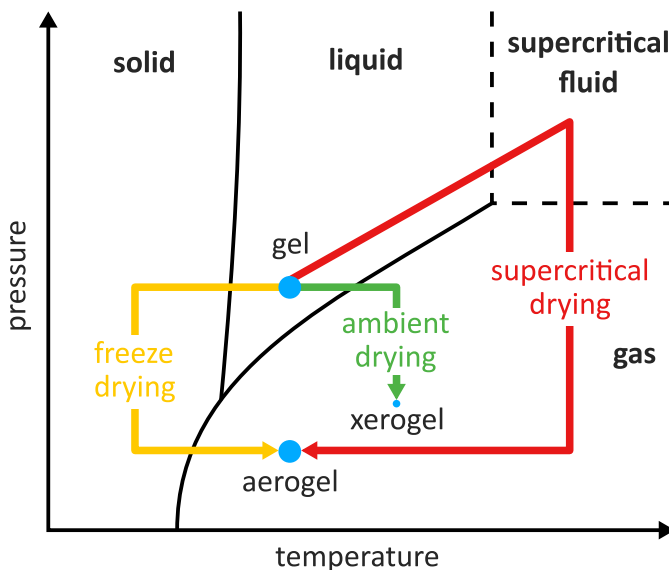


Figure 2.4: General phase diagram of the solvent in a wet gel and the pressure-temperature changes during supercritical, ambient and freeze drying. Strong capillary forces during the transition from the liquid to the gas phase results in drastic shrinkage and the formation of an xerogel. In contrast, supercritical and freeze drying preserve the high porosity of the wet gel with minimum shrinkage in form of an aerogel by avoiding a direct transition from the liquid to the gas phase.

2.4 Literature Review – State of the Art Nanoparticle-Based Aerogels

Following the principles of gelation and solvent extraction, a broad variety of nanomaterials can be processed into aerogels. Examples of typical aerogels are shown in Figure 2.5. These include metals, metal oxides, metal nitrides, metal phosphide, transition metal chalcogenides, carbon materials as well as combinations thereof. However, what stands out when looking at the different aerogels is their cylindrical shape. This is because gelation either results in volume-filling gels, which adapt the geometry of the surrounding mold, or in loosely packed, voluminous precipitate, that flocculate as gel fragments from solution. However, to apply these materials for different kinds of applications the properties of the nanoscale building blocks not only need to be preserved in a macroscopic body, but more importantly the shape needs to be tailored for the target application to extract the maximum performance from the nanoporous material. We will discuss potential aerogel shaping methods in chapter 3.

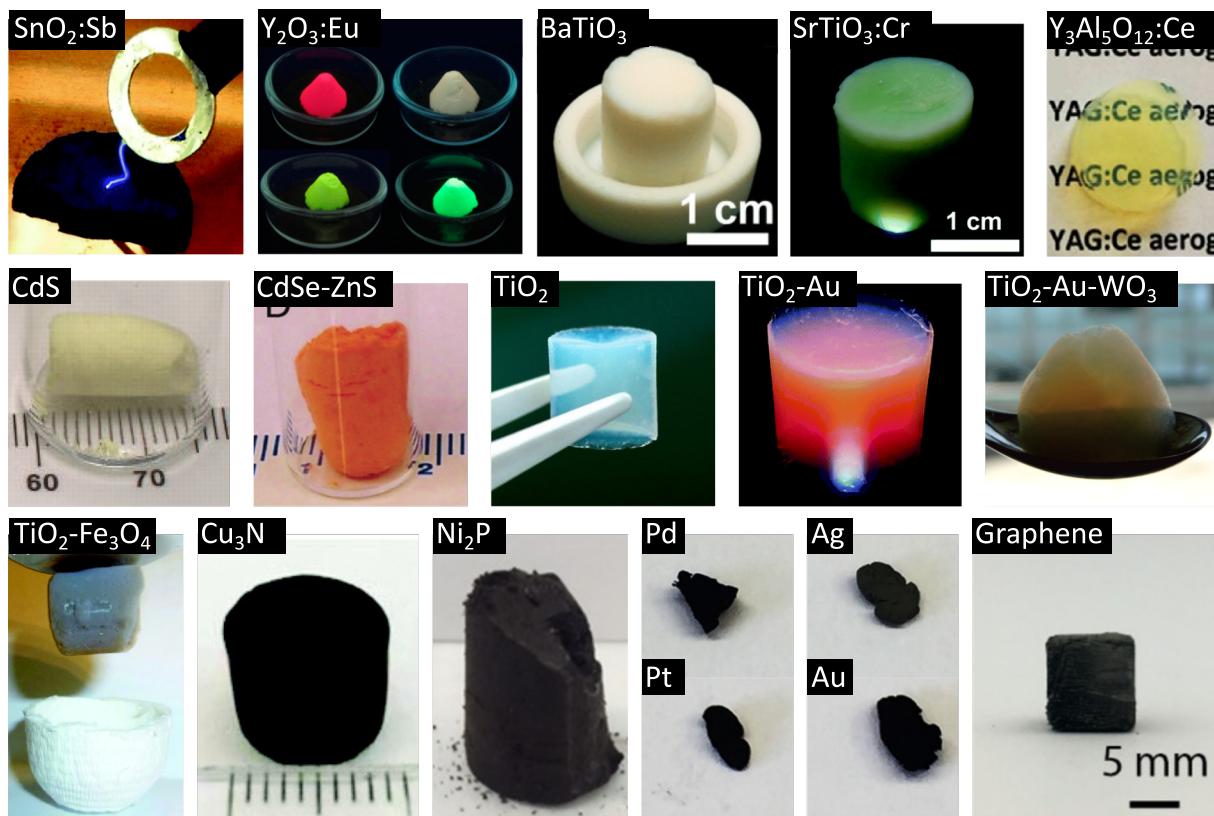


Figure 2.5: Examples of nanoparticle-based aerogels. By gelation of nanoparticle dispersion and subsequent solvent extraction, a large variety of different nanomaterials can be processed into macroscopic aerogels, including metals, metal oxides, nitrides, phosphides, chalcogenides, and carbon materials. Adapted with permission from reference [14]. Figures reprinted with permission from reference SnO₂:Sb,^[32] Y₂O₃:Eu,^[33] BaTiO₃,^[34] SrTiO₃:Cr,^[35] Y₃Al₅O₁₂:Ce,^[19] CdS,^[20] CdSe-ZnS,^[20] TiO₂,^[16] TiO₂-Au,^[5] TiO₂-Au-WO₃,^[36] TiO₂-Fe₃O₄,^[37] Cu₃N,^[38] Ni₂P,^[39] Pd, Ag, Pt and Au,^[40] graphene,^[41].

Bibliography

- [1] J. Fricke and A. Emmerling, *J. Sol-Gel Sci. Technol.*, 1998, **13**, 299–303.
- [2] A. C. Pierre and G. M. Pajonk, *Chem. Rev.*, 2002, **102**, 4243–4266.
- [3] D. W. Schaefer and K. D. Keefer, *Phys. Rev. Lett.*, 1986, **56**, 2199–2202.
- [4] H. D. Gesser and P. C. Goswami, *Chem. Rev.*, 1989, **89**, 765–788.
- [5] F. Rechberger and M. Niederberger, *Nanoscale Horiz.*, 2017, **2**, 6–30.
- [6] C. Ziegler, A. Wolf, W. Liu, A.-K. Herrmann, N. Gaponik and A. Eychmüller, *Angew. Chem. Int. Ed.*, 2017, **56**, 13200–13221.
- [7] J. Fricke and A. Emmerling, in *Aerogels—Preparation, properties, applications*, ed. R. Reisfeld and C. K. Jørgensen, Springer Berlin Heidelberg, Berlin, Heidelberg, 1992, pp. 37–87.
- [8] S. S. Kistler, *Nature*, 1931, **127**, 741–741.
- [9] D. V. Talapin, J.-S. Lee, M. V. Kovalenko and E. V. Shevchenko, *Chem. Rev.*, 2010, **110**, 389–458.
- [10] D. Mateo, J. L. Cerrillo, S. Durini and J. Gascon, *Chem. Soc. Rev.*, 2021, **50**, 2173–2210.
- [11] M. A. Boles, D. Ling, T. Hyeon and D. V. Talapin, *Nat. Mater.*, 2016, **15**, 141–153.
- [12] A. Heuer-Jungemann, N. Feliu, I. Bakaimi, M. Hamaly, A. Alkilany, I. Chakraborty, A. Masood, M. F. Casula, A. Kostopoulou, E. Oh, K. Susumu, M. H. Stewart, I. L. Medintz, E. Stratakis, W. J. Parak and A. G. Kanaras, *Chem. Rev.*, 2019, **119**, 4819–4880.
- [13] A. M. Green, C. K. Ofosu, J. Kang, E. V. Anslyn, T. M. Truskett and D. J. Milliron, *Nano Lett.*, 2022, **22**, 1457–1466.
- [14] F. Matter, M. Niederberger and F. Putz, *Chimia*, 2021, **75**, 387–397.
- [15] Z. Ren, J. Yu, Z. Pan, J. Wang and X. Zhong, *ACS Appl. Mater. Interfaces*, 2017, **9**, 18936–18944.
- [16] F. Matter, A. L. Luna and M. Niederberger, *Nano Today*, 2020, **30**, 100827.
- [17] K. G. S. Ranmohotti, X. Gao and I. U. Arachchige, *Chem. Mater.*, 2013, **25**, 3528–3534.
- [18] J. M. Berg, A. Romoser, N. Banerjee, R. Zebda and C. M. Sayes, *Nanotoxicology*, 2009, **3**, 276–283.
- [19] M. Odziomek, F. Chaput, F. Lerouge, C. Dujardin, M. Sitarz, S. Karpati and S. Parola, *Chem. Mater.*, 2018, **30**, 5460–5467.
- [20] I. U. Arachchige and S. L. Brock, *J. Am. Chem. Soc.*, 2007, **129**, 1840–1841.
- [21] F. J. Heiligtag, M. D. Rossell, M. J. Süess and M. Niederberger, *J. Mater. Chem.*, 2011, **21**, 16893–16899.
- [22] C. A. S. Cabezas, G. K. Ong, R. B. Jadrich, B. A. Lindquist, A. Agrawal, T. M. Truskett and D. J. Milliron, *Proc. Natl. Acad. Sci.*, 2018, **115**, 8925–8930.

- [23] J. Song, M. H. Rizvi, B. B. Lynch, J. Ilavsky, D. Mankus, J. B. Tracy, G. H. McKinley and N. Holten-Andersen, *ACS Nano*, 2020, **14**, 17018–17027.
- [24] C. C. Hewa-Rahinduwage, K. L. Silva, S. L. Brock and L. Luo, *Chem. Mater.*, 2021, **33**, 4522–4528.
- [25] V. Sayevich, B. Cai, A. Benad, D. Haubold, L. Sonntag, N. Gaponik, V. Lesnyak and A. Eychmüller, *Angew. Chem. Int. Ed.*, 2016, **55**, 6334–6338.
- [26] A. L. Robinson, V. Stavila, T. R. Zeitler, M. I. White, S. M. Thornberg, J. A. Greathouse and M. D. Allendorf, *Anal. Chem.*, 2012, **84**, 7043–7051.
- [27] J. Kang, S. A. Valenzuela, E. Y. Lin, M. N. Dominguez, Z. M. Sherman, T. M. Truskett, E. V. Anslyn and D. J. Milliron, *Sci. Adv.*, 2022, **8**, eabm7364.
- [28] S. L. Brock, in *Aerogels: Disordered, Porous Nanostructures*, John Wiley & Sons, Ltd, 2009, book section 8, pp. 207–241.
- [29] Z. Zhao, D. Chen and X. Jiao, *J. Phys. Chem. C*, 2007, **111**, 18738–18743.
- [30] H. Kong, Y. Chen, G. Yang, B. Liu, L. Guo, Y. Wang, X. Zhou and G. Wei, *Nanoscale Horiz.*, 2022, **7**, 112–140.
- [31] F. Mißfeldt, P. Gurikov, W. Lölsberg, D. Weinrich, F. Lied, M. Fricke and I. Smirnova, *Ind. Eng. Chem. Res.*, 2020, **59**, 11284–11295.
- [32] F. Rechberger, G. Ilari and M. Niederberger, *Chem. Commun.*, 2014, **50**, 13138–13141.
- [33] W. Cheng, F. Rechberger and M. Niederberger, *ACS Nano*, 2016, **10**, 2467–2475.
- [34] F. Rechberger, F. J. Heiligttag, M. J. Süess and M. Niederberger, *Angew. Chem. Int. Ed.*, 2014, **53**, 6823–6826.
- [35] F. Rechberger, G. Ilari, C. Willa, E. Tervoort and M. Niederberger, *Mater. Chem. Front.*, 2017, **1**, 1662–1667.
- [36] F. J. Heiligttag, W. Cheng, V. R. de Mendonça, M. J. Süess, K. Hametner, D. Günther, C. Ribeiro and M. Niederberger, *Chem. Mater.*, 2014, **26**, 5576–5584.
- [37] F. J. Heiligttag, M. J. I. Airaghi Leccardi, D. Erdem, M. J. Süess and M. Niederberger, *Nanoscale*, 2014, **6**, 13213–13221.
- [38] R. Deshmukh, E. Tervoort, J. Käch, F. Rechberger and M. Niederberger, *Dalton Trans.*, 2016, **45**, 11616–11619.
- [39] A. Hitihami-Mudiyanselage, K. Senevirathne and S. L. Brock, *Chem. Mater.*, 2014, **26**, 6251–6256.
- [40] R. Du, Y. Hu, R. Hübner, J.-O. Joswig, X. Fan, K. Schneider and A. Eychmüller, *Sci. Adv.*, 2019, **5**, eaaw4590.
- [41] M. Yang, N. Zhao, Y. Cui, W. Gao, Q. Zhao, C. Gao, H. Bai and T. Xie, *ACS Nano*, 2017, **11**, 6817–6824.

3 Geometric Control during Aerogel Processing

This chapter presents the geometrical length scales covered in traditional and novel aerogel shaping methods. We review potential 3D printing techniques, introduce fundamental ink design principles, and discuss drawbacks of already reported aerogel printing methods. Based on that, we derive guidelines for the formulation of a new class of so-called *gelled nanoinks*, which lay the foundation for the 3D printing process developed in this Ph.D. thesis.

3.1 Traditional Shaping Methods

Aerogels are often brittle materials, thus shape control via subtractive approaches such as drilling, milling, or sawing are difficult to achieve. To circumvent this problem, the aerogel geometry is defined by shaping the still liquid or slightly gelled dispersion before gelation is fully completed. This approach was successfully demonstrated for a range of traditional shaping methods including spin coating,^[1] wet spinning,^[2-6] emulsion techniques,^[7-9] spraying processes,^[10,11] and gel casting,^[12,13] to prepare thin films, thin fibers, microspheres, and macroscopic objects, as illustrated in Figure 3.1a. However, if we compare the covered geometrical length scale of each technique in Figure 3.1.b, we see that each traditional shaping method is limited to a narrow length scale interval. For example, microspheres or fibers maintain nanoscopic properties on a micrometer length scale, but are present as a loose accumulation with no discrete macroscopic shape. Similarly, gel casting maintains nanoscopic properties in macroscopic 3D objects, but preclude a well-defined microstructure in between. Although some microstructuring can be achieved by incorporating scaffolds,^[14] the range of geometries is still limited due to difficulties of subsequent mold removal. To overcome this obstacle, another way of aerogel processing is needed that enables the fabrication of very complex architectures which cover multiple length scales at once. Here 3D printing can make a huge impact since this technology already demonstrated the creation of intricate geometries with widespread feature sizes - from nanometric metamaterials to meter sized buildings.^[15,16] To translate the class of nanoparticle-based aerogels to 3D printing, we first need to understand the underlying principle of the novel fabrication technique. We cover the most common 3D printing technologies in the following section and discuss the advantages, limitations, and opportunities of each technique. Based on that we evaluate the eligibility of each method for the 3D printing of aerogels and review state-of-the-art aerogel printing approaches from literature.

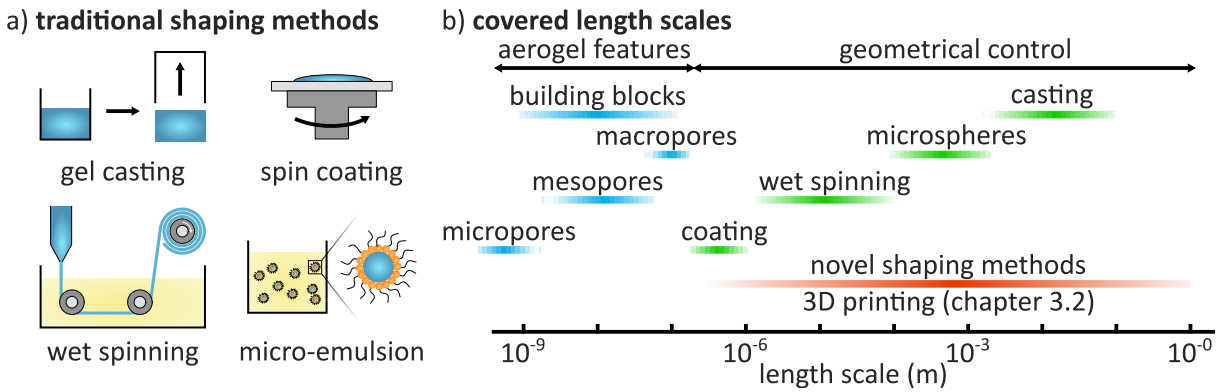


Figure 3.1: Length scale control during aerogel processing. a) Scheme of traditional shaping methods including gel casting, spin coating, wet spinning, and micro-emulsion. b) Traditional shaping methods preserve the nanoscopic feature sizes of aerogels while controlling the geometry in a narrow length scale window. 3D Printing is a novel shaping method and enables geometric control from sub-micrometer to macroscopic length scales.

3.2 3D Printing – A Novel Shaping Method

3D printing is an additive, bottom-up fabrication process that creates physical objects from digital models in a layer-by-layer fashion and several approaches have been invented since the late 1970s.^[17] We summarize the most common methods in Figure 3.2. They are generally classified into resin-based, powder-based, and extrusion-based printing approaches.

Extrusion-based techniques are subdivided in fused-deposition modeling (FDM, Figure 3.2a) and direct ink writing (DIW, Figure 3.2.b). FDM creates objects by extruding a molten plastic filament through a heated nozzle which is followed by material solidification upon cooling. The printing approach relies on thermoplastics and nanomaterials can only be printed by formulating polymer based composites.^[18] Here, the main challenge is particle agglomeration that leads to clogging at high particle loadings and prevents use of fine nozzles for high printing resolution.^[19] In contrast, DIW is not limited to thermoplastics, but uses materials that are already soft at ambient conditions and extruded through thin nozzles from a cartridge. Patented in 1997, DIW was initially developed to 3D print ceramic pastes.^[20,21] Since then, the material library extended to process practically any soft material, as long as the ink maintains its shape after extrusion. Examples include cellular gels, polymers, cement, glass, metals or even chocolate.^[22] The minimum printable feature size is defined by the nozzle diameter and sizes as low as 600 nm were reported.^[23–25] As for FDM, DIW can combine multiple printheads into single print. Moreover, DIW allows the use of inline mixers to create material gradients for regional differences in material composition and functionality.^[26,27] The extrusion driving force for DIW is either based on pneumatic pressure, a syringe pump, or a screw extruder (Figure 3.2b).

For optical printing methods the material to be printed is spread on a build plate in form of a precursor which is converted into the final material by the use of light. Stereolithography (SLA) and digital light processing (DLP) selectively polymerize a liquid resin with UV light either by scanning a laser over the resin surface (Figure 3.2c) or by projecting an entire 2D slice (Figure 3.2d). Here, the resolution is constrained to the dimension of the laser, pixels, or micromirrors and is typically below 50 μm . Two-photon lithography is a related printed technique

than can achieve much finer resolutions down to hundreds of nanometers, but with a throughput too slow for practical applications.^[28] For optical printing the resins are typically a mixture of epoxides, acrylates, and a photoinitiator. Inorganic materials such as ceramics or glass can be 3D printed by suspending particles in the photoresin.^[29,30] However, incorporating concentrated suspensions can be a challenge because of increased light scattering and an accompanied loss in resolution. Also, thermal post-processing are required to obtain pure inorganic materials which goes along with shrinkage and the formation of a densified object.^[31]

Powder-based methods selectively fuse particles in a thin layer of powder spread across the build plate area. Here, particle fusion can be achieved by raster scanning a high-power laser beam on the surface (Selective Laser Sintering (SLS), Figure 3.2e) or by depositing a liquid binder with an inkjet printhead (binder jetting, Figure 3.2f). In both processes, the removal of unfused powder is a challenge. Also, thermal post-processing is needed to remove the binder and to complete sintering. The typical resolution for SLS and binder jetting is around 20 μm and 100 μm , respectively.^[31]

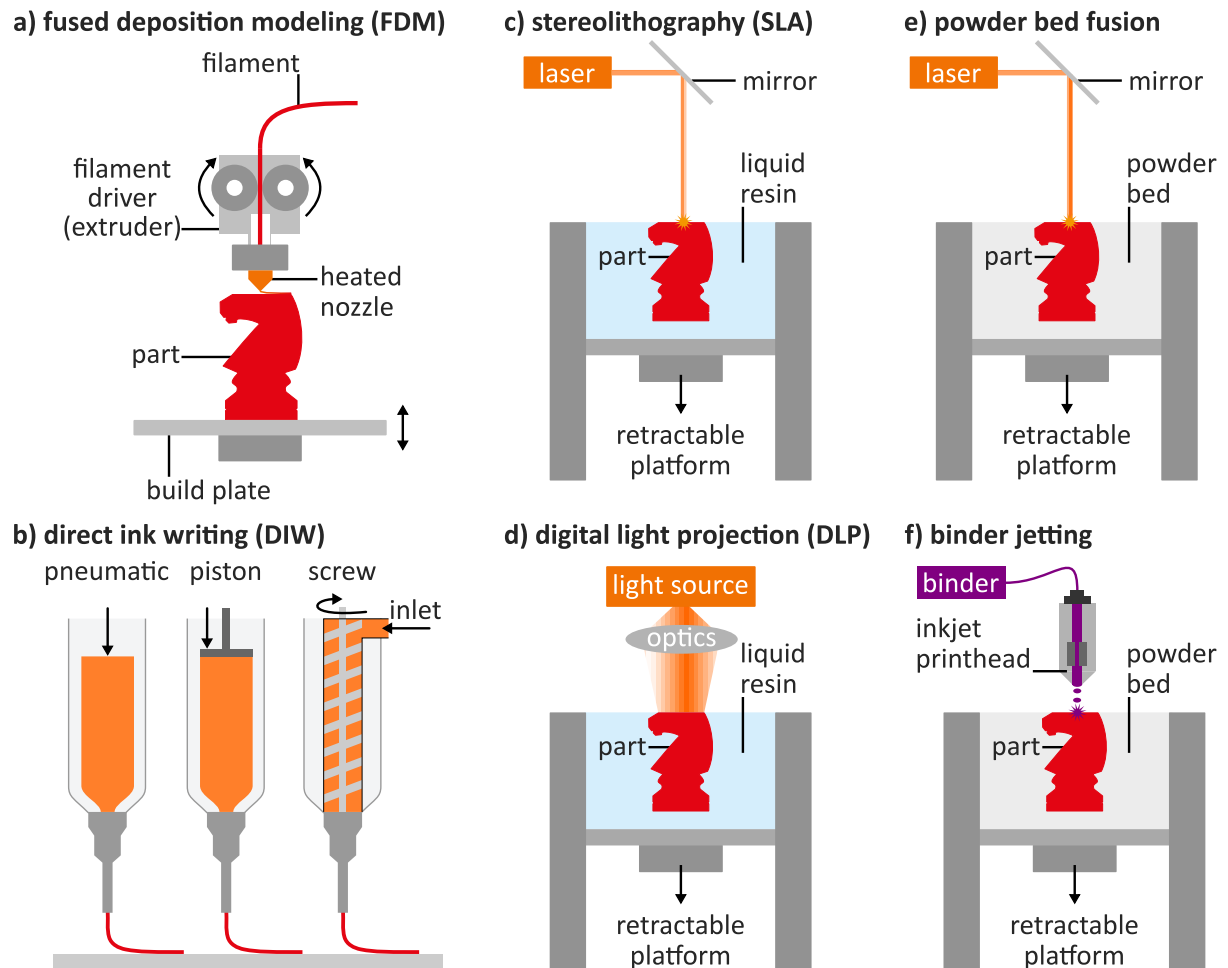


Figure 3.2: Scheme of common 3D printing methods including a) fused deposition modeling FDM, b) direct ink writing DIW, c) stereolithography (SLA), d) digital light processing (DLP), e) selective laser sintering (SLS), and f) binder jetting. a-e) adapted with permission from reference [32]. d) Own creation following similar format.

Independent of the 3D printing method, all approaches enable a unique pathway for geometric complexity and structuring from the micro- to macroscopic length scale. Combined with the ongoing introduction of new materials, 3D printing currently transforms from rapid prototyping to manufacturing of functional materials including lightweight bionic aircraft parts,^[33] wearable electronics,^[34] batteries,^[28] or catalytic systems.^[35] In terms of functionality, nanoparticle-based aerogels are a highly promising material class for 3D printing, since their intriguing macroscopic properties are a result of the atomically defined nanobuilding blocks, as discussed in chapter 2.

3.3 3D Printed Aerogels

The FDM, SLS and binder jetting method either rely on thermoplastic materials or sintering of a micropowder into a densified object and are thus not suited for the 3D printing of highly porous, nanoparticle-based aerogels. DIW and optical resin-based techniques such as SLA are more promising due to a higher flexibility in ink composition. However, aerogels are a relatively new class of material in the context of 3D printing and reported procedures still cannot process nanoparticle-aerogels of comparable quality and material variety as for the traditional shaping methods presented in chapter 2. Therefore, development of new ink compositions and 3D printing routines are still needed and an ongoing process. The first 3D printed aerogels date back to 2015 when graphene and a silica-polymer composite aerogel were fabricated by DIW and SLA, respectively.^[36,37] Even though both approaches could demonstrate 3D printing of aerogels in the same year, DIW nowadays evolved into the method of choice.^[22,38] One fundamental limitation for light-based processes such as SLA is light scattering at the dispersed nanomaterials, which typically has a adversely effect on the curing and either reduces resolution or prevents solidification.^[39] Moreover, SLA relies on acrylate resins and photoinitiators that remain trapped in the final aerogel post-printing which results in much lower specific surface areas and porosity than aerogels prepared by traditional shaping methods such as gel casting. Furthermore, when materials like silica-polymer composites are heat treated to burn off the organic, fused silica glass instead of an silica aerogel is obtained.^[30] Inks for DIW do not rely on certain ingredients, but should meet specific rheologic requirements to be printable.^[40] The following sections will discuss a general ink formulation guideline and review typical ingredients for aerogel inks. We shall learn that established inks recipes compromise the quality of the aerogel to achieve printability and that material composition differ drastically from gelation procedures of nanoparticle-based aerogels discussed in chapter 2. Based on that we will define targets that a newly developed ink should fulfill to 3D print nanoparticle-based aerogels of comparable quality than traditional shaping methods.

3.3.1 Ink Formulation Guidelines

An ink for DIW is considered printable if it can be extruded through a nozzle in form of a continuous filament and if the printed object accurately represents a predefined digital model. For this, we can identify the following ink requirements:^[41]

1. The ink should flow smoothly through the fine orifice of the deposition nozzle without forming any agglomerates to avoid clogging.
2. The flow of the ink should be initiated by a moderate pressure to enable extrusion through thin micronozzles for highest printing resolution.
3. After deposition, the ink must rapidly transition from a fluid-like to a solid-like substance to retain the shape of the extruded filament.
4. The ink needs to possess a high enough mechanical strength to support the weight of the printed structure.

Above ink requirements are typically fulfilled by tuning the ink composition for a shear-thinning, viscoelastic characteristic and often involves the addition of rheologic additives. Here, the ink formulation is guided by the use of a rheometer, which mimics the shear stress present during 3D printing. We will cover the key principles of rheology in chapter 4.

3.3.2 State of the Art Aerogel Inks

Ink formulation for DIW of nanomaterials historically evolved from ceramic processing. In fact, DIW was originally developed for the fabrication of complex ceramic structures and significant effort has been devoted to the study of ceramic inks in the past.^[42,43] Here, inks were formulated by electrostatically stabilizing ceramic particles with polyelectrolytes such as polyacrylic acid or polyethylenimine, followed by a change of pH or addition of salts to induce gelation,^[25,44,45] or by utilizing a weak hydrogel such as Pluronic F127 as a ink matrix which was loaded with ceramic powder.^[41,46] Since ceramics were meant to result in densified objects without any further functionality, organics could easily be burned off post printing. Today, inks for the preparation of aerogels are still formulated following similar design principles – just with nanoscopic sized building blocks instead of microscopic ceramic particles – although highly porous and functional materials instead of densified ceramics are desired. Table 3.1 summarizes the main raw materials for molecular and nanoparticle-based aerogel inks. We see that nanoparticle-based inks are limited to anisotropic building blocks where graphene oxide plays a major role in most reported recipes and that aerogels with a 0D particle backbone are only accessible following the less attractive molecular gelation route.

Table 3.1: Examples of molecular and nanoparticle-based inks for DIW of aerogels.

aerogel type	particle	main raw materials	drying	ref.
SiO ₂ (molecular based)	0D	Dynasylan 40, SiO ₂ aerogel microparticle, poly(propylene glycol), bis(2-aminopropyl ether), 1-pentanol	supercritical drying	[47]
SiO ₂ -silk fibronin (molecular based)	0D	Silkworm cocoons, tetramethylorthosilicate, trimethoxysilane	supercritical drying	[48]
carbon (molecular based)	0D	resorcinol, formaldehyde, hydroxypropyl methyl- cellulose, fumed SiO ₂	supercritical drying	[49]
silver (nanomaterial-based)	1D	Ag nanowire, graphene oxide	freeze drying	[50]
graphene (nanomaterial-based)	2D	Graphene oxide poly(methacrylic acid)- polyethylene glycol co- polymer, glucono- δ -lactone	freeze drying	[37]
graphene (nanomaterial-based)	2D	Graphene oxide, fumed SiO ₂ , resorcinol, formaldehyde	freeze drying	[51,52]
graphene/ Ni _{0.33} Co _{0.66} (OH) ₂ (nanomaterial-based)	2D	Graphene oxide, Ni _{0.33} Co _{0.66} (OH) ₂ sodium alginate	freeze drying	[53]
graphene (nanomaterial-based)	2D	Graphene oxide, Pluronic F127 polypyrrole	freeze drying	[54]
graphene (nanomaterial-based)	2D	Graphene oxide, CaCl ₂	freeze drying	[55]
g-C ₃ N ₄ sodium alginate (nanomaterial-based)	2D	g-C ₃ N ₄ , Pluronic F127 sodium alginate	supercritical drying	[56]

The reason for the more frequent use of 2D materials in 3D printing is the more convenient processing. For instance, the anisotropic shape enables drastically lower volumetric loadings for the formation of a percolation network than 0D nanomaterials.^[57] Therefore, pore sizes are typically two orders of magnitude larger which substantially reduces capillary pressure during solvent evaporation and makes the aerogels network less prone to collapse.^[58] Moreover, graphene oxide features plenty functional groups that can induce gelation by electrostatic interaction. Thus, it was only a matter of time until 3D printing of a graphene aerogel was reported in 2015 by mixing graphene oxide with an polyelectrolyte as additive (Figure 3.3a-d).^[37] Based on that, multiple recipes for 3D printing of graphene aerogels were reported, that mostly continued to

use similar ink additives as for ceramic processing. However, in terms of applications additives are inactive species and limit the performance of the final device – for example in energy storage for graphene aerogels.^[43] Thus, additives must be removed at high temperatures, increasing the complexity and cost of the manufacturing process,^[43] and altering the properties of the incorporated nanomaterial due to change in morphology, crystal phase transition or drastic shrinkage of the printed object. To overcome this limitation, additive-free graphene oxide inks were formulated by concentrating a dispersion. Although graphene oxide is known to gel at mass loadings as low as 2.5 mg mL^{-1} ,^[59] much higher concentrations of up to 100 mg mL^{-1} were needed which compromises the porosity of the aerogel.^[60] To formulate a 3D printable ink at moderate GO concentration of 20 mg mL^{-1} and without the need of any polymeric additives, an electrostatic crosslinking via CaCl_2 was employed.^[55] Besides defining a dedicated class of inks, 2D nanomaterials are instrumental in enabling 3D printed aerogels based on 1D nanomaterials. So far, aerogels of such a nanoparticle backbone were only reported for 1D Ag nanowires where graphene oxide is needed to formulate printable inks by stabilizing the intersecting Ag nanowires, as illustrated in Figure 3.3e-g.

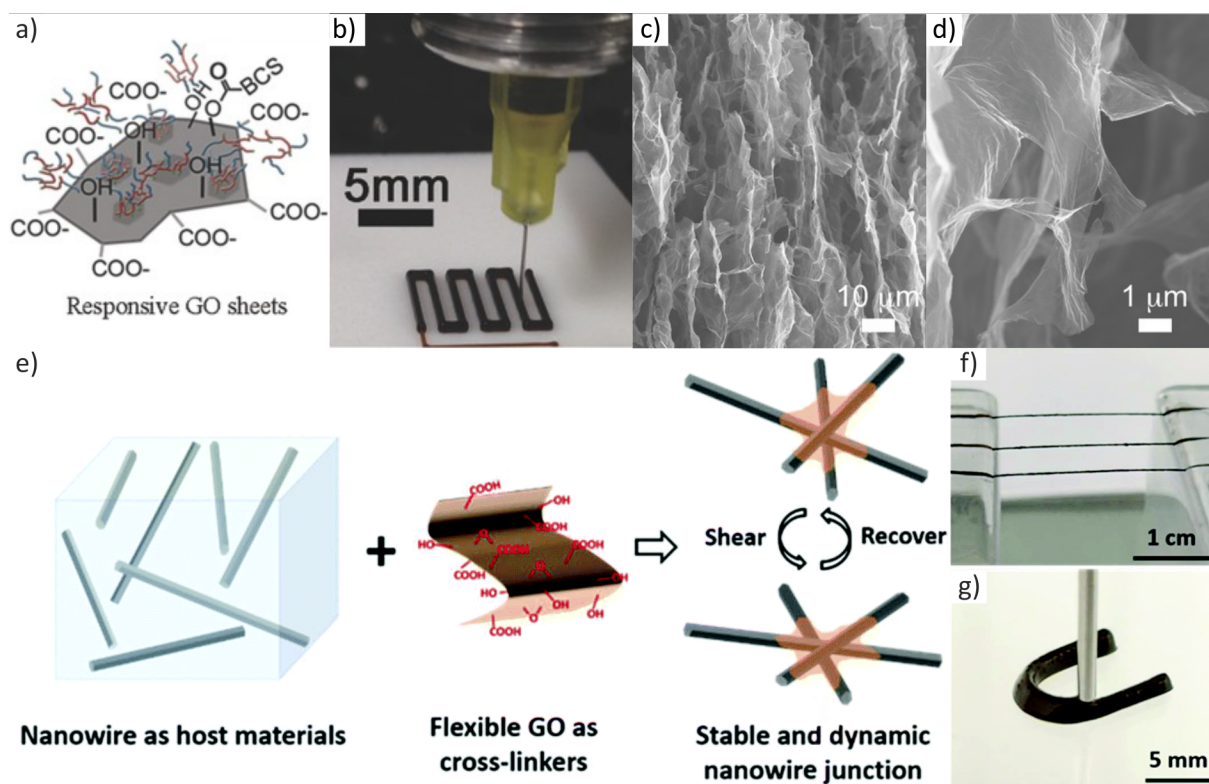


Figure 3.3: Examples of nanoparticle-based inks for DIW of aerogels. a) Schematic of a single graphene oxide sheet covered with a polyelectrolyte which enables the formulation of a 3D printable ink via electrostatic interaction. b) Photograph of the 3D printing process. c-d) Scanning electron microscopy images of the final aerogel reveal a pore size on the micrometer range and show that the aerogel is composed of stacked nanosheets. e) Ink formulation principle for 1D nanowires. A highly concentrated nanowire dispersion is crosslinked by the addition of graphene oxide sheets. f-g) Photographs of 3D printed Ag nanowire-based gels. Adapted with permission from reference [37] and [50].

Aerogels with a 0D particle backbone are only accessible via the less attractive molecular gelation route. Especially, metal oxide aerogels were believed to be unprintable due to a combination of solvent evaporation and poor rheological properties.^[61] Therefore, traditional recipes for molecular-derived metal oxide aerogels were vastly modified to achieve printability. Water and alcohol were replaced with high-boiling point solvents to limit evaporation while printing. However, a change in solvent composition also required a change in the gelation chemistry and inks could no longer be formulated according to classical hydrolysis and condensation reactions of metal-alkoxides. Instead commercial silica aerogel microparticles, polyethoxysiloxane and homogenizing, polymeric additives were dispersed in the high-boiling point solvent (Figure 3.4a-b).^[47] By loading the ink with other materials such as MnO_2 , composite aerogels can be printed. Even though the black color of the MnO_2 loaded aerogel appears homogenous on a macroscopic scale (Figure 3.4c), X-ray tomography measurements revealed an inhomogeneous distribution of MnO_2 on a microscopic level (Figure 3.4d). Further analysis of the unloaded SiO_2 aerogel via scanning electron microscopy indicates that the inhomogeneous distribution of MnO_2 is caused by the silica aerogel microparticles that are necessary to formulate a printable ink in the first place (Figure 3.4e-g).^[47] To avoid such microscopic grain boundaries and to enable nanoparticle-based aerogels based on a 1D nanoparticle backbone, we introduce *gelled nanoinks* as a new ink formulation concept in chapter 3.3.3.

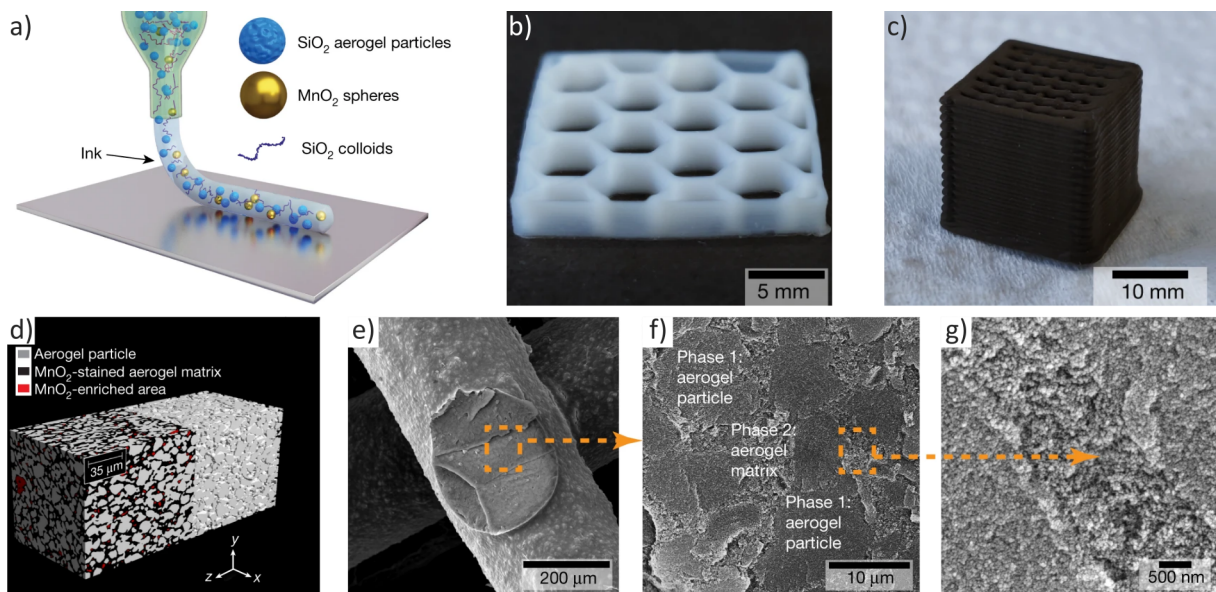


Figure 3.4: Examples of molecular-based inks for DIW of aerogels. a) The ink is formulated by dispersing SiO_2 aerogel microparticles, polymer additives, and SiO_2 colloids in a high-boiling point solvent. Optionally MnO_2 microparticles are added. b-c) Photograph of a pure SiO_2 and a $\text{MnO}_2/\text{SiO}_2$ aerogel, respectively. d) Tomographic 3D rendering of a $\text{MnO}_2/\text{SiO}_2$ composite aerogel. The rendering on the right side only displays the phase formed by SiO_2 aerogel microparticles. The rendering on the left shows the SiO_2 aerogel microparticles and a surrounding composite aerogel matrix which is formed from SiO_2 colloids loaded with MnO_2 microparticles. e) Scanning electron microscopy image of a single SiO_2 aerogel filament. f) Magnification of the orange boxed area in e) shows interlocked aerogel microspheres (darker grey) embedded in a silica aerogel matrix formed from SiO_2 colloids (lighter grey). g) Magnification of the grain interface. Adapted with permission from reference [47].

3.3.3 The Next Generation - Gelled Nanoinks

Looking back at the large nanomaterial library that could be processed via gel casting (Figure 2.5), we see that graphene oxide is the only nanomaterial building block that made the transition from traditional to novel shaping methods. Therefore, 3D printed nanomaterial-based aerogels can only take advantage of the high electrical conductivity of graphene and many other nanospecific properties like photoluminescence of quantum dots, plasmonic excitation in metallic nanostructures, or catalytic activity of metal oxides are not accessible so far. To overcome this problem, we set the goal to expand the aerogel ink library to other types of nanomaterials. Since additives were already shown to be detrimental for the performance of graphene aerogels in energy storage,^[43] we focus on designing an additive-free ink from scratch. To this end, we need to rethink the ink formulation principles that are currently omnipresent in the DIW community and leave the historic roots of ceramic processing behind. Instead, we need to transfer the principles of nanoparticle gelation discussed in chapter 2 to 3D printing. From the variety of nanoparticle gelation approaches (Figure 2.3) we identify controlled destabilization as the most promising route to formulate an additive-free ink. Moreover, we aim to eventually apply the 3D printed aerogels as a photocatalyst. Since TiO_2 is one of the most studied photoactive materials and is hence considered as a benchmark in photocatalysis,^[62] we select TiO_2 nanoparticles as our primary ink building block. From the previous discussion we learned that solvent evaporation is one of the major problems for 3D printing molecular-based metal oxide aerogels. Especially for printing of fine details, solvent evaporation can be extremely fast due to the large surface-to-volume ratio of the extruded filaments.^[61] Although high boiling point solvents relieve this problem, they are generally hydrophobic and lead to phase separation when combined with metal oxides in absence of additives.^[61] Therefore, a different approach is needed to avoid an evaporation induced damage of the gel network. Besides, formulating a viscoelastic ink with sufficient mechanical stability is another obstacle that needs to be solved to translate the principles of nanoparticle gelation to 3D printing. We shall learn in chapter 5 that we overcome both aspects by performing the print in a liquid bath charged with ammonia. Here, the liquid bath prevents solvent evaporation and the presence of ammonia increases the mechanical strength of the extruded ink by inducing further crosslinking in the gelled TiO_2 nanoparticle network. Our approach is a first step to translate the nanoparticle-based gelation scheme towards 3D printing and establishes a perspective to process other nanomaterials according to a similar protocol.

Bibliography

- [1] M.-H. Jo, J.-K. Hong, H.-H. Park, J.-J. Kim, S.-H. Hyun and S.-Y. Choi, *Thin Solid Films*, 1997, **308-309**, 490–494.
- [2] Z. Xu, Y. Zhang, P. Li and C. Gao, *ACS Nano*, 2012, **6**, 7103–7113.
- [3] Z. Xu, L. Peng, Y. Liu, Z. Liu, H. Sun, W. Gao and C. Gao, *Chem. Mater.*, 2017, **29**, 319–330.
- [4] G. Li, G. Hong, D. Dong, W. Song and X. Zhang, *Adv. Mater.*, 2018, **30**, 1801754.
- [5] O. A. Tafreshi, S. G. Mosanenzadeh, S. Karamikamkar, Z. Saadatnia, C. B. Park and H. E. Naguib, *Mater. Today Chem.*, 2022, **23**, 100736.
- [6] Y. Du, X. Zhang, J. Wang, Z. Liu, K. Zhang, X. Ji, Y. You and X. Zhang, *ACS Nano*, 2020, **14**, 11919–11928.
- [7] S. Gu, C. Zhai and S. C. Jana, *Langmuir*, 2016, **32**, 5637–5645.
- [8] M. Alnaief and I. Smirnova, *J. Supercrit. Fluids*, 2011, **55**, 1118–1123.
- [9] P. Paraskevopoulou, D. Chriti, G. Raptopoulos and G. C. Anyfantis, *Materials*, 2019, **12**, 1543.
- [10] S. Liao, T. Zhai and H. Xia, *J. Mater. Chem. A*, 2016, **4**, 1068–1077.
- [11] F. Mißfeldt, P. Gurikov, W. Lölsberg, D. Weinrich, F. Lied, M. Fricke and I. Smirnova, *Ind. Eng. Chem. Res*, 2020, **59**, 11284–11295.
- [12] Z. Saadatnia, S. G. Mosanenzadeh, E. Esmailzadeh and H. E. Naguib, *Sci. Rep.*, 2019, **9**, 1370.
- [13] L. S. White, D. R. Echard, M. F. Bertino, X. Gao, S. Donthula, N. Leventis, N. Shukla, J. Kośny, S. Saeed and K. Saoud, *Transl. Mater. Res.*, 2016, **3**, 015002.
- [14] M. Schreck, N. Kleger, F. Matter, J. Kwon, E. Tervoort, K. Masania, A. R. Studart and M. Niederberger, *Small*, 2021, **17**, 2104089.
- [15] L. R. Meza, S. Das and J. R. Greer, *Science*, 2014, **345**, 1322–1326.
- [16] H. Yin, M. Qu, H. Zhang and Y. Lim, *Technology/Architecture + Design*, 2018, **2**, 94–111.
- [17] X. Zhou and C.-j. Liu, *Adv. Funct. Mater.*, 2017, **27**, 1701134.
- [18] P. Zhang, Z. Wang, J. Li, X. Li and L. Cheng, *Nanotechnology Reviews*, 2020, **9**, 1594–1609.
- [19] A. D. Valino, J. R. C. Dizon, A. H. Espera, Q. Chen, J. Messman and R. C. Advincula, *Prog. Polym. Sci.*, 2019, **98**, 101162.
- [20] I. J. Cesarano and P. D. Calvert, *Freeforming objects with low-binder slurry*, U.S. Patent 6 027 326, October 1997.
- [21] J. Cesarano and S. Grieco, *Mater Technol*, 1997, **12**, 98–100.

- [22] M. A. S. R. Saadi, A. Maguire, N. T. Pottackal, M. S. H. Thakur, M. M. Ikram, A. J. Hart, P. M. Ajayan and M. M. Rahman, *Adv. Mater.*, 2022, **34**, 2108855.
- [23] G. Gratson, F. García-Santamaría, V. Lousse, M. Xu, S. Fan, J. Lewis and P. Braun, *Adv. Mater.*, 2006, **18**, 461–465.
- [24] G. M. Gratson, M. Xu and J. A. Lewis, *Nature*, 2004, **428**, 386–386.
- [25] J. Smay, G. Gratson, R. Shepherd, J. Cesarano III and J. Lewis, *Adv. Mater.*, 2002, **14**, 1279–1283.
- [26] D. Kokkinis, M. Schaffner and A. R. Studart, *Nat. Commun.*, 2015, **6**, 8643.
- [27] D. Kokkinis, F. Bouville and A. R. Studart, *Adv. Mater.*, 2018, **30**, 1705808.
- [28] K. Narita, M. A. Saccone, Y. Sun and J. R. Greer, *J. Mater. Res.*, 2022, **37**, 1535–1546.
- [29] J. W. Halloran, *Annu. Rev. Mater. Res.*, 2016, **46**, 19–40.
- [30] F. Kotz, K. Arnold, W. Bauer, D. Schild, N. Keller, K. Sachsenheimer, T. M. Nargang, C. Richter, D. Helmer and B. E. Rapp, *Nature*, 2017, **544**, 337–339.
- [31] C. Parra-Cabrera, C. Achille, S. Kuhn and R. Ameloot, *Chem. Soc. Rev.*, 2018, **47**, 209–230.
- [32] R. L. Truby and J. A. Lewis, *Nature*, 2016, **540**, 371–378.
- [33] L. Nickels, *Metal Powder Report*, 2015, **70**, 300–303.
- [34] A. D. Valentine, T. A. Busbee, J. W. Boley, J. R. Raney, A. Chortos, A. Kotikian, J. D. Berrigan, M. F. Durstock and J. A. Lewis, *Adv. Mater.*, 2017, **29**, 1703817.
- [35] S. Lawson, X. Li, H. Thakkar, A. A. Rownaghi and F. Rezaei, *Chem. Rev.*, 2021, **121**, 6246–6291.
- [36] S. Saeed, R. M. Al-Sobaihi, M. F. Bertino, L. S. White and K. M. Saoud, *J. Mater. Chem. A*, 2015, **3**, 17606–17611.
- [37] E. García-Tuñón, S. Barg, J. Franco, R. Bell, S. Eslava, E. D’Elia, R. C. Maher, F. Guitian and E. Saiz, *Adv. Mater.*, 2015, **27**, 1688–1693.
- [38] H. Tetik, Y. Wang, X. Sun, D. Cao, N. Shah, H. Zhu, F. Qian and D. Lin, *Adv. Funct. Mater.*, 2021, **31**, 2103410.
- [39] C. Zhu, A. J. Pascall, N. Dudukovic, M. A. Worsley, J. D. Kuntz, E. B. Duoss and C. M. Spadaccini, *Annu Rev Chem Biomol*, 2019, **10**, 17–42.
- [40] A. Corker, H. C. H. Ng, R. J. Poole and E. García-Tuñón, *Soft Matter*, 2019, **15**, 1444–1456.
- [41] E. Feilden, E. G.-T. Blanca, F. Giuliani, E. Saiz and L. Vandeperre, *J. Eur. Ceram. Soc.*, 2016, **36**, 2525–2533.
- [42] G. V. Franks, C. Tallon, A. R. Studart, M. L. Sesso and S. Leo, *J. Am. Ceram. Soc.*, 2017, **100**, 458–490.
- [43] S. Tagliaferri, A. Panagiotopoulos and C. Mattevi, *Materials Advances*, 2021, **2**, 540–563.
- [44] J. A. Lewis, J. E. Smay, J. Stuecker and J. Cesarano, *J. Am. Ceram. Soc.*, 2006, **89**, 3599–3609.
- [45] Q. Li and J. Lewis, *Adv. Mater.*, 2003, **15**, 1639–1643.
- [46] E. Munch, J. Franco, S. Deville, P. Hunger, E. Saiz and A. P. Tomsia, *JOM*, 2008, **60**, 54–58.
- [47] S. Zhao, G. Siqueira, S. Drdova, D. Norris, C. Ubert, A. Bonnin, S. Galmarini, M. Ganobjak,

- Z. Pan, S. Brunner, G. Nyström, J. Wang, M. M. Koebel and W. J. Malfait, *Nature*, 2020, **584**, 387–392.
- [48] H. Maleki, S. Montes, N. Hayati-Roodbari, F. Putz and N. Huesing, *ACS Appl. Mater. Interfaces*, 2018, **10**, 22718–22730.
- [49] S. Chandrasekaran, B. Yao, T. Liu, W. Xiao, Y. Song, F. Qian, C. Zhu, E. B. Duoss, C. M. Spadaccini, Y. Li and M. A. Worsley, *Mater. Horiz.*, 2018, **5**, 1166–1175.
- [50] S. Liu, X. Shi, X. Li, Y. Sun, J. Zhu, Q. Pei, J. Liang and Y. Chen, *Nanoscale*, 2018, **10**, 20096–20107.
- [51] C. Zhu, T. Y.-J. Han, E. B. Duoss, A. M. Golobic, J. D. Kuntz, C. M. Spadaccini and M. A. Worsley, *Nat. Commun.*, 2015, **6**, 6962.
- [52] C. Zhu, T. Liu, F. Qian, T. Y.-J. Han, E. B. Duoss, J. D. Kuntz, C. M. Spadaccini, M. A. Worsley and Y. Li, *Nano Lett.*, 2016, **16**, 3448–3456.
- [53] X. Tang, C. Zhu, D. Cheng, H. Zhou, X. Liu, P. Xie, Q. Zhao, D. Zhang and T. Fan, *Adv. Funct. Mater.*, 2018, **28**, 1805057.
- [54] Z. Qi, J. Ye, W. Chen, J. Biener, E. B. Duoss, C. M. Spadaccini, M. A. Worsley and C. Zhu, *Adv. Mater. Technol.*, 2018, **3**, 1800053.
- [55] Y. Jiang, Z. Xu, T. Huang, Y. Liu, F. Guo, J. Xi, W. Gao and C. Gao, *Adv. Funct. Mater.*, 2018, **28**, 1707024.
- [56] P. He, X. Tang, L. Chen, P. Xie, L. He, H. Zhou, D. Zhang and T. Fan, *Adv. Funct. Mater.*, 2018, **28**, 1801121.
- [57] F. Rasch, F. Schütt, L. M. Saure, S. Kaps, J. Strobel, O. Polonskyi, A. S. Nia, M. R. Lohe, Y. K. Mishra, F. Faupel, L. Kienle, X. Feng and R. Adelung, *ACS Appl. Mater. Interfaces*, 2019, **11**, 44652–44663.
- [58] M. A. Riaz, P. Hadi, I. H. Abidi, A. Tyagi, X. Ou and Z. Luo, *RSC Adv.*, 2017, **7**, 29722–29731.
- [59] S. Naficy, R. Jalili, S. H. Aboutalebi, R. A. Gorkin Iii, K. Konstantinov, P. C. Innis, G. M. Spinks, P. Poulin and G. G. Wallace, *Mater. Horiz.*, 2014, **1**, 326–331.
- [60] S. D. Lacey, D. J. Kirsch, Y. Li, J. T. Morgenstern, B. C. Zarket, Y. Yao, J. Dai, L. Q. Garcia, B. Liu, T. Gao, S. Xu, S. R. Raghavan, J. W. Connell, Y. Lin and L. Hu, *Adv. Mater.*, 2018, **30**, 1705651.
- [61] M. F. Bertino, *J. Sol-Gel Sci. Technol.*, 2018, **86**, 239–254.
- [62] H. Xu, S. Ouyang, L. Liu, P. Reunchan, N. Umezawa and J. Ye, *J. Mater. Chem. A*, 2014, **2**, 12642–12661.

4 Experimental Methods and Computational Modeling Tools

This chapter presents the main experimental methods and modeling tools that were established during this Ph.D. project. These include a 3D printing and photocatalysis setup, the basics of rheology, computational fluid dynamics, and the Monte Carlo Method for modeling of photon transport.

4.1 3D Printing Setup

The 3D printing method is based on DIW and uses an Engine HR 3D printer from Hyrel 3D. The printer utilizes a Cartesian motion system that moves the build plate in x-y and the printhead in z-direction, as indicated in Figure 4.1a. The motion on all axis is performed with ball screws and linear bearing systems that feature a positional resolution and repeatability of 1.25 μm and 12 μm , respectively. The 3D printer offers slots for up to five print heads which can be combined for a single, multi-material print. The front and side views of a print head are shown in Figure 4.1b-c. Here, the rotation of a stepper motor is translated into a linear displacement of a piston, which enables ink extrusion from a syringe. The 3D printer control software calculates the required movement of the stepper motor to adapt the flow rate of the extrusion process to the traveling speed of the motion system. The width of the extruded filament is defined via the diameter of the nozzle which is either a straight metal or a tapered plastic tip with inner diameters in the range of 0.1 to 1.6 mm and attached to the syringe via a Luer-Lock fitting. Although both types of nozzles were successfully utilized in this thesis, the tapered nozzles are preferred for smaller inner diameters because they enable extrusion at a lower pressure compared to the straight nozzle geometry. The printing path is controlled via G-code which stores the x, y, z coordinates of the motion system, as well as the speed of the printing and non-printing moves.

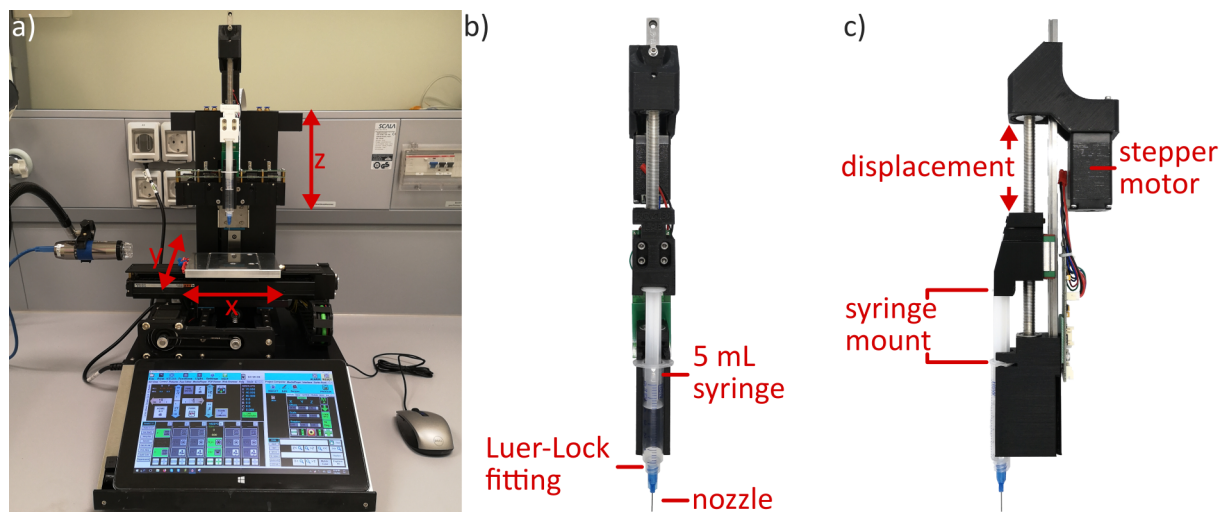


Figure 4.1: a) Photograph of the 3D printer and b-c) closeup views of the print head loaded with a syringe and nozzle.

4.2 Basics of Rheology

In chapter 3.3.1 we defined general guidelines to formulate a printable ink and we learned that ink compositions are tuned for a shear-thinning, viscoelastic characteristics by studying the rheology. Shear-thinning describes a decrease in viscosity with increasing shear rate and assures extrudability of the ink through fine nozzles at low extrusion pressures.^[1] Viscoelasticity is a mechanical property of materials that exhibit both viscous and elastic behavior upon deformation. To quantify the rheologic features of inks during 3D printing, a rheometer mimics the shear stress present during extrusion through a nozzle. The instrument consists of a steady and a moveable plate, with the ink placed in between, as illustrated in Figure 4.2a. Rheology test can be rotational to evaluate the degree of shear thinning as a function of applied shear rate (Figure 4.2b), or oscillatory to deduce elastic G' and viscous G'' moduli of the viscoelastic material as a function of the applied shear stress (Figure 4.2c). The moduli G' and G'' provide insights into the mechanical behavior of the ink during printing: 1) The relation of G' and G'' describes whether the material is predominantly elastic ($G' < G''$) or viscous ($G' > G''$) at a given stress, 2) the onset of fall in the value of G' indicates irreversible deformation of the ink and defines the yield stress τ_y , and 3) the crossover of G' and G'' describes the transition from a solid-like to a liquid-like ink and defines the flow stress τ_f .

Another oscillatory test is the three-interval thixotropy test which allows to study the recovery behavior of an ink by changing the oscillation amplitude during an oscillatory rheologic measurement (Figure 4.2d).^[2,3] Here, the ink is first sheared at low oscillation amplitude to allow the microstructure to stabilize and to derive initial values of G' and G'' . A high-stress interval follows, which destroys the microstructure of the ink, mimicking the flow inside the nozzle. Finally, during the last interval, a low shear stress is applied, and the recovery kinetics of G' and G'' are measured.^[4] The rheologic responses of a strong, intermediate and weak ink are illustrated in Figure 4.2d. Typically, recovery times shorten with increasing ink strength. During DIW, a high strength and a short recovery time avoid slumping of the printed object and enable architectures with unsupported, freestanding features.

All rheology measurements in this Ph.D. thesis were performed on a MCR 502 rheometer from Anton Paar located in the group of Prof. Volker Abetz at the Department of Physical Chemistry, University of Hamburg.

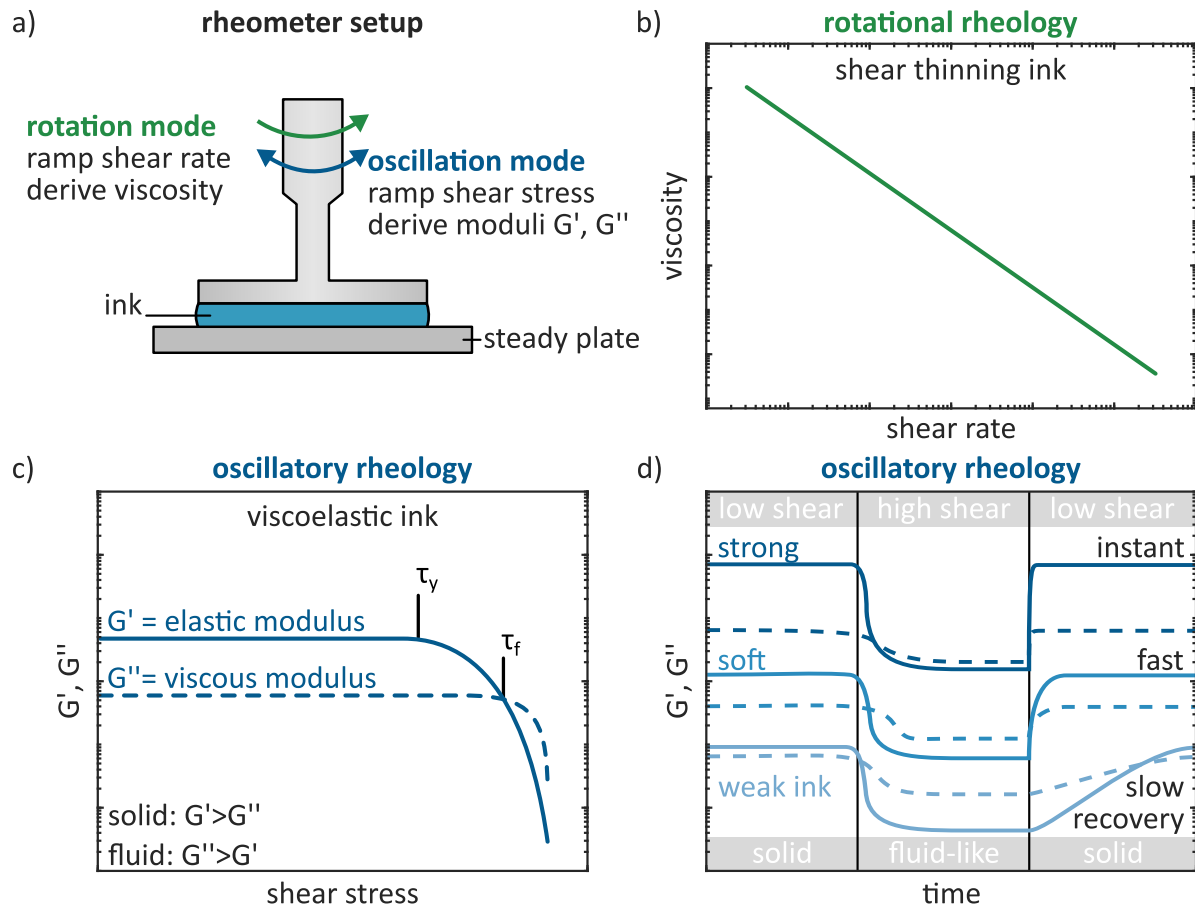


Figure 4.2: Standard rheological performance test for DIW inks. a) The ink is sandwiched between a steady and moveable plate of a rheometer. b) Rotational shear ramps study the dependence of viscosity on the applied shear rate. Inks for DIW should have a shear-thinning characteristic to enable a smooth flow through the fine nozzle. c) Oscillatory tests with increasing oscillation amplitude measure the elastic G' and viscous G'' moduli of the ink as a function of the applied shear stress. The yield stress τ_y indicates irreversible deformation of the ink and the flow stress τ_f describes the transition from a solid-like to liquid-like ink characteristic. τ_y and τ_f are defined at the onset of fall in the value of G' and at the intersection of G' and G'' , respectively. d) Three-interval thixotropy test evaluate the recovery behavior of an ink by applying a sequence of low, high, and low oscillation amplitude. Here, the first interval at low shear measures the initial viscoelastic ink characteristics and the transition from the subsequent high to low shear interval monitors the reformation of a solid-like ink behavior after extrusion. Typically, recovery times shorten with increasing ink strength.

4.3 Photocatalysis Setup

The photocatalytic activity of aerogels and powdered samples was tested in a custom-made photoreactor setup in the gas phase. The four main components of the setup are a gas supply, a flow-through reactor, two types of light sources, and a gas analysis system. The setup is designed in a modular fashion to enable illumination with different light sources and to study different kinds of photocatalytic reactions in the future. In this thesis the setup was used to investigate the hydrogen evolution from a water/methanol saturated gas stream.

Gas supply, Reactor, and Light Sources

The gas supply system provides a steady gas stream through the reactor and to the gas analysis system. The flow rate is regulated with Mass Flow Controllers (MFCs) from Bronkhorst in a range of 0 to 20 mL min⁻¹ and the gas is either dry synthetic air to clean the sample with UV light or helium enriched with water/methanol to perform the photocatalytic experiment. The flow schemes of both layouts and photographs of the corresponding setup are shown in Figure 4.3. Different light sources are utilized for UV cleaning and photocatalytic experiments. For UV cleaning, a 200 W Hg/Xe arc lamp from Newport Corporation is mounted. The arc lamp emits intense UV light down to 200 nm and enables ozone generation in proximity to the photocatalyst for efficient removal of organic impurities.^[5,6] Besides UV, the arc lamp also emits in the visible and near-infrared range. To remove the infrared radiation from the spectrum and to prevent uncontrolled sample heating, a water-based filter is installed in the beam path. The light beam is directed to the reactor with a mirror and illuminates the sample through a viewport. For photocatalytic experiments, a UV LED is mounted on top of the viewport and centered with a 3D printed adapter. The UV LED emits at 375 nm and provides a more stable, reproducible light intensity than the arc lamp. Stable lighting conditions are a key requirement to study and compare the photocatalytic activity of various samples. The LED intensity is controlled with an Arduino Nano and calibrated using a power sensor from Thorlabs Inc..

The reactor cell is designed according to the following requirements to fulfill the high demands on chemical inertness, sample integration, and air tightness:

1. The reactor must be chemically stable under UV illumination to avoid a misleading interpretation of the catalytic activity.
2. The reactor should enable an easy sample exchange to minimize the downtime in between measurements.
3. The reactor should provide a reliable alignment of the sample to achieve comparable reaction conditions.
4. The illumination and gas flow should enforce a steady interaction with the sample to achieve highest photocatalytic production rates.
5. The reactor must be airtight at ambient pressure to guarantee that all evolving products are directed to the gas chromatograph for quantitative analysis.

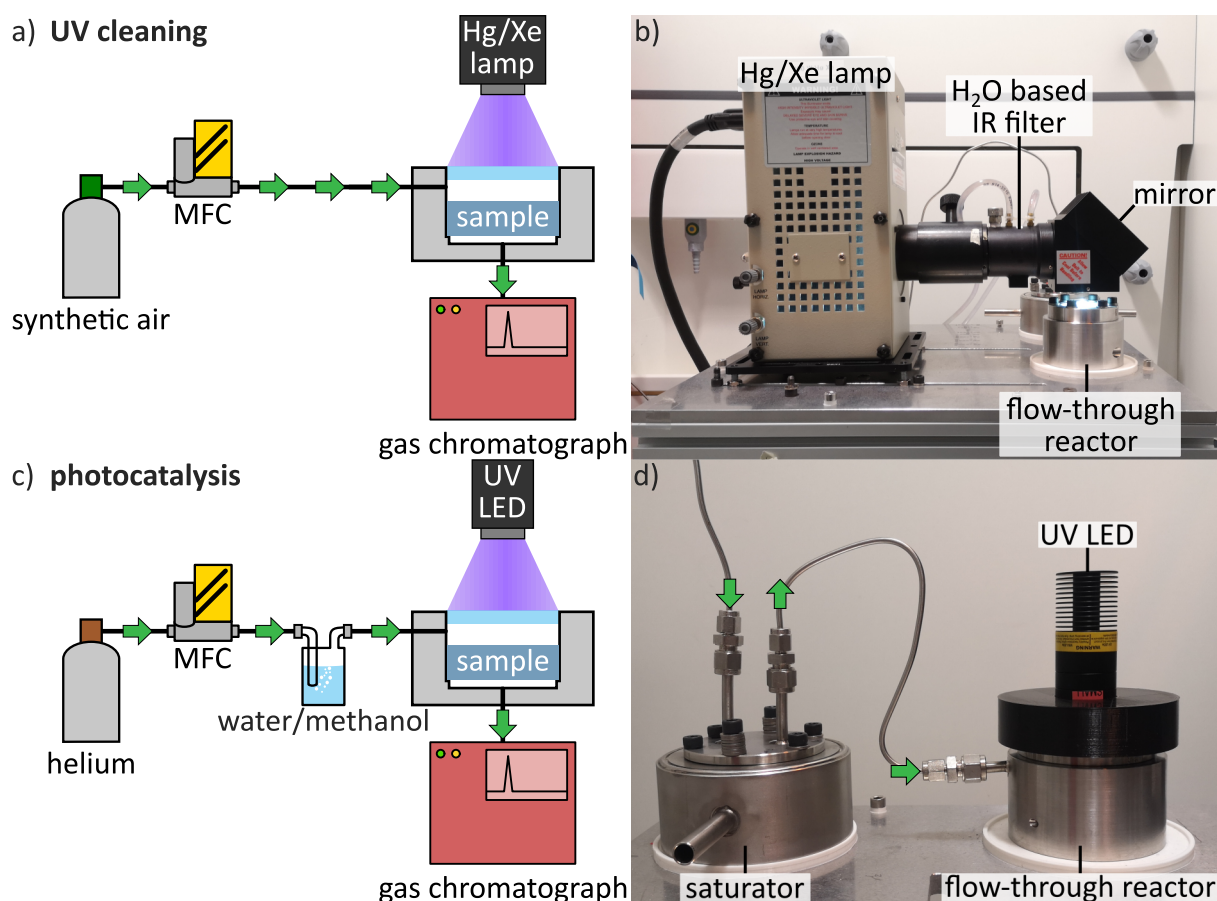


Figure 4.3: Flow schemes and photographs of the setup configured for a-b) UV cleaning with a Hg/Xe arc lamp in a dry synthetic air stream and c-d) photocatalysis with a UV LED in a helium gas stream saturated with water/methanol.

Having identified the above requirements, we continue by discussing each component of the reactor. The reactor and tubing are machined from stainless steel which is usually used for ultra-high vacuum and purity applications. Besides, all gas connections are realized by Swagelok fittings to achieve air tightness. The reactor is equipped with a fused silica viewport at the top (Figure 4.4a), an insert to mount the sample in the center (Figure 4.4b), and gas inlet and outlet at the side and bottom of the reactor, respectively. The location of the light source and gas connections enforces that light and reactants permeate the sample and takes full advantage of the high surface area of the flat 3D printed aerogels. The insert features a quadratic sample tray and a through-hole which can be fabricated with different dimensions to fit samples of various sizes. Also, the sample tray guarantees that the photoactive sample is always centered in the reactor to maintain an identical location relative to the light source for comparable illumination across multiple sample changes. The insert has an O-ring to avoid any bypass of gas when mounted in the reactor (Figure 4.4c) and consists of a UV-resistant fluoroelastomer. Moreover, the reactor provides holes in the stainless-steel body for heating cartridges and thermocouples to study catalytic activity at elevated temperatures.

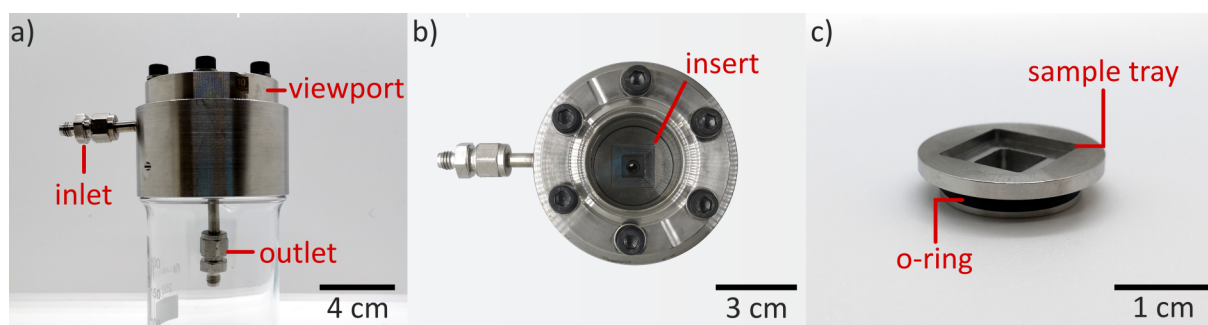


Figure 4.4: Photographs of the custom-made flow-through reactor in a) side and b) top-view. c) Closeup view of the insert which is used to mount the sample in the reactor in a centralized position.

Gas Chromatography

Analysis of the gas stream exiting the reactor is performed with a gas chromatograph manufactured by Agilent and customized by Joint Analytical Systems GmbH according to the specific requirements of the setup. The gas chromatograph consists of three main components: gas injection, gas separation, and gas detection. Gas injection from the gas stream of the reactor is automatically performed every 29 min with a sample loop. The principle is illustrated in Figure 4.5a-b. In the initial state, the gas exiting the reactor permanently purges the sample loop and eventually flows to the ventilation system. The sample loop is part of a 6-port valve and by adjusting the position of the valve, the gas phase inside the loop is injected into the gas separation system of the gas chromatograph (Figure 4.5b). The injection takes 0.5 min and after that the 6-port valve goes back to the initial state.

For photocatalytic hydrogen formation from a water/methanol mixture, the injected gas phase can include hydrogen, oxygen, water, methanol, and carbon dioxide. To separate these compounds, the gas chromatograph uses two columns, a polymer-coated capillary column (Plot U) and a molecular-sieve-coated capillary column (Molsieve 5Å). The Plot U column separates compounds by the difference in their adsorption affinity and is used for the separation of water, methanol, and carbon dioxide. Hydrogen and oxygen do not interact with the column and just pass through. These compounds are separated by the subsequent Molsieve 5Å column. However, water is not allowed to interact with the Molsieve 5Å. Therefore, a dean switch is placed after the Plot U column which bypasses the gas stream containing water, methanol, and carbon dioxide, as depicted in Figure 4.5c.

After passing through the columns, all compounds are spatially separated due to their characteristic elution times. The compounds are detected with three detectors: A helium pulsed discharge ionization detector (HID), a flame ionization detector (FID), and a thermal conductivity detector (TCD). The HID is most sensitive, followed by FID and TCD. Usage of multiple detectors offers higher flexibility for future photocatalytic experiments since each detector is sensitive for different compounds. The HID utilizes a low power, DC discharge to excite a helium gas stream. Upon returning to the ground state, the ions emit photons with an energy of 17.7 eV and ionize any compound in the gas stream with lower ionization energy. The electrons generated by the ionization process are collected by an electrode and eventually detected as a current. The detector is essentially non-destructive and highly sensitive with minimum detectable quantities in

the low parts per billion range.^[7]

The FID detects ions formed during the combustion process of analytes in a hydrogen flame. The ions are directed to a collector electrode and the resulting current is measured. Since the ion formation relies on a combustion process, fully oxidized species such as carbon dioxide will give no response.^[8]

The TCD measures the difference in thermal conductivity and specific heat between a reference carrier gas flow and the eluting carrier gas plus analyte. Since every compound possesses some thermal conductivity, the TCD is generally a universal detector. However, the thermal conductivity of the analyte must be very different from the thermal conductivity of the carrier gas to achieve high sensitivity down to 10 parts per million. For example, hydrogen and helium have similar thermal conductivities, but carbon dioxide or water have only about one tenth of the thermal conductivity of helium.^[8] Since the gas chromatograph relies on helium as the carrier gas for the operation of the HID, the TCD is not suited for hydrogen detection, but carbon dioxide and water can be readily detected.

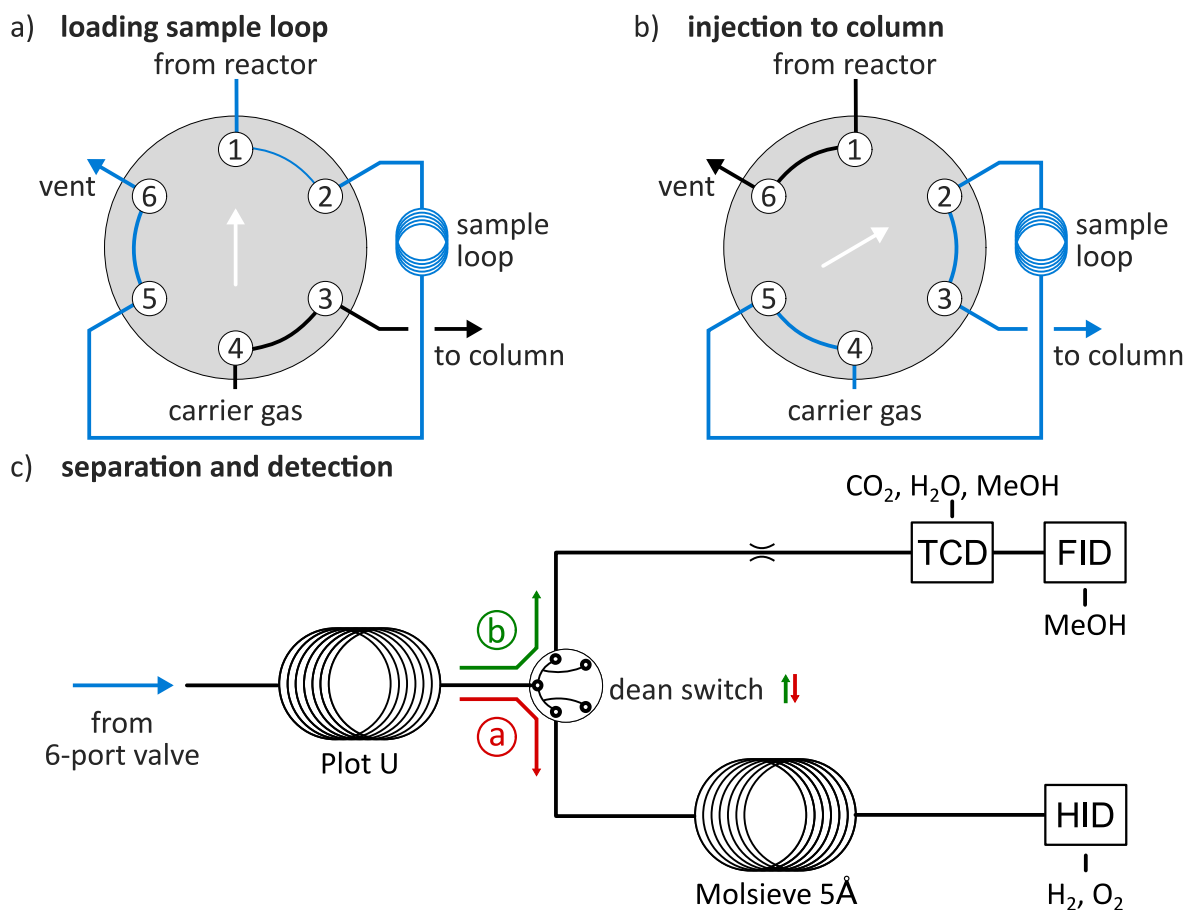


Figure 4.5: Flow scheme of the gas chromatograph. a) The gas stream exiting the reactor purges a sample loop which is part of a 6-way valve. b) By changing the position of the valve, helium carrier gas injects the content of the filled sample loop into the column. c) The gas coming from the 6-port valve is spatially separated with Plot U and Molsieve 5Å columns and quantified using various detectors. A dean switch is used to direct carbon dioxide (CO₂), water (H₂O) and methanol (MeOH) to the TCD and FID. The amount of hydrogen (H₂) and oxygen (O₂) are measured on the HID. A list of events for all valve positions are given in Table 4.1

In this thesis, gas chromatography is utilized for the quantitative analysis of hydrogen during photoreforming of a water/methanol mixture. The area of the hydrogen peak A_{H_2} in the recorded chromatogram is converted into a volumetric concentration using a calibration factor C_{H_2} which is obtained by injecting known quantities of hydrogen gas. Next, a molar hydrogen evolution rate r_1 or mass normalized production rate r_2 are calculated following equation 4.1 and 4.1, respectively.^[9,10]

$$r_1 = \frac{Q \cdot A_{\text{H}_2}}{V_{\text{M,H}_2} \cdot C_{\text{H}_2}} \quad (4.1)$$

$$r_2 = \frac{Q \cdot A_{\text{H}_2}}{V_{\text{M,H}_2} \cdot m_{\text{cat}} \cdot C_{\text{H}_2}} \quad (4.2)$$

Here, Q is the volumetric flow rate of the gas stream passing the reactor, $V_{\text{M,H}_2}$ is the molar volume of hydrogen and m_{cat} is the catalyst mass.

Table 4.1: List of events during a single run of the gas chromatograph. Position 1 and 2 of 6-port valve are illustrated in Figure 4.5a-b, respectively. Position a and b of the dean switch are indicated in Figure 4.5c.

time	action
initial state	6-port valve in position 1, dean switch in position a, column temperature at 60 °C
0.0 min	set 6-port valve to position 2
0.5 min	set 6-port valve to position 1
3.3 min	set dean switch to position b
4 min	set column temperature to 190 °C with a ramp of 15 °C min ⁻¹
25.7 min	set all values to the initial state
29 min	initial state reached; gas chromatograph ready for next injection

4.4 Computational Fluid Dynamics

This section covers the underlying physics of computational fluid dynamics simulations which we utilize in chapter 6 to evaluate the mass transfer characteristics of a 3D structured aerogel during photocatalysis. The mass transport in 3D aerogels takes places at multiple length scales ranging from the macroscopic dimensions of the sample on the centimeter scale, a 3D structuring on the micrometer scale, and the nanoporous structure of the aerogel. Here, the governing equations are the Navier-Stokes and Brinkman equations and are coupled in COMSOL's '*Free and Porous Media Flow*' module. The Navier-Stokes equation describes the flow in free space and is given as

$$\rho \frac{du}{dt} = -\nabla p + \mu \nabla^2 u + F \quad (4.3)$$

where u is the fluid velocity, ρ is the fluid density, t is the time, p is the pressure, μ is the fluid viscosity, and F is an external body force acting on the fluid such as gravity.

The Brinkman equation describes the fluid flow through the porous media and is defined as

$$\nabla p = -\frac{\mu}{k} u + \mu \nabla^2 u. \quad (4.4)$$

Here, the first term is Darcy's law which states that the Darcy velocity \bar{u} is directly proportional to the pressure gradient ∇p , the gas viscosity μ and the permeability of the medium k , which is defined by the pore size of the medium. The Darcy velocity \bar{u} is related to the fluid velocity u through the porosity ϕ as $\bar{u} = \phi \cdot u$. The second term is a boundary shear stress and is employed to obtain a shear stress continuity at the interface of the porous and free flow medium.^[11] The '*Free and Porous Media Flow*' interface of COMSOL couples the physics of the Navier-Stokes and the Brinkmann equations so that continuity is enforced between the fluid velocity in the free flow domain and the Darcy velocity in the porous medium.^[12] To solve the above equations for the pressure and velocity fields, physical and geometrical boundary conditions are applied, which result from the flow rate, the pressure at the outlet of the geometry, and the shape of the 3D aerogel.

4.5 Monte Carlo Method

This section outlines the fundamental concept of Monte Carlo light transport simulations. We utilize this method in chapter 6 to derive a 3D aerogel architecture that enables an effective illumination of the photocatalyst. Light propagation in macroscopic, microstructured aerogels is defined by light-matter interaction within the nanoscopic particle network. Here, absorption leads to a decrease of light intensity and scattering cause a redirection of the photon path. If photons are scattered randomly in any direction, the scattering is isotropic. The light propagation in differently structured aerogel geometries is calculated utilizing an open-source mesh-based Monte Carlo Method called MMCLAB.^[13] The big benefit of the mesh-based method in contrast to layered approaches is that arbitrarily shaped geometries can be studied.^[14] The calculation uses absorption and scattering coefficients of the aerogel derived by solving the inverse problem of the Radiative Transfer Equation (RTE). The solution of the RTE is presented in chapter 6. The Monte Carlo method simulates light transport by tracing the random walk steps of a single photon package within the mesh of the geometry. To achieve this, the method follows the simplified decision scheme shown in Figure 4.6. First, a photon is launched at the position of the source along an incident direction vector with an initial weight of 1. Based on the scattering coefficient of the current mesh cell, a scattering length is computed. The photon propagates along the scattering trajectory to the next mesh element and based on the local absorption coefficient the photon weight is attenuated using the propagation distance and the Beer-Lambert law. The weight loss of the photons is assigned to the nodes of the participating mesh element. The procedure is repeated until the photon has traveled the total computed scattering length. From there, a new random scattering direction vector is calculated, and the above procedure is repeated until the time gate is exceeded or the photon weight falls below a pre-defined threshold. Once a pre-set number of photons are launched, the cumulative distribution of all photon paths provides the light distribution in the sample. A detailed description of the algorithm implementation in MMCLAB is given elsewhere.^[14]

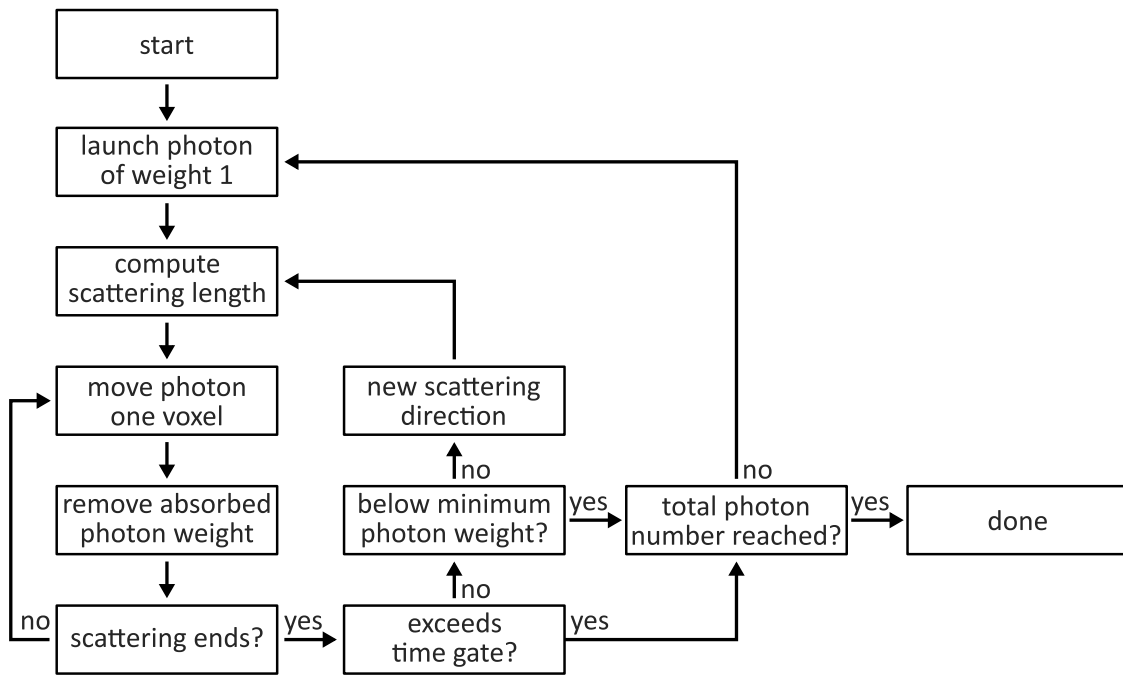
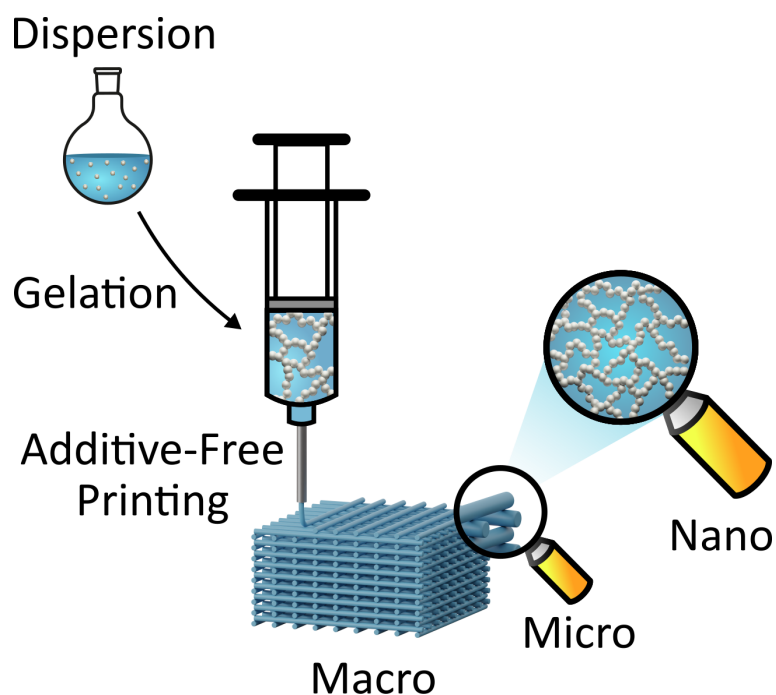


Figure 4.6: Simplified decision scheme for Monte Carlo photon transport simulations in absorbing and scattering media.

Bibliography

- [1] M. A. S. R. Saadi, A. Maguire, N. T. Pottackal, M. S. H. Thakur, M. M. Ikram, A. J. Hart, P. M. Ajayan and M. M. Rahman, *Adv. Mater.*, 2022, **34**, 2108855.
- [2] S. Tagliaferri, A. Panagiotopoulos and C. Mattevi, *Materials Advances*, 2021, **2**, 540–563.
- [3] B. Nan, F. J. Galindo-Rosales and J. M. F. Ferreira, *Mater Today*, 2020, **35**, 16–24.
- [4] A. Corker, H. C. H. Ng, R. J. Poole and E. García-Tuñón, *Soft Matter*, 2019, **15**, 1444–1456.
- [5] H. Claus, *Photochem. Photobiol.*, 2021, **97**, 471–476.
- [6] H. Joshi, D. Jalalpoor, C. Ochoa-Hernández, W. Schmidt and F. Schüth, *Chem. Mater.*, 2018, **30**, 8905–8914.
- [7] J. Y. Y. Loh, A. Mohan, A. G. Flood, G. A. Ozin and N. P. Kherani, *Nat. Commun.*, 2021, **12**, 402.
- [8] J. Swinley and P. de Coning, *A Practical Guide to Gas Analysis by Gas Chromatography*, Elsevier, San Diego, United States, 2019.
- [9] S. Kreft, R. Schoch, J. Schneidewind, J. Rabeah, E. V. Kondratenko, V. A. Kondratenko, H. Junge, M. Bauer, S. Wohlrab and M. Beller, *Chem*, 2019, **5**, 1818–1833.
- [10] S. Bernadet, E. Tavernier, D.-M. Ta, R. A. L. Vallée, S. Ravaine, A. Fécant and R. Backov, *Adv. Funct. Mater.*, 2019, **29**, 1807767.
- [11] C. K. Ho and S. W. Webb, *Gas transport in porous media*, Springer Dordrecht, x, 2006, vol. 20.
- [12] COMSOL, *CFD Module User's Guide*, COMSOL Multiphysics 5.4, 2018.
- [13] R. Yao, X. Intes and Q. Fang, *Biomed. Opt. Express*, 2016, **7**, 171–184.
- [14] Q. Fang, *Biomed. Opt. Express*, 2010, **1**, 165–175.

5 Additive-Free, Gelled Nanoinks: A 3D Printing Toolbox for Hierarchically Structured Bulk Aerogels



The content of this chapter, which presents a 3D printing strategy for TiO_2 nanoparticle-based aerogels, was published in *Advanced Functional Materials*. The manuscript was co-authored by Malte Trommler, Irina Lokteva, Samanehalsadat Ehteram, Andreas Schropp, Sandra König, and Michael Fröba with Dorota Koziej as corresponding author.

5.1 Abstract

Aerogels are highly porous solids that maintain the properties of individual nanomaterials at a macroscopic scale. However, the inability to fabricate hierarchical architectures limits technological implementation in energy storage, gas-sorption, or catalysis. A 3D-printing methodology for additive-free TiO_2 nanoparticle-based aerogels is presented with full control of the nano-, micro-, and macroscopic length-scales. To compensate for ink's low solid loading of 4.0 vol. % and to enable subsequent processing into aerogels via supercritical drying, the printing is done in a liquid bath of alkaline pH. The 3D-printing protocol retains a high specific surface area of $539 \text{ m}^2 \text{ g}^{-1}$ and a mesopore diameter of 20 nm of conventionally casted aerogels while offering an unparalleled designability on the micrometer scale. To illustrate the new geometric freedom of 3D-printed aerogels, the microstructure of a strongly light-absorbing, photothermal Au-nanorod/ TiO_2 aerogel is defined. To date, photothermal nanomaterials are mainly applied in the form of unstructured films where scalability is limited by light attenuation. Microstructures in 3D enhance light penetration by a factor of four and facilitate spatially defined heating on a macroscopic scale. The process can be generalized for a broad material library and allows to design inks with specific functionality, thus making aerogels adaptable for their target application.

5.2 Introduction

Nowadays, colloidal nanochemistry can provide well-defined nanomaterials of various sizes, shapes, compositions, and surface chemistry with remarkable properties on a large scale.^[1–4] However, the high-volume manufacturing of macroscopic, nanomaterial-based devices is still challenging. The main difficulty of nanomaterial processing is the preservation of nanoscopic properties across multiple length scales.^[5] An attractive approach to bridge the nanoscopic and macroscopic world is to process nanomaterials into aerogels via gel casting.^[6–10] This method translates the intrinsic properties of nanoparticle dispersions into highly porous bulk solids with immense surface area. However, the restricted range of mold geometries and aerogel’s poor subtractive processing abilities limit shape tunability and prevent complex microstructured geometries. A promising technology that could enable free-form fabrication of nanoparticle-based aerogels is the use of direct ink writing (DIW), a subcategory of extrusion-based 3D printing. DIW evolved from ceramic processing which similarly to nanoparticle-based aerogels fabricate materials and devices from preformed particles.^[5,11] Nevertheless, ceramics and nanoparticle-based aerogels have fundamentally distinct properties defined by large differences in the particle size of the primary building blocks and the porosity of the final product. Nanoparticle-based aerogels feature porosities of up to 99.8% and preserve the outstanding properties of the individual, nanometer-sized particles in a nanostructured macroscopic solid.^[6–9,12,13] In contrast, ceramics are dense solids, where size-specific properties of the individual particles are lost upon sintering. Thus, to enable optimal processing into dense, mechanically stable solids, particles are typically larger than 100 nm.^[5,14] The low porosity of ceramics implies that highly concentrated inks can be printed to obtain objects that marginally shrink upon drying in air.^[15–18] In contrast, solvent evaporation is still a major challenge for DIW of highly porous aerogel materials.^[19] To compensate, recent studies formulated inks based on high boiling point solvents.^[20,21] However, these inks rely on high volumetric loadings of preformed aerogel microparticles which are bound by polymers to ensure their printability. These recipes drastically differ from gelation protocols of conventionally casted nanoparticle-based aerogels which don’t require any rheological additives or preformed aerogels microparticles.^[9] While organic residues degrade the performance as a catalyst or thermal insulator by blocking active sites or compromising aerogel’s exceptional low thermal conductivity,^[21,22] the use of 10 μm aerogel particles results in grain boundaries and impedes a true bottom-up fabrication with full control of the nano-, micro- and macroscopic length scales.^[20] Thus, to fully exploit intrinsic or even synergistic properties of nanomaterials in a 3D printed aerogel, additive-free inks similar to conventionally casted aerogels need to be formulated.

In this study, we close the gap and report a 3D printing process for the fabrication of TiO_2 -based aerogels. We formulate additive-free inks of gelled TiO_2 nanoparticles with a volumetric loading of 4 vol. %. Instead of using rheologic additives, we compensate for the low particle concentration by printing in a liquid bath of alkaline pH. This allows us to maintain the ink’s nanoscopic characteristic and to fabricate macroscopic translucent aerogel geometries. Moreover, we demonstrate that multicomponent inks can be easily processed by mixing TiO_2 with additional nanoparticle dispersions such as spherical Au nanoparticles (AuNPs) or Au nanorods (AuNRs) prior gelation.

To demonstrate the design flexibility of our method, we print various geometries with high shape fidelity and precision, including void-free cubes, 3D grids, boats with large overhangs, and various multi-material geometries. The 3D printed aerogels inherently feature a randomly organized interconnected mesoporous network with pore sizes in the range of 20 nm, a large specific surface area of up to $539 \text{ m}^2 \text{ g}^{-1}$, and a low density of 0.2 g cm^{-3} – typical values for conventionally casted metal oxide aerogels.

To give a first glimpse of the new design freedom for 3D printed nanoparticle aerogels, we combine the superior thermal insulating capabilities of metal-oxide aerogels with photothermal properties of plasmonic AuNRs. Here, the 3D printing process defines not only the dimension of the printed material but also the material composition and photothermal properties at any desired spot. Finally, we engineer the microstructure of the photothermal aerogel for improved light penetration and more homogeneous heating in 3D. This enables a new generation of photothermal devices for solar steam generation or thermochemical heat storage.

5.3 Results and Discussion

Figure 5.1a provides an overview of the 3D printing process developed in this work which consists of three steps: (i) ink formulation by nanoparticle gelation, (ii) 3D printing in a liquid bath, and (iii) post-processing via supercritical drying. Key challenges are formulating a printable, additive-free ink of low solid loading and designing a process that maintains the nanoscopic characteristics of gelled nanoparticles in a macroscopic, 3D printed aerogel. Having solved these problems, geometries of various complexity and material composition can be fabricated as indicated in Figure 5.1b-g.

Ink Formulation

We have synthesized ligand-free 4 nm anatase TiO_2 nanoparticles by adopting a synthesis described elsewhere.^[23] For ink formulation we transformed the liquid dispersion into a volume-filling nanoparticle gel, as illustrated in Figure 5.1a. To this end, we destabilize the TiO_2 dispersion in a controlled manner and crosslink the nanoparticles by a subsequent thermal treatment. Unlike previous reports, where selective ligand removal has been used for destabilization,^[7,13,24,25] we modify the force balance of electrostatically stabilized TiO_2 nanoparticles. The range of electrostatic forces can be described by the Debye length where high values increase colloidal stability.^[9] The addition of solvents with lower dielectric constants such as acetonitrile (ACN) reduce the Debye length and cause an overall net attraction between particles. For optimal results we dilute the aqueous dispersion to one-third with ACN. ACN contents of 50 vol. % or higher cause precipitation, whereas the absence of ACN prohibits gelation, as illustrated in Figure 5.8.

Previous inks for 3D printing of aerogels were gelled by increasing the attractive hydrogen bonding via the addition of additives.^[21,26] We would like to point out that such inks are special recipes to enable 3D printing of aerogels and feature a different chemical composition than recipes for conventionally casted aerogel materials. In our approach, we stick to the well-established concept for casted nanoparticle-aerogels which consists of the two steps: 1) Preparation of stable

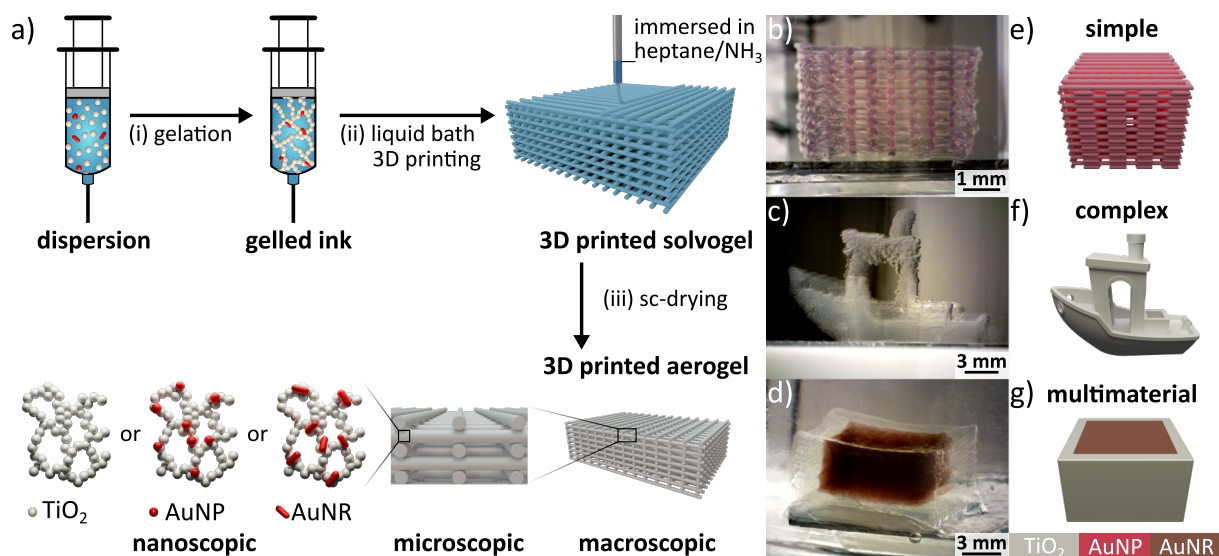


Figure 5.1: Modular 3D printing approach of TiO_2 nanoparticle-based aerogels. a) Schematic showing the three steps of our 3D printing process: (i) Inks, either neat TiO_2 or loaded with AuNPs or AuNRs, are formulated by gelation of respective nanoparticle dispersions. (ii) As prepared inks are 3D printed by mechanical extrusion of the nanoparticle gel within a liquid bath. (iii) The resulting macroscopic, microstructured solvogels are processed to aerogels by CO_2 supercritical drying. b-d) Photographs of 3D prints and e-g) corresponding models highlight the accessible range of geometrical complexity.

nanoparticle dispersions and 2) gelation via controlled destabilization.^[6,8,9] Thus, all intriguing properties of casted nanoparticle-aerogels will remain in a 3D printable ink.

Ultimately, 3D printing relies on extrusion of microscopic filaments; high particle loadings facilitate filament extrusion, but reduce the porosity of the final aerogel. To estimate the minimum concentration for 3D printing, we gelled inks with TiO_2 loadings of 0.2 vol. %, 1.2 vol. % and 4.0 vol. % and checked the optical appearance upon extrusion through a $410\ \mu\text{m}$ nozzle in Figure 5.2a-c. Figure 5.2c demonstrates successful filament formation for a 4.0 vol. % ink, but further rheological criteria need to be fulfilled for good printability. Suitable inks must possess high viscosity and paste or gel-like characteristic at rest, but also feature a low viscosity and fluid-like character while passing through thin deposition nozzles.^[27,28] Besides, the ink must rapidly transform from a fluid-like into a solid-like material after leaving the nozzle to preserve the shape of the extruded filament - especially when spanning gaps in the underneath layer.^[29] We assess the rheological fingerprint of each ink by shear rheology. To replicate the flow characteristic of each ink at rest and while printing, we investigate the apparent viscosity as a function of shear rate in Figure 5.2d. We demonstrate a profound shear-thinning behavior. Thus, during extrusion the flow resistance is drastically reduced for typical shear rates of 10 to $150\ \text{s}^{-1}$,^[30] whereas at rest the ink has a low tendency to spread. Further, we clarify the microstructure of gelled inks via oscillatory frequency sweeps shown in Figure 5.2e. Here, the elastic modulus G' and viscous modulus G'' are plotted as a function of time for a frequency range of 1 to $50\ \text{Hz}$. G' and G'' are nearly frequency-independent for a particle concentration of 4.0 vol. %. Thus, we conclude that an elastic, solid-like network has formed.^[31] The mechanical stability of the ink is defined via the interaction of particles within the gelled network. As soon as the applied shear

stress exceeds the yield stress τ_y , the connection between individual particles or larger clusters starts to break apart.^[32] When the shear stress overcomes the flow stress τ_f , a sufficient number of bonds in the particle network are disrupted and the ink eventually flows with a shear-thinning behavior. We estimate τ_y and τ_f based on oscillatory amplitude sweeps shown in Figure 5.2f, which is a plot of G' and G'' versus the stress amplitude. Here, τ_y is taken as the stress required for a 90% decrease of the initial elastic modulus G'_0 and τ_f is defined as the crossover between G' and G'' .^[30,33] At low stresses the ink shows characteristics of an elastic solid since G' is larger than G'' . At higher stresses G' slowly decreases until it sharply drops and eventually approaches values lower than G'' ; thus representing a viscous fluid. For a particle concentration of 4.0 vol. % we determine τ_y and τ_f as 104 Pa and 210 Pa, respectively.

After leaving the nozzle, the flowing ink needs to rapidly regain a gel-like attribute to preserve its shape. To track this recovery, we performed an oscillatory recovery test shown in Figure 5.2g. Here, the 4.0 vol. % sample instantly recovers a solid-like characteristic ($G' > G''$) as soon as the oscillation amplitude changes from a high to a low value mimicking the transition from high to low shear stress once the ink exits the nozzle during 3D printing.

In summary, the ink with a particle concentration of 4.0 vol. % is not only best suited for 3D printing based on the ability to reliably form filaments, but also due to a distinct shear-thinning behavior, a pronounced gel-character at rest and an immediate gel recovery after extrusion. These properties are simply achieved by careful control of solvent composition and particle concentration without the need of any rheologic additives. In comparison, inks with lower particle loadings display strong frequency dependency of G' and G'' and feature lower τ_y and τ_f as shown in Figure 5.2e and f, respectively. Thus, these inks represent characteristics of a viscoelastic fluid that tends to form droplets instead of filaments during extrusion. Moreover, multicomponent inks can directly be obtained by performing TiO_2 gelation in the presence of other nanomaterials such as AuNPs or AuNRs, as long as the rheologic properties of neat TiO_2 are preserved, as shown in Figure 5.9 for Au loadings of up to 0.49 wt. %. We expect that rheological properties of inks will change more drastically when much higher loadings of AuNPs or AuNRs are present. Thus, the rheological properties of the ink would have to be adjusted by tuning the temperature and duration of the thermal treatment or by adjusting the volumetric ratio of water and ACN.

3D Printing of Stable Complex Structures - A Force Balance Approach

We use optimized inks with TiO_2 loading of 4.0 vol. % to design a 3D printing scheme that enables processing into aerogels. This step requires well-controlled drying of the wet gel to preserve the three-dimensional nanoparticle framework. When dried in air, capillary forces at the liquid/gas interfaces lead to drastic shrinkage and the nanoporous network eventually collapses. The most common drying method for casted aerogels is supercritical drying where a liquid/gas interface no longer exists, and stress is minimized.^[12] However, 3D printing is typically performed in air and extruded filaments quickly dry based on their high surface-to-volume ratio. Thus, a filament of the gelled ink turns opaque within seconds of extrusion in air, as shown in Figure 5.3a, and eventually collapses. We overcome evaporation-induced gel damage by performing the 3D print in a liquid bath.^[18,30,34] Buoyancy force necessitates that the density of

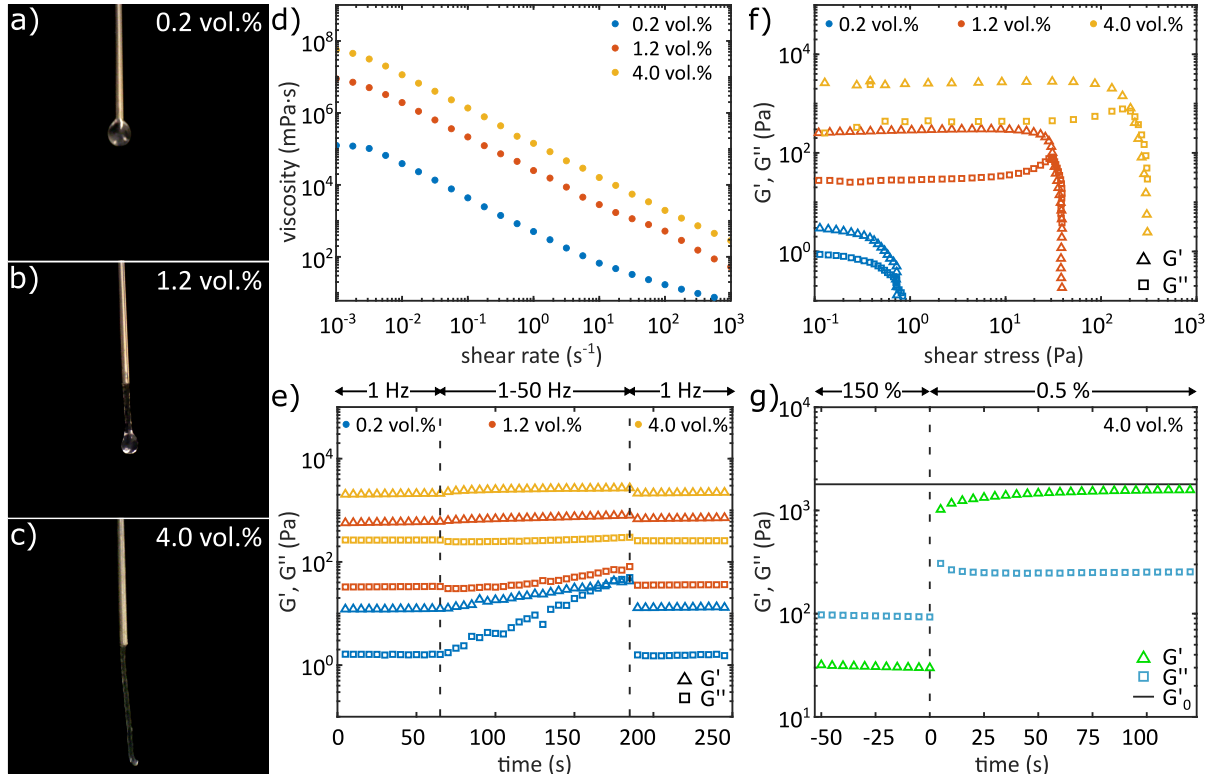


Figure 5.2: Rheological properties of inks with TiO_2 loadings of 0.2 vol. %, 1.2 vol. % and 4.0 vol. %. a-c) Optical images of inks after extrusion through a nozzle with an inner diameter of $410 \mu\text{m}$. Increase of TiO_2 loading from 0.2 to 4.0 vol. % enables extrusion of gel filaments instead of liquid droplets. d) Rotational sweep measurements demonstrate a decrease of viscosity with increasing shear rate for all TiO_2 loadings. e) Oscillatory frequency sweeps in a range of 1 to 50 Hz reveal a more pronounced frequency independence of the storage G' and loss G'' moduli with increasing TiO_2 loading. f) Oscillatory amplitude sweeps demonstrate an increase of elastic G' and viscous G'' moduli with TiO_2 loading. g) Oscillatory recovery curves of G' and G'' at large and low oscillation amplitude mimic the shear transition of the ink while exiting the nozzle during 3D printing. Solid line indicates initial storage modulus G'_0 before applying high strain amplitudes to the sample.

the bath is significantly lower than the density of the ink. Moreover, ink adhesion demands that the substrate is preferentially wetted by the ink and not by the bath. Alkanes such as n-heptane fulfill both requirements. Figure 5.3 shows an optical micrograph time series of a grid geometry printed in n-heptane. While printing in n-heptane is possible, severe post printing deformation take place on a time scale of 24 hours. Printing in a liquid bath suppresses solvent evaporation, however the ink remains soft and is still able to deform. Based on the shape evolution of the printed geometry in Figure 5.3b-d we identify gravity and capillary pressure as primary external forces acting on the print. To compensate adjustments on the 3D printing process need to be made. To this end, we identify the main driving force of deformation and estimate the contribution of each component. For sagging, the weight of the entire geometry needs to surpass the yield stress τ_y of the lowest layer. As illustrated in Figure 5.3e each layer of the grid geometry consists of an array of filaments of diameter d and spacing h . Due to a periodicity of h , the filament in the lower layer (colored in red) only needs to carry a small

section of filament in the layer above (colored in blue). The gravitational pull of this section is defined via the weight m_{ink} , volume V_{ink} and density ρ_{ink} as $m_{\text{ink}}g = (\rho_{\text{ink}}(\pi d^2 h)/4)g$. The gravitational pull of this filament segment is partly compensated by the buoyancy forces of the liquid bath. The resulting net force is distributed over the filament's interfacial area d^2 and causes a gravitational pressure of $p_g = g\pi h(\rho_{\text{bath}} - \rho_{\text{ink}})/4$. Multiplying the gravitational pressure of a single layer p_g with the number of layers yields the total gravitational pressure $p_{g,\text{total}}$ onto the first layer. Consequently, the weight of the geometry shown in Figure 5.3b imposes a gravitational pressure $p_{g,\text{total}}$ of 32 Pa and gravity is therefore excluded as the main driving force of deformation ($p_{g,\text{total}} < \tau_y$). However, according to the Young-Laplace equation ($\Delta p = 2\gamma/r$) a capillary pressure of 320 Pa can be approximated by taking the filament radius of $r = d/2 = 125 \mu\text{m}$ and interfacial tension of $\gamma = 20.0 \text{ mN m}^{-1}$ (Figure 5.10) into account. Therefore, even a single pending filament with negligible gravitational pressure tries to reduce its total curvature and interfacial energy by forming a droplet at the tip as shown in Figure 5.10. Hence, capillary pressure can be defined as the main driving force of print deformation ($\Delta p > \tau_y$). In principle, capillary pressure driven deformation can be lowered by either employing surfactants for a reduced bath-ink interfacial tension or by increasing TiO_2 concentration for a higher yield stress. In practice, both turned out to be insufficient as discussed in the supporting information (chapter 5.6). Instead, we have developed a condensation process, which significantly increases the yield stress of the ink after extrusion. Although TiO_2 particles are pre-gelled during ink formulation, the gel network is not fully developed and TiO_2 particles are still able to crosslink via condensation reactions. The condensation rate can be precisely controlled via pH. While an acidic pH induces a slow condensation, which is ideal to formulate a pre-gelled ink with suitable rheologic properties, alkaline conditions significantly accelerate condensation.^[35–37] We exploit the change of condensation reaction rates to strengthen the particle network after extrusion. For this purpose, we additionally load the heptane bath with NH_3 . As soon as the NH_3 diffuses into the aqueous ink, NH_3 deprotonates a small fraction of the water to yield ammonium and hydroxide ions. As a result, the pH of the ink rises and the printed microgrid, which eventually formed a droplet in a heptane bath within 24 hours, fully remained its 3D architecture in heptane/ NH_3 (Figure 5.3f-h). Here, the pH assisted condensation is verified by a color change of the loaded pH indicator from red to yellow. Similarly, a pendant TiO_2 filament shows no apparent deformation as illustrated in Figure 5.10. Thus, the role of our heptane/ NH_3 bath is twofold and goes beyond other liquid bath approaches where the liquid is only used to prevent solvent evaporation during 3D printing.^[18,30,34] In our approach, the liquid is charged with NH_3 to solidify the ink via pH-induced condensation reactions which counters the deformation by external forces. In other approaches, deformation by external forces was balanced by performing the print in soft supporting materials such as Polydimethylsiloxan (PDMS), Laponite, or Carbopol.^[38–40] However, prints either remain embedded in the viscoelastic PDMS matrix or cannot be removed as easily as for the liquid heptane/ NH_3 bath used within this work.

After condensation, the solvent within the gel is still a $\text{H}_2\text{O}/\text{ACN}$ mixture as defined during ink formulation. To enable processing into aerogels via solvent exchange and supercritical CO_2 drying, the printed geometries need to be removed from the heptane/ NH_3 bath. For this purpose, prints are performed on polymer coated silicon substrates. The polymer coating is needed for a reliable removal of the print from the silicon substrate and consists of a polyvinyl-

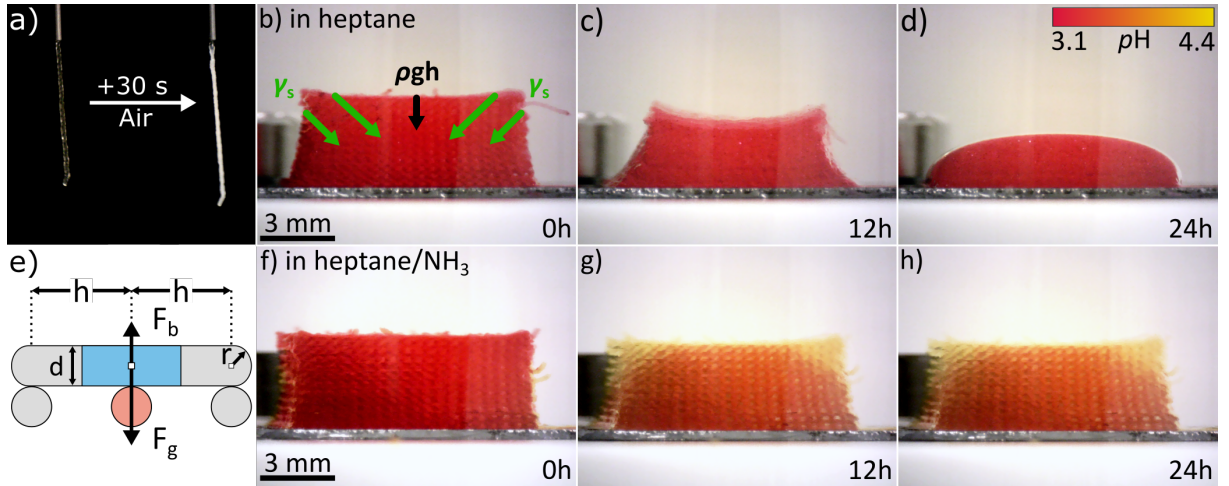


Figure 5.3: Experimental obstacles for DIW of TiO_2 nanoparticle-based aerogels. a) Optical micrograph timeseries of a pending TiO_2 gel filament after extrusion through a nozzle with inner diameter of $410\ \mu\text{m}$ in air. Optical micrograph timeseries of a microgrids 0 h, 12 h and 24 h after printing in b-d) heptane and f-h) heptane charged with NH_3 , respectively. e) Schematic representation of a microgrid printed with a nozzle of diameter $d = 2r$ and filament center-to-center distance of h . All inks except the one shown in a) are loaded with a pH indicator to illustrate the pH induced condensation of the TiO_2 gel. The microgrids in b+f) were printed with a $250\ \mu\text{m}$ nozzle and consist of 23 layers where each layer is an array of parallel filaments with a center-to-center distance h of $500\ \mu\text{m}$. Consecutive layers are normally oriented to each other.

pyrrolidone (PVP)/poly(methyl methacrylate) (PMMA) bilayer. PVP is soluble in water. Thus, it easily dissolves when transferring the substrate from the heptane/ NH_3 bath to a water/ACN mixture. In this step the PMMA layer and printed gel detach from the silicon substrate, as illustrated in Figure 5.11c. Moreover, heptane residues which are still attached to the gel automatically rise to the surface due to its lower density. The PMMA layer is dissolved during the subsequent solvent exchange to ACN which in any case is necessary to enable solvent removal via CO_2 supercritical drying.

External forces affect the gelled ink not only after but also during extrusion. Figure 5.4a illustrates that a two-zone flow pattern arises when the ink passes through a nozzle. Based on the radially varying shear stress $\tau(r)$ profile, plug flow of a gel core occurs at lower shear stress in the inner part of the nozzle, whereas laminar flow of a fluid shell develops at stresses larger than τ_f .^[30,41] In the supporting information (chapter 5.6) we estimate a fluid-like characteristic for about 76% of the filament's cross-sectional area. After leaving the nozzle, the fluid shell regains a gel characteristic within a fraction of a second (Figure 5.2g). We take advantage of the intermediate fluid shell to affect the internal structure of printed parts. When printed in a microstructured geometry, the ink easily fuses with the layer underneath for excellent layer adhesion as shown in Figure 5.4b. When printed in an unstructured geometry, filaments fuse into a compact, void free object as verified by X-ray microtomography and cross-sectional scanning electron microscopy (SEM) images in Figure 5.4c-d, respectively. For both geometries, the ink needs to fulfil two contradictory requirements. The microstructured architecture demands an ink with high mechanical stability that bridges gaps in the layer underneath and does not

spread after extrusion, whereas the compact, void-free geometry requires a soft ink that easily flows to merge into continuous layers. In our approach, we satisfy both criteria with a single ink by combining shear forces during extrusion with a subsequent stabilization of the soft ink in an alkaline liquid bath. Further mechanical characterization in Figure 5.12 and 5.13 indicate that the 3D printed samples remain stable even when loaded with the 645-fold of the own weight or when trying to peel of layers with adhesive tape, respectively.

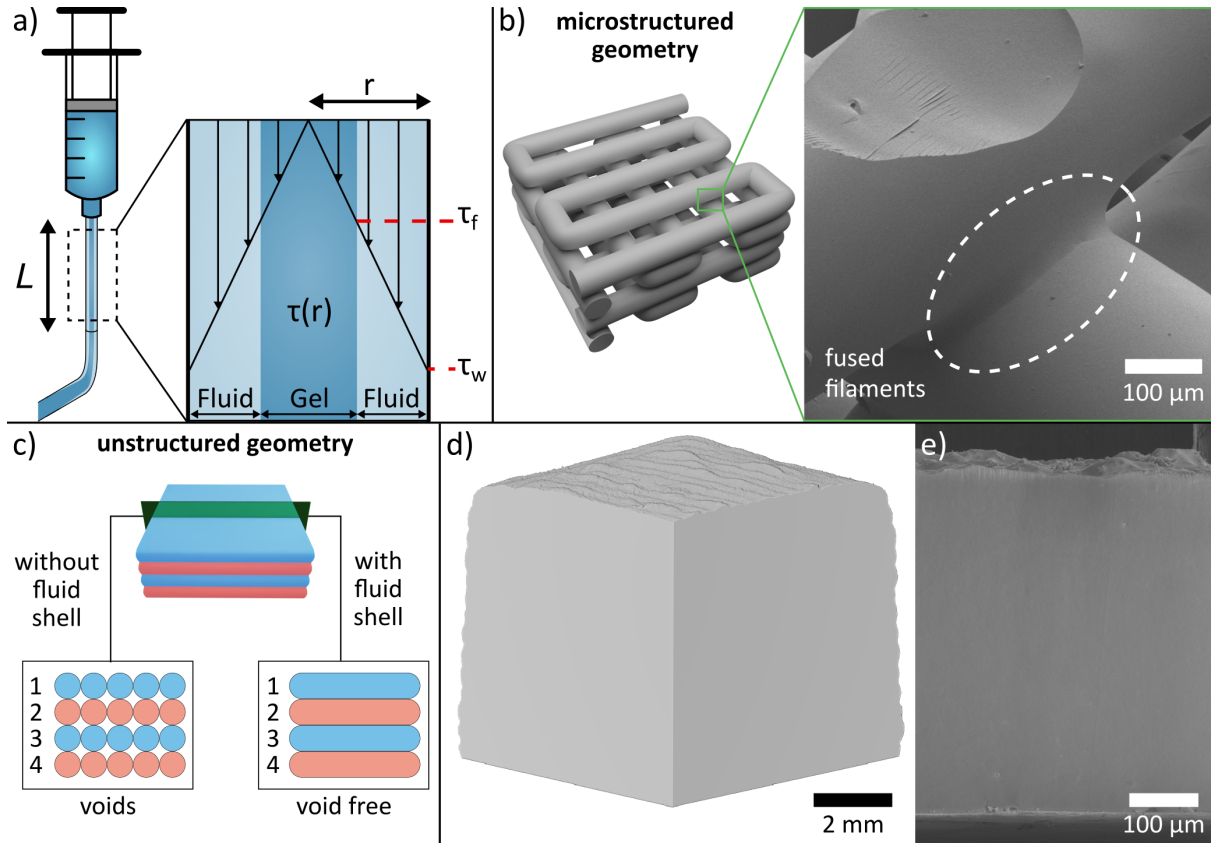


Figure 5.4: Illustration of the shear-induced fluid-shell formation and the impact on filament's interface in a microstructured and an unstructured geometry. a) Based on the radial dependence of shear stress within the nozzle, a two-zone flow pattern evolves where a gel core is surrounded by a fluid shell. b) Schematic representation of a microstructured geometry and SEM close-up of a 3D printed sample. Due to fluid-shell, filaments easily fuse with the layer underneath. c) Illustration of the expected internal structure for an unstructured geometry in absence and presence of a fluid-shell. d) X-ray microtomography and e) SEM cross-sectional images reveal that no voids are present underlying the fluid-shell character of our ink.

Combining inks of gelled nanoparticles with a macroscopic fabrication technique bridges multiple length scales at once. For illustration, we printed a grid architecture with lateral dimension of 1.3 cm and highlight the macro-, micro- and nanoscopic length scales in Figure 5.5. Here, the microscopic features are defined by the nozzle diameter. The print in Figure 5.5 was performed with a 250 μm nozzle, but nozzle sizes in a range of 150 to 1540 μm were successfully tested throughout this study. Due to the nanoscopic particle size of our ink's components, we expect that even finer nozzles diameters can be used without causing any clogging. Optical and SEM

images in Figure 5.5a-c demonstrate that the macroscopic geometry consists of individual filaments with a diameter of about $200\ \mu\text{m}$, which indicates shrinkage to about 80% of the initial nozzle diameter. We observed similar values for casted aerogels. Shrinkage mainly occurred during solvent exchange, partly during CO_2 supercritical drying and could be minimized by extending the gel aging periods.^[42] A SEM image of the filament surface in Figure 5.5d shows a homogeneous porous network over the whole area displayed. A closer look via high magnification SEM and transmission electron microscopy (TEM) images in Figure 5.5e-f reveals a delicate, continuous 3D pore network consisting of individually crosslinked TiO_2 nanoparticles with an original particle size of about 4 nm.

For further quantification of the pore network we performed nitrogen physisorption measurements. Nitrogen isotherms and pore size distributions in Figure 5.14 reveal that a 3D printed and casted aerogels feature a mean pore size of 20 nm and specific surface areas of $539\ \text{m}^2\ \text{g}^{-1}$ and $489\ \text{m}^2\ \text{g}^{-1}$, respectively. Besides, a total porosity of 95% can be approximated for both samples by taking the bulk density of anatase ($3.9\ \text{g}\ \text{cm}^{-3}$) and the density of the aerogel samples ($0.20\ \text{g}\ \text{cm}^{-3}$) into account. We conclude that the mesoporous structure of the aerogel is fully preserved and not affected by the 3D printing process.

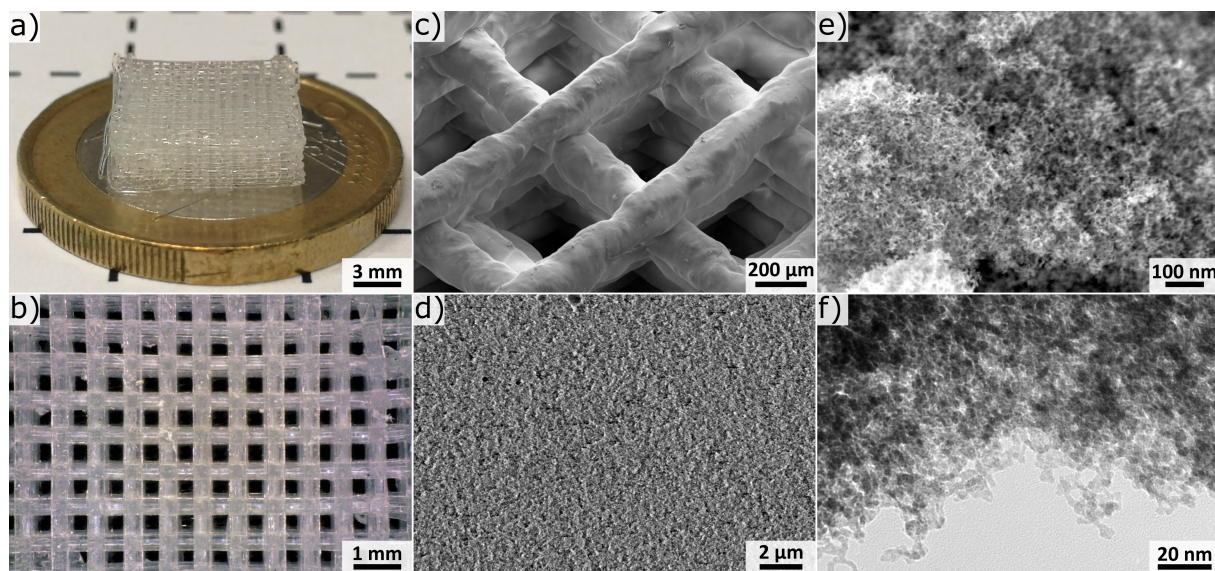


Figure 5.5: Hierarchical architecture of a 3D printed TiO_2 aerogel. Optical micrographs of a centimeter scale 3D printed TiO_2 aerogel in a) side and b) top view. SEM images of c) multiple freestanding filaments, and the filament surface at d) low and e) high magnification highlight that the microstructured TiO_2 aerogel consists of a delicate nanoporous network. The object was printed with a conical $250\ \mu\text{m}$ nozzle. f) TEM image of an aerogel fragment indicates that the individual branches of the TiO_2 aerogel consist of crosslinked TiO_2 nanoparticles.

Photothermal Properties in 3D

The use of two print heads loaded with different nanomaterials expands our 3D printing approach to multimaterial geometries. As an example, we formulate inks with distinct optical properties. The TiO_2 ink only absorbs UV radiation and appears translucent, whereas an TiO_2 ink loaded with AuNRs features strong extinction in the visible- and near-infrared range due to plasmonic excitations. We join both inks and print letters with the AuNR loaded ink on top of pure TiO_2 plates. Figures 5.6a-b demonstrate that TiO_2 preserves a translucent character upon supercritical drying, whereas the AuNR/ TiO_2 gel changes color from reddish to green. UV-vis spectra in Figure 5.6c confirm that both plasmonic peaks of AuNRs remain during the drying process, but that the longitudinal peak blue shifts by 144 nm. Since AuNRs are homogeneously dispersed in the TiO_2 aerogel matrix, as verified by high-angle annular dark field scanning transmission electron microscopy images in Figure 5.15, we attribute this color change to a change of the AuNR's dielectric environment upon removal of the solvent from the wet gel.^[43] We utilize AuNR's strong light extinction coefficient and free-form fabrication capabilities of 3D printing to locally define photothermal properties. As illustrated in Figure 5.6d-g, structured aerogels are selectively heat up to 47 °C upon illumination with a 300 W Xe light source.

Furthermore, with three selected examples we demonstrate how 3D structuring improves light-matter interaction. As a benchmark we printed an unstructured AuNR/ TiO_2 block of 7 mm \times 7 mm \times 4 mm that can also be fabricated via conventional gel casting techniques. We measure the temperature increase ΔT with an IR camera upon illumination with a 300 W Xe light source as illustrated in Figure 5.7a. We observe a rapid temperature increase of up to 62 °C (absolute 89 °C) for the light facing surface, as displayed in Figure 5.7b. Moreover, after illumination is stopped the temperature drops sharply and continues into a longer tail until all thermal energy is dissipated, similar to previously reported plasmonic nanoheaters.^[43–49] Besides, neat TiO_2 aerogel does not show significant heat generation under same experimental conditions due to the absence of AuNR as verified in Figure 5.16.

The nanoporous TiO_2 framework not only aids as structural support for AuNR, but also provides an excellent heat insulating environment with thermal conductivities similar to air.^[12,43] While this enables rapid heat generation upon illumination, high temperatures are limited to the light facing surface and drop strongly with increasing sample thickness, as illustrated in Figure 5.7a. To expand photothermal heating from a thin layer to a 3D object, we improve light penetration by designing two microstructured grid geometries as shown in Figure 5.7c. For both grids, each layer consists of an array of parallel filaments and alternating layers are orientated 90° to each other. Consecutive layers of same orientation are aligned without any shift or shifted by half of the filament separation distance. We call these geometries 'aligned' and 'shifted', respectively. For an unstructured block, light intensity drops exponentially as determined by the material's extinction coefficient. For microstructured geometries, light extinction is lower because of an increase in porosity. Moreover, for similar porosity, maximum light penetration is expected for the 'shifted' geometry due to the absence of a direct line of sight.

Figure 5.7d compares the temperature distribution as a function of sample thickness for all geometries. We observe that temperature decays strongest for the unstructured geometry and less for the microstructured geometries. For a penetration depth of about 7 mm, we measure a six times higher temperature increase ΔT of 18 °C and 3 °C for the shifted and unstructured geome-

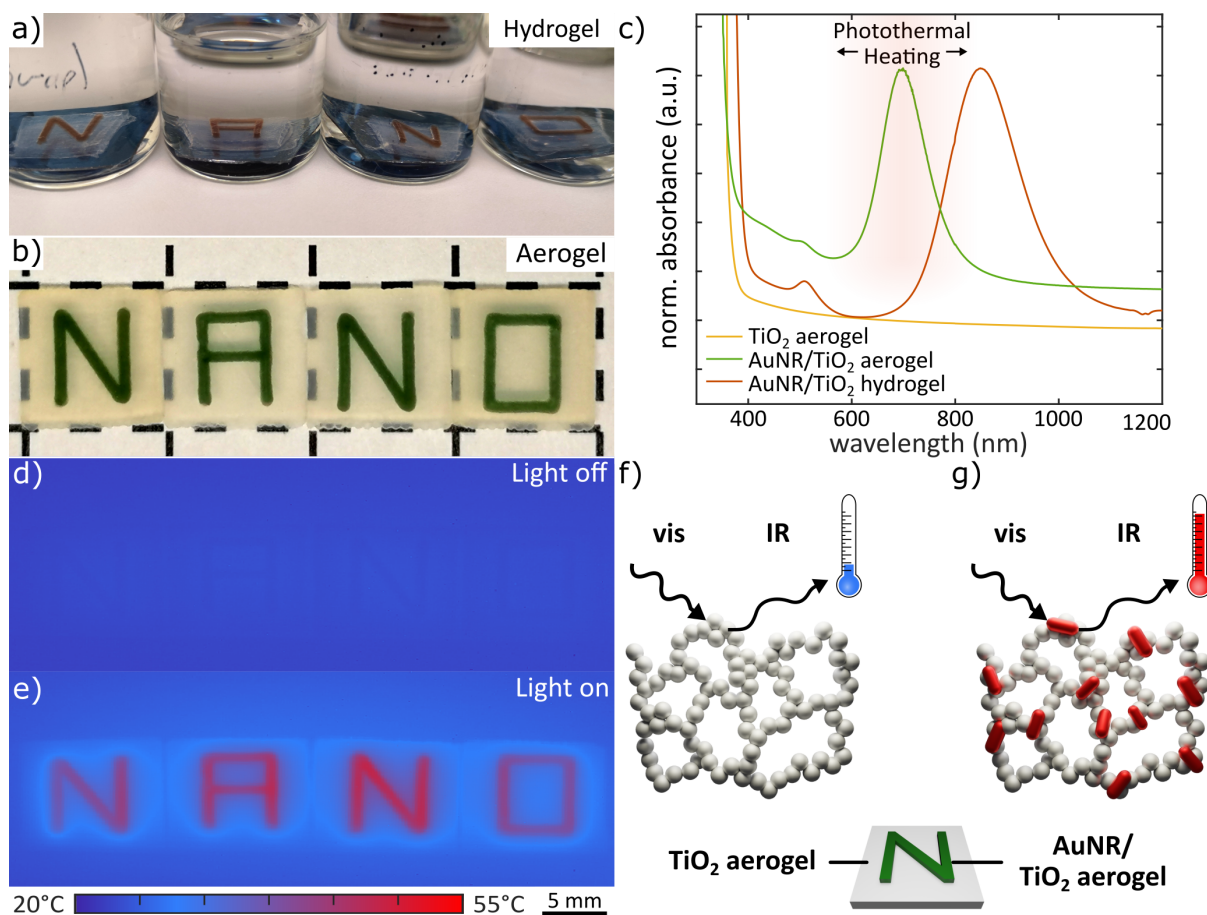


Figure 5.6: Multimaterial prints of neat TiO_2 and AuNR/ TiO_2 hybrid inks. The AuNR loaded ink appears a) reddish in form of a hydrogel and b) green in form of an aerogel. c) UV-vis absorbance spectroscopy reveals that the color change is caused by a blue shift of the longitudinal plasmon resonance peak while changing the dielectric environment from liquid to air by supercritical drying. d-e) Thermal IR camera images of the structured aerogel while illumination with a 300 W Xe light source is switched off and on, respectively. f-g) Schematic illustration of photothermal heating for a TiO_2 and AuNR/ TiO_2 aerogel upon visible light illumination. The pure TiO_2 aerogel remains cold, whereas the AuNR loaded aerogel heats up due to strong light absorption of plasmonic AuNRs.

try, respectively. To further quantify the light penetration improvement for the microstructured geometries, we first derive an attenuation coefficient for the AuNR/ TiO_2 aerogel by fitting the temperature profile of the unstructured block with an exponential function. In a next step, we relate the coefficient to the temperature distribution of both grid geometries. For the aligned geometry, the temperature decay is well described with about half of the block's value $1/2 \sigma_{\text{block}}$ – corresponding well with light absorption in every second layer of a freestanding filament. The temperature decay of the shifted geometry drops half as much as for the aligned grid and thus follows a quarter of block's attenuation coefficient $1/4 \sigma_{\text{block}}$. Consequently, microstructuring in 3D enables spatially tunable light harvesting on a macroscopic scale as reflected by a more homogeneous temperature distribution within the sample.

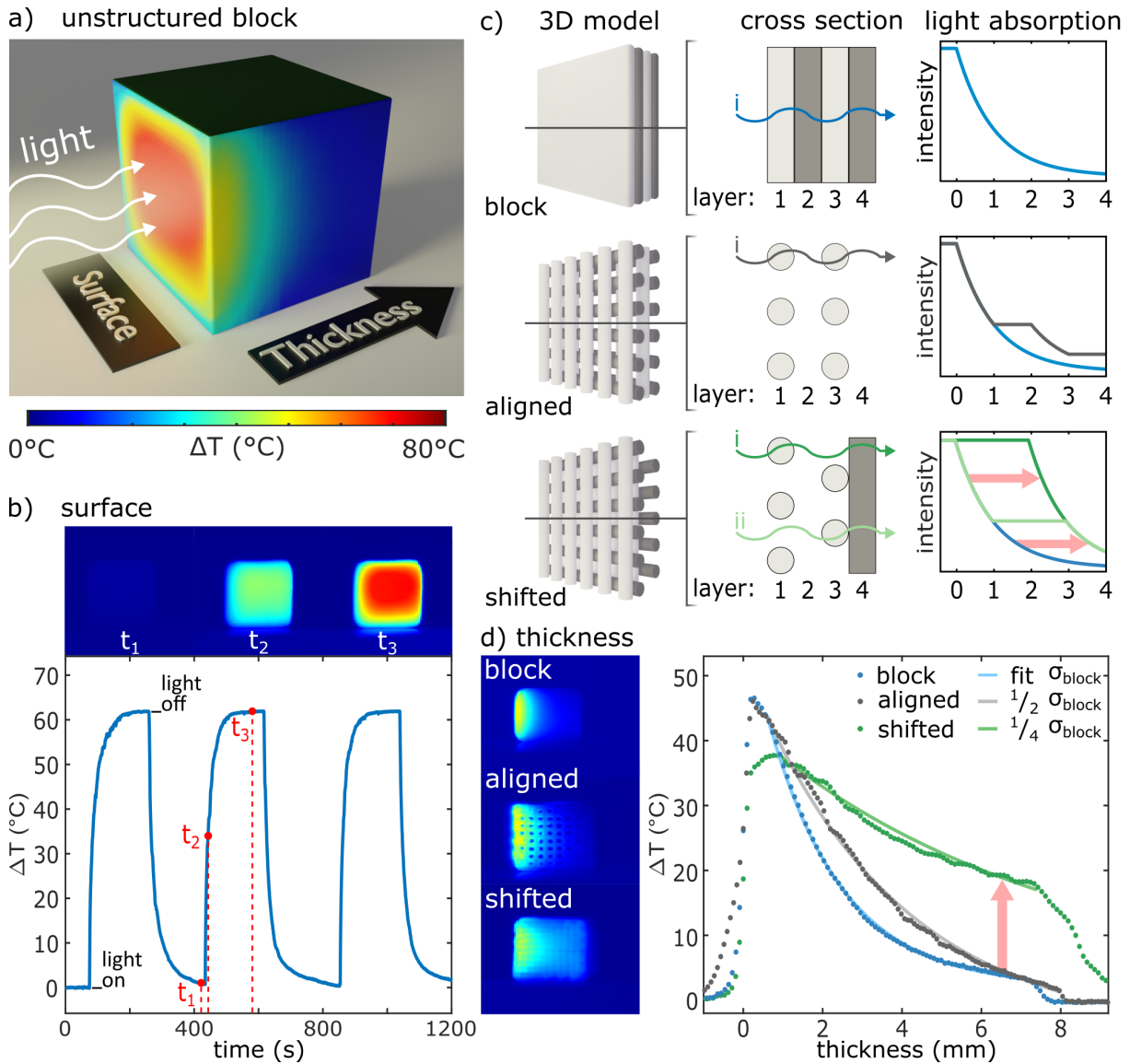


Figure 5.7: Effect of microstructuring on temperature and light distribution in 3D printed AuNR/TiO₂ aerogels. a) Schematic depiction of a typical photothermal measurement. Samples are illuminated from one side while an IR camera records the temperature either at the front or at one of the side surfaces. Exemplary temperature data for the bulk geometry are shown as an overlay on the cubic unstructured sample. b) Temperature time trace of the bulk surface temperature under repeated illumination. Insets show IR camera images at t_1 , t_2 , t_3 as indicated in the time trace plot. c) Schematic representation of light penetration into the three types of microstructure (unstructured block, aligned and shifted). From left to right the 3D model, the cross-section and the expected light absorption of each geometry are shown. For clarity, neighboring layers of the geometry are colorized. d) Measured thickness dependency of the temperature distribution for the three types of microstructuring. Bulk temperature distribution is fitted with exponential function to extract bulk extinction coefficient σ_{block} . Temperature distribution of aligned and shifted geometries follow an exponential trend but with $1/2$ or $1/4$ of the bulk decay constant σ_{block} , respectively.

5.4 Conclusion

We demonstrate a strategy for additive manufacturing of TiO₂ nanoparticle-based aerogels. Unlike typical 3D printing protocols, we do not incorporate any rheologic modifiers or non-volatile solvents to compensate for the low solid loading of gelled inks. Instead, we print in an alkaline liquid bath that prevents premature solvent evaporation and increases mechanical stability of the additive-free ink during 3D printing. Thus, the beauty of our approach lies in the fact that inks of low solid loadings can be made printable without affecting the nanoscopic properties of conventionally casted aerogels. As a result, we are able to structure aerogels on seven orders of magnitude in single or multimaterial architectures of arbitrary complexity. Our strategy of printing in a liquid bath charged with a gelation agent can be applied to other colloidal chemistries than TiO₂. The as reported approach of pH assisted condensation in a heptane/NH₃ bath should be easily applied to other metal oxides aerogels such as SiO₂, Al₂O₃ or ZrO₂ due to their similar surface chemistry. Moreover, the strategy should also be universally applicable to other material classes such as noble metal aerogels by replacing the NH₃ with a corresponding gelation agent.

To illustrate the new fabrication freedom of 3D printed nanoparticle-based aerogels, we spatially control the photothermal functionality of plasmonic AuNRs. In the past, photothermal heating of plasmonic nanoparticles was already exploited in several prototypes for clean water regeneration, triboelectric energy generation or photothermal catalysis.^[43,43,45,46,48–51] However, due to the inability to structure nanoscopic properties on a three-dimensional macroscopic scale, postulated devices mainly consist of thin films where heating is limited to the surface and scalability needs to be improved. We show for three selected geometries that 3D structuring improves light penetration by a factor of four – thus enabling a more homogeneous heat generation in a macroscopic object. Moreover, we demonstrate that 3D printing of inks with different photothermal activity allows to restrict heating to locally defined spots.

Ultimately, our 3D printing approach offers a completely new approach to engineer large scale 3D structured architectures with a significantly lower areal footprint than already reported thin-films. As applications of nanoparticle-based aerogels go well beyond photothermal devices, this work presents a versatile method for fabricating macroscopic aerogels of determined geometry and functionality.

5.5 Experimental Section

Materials: Acetonitrile (ACN, 99.95 %), diethyl ether ($\geq 99.9\%$), ethanol (EtOH, anhydrous, $\geq 99.97\%$) were purchased from VWR. Ammonium hydroxide solution (28.0-30.0 % NH_3 basis), benzyl alcohol (anhydrous, 99.8 %), gold(III) chloride trihydrate ($> 99.9\%$), L-ascorbic acid (99.5 %), methyl orange, poly(methyl methacrylate) (PMMA, average $M_w = 120000$), poly(vinylpyrrolidone) (PVP, average $M_w = 40000$), silver nitrate (AgNO_3 , $\geq 99.0\%$), sodium borohydride (NaBH_4 , 99 %), sodium citrate tribasic dihydrate ($\geq 99.0\%$), titanium(IV) tetrachloride (TiCl_4 , 99.9 % trace metal basis) were purchased from Sigma Aldrich. Cetyltrimethylammonium bromide (CTAB, $> 98.0\%$) and sodium oleate (NaOL, $> 97.0\%$) were purchased from TCI Deutschland GmbH. HCl (37 wt. % in water) was purchased from Carl Roth. n-heptane (95 %) was purchased from Alfa Aesar. Liquid CO_2 was purchased from Westfalen. All chemicals were used as received without further purification.

TiO₂ synthesis: TiO₂ nanoparticle synthesis was adopted from a previously published protocol.^[23] While stirring, 1 mL of TiCl_4 was dropwise added to a 50 mL round bottom flask containing 5 mL of Ethanol (EtOH) resulting in a transparent yellow solution. Next, 20 mL of benzyl alcohol were added and the solution was continuously stirred and heated to 80 degreeCelsius while keeping the flask open. After 24 h the flask was immersed into a water bath at room temperature to quench the reaction. Next, the suspension was washed with diethyl ether (≈ 4.7 mL per mL suspension) by three dispersion-centrifugation cycles (3500 rpm, 5 min, room temperature). Afterwards, the supernatant was removed by decantation and the vial was loosely covered with its cap for slow evaporation of the remaining solvent. Finally, the dried precipitate was mortared to yield approximately 550 mg of a white powder. TiO₂ nanoparticle characterization by dynamic light scattering (DLS), X-ray diffraction and IR spectroscopy is shown in Figure 5.17-5.18.

AuNP synthesis: AuNP synthesis was adopted from a previously published protocol.^[52] For this 37 mg sodium citrate tribasic dihydrate was added to a 250 mL round bottom flask containing 150 mL of water. Next, the flask was immersed into an oil bath which temperature was set to 120 °C. As soon as the solution started boiling, 375 μL of a 0.1 M HAuCl_4 solution was added and the solution turned from colorless to purple and red within a couple of minutes. After refluxing for 24 h at 120 °C, the dispersion was cooled down to room temperature and stored in a fridge for further use. AuNP characterization by TEM and UV-vis absorbance spectroscopy is shown in Figure 5.19a-c.

AuNR synthesis: AuNR synthesis was adopted from a previously published seeded growth protocol.^[53] The seed solution was prepared as follows: 5 mL of 0.5 mM HAuCl_4 was mixed with 5 mL of 0.2 M CTAB in a 30 mL scintillation vial. Next, 0.6 mL of fresh 0.01 M NaBH_4 was diluted to 1 mL with water and then injected into the HAuCl_4 -CTAB solution under vigorous stirring (≥ 1200 rpm). The stirring was stopped after 2 min. The yellow-brownish seed solution was aged at room temperature for 7 to 8 min before use.

To prepare the growth solution, 7.0 g of CTAB and 1.234 g of NaOL were dissolved in 250 mL of water in a 1 L Erlenmeyer flask heated to 50 °C in a water bath. Next, the solution was cooled down to 30 °C and 18 mL of 4 mM AgNO_3 solution was added. The mixture remained undisturbed at 30 °C for 15 min, after which 250 mL of 1 mM HAuCl_4 solution was added. The

solution became colorless after 90 min of stirring at 700 rpm and, after that, 2.1 mL of HCl was added. After another 15 min of slow stirring at 400 rpm, 1.25 mL of 64 mM ascorbic acid was added and the solution was vigorously stirred at ≥ 1200 rpm for 30 s.

Finally, 0.8 mL of seed solution was injected into the growth solution under vigorous stirring (1200 to 1500 rpm). The resultant mixture was stirred for 30 s and the stirring was turned off. The solution remained undisturbed at 30 °C for at least 12 h for the AuNR growth. The final product was isolated by centrifugation at 7000 rpm for 30 min followed by removal of the supernatant. Subsequently, AuNRs were redispersed in 10 mL of water. AuNR characterization by TEM and UV-vis absorbance spectroscopy is shown in Figure 5.19d-f.

Ink Formulation: Inks for 3D printing were formulated by dispersing a dry TiO₂ powder in a water/ACN mixture (2 : 1 vol. ratio) yielding a mass loading of 15 wt. % which corresponds to a volumetric concentration of 4.0 vol. %. The use of dry TiO₂ powder is necessary for reliably ink formulation with similar particle concentrations and rheologic properties across multiple particle batches. The dispersing procedure consisted of a repetitive cycle of stepwise addition of TiO₂ nanoparticles, 1 min vortex mixing, followed by 1 min ultrasonication in an ice bath. An ice bath was used to impede temperature induced gelation due to frictional heating during vortex mixing. Multimaterial inks were formulated by replacing the corresponding volume fraction of water with an aqueous dispersion of AuNPs or AuNRs. For pH tests the neat TiO₂ ink was charged with 0.05 wt. % methyl orange. Eventually, inks were stored in a refrigerator prior gelation. Before gelation, inks were homogenized two times for 5 min at 2000 rpm with a single degassing step of 5 min at 2500 rpm in between using an ARE-250 planetary speed mixer (Thinky Corporation, Japan). Gelation was performed in 5 cm³ syringes in a preheated oven (60 °C) for 16.5 min while the open tip of the syringe was pointing upwards. After gelation, the tip of the syringe was sealed with an airtight cap and the ink was typically used within 2 days.

3D Printing: Prints were performed in a liquid bath with an Engine HR 3D printer (Hyrel 3D, USA) equipped with multiple SDS-5 syringe displacement printheads. Syringes charged with the nanoparticle gel were loaded into the print head and equipped with Luer-Lock needles to define the filament diameter (150 to 1540 μm). Throughout this study either burr-free polished passivated stainless-steel nozzles from Nordson EFD or conical polyethylene nozzles from Gono Dosiertechnik GmbH were used. For the former nozzle type the printed filaments appear smooth, whereas for the latter the surface is more uneven, as indicated in Figure 5.4b and 5.5c, respectively. Depending on needle diameter, prime and unprime values of the printhead were adjusted to achieve reliable start and stop of ink flow without oozing. Volumetric flowrate is calculated by the 3D printer's software depending on needle diameter d , layer height ($0.9d$) and printing speed (typical 2 to 6 mm s^{-1}). Before each print the distance of the nozzle and printbed is calibrated via an optical microscope camera (Dino-lite, USA). Printing paths were generated via custom-made Python-scripts.

The print itself is performed on silicon substrates coated with a PVP/PMMA bilayer. For this, silicon substrates (2.5 cm \times 2.5 cm) were cleaned with acetone, isopropanol, and Milli-Q water in an ultrasonic bath and treated with air plasma for 5 min at 100 W (Femto, Diener Elektronik, Germany). For polymer deposition, the substrates were placed onto a spin-coater and fully covered with the polymer solution (First layer: 5 wt. % PVP in EtOH. Second layer: 20 wt. %

PMMA in acetone) before starting the spinning process (PVP: 5 s at 500 RPM followed by 60 s at 1000 RPM, PMMA: 30 s at 3000 RPM). After each deposition cycle substrates were baked on a hotplate for 2 min at 50 °C.

Before the print, parts of the polymer bilayer along the edge of the substrate were removed to make the PVP layer more accessible for the lift off process after the print. As prepared substrate was fixed with two screws in a custom-made printing container which contained a liquid bath (Figure 5.11a-b). The bath was obtained by vigorously shaking a mixture of 10 mL of n-heptane and 4 mL of an aqueous NH₃ solution in a flask. Next, the NH₃-enriched heptane phase was transferred to the printing container. During printing a fraction of the liquid bath was transferred back to the flask containing the NH₃ solution and the process of NH₃ enrichment was repeated every 5 min. After the print, the liquid bath was refreshed a final time and the printing container was covered with a glass slide for 90 min. Subsequent, the substrate was immersed into a water/ACN mixture (2 : 1 vol. ratio) for lift off (Figure 5.11c). Finally, a stepwise solvent exchange to ACN and CO₂ supercritical drying in a Quorum E3100 was performed.

Photothermal Measurements: Aerogels were placed on a Teflon plate and illuminated with a 300 W Xe lamp equipped with a H₂O filter to remove IR light from the light source. For each measurement the distance of sample and light source was kept constant at 30 cm to illuminate all samples with similar light intensities. Temperature evolution was recorded with a high-resolution IR camera (SC7000, FLIR, USA).

Characterization: Scanning electron microscopy images were taken with a Regulus 8220 (Hitachi High Technologies Corp., Japan). Transmission electron microscopy images were taken with a JEM 1011 (JEOL Ltd., Japan). N₂-Physisorption measurements were performed at 77 K with a Quantachrome Autosorb 6-MP (Anton Paar QuantaTec Inc., USA). The specific surface area and pore size were determined via the Brunauer-Emmet-Teller (BET) method and Density Functional Theory (DFT) analysis, respectively. For DFT analysis a Non Local DFT (NLDFT) calculation model for nitrogen at 77 K using the equilibrium branch was applied and cylindrical pores in silica were assumed. Prior to measurement, samples were degassed at 100 °C for 24 h. The density of the aerogel was calculated from the mass and dimensions of a rectangular aerogel plate. We used the mass of an aerogel dried in a vacuum oven at 100 °C and <2 mbar for 24 hours, because the initial aerogels contain significant amounts of physisorbed water which results in an artificially high density. The amount of gold was determined after digestion in aqua regia using graphite furnace atomic absorption spectroscopy (Analytik Jena contraAA 700). Powder X-ray diffraction measurements were performed on a Bruker D8 Discovery using Cu-K_α X-ray radiation. UV-vis-NIR absorbance spectra of nanoparticle dispersions and aerogel plates were recorded using an Agilent Cary 5000 spectrophotometer. Fourier transform infrared spectra were recorded on a Bruker Alpha II spectrometer equipped with an attenuated total reflection module. Rheologic measurements were performed on MCR 502 rheometer (Anton Paar, Germany) in cone plate geometry (20 mm, 1° slope) at 20 °C. After loading the sample, a rotational pre-conditioning at 1 s⁻¹ for 1 min followed by 1 min rest was applied to homogenize the sample. Shear tests were performed using shear rate controlled flow ramps in range from 0.001 to 1000 s⁻¹. Strain-controlled oscillatory amplitude sweeps were performed at constant frequency of 1 Hz. Oscillatory frequency sweeps were performed in a range of 1 to 50 Hz at 0.5 %

strain. Structural recovery tests were performed at fixed frequency of 1 Hz and consisted of 3 steps. Step 1 at low amplitude of 0.5 % determines the initial structure and stability over time, step 2 at high amplitude of 150 % disintegrates initial gel structure and ensures that the ink is in the fluid-like regime, and step 3 at low amplitude of 0.5 % monitors the structural recovery from a fluid-like to gel-like sample characteristic. Interfacial tension was determined by pendant drop tensiometry with n-heptane as surrounding phase (DSA100, Krüss, Germany). DLS was performed with a Zetasizer Nano ZS instrument (Malvern Instrument Ltd., UK) equipped with a HeNe laser operating at 632.8 nm in backscatter detection mode. X-ray microtomography imaging was performed on a custom-built setup as described elsewhere.^[54] The X-ray microtube was operated at 60 keV and 50 μ A. The sample was placed 111.2 mm from the source and 42.4 mm from the detector. For each scan 1440 projections were collected over 360° with an exposure time of 10 s. Projections were acquired at a magnification of 1.38 with an Andor Zyla sCMOS HF camera (Oxford Instruments, 2160 x 2560 pixels, 6.5 μ m pixel size, 4x binning), resulting in an effective pixel size of $4 \cdot 6.5 \mu\text{m} / 1.38 \approx 19 \mu\text{m}$. The data was corrected by a series of dark- and flat-field images and tomographically reconstructed in cone-beam geometry using a custom-made Python-script based on the ASTRA toolbox.^[55,56] Reconstructed data was visualized and analyzed in Avizo software version 2020.2.

5.6 Supporting Information

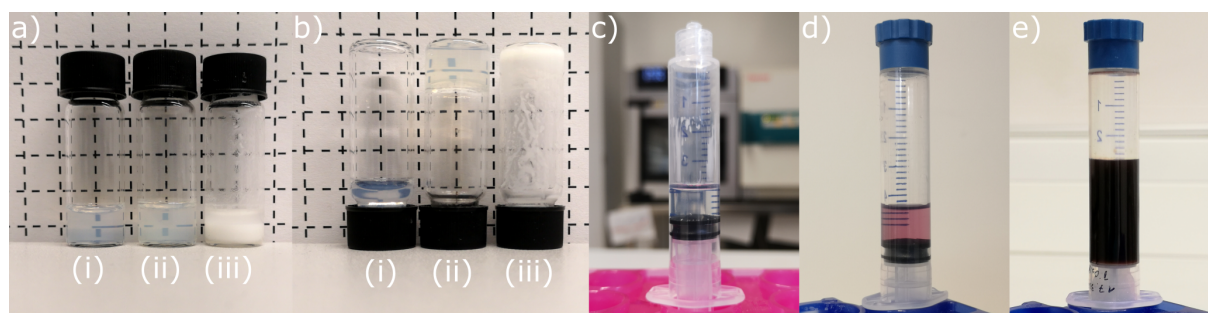


Figure 5.8: Ink stability for increasing ACN contents and different nanomaterial compositions. Photographs of TiO_2 dispersion in (i) pure H_2O , H_2O :ACN mixture with volumetric ratios of (ii) 2:1, and (iii) 1:1 a) prior and b) after thermal treatment at 60°C indicate a destabilizing effect of ACN on aqueous TiO_2 dispersions. Particles precipitate for a 1:1 ratio and did not gel during the thermal treatment in absence of ACN. Therefore, inks for 3D printing are formulated at a volumetric ratio of 2:1 and photographs of gelled inks of neat TiO_2 , AuNP/ TiO_2 , and AuNR/ TiO_2 are shown in c-e), respectively.

Table 5.1: Yield stress τ_y and flow stress τ_f derived from oscillatory amplitude sweeps for TiO_2 inks with particle concentrations of 15 and 20 wt. %, which corresponds to a volumetric concentration of 4.0 and 5.6 vol. %, respectively. τ_y and τ_f are defined as required stress at which G' falls below 90 % of its initial value and stress at which $G' = G''$, respectively.

concentration (wt. %)	yield stress τ_y (Pa)	flow stress τ_f (Pa)
15	104	210
20	165	307

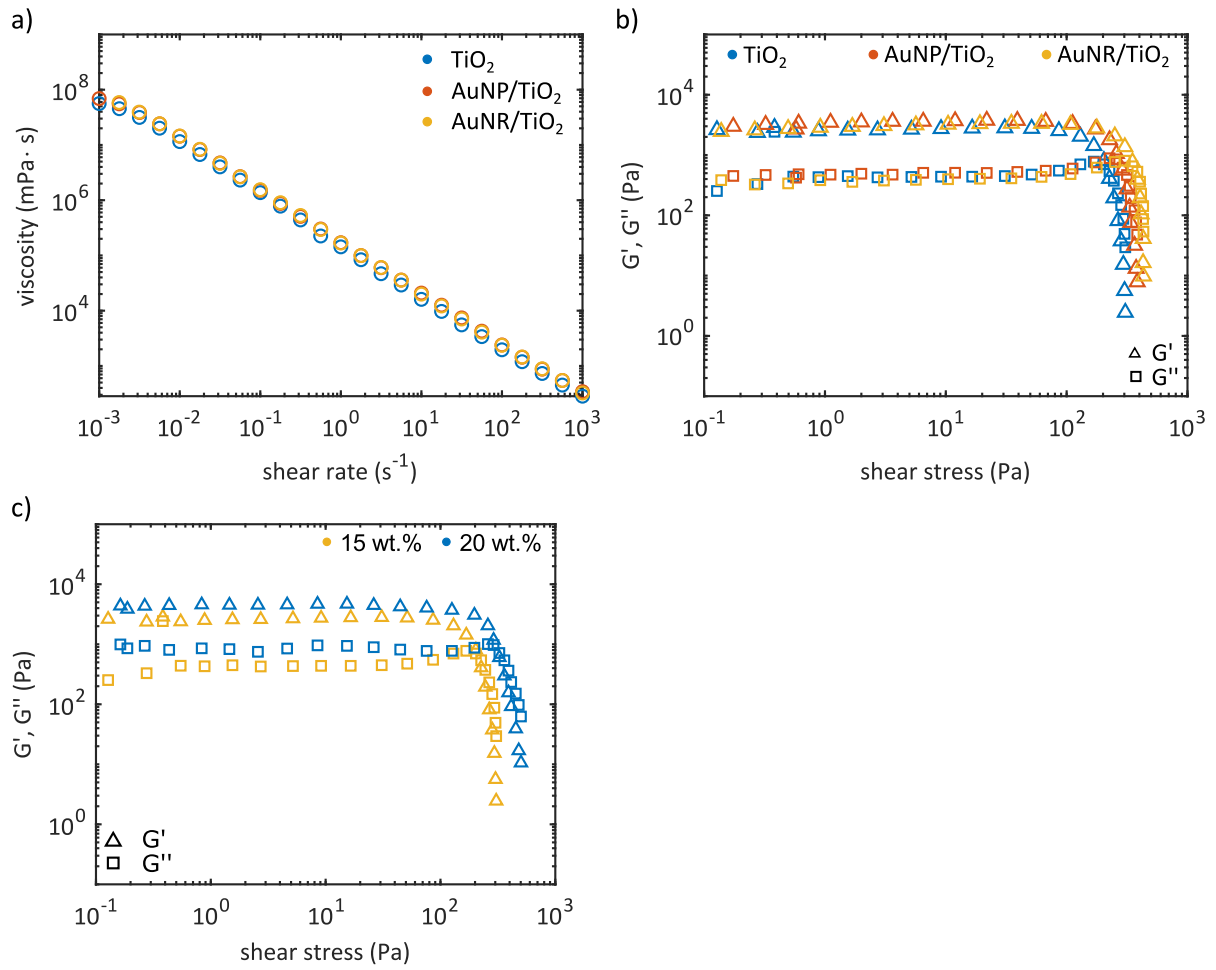


Figure 5.9: a) Rotational sweep and b) oscillatory amplitude sweep measurements of TiO_2 , $AuNP/TiO_2$ and $AuNR/TiO_2$ inks. The $AuNP/TiO_2$ and $AuNR/TiO_2$ inks contain 0.045 wt. % and 0.49 wt. % Au relative to TiO_2 , respectively. c) Oscillatory amplitude sweep of TiO_2 inks with particle concentrations of 15 wt. % and 20 wt. %, which corresponds to a volumetric concentration of 4.0 vol. % and 5.6 vol. %, respectively. The yield stress τ_y and flow stress τ_f for TiO_2 inks of 15 wt. % and 20 wt. % are listed in Table 5.1.

Stress Estimation

Upon printing the gel is exposed to gravitational and capillary forces that cause deformation of the soft material as long as the yield stress is exceeded by these forces, as exemplified for a 3D printed grid geometry in Figure 5.10a.^[30,57,58] Estimating the contribution of each component helps to define the driving force of the deformation. A typical grid geometry consists of an array of filaments of diameter d and spacing h , where neighboring layers are orientated 90° to each other (Figure 5.10a). Due to a periodicity of h , the filament in the lower layer colored in red effectively only needs to carry a small filament section colored in blue. The gravitational pull of this filament segment (equation 5.1) is partly compensated by buoyancy forces of the liquid bath (equation 5.2). The net force of the filament section $F_{\text{effective}} = F_{\text{gravity}} + F_{\text{buoyancy}}$ is distributed over the filament's interfacial area d^2 and causes a pressure $p_{\text{total},1}$ on the layer below (equation 5.3). Multiplying the gravitational pressure of a single layer with the number of total layers yields the total gravitational pressure onto the lowest layer owing to the overall weight of the printed grid architecture.

$$F_{\text{gravity}} = -m_{\text{ink}}g = -\rho_{\text{ink}}V_{\text{ink}}g \approx -\rho_{\text{ink}} \left(\frac{\pi d^2}{4} h \right) g \quad (5.1)$$

$$F_{\text{buoyancy}} = m_{\text{bath}}g_{\text{bath}} \approx \rho_{\text{bath}} \left(\frac{\pi d^2}{4} h \right) g \quad (5.2)$$

$$\begin{aligned} p_{\text{total},1} &\approx \frac{F_{\text{effective}}}{d^2} \\ &= \frac{F_{\text{gravity}} + F_{\text{buoyancy}}}{d^2} \\ &= \frac{g \left(\frac{\pi d^2}{4} h \right) (\rho_{\text{bath}} - \rho_{\text{ink}})}{d^2} p_{\text{gravity}} \\ &= \frac{g\pi h (\rho_{\text{bath}} - \rho_{\text{ink}})}{4} \end{aligned} \quad (5.3)$$

Besides gravity, the existence of interfacial tension has profound consequences for the equilibrium shape of gels due to the presence of a pressure difference ΔP between the gel-liquid interface. ΔP is generally described by the Young-Laplace equation in equation 5.4. Here, the pressure difference across the interface is equal to the product of the interfacial tension γ and the mean curvature κ . For spherical shapes the curvature can be expressed via its radius r :

$$\Delta P = 2 \cdot \gamma \cdot \kappa = \frac{2 \cdot \gamma}{r} \quad (5.4)$$

The shape of the gel-liquid interface of a printed grid geometry is complex and features different kinds of curvatures. Due to its circular cross-section individual filaments of the print can be idealized as a spherocylinder with hemispherical end caps of curvature $1/r$. It was reported that filaments of any aspect ratio are stable as long as interfacial tension and filament radius result

in a capillary pressure (equation 5.4) smaller than its yield stress τ_y .^[59,60] Besides, drastically higher curvatures are present at filament intersections, as indicated in Figure 5.10a. To minimize the influence of the latter and of gravitational pressure, pending filaments were complementary investigated where the tip can be initially approximated as a sphere of radius $r = d/2$, as shown in Figure 5.10b.

We summarize the geometrical parameters for two exemplary grid geometries of different filament diameter, gravitational pressure on the lowest layer, and capillary pressure of a single filament in Table 5.2 and show optical micrographs of the printed grid geometries in Figure 5.10d-g. The geometries were printed with a nozzle diameter of 250 μm and 1540 μm , respectively. We observe that the grid geometry printed with a 250 μm nozzle completely loses its initial shape and forms a droplet within 24 hours, whereas the grid geometry printed with a 1540 μm features less deformation and the outline of individual filaments remains visible. For both nozzle diameters d , the spacing h and the number of layer N were adapted to achieve similar gravitational pressure on the first layer. We calculate a gravitational pressure p_g of about 30 Pa for both filament diameters which is too low to cause any yielding ($\tau_y = 104$ Pa). Besides, we estimate a capillary pressure of 320 Pa and 59 Pa for the 250 μm and 1540 μm diameter, respectively.

Since the capillary pressure for diameter of 250 μm already exceeds the yield stress by a factor of three, we deduce the energetic unfavorable ink/n-heptane interface as main driving force of deformation. As a result, the grid geometry minimizes its interfacial area by forming a droplet as shown in Figure 5.10e. For the thicker filament diameter of 1540 μm , the capillary pressure and even the sum of gravitational and capillary pressure of 81 Pa are slightly lower than the yield stress of 104 Pa. Nevertheless, we still observe a slight deformation of the grid geometry in Figure 5.10g. This behavior may be explained by the presence of higher curvatures at filament intersections in the grid geometry as indicated in Figure 5.10a, which lead to higher capillary pressures than initially assumed.

To eliminate the influence of higher curvatures at filament intersections, we investigated the deformation of pending gel filaments. We extruded pending gel filaments of 250 μm and 1540 μm into a heptane bath and show an optical micrograph time series in Figure 5.10h-i and j-k, respectively. With increasing the nozzle diameter d from 250 to 1540 μm we observe a less pronounced filament deformation which is in line with a reduced capillary pressure and observations for printed grid geometries. However, slight deformation took still place although the capillary pressure of 52 Pa is lower than the yield stress of 104 Pa. This can be justified by the fact that the tip of the pending filament does not represent the idealized shape of a sphere with radius $r = d/2$ and consequently features a higher capillary pressure than assumed.

To proof that capillary pressure is the main driving force of deformation, we charged the heptane bath with Triton X-100 – a nonionic surfactant. We show in Figure 5.10l-m that the filament maintains its shape in presence of Triton X-100 and assign this to a drastically reduced interfacial tension. Since deformation reduces with increasing filament diameter and even vanishes in presence of surfactants such as Triton X-100, we identify capillary pressure as the main driving force of deformation. Moreover, we expect that no distortion should be present for nozzle diameters much larger than 1540 μm .

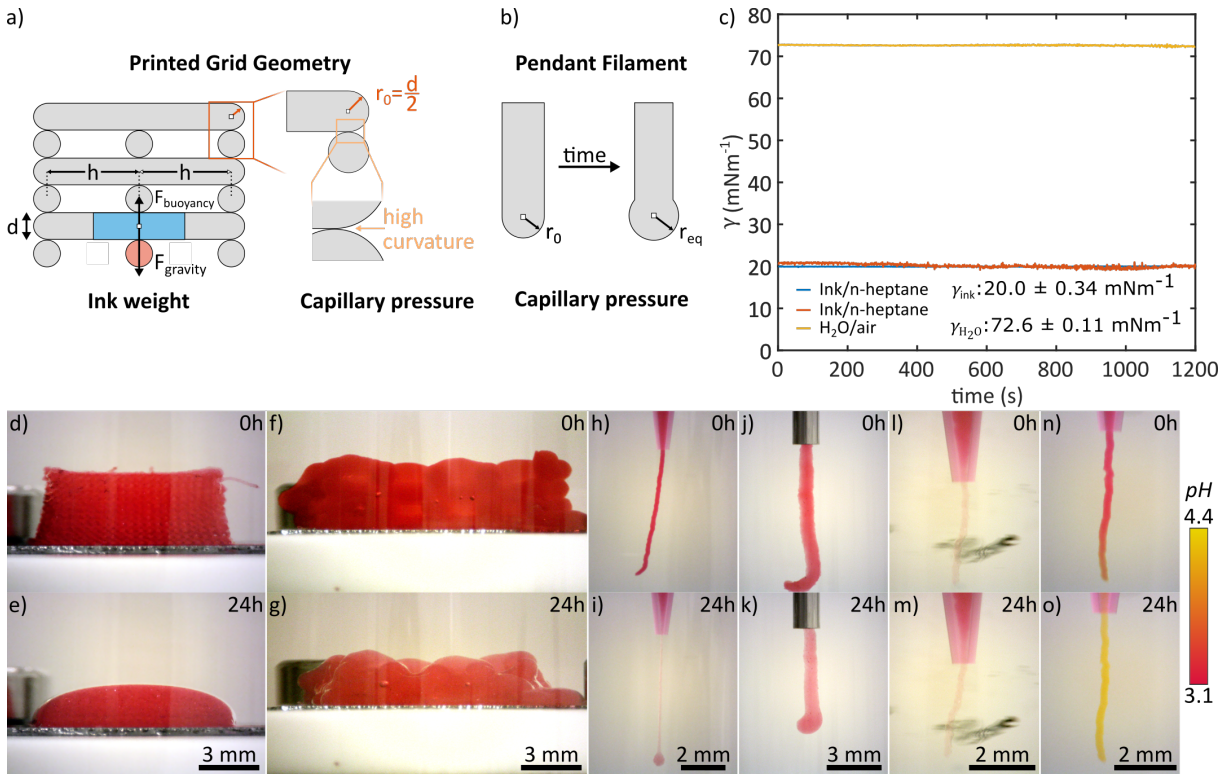


Figure 5.10: a-b) Stress estimation for a 3D printed grid geometry and a pending gel filament, respectively. a) Ink weight: Due to a periodicity of h , the filament in the lower layer colored in red effectively only needs to carry a small filament section colored in blue. Capillary pressure: Capillary pressure is inversely proportional to the effective radius of the interface. Printing with a nozzle diameter of $d = 2r_0$ results in objects featuring curvatures of $1/r_0$ at the outer edges and undefined higher curvatures at filament intersections. b) The tip of a pending filament can be represented by a sphere of radius $r_0 = d/2$ which changes its shape to an equilibrium radius of r_{eq} if the resultant capillary pressure is higher than the yield stress. c) Interfacial tension γ time trace of TiO $_2$ ink in n-heptane and H $_2$ O in air as surrounding phase after equilibrium was reached. TiO $_2$ ink was not gelled before measurement so that the shape of the drop is not affected by its yield stress. For the ink/n-heptane interface the data of two consecutive measurements are shown. The H $_2$ O/air measurements matches literature value of 72.8 mN m $^{-1}$ and validates the measurement procedure.^[61] d-o) Deformation studies of 3D printed grid geometries and pending filaments. Optical micrograph time series show d-g) grid geometries 3D printed in a heptane bath and pending gel filaments in h-k) a heptane bath, l-m) a heptane bath charged with Triton X-100 and n-o) a heptane bath charged with ammonia, respectively. The grid geometries in d-e) and f-g) were printed with a 250 μm and 1540 μm nozzle, respectively. Pending filaments in h-i, l-o) and j-k) were extruded through a 250 μm and 1540 μm nozzle, respectively. For each experiment, the TiO $_2$ ink was loaded with a pH indicator.

Table 5.2: Physical description of the grid geometries shown in Figure 5.10d+f by center-to-center distance h , number of layers N , filament diameter d , radius $r = d/2$, interfacial tension γ . Besides, capillary pressure ΔP and gravitational pressure p_g on the first layer of the grid geometry are listed as calculated by equation 5.3 and 5.4, respectively.

d (μm)	N	h (μm)	r (μm)	γ (mN m^{-1})	ΔP (Pa)	p_g (Pa)
250	22	500	125	20.0	320	32
1540	4	3080	770	20.0	52	29

In the main section of this publication we report an NH_3 assisted condensation process to overcome capillary pressure driven deformations by an increase of the ink's yield stress during 3D printing. Other procedures to reduce capillary pressure driven deformation during 3D printing might be achieved by either employing surfactants such as Triton X-100 for a reduced ink/bath interfacial tension or by increasing TiO_2 concentration for a higher yield stress. Although Triton X-100 successfully eliminates distortions for a pending TiO_2 filament as shown in Figure 5.10l-m, 3D printing in a Triton X-100 loaded heptane bath was not practical due to insufficient layer adhesion. In our liquid bath approach, we utilize the fact that the ink and substrate are both hydrophilic, whereas the liquid bath is hydrophobic. In this case the ink has significant higher preference to stick to the substrate than the surrounding liquid, which enables good layer adhesion. Employing surfactants such as Triton X-100 render the hydrophilic surface of the ink hydrophobic. Therefore, the ink and liquid bath have similar wetting abilities that prevent a reliable adhesion of the ink to the substrate.

Another approach to reduce capillary pressure-driven deformation is to rise the ink's yield stress to values much larger than its capillary pressure of 320 Pa. Since an increase of the TiO_2 loading from 15 to 20 wt. % only leads to a growth of the yield stress from 104 to 165 Pa (Figure 5.9c, Table 5.1), significantly higher TiO_2 loadings are required to achieve yield stress high enough for compensation of the capillary pressure of 320 Pa. However, this goes along with a loss of the ink's exceptional structural aerogel properties such as low density, high porosity, and specific surface area that gives this class of material great prospects in many applications. Moreover, since capillary pressure scales with $1/r$, even higher yield stresses are needed to achieve deposition through thinner nozzles.

Thus, the beauty of our NH_3 assisted condensation process lies in the fact that inks of low solid loadings can be made printable without affecting the wettability of the substrate or compromising aerogel characteristic. Moreover, based on the nanoscopic size of the ink's building blocks much thinner nozzle diameters than 250 μm should be achievable without causing any clogging.

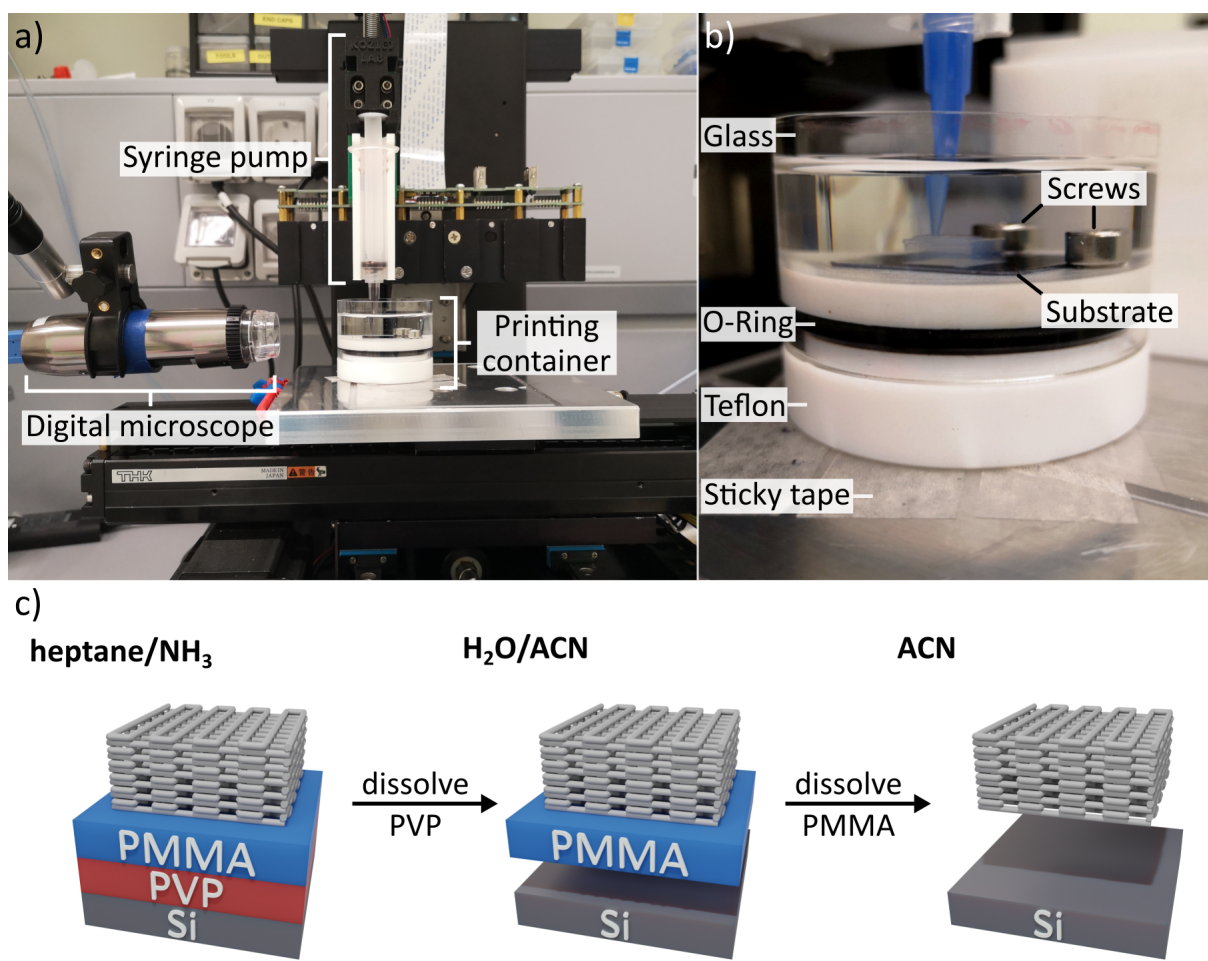


Figure 5.11: Photograph of a) the 3D printing setup, b) a close-up of the printing container, and a schematic of the c) lift-off procedure for reliable removal of the print from the substrate. a-b) The setup consists of a 3D printer equipped with a mechanical syringe pump, a custom-made printing container, and a digital microscope. The container is designed to enable visual inspection through the glass cylinder while printing in a liquid bath. The substrate is fixed with two stainless-steel screws. c) The silicon substrate is coated with a PVP/PMMA bilayer. The PVP layer easily dissolves when transferring the substrate from the heptane/NH₃ bath to a water/ACN mixture. As a result, the PMMA layer and printed gel detach from the silicon substrate. The PMMA layer is dissolved during the subsequent solvent exchange to ACN which is in any case necessary to enable solvent removal via CO₂ supercritical drying.

Liquid Shell Estimation

The ink flowing through a cylindrical nozzle may adopt a two-zone flow pattern where plug flow of an unyielded gel core occurs in the inner part of the nozzle featuring lower shear stresses and laminar flow of a yielded shell arises at the higher stresses closer to the nozzle. The type of flow depends on the yield stress of the ink and the shear stress profile across the nozzle radius. The shear stress τ along the radius of a cylindrical nozzle can be calculated as follows:^[30,41]

$$\tau = \frac{\Delta P}{2L} r \quad (5.5)$$

where L is the nozzle length, r is the radial position from the nozzle center and ΔP is the applied pressure difference to initiate flow. Based on this equation, maximum shear stress τ_{\max} occurs at the wall ($r = d/2$) and decreases linearly towards the center of the nozzle. The radial position at which the transition from laminar to plug flow occurs is defined as r_{gel} and corresponds to the radius at which the applied shear stress equalizes the flow stress τ_f of the ink. Following equation 5.5 r_{gel} can be calculated as:

$$r_{\text{gel}} = \frac{2L\tau_f}{\Delta P} \quad (5.6)$$

We use equation 5.6 to estimate r_{gel} for the two typical nozzle sizes used during this study. The physical dimensions of the nozzles, the estimated r_{gel} , and the share on the total cross-sectional area for a 15 wt. % ink are listed in Table 5.3. We calculate that the ink adopts a two-zone pattern that consists to 76 % of a fluid shell, due to the low flow stress of 206 Pa. Oscillatory recovery measurements indicate that the fluid shell recovers to a gel within one second after extrusion (Figure 5.2d). We assume that the fluid shell enables the ink to easily bond to neighboring filament for good intralayer adhesion and to form continuous objects without any voids as shown in Figure 5.4b and 5.4c-e, respectively.

Table 5.3: Fluid-shell estimation for two nozzles of diameter d and length L . The pressure drop ΔP corresponds to the required pressure for a steady extrusion of filaments via a pneumatic print head (Ultimus V, Nordson) at a deposition speed of 4 mm s^{-1} . r_{gel} is calculated following equation 5.6. The gel and fluid fraction define the areal contribution of the respective flow type to the total cross-sectional area of the nozzle.

d (μm)	$r = d/2$ (μm)	L (mm)	ΔP (bar)	r_{gel} (μm)	gel (%)	fluid (%)
410	205	12.7	1.1	50	24	76
250	125	12.7	1.8	30	24	76

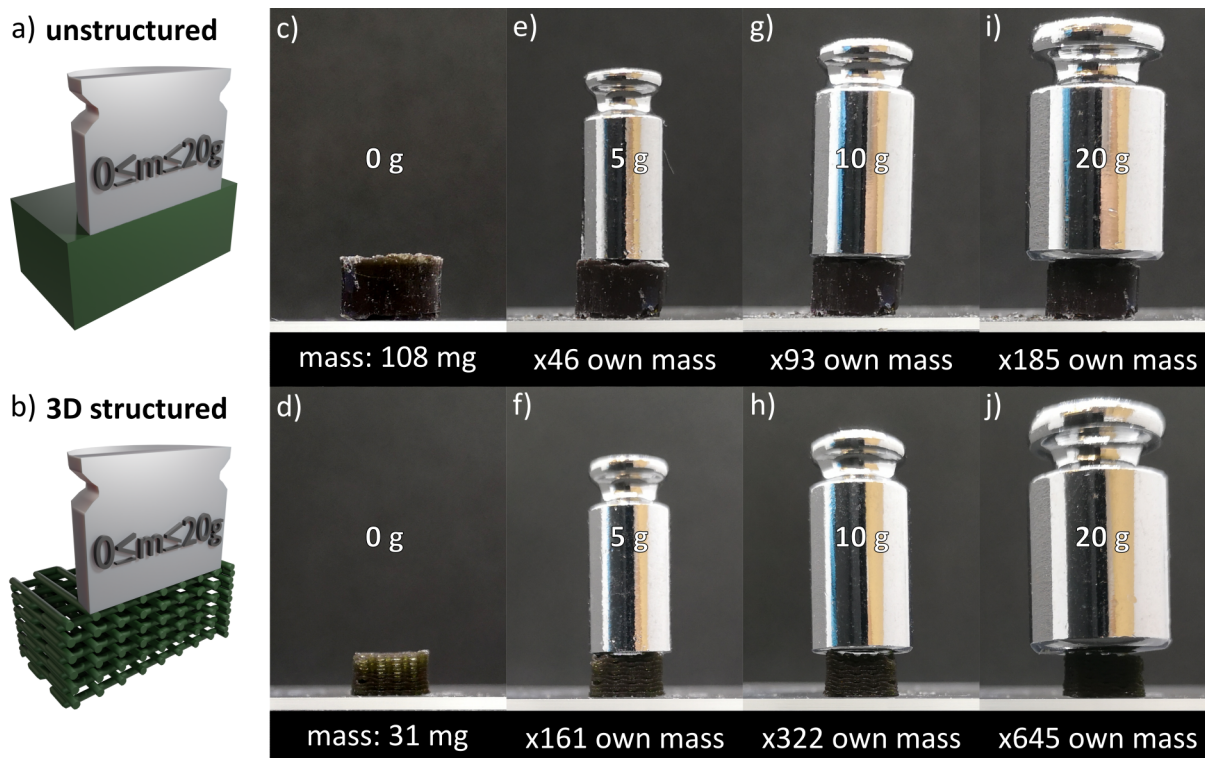


Figure 5.12: Mechanical compression test of an unstructured and 3D structured AuNR/TiO₂ aerogel. a) and b) shows a schematic of the experiment. c-i) and d-j) show unstructured and 3D structured aerogels loaded with 0 g, 5 g, 10 g and 20 g, respectively. The loadings relative to the aerogel's weight is given in each subfigure. For example, a loading of 20 g corresponds to 185-times and 645-times of the own weight for the unstructured and 3D structured aerogel, respectively.

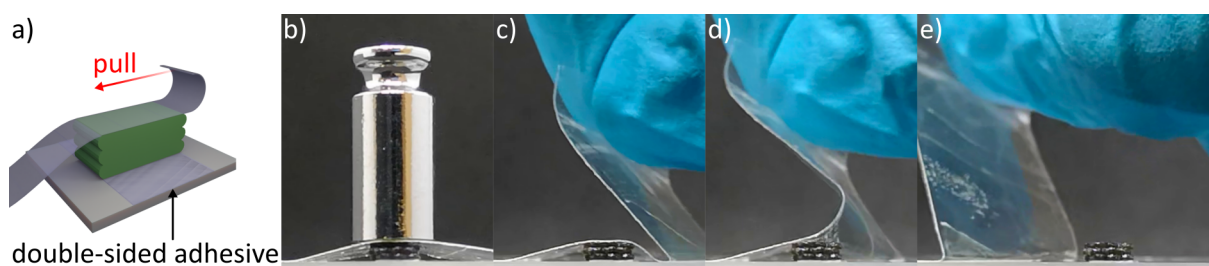


Figure 5.13: Exfoliation test of an unstructured AuNR/TiO₂ aerogel. Schematic and representative snapshots of the experiment are shown in a) and b-e), respectively. The bottom side of the 3D printed sample was fixed on a glass slide with double-sided adhesive tape. Another tape was detached from the top side of the aerogel and no exfoliation of the printed layers was observed.

Aerogel Characterization

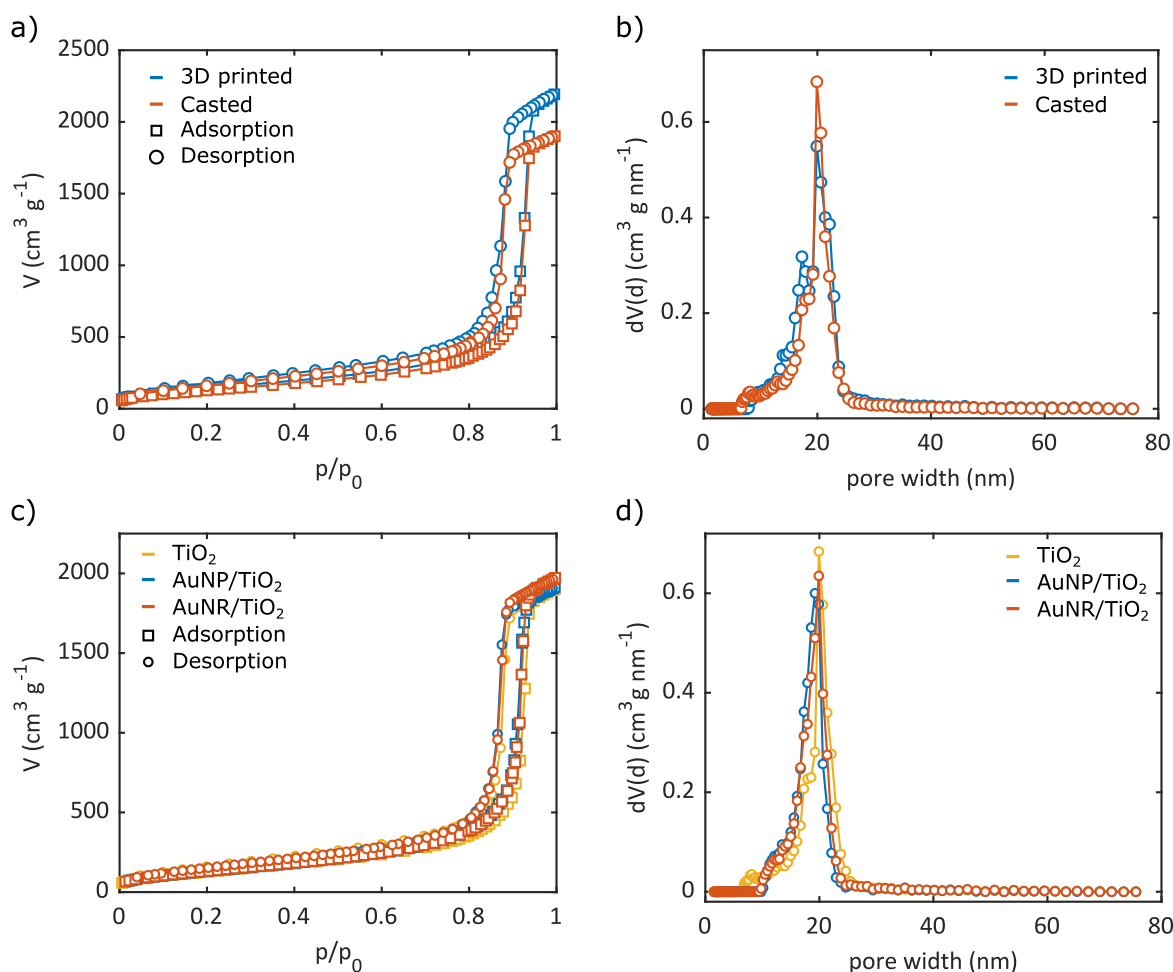


Figure 5.14: Structural characterization of 3D printed and conventionally casted aerogel samples. a) Nitrogen gas sorption isotherm and b) corresponding pore size distribution of a 3D printed and casted TiO₂ samples. c) Nitrogen gas sorption isotherm and d) corresponding pore size distribution of casted TiO₂, AuNP/TiO₂, and AuNR/TiO₂ aerogels. All samples show a type IVa isotherm with an H1-hysteresis loop attributed to an interconnected mesoporous material.^[62] Mean pore size and specific surface area are listed in Table 5.4, respectively.

Table 5.4: Specific surface area and mean pore size of TiO₂, AuNP/TiO₂, AuNR/TiO₂ aerogels. Values were obtained by multi-point BET and DFT analysis, respectively. The corresponding isotherms are displayed in Figure 5.14.

sample	specific surface area (m ² g ⁻¹)	pore size (nm)
TiO ₂ (3D printed)	539	19.9
TiO ₂ (casted)	489	19.9
AuNP/TiO ₂ (casted)	505	19.2
AuNR/TiO ₂ (casted)	508	19.9

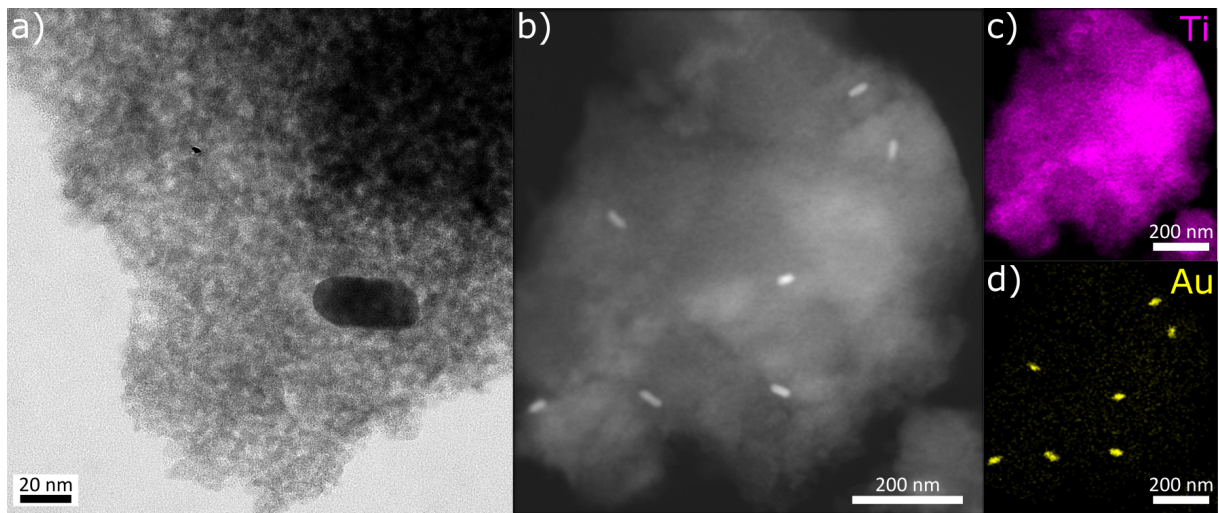


Figure 5.15: a) TEM image of a single AuNR embedded in a mesoporous TiO₂ aerogel matrix. b) HAADF-STEM image of AuNR/TiO₂ aerogel and corresponding elemental distribution map of c) Ti and d) Au obtained by energy-dispersive X-ray spectroscopy.

Photothermal Heating of Aerogels

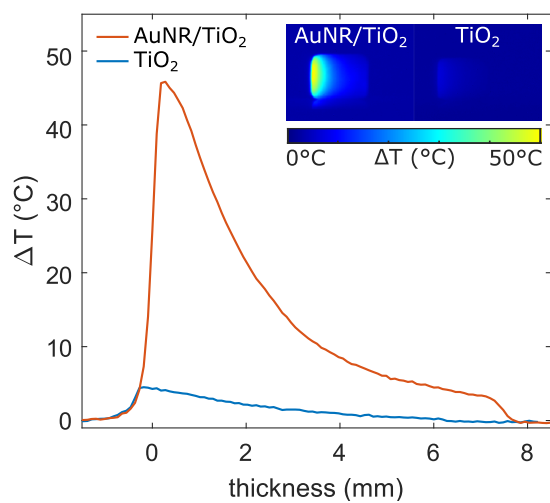


Figure 5.16: Photothermal heating ability of TiO₂ and AuNR/TiO₂ aerogels 3D printed in a bulk geometry. Inset shows respective IR camera snapshots of both samples upon illumination with a 300 W Xe light source from the left side. For neat TiO₂ only marginal heating can be observed in contrast to the AuNR loaded sample.

TiO₂ Nanoparticles Characterization

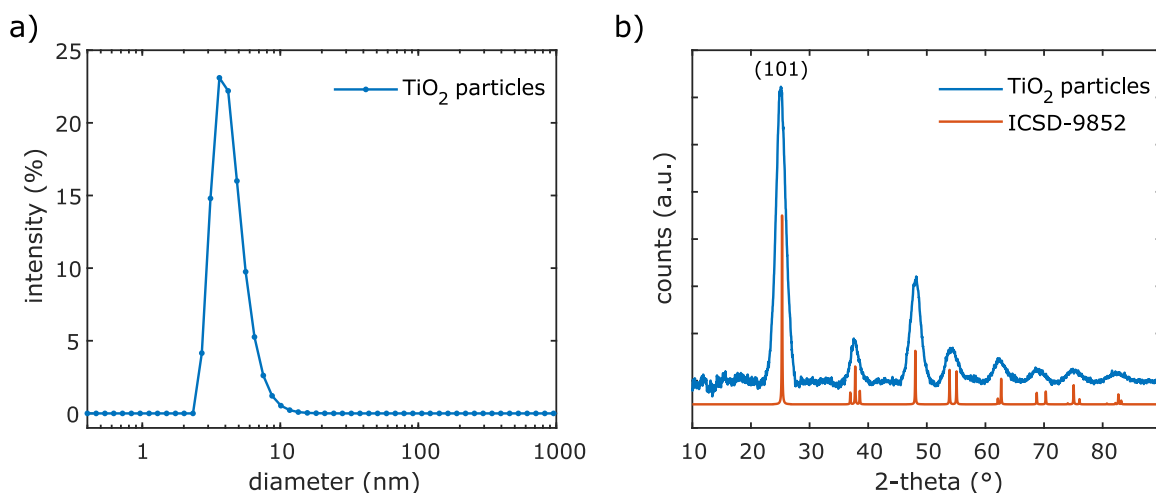


Figure 5.17: a) DLS and b) XRD data of TiO₂ nanoparticles that are used as the main building block for ink formulation. The number-weighted size distribution of the DLS data and Scherrer analysis of the (101) reflex suggest single-crystalline anatase particles of about 4 nm.

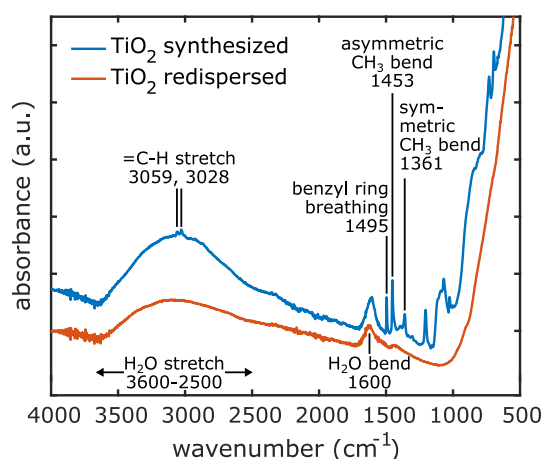


Figure 5.18: Attenuated total reflection infrared spectra of dried TiO₂ particles after synthesis and redispersion in water/ACN, respectively. For as-synthesized particles, benzyl groups can be identified from peaks at 3059 and 3028 cm⁻¹ (two forms of =C-H stretching), 1495 cm⁻¹ (benzyl ring breathing), and ethoxide groups can be recognized from peaks 1453 cm⁻¹ (asymmetric CH₃ bending) and 1361 cm⁻¹ (symmetric CH₃ bending). In both spectra, water is easily recognizable by the broad OH stretching band from 2500 to 3600 cm⁻¹ and OH bending at 1600 cm⁻¹. After redispersion in water/ACN and drying only the water bands remain.

Secondary Building Block Characterization

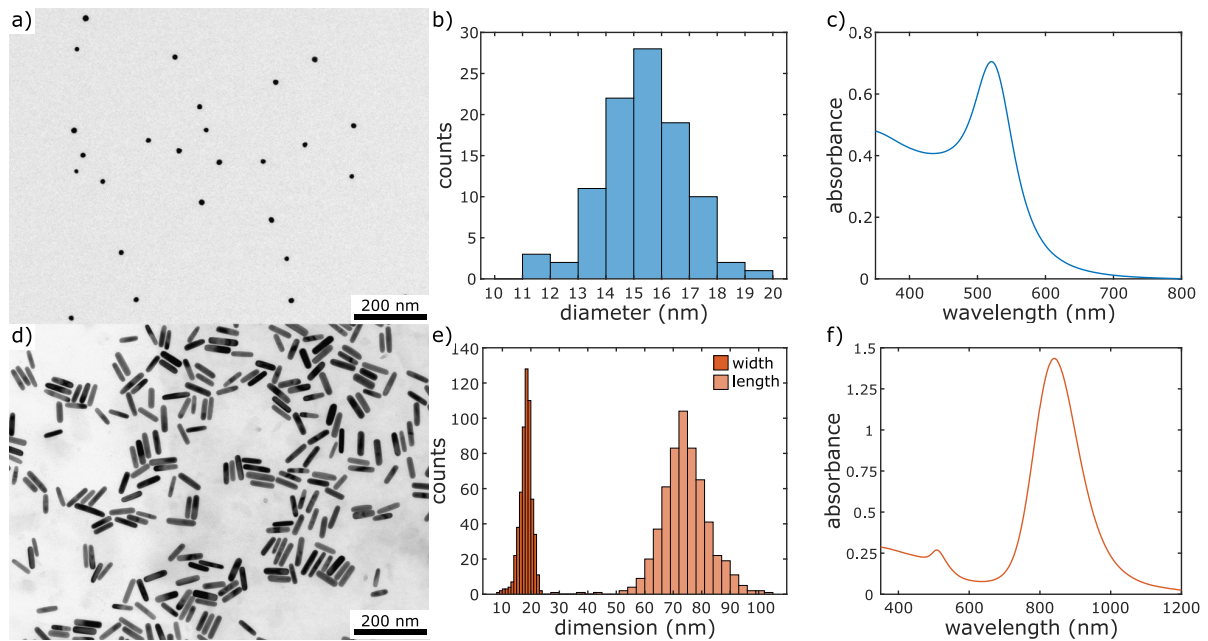


Figure 5.19: Structural and optical characterization of AuNPs and AuNRs that are used as secondary building blocks in TiO_2 -composite inks. Figures a-c) and d-f) show a representative TEM image, size histogram and UV-vis absorbance spectra of AuNPs and AuNRs, respectively.

5.7 Acknowledgment

This work was supported by the Cluster of Excellence 'CUI: Advanced Imaging of Matter' of the Deutsche Forschungsgemeinschaft (DFG) - EXC 2056 - project ID 390715994, and by GRK 2536 NANOHYBRID of the DFG. The authors thank Dr. Dirk Eifler and Nuray Eroglu for elemental analysis, Stefan Werner and Andrea Köppen for TEM imaging and Charline Becker for DLS measurements. Matthias Rebber thanks Ferdinand Otto and Merlina Thiessen for drop-shape analyzer and rheometer training, respectively. Moreover, the authors thank Prof. Volker Abetz, Prof. Gerhard Grübel, Prof. Wolfgang Parak and Prof. Christian Schroer for providing lab access.

5.8 Appendix

Corrigendum (Figure 7)

In the version of this article originally published, the temperature scale on 58 Figure 5.7b was incorrect, the maximal changes of the temperature on 58 Figure 5.7b should have read '72 °C'. On the same page Figure Figure 5.7c, the orientation of the sample was incorrectly plotted along the stacking direction of the sample, although the sample was illuminated perpendicular to the stacking direction. We updated the illustration; the conclusion remains the same, the deepest light penetration is expected for the 'shifted' geometry.

In Figure 5.7d we showed the temperature distribution as a function of sample thickness for a block, aligned, and shifted AuNR/TiO₂ geometry. We learned that the shifted geometry was slightly misaligned in respect to the illumination direction, which allowed light to hit the sample from the side. For the perfectly aligned samples, we still observe a more homogeneous heating for the shifted geometry than for aligned or block, but the temperature decays differently with about $3/4 \sigma_{\text{block}}$ and $1/2 \sigma_{\text{block}}$ instead of $1/2 \sigma_{\text{block}}$ and $1/4 \sigma_{\text{block}}$ for the aligned and shifted geometry, respectively. The overall conclusion that 3D microstructuring enables a macroscopic spatial tunable light absorption and temperature distribution is unchanged. Figure 5.20 shows a corrected version of Figure 5.7. These changes do not affect the results of the Article.

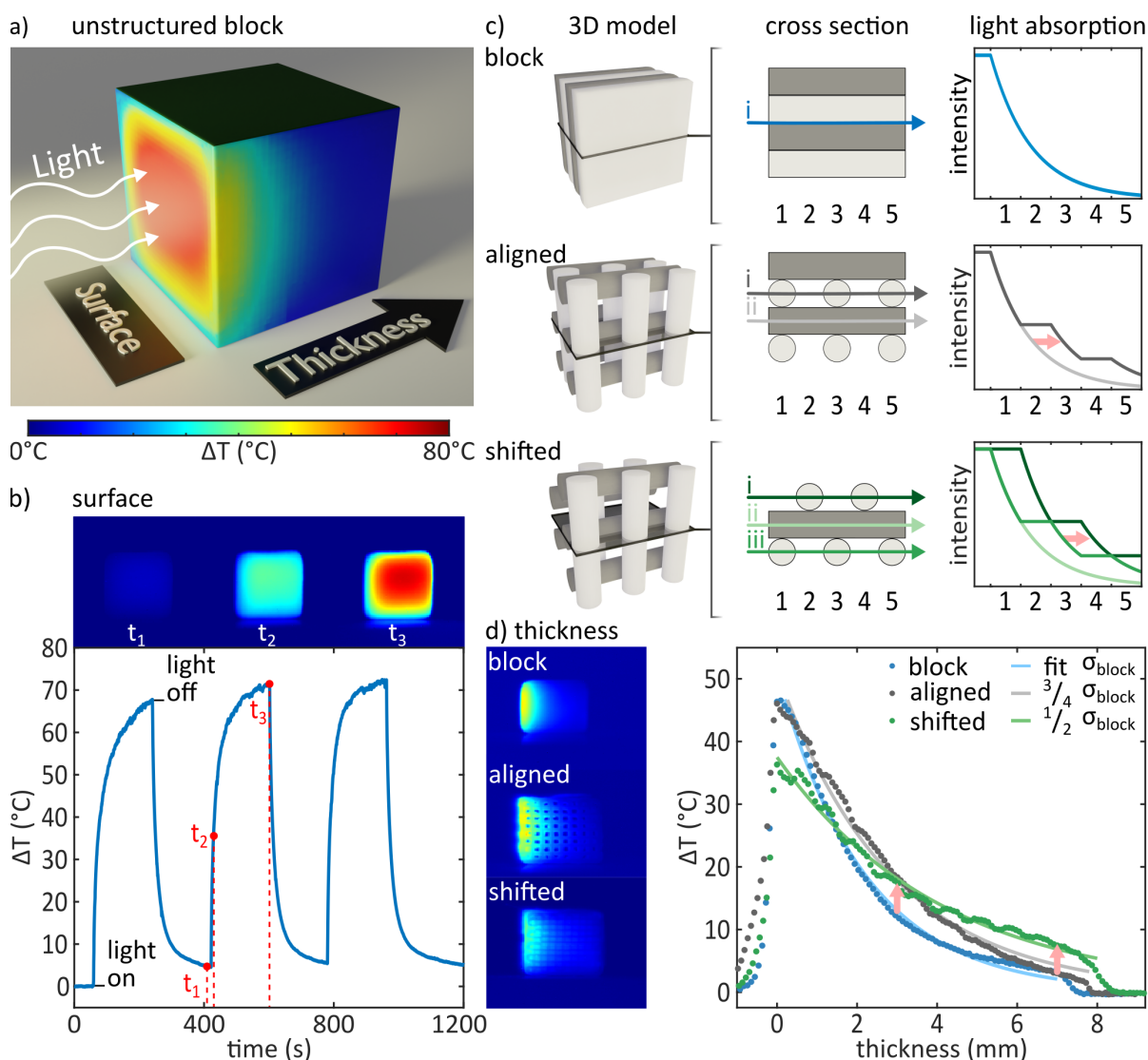


Figure 5.20: Effect of microstructuring on temperature and light distribution in 3D printed AuNR/TiO₂ aerogels. a) Schematic depiction of a typical photothermal measurement. Samples are illuminated from one side while an IR camera records the temperature either at the front or at one of the side surfaces. Exemplary temperature data for the bulk geometry are shown as an overlay on the cubic unstructured sample. b) Temperature time trace of the bulk surface temperature under repeated illumination. Insets show IR camera images at t_1 , t_2 , t_3 as indicated in the time trace plot. c) Schematic representation of light penetration into the three types of microstructure (unstructured block, aligned and shifted). From left to right the 3D model, the cross-section and the expected light absorption of each geometry are shown. For clarity, neighboring layers of the geometry are colored. d) Measured thickness dependency of the temperature distribution for the three types of microstructuring. Bulk temperature distribution is fitted with exponential function to extract bulk extinction coefficient σ_{block} . Temperature distribution of aligned and shifted geometries follow an exponential trend but with $1/2$ or $1/4$ of the bulk decay constant σ_{block} , respectively.

Addendum (Table S12)

In the Supporting Information on page 72 we estimated a fluid shell for about 76 % of the ink's cross-section based on the shear stress profile for the given nozzle geometry. Further experiments revealed that the required pressure ΔP depends on the age of the ink and the type of piston, which might be explained by time-dependent rheologic properties and a different break-loose and glide force during extrusion, respectively. Therefore, the fluid shell also varies for aged and fresh samples respectively. Table 5.5 shows the updated version of the initially provided Table 5.3.

Table 5.5: Fluid-shell estimation for two nozzles of diameter d and length L . The pressure drop ΔP corresponds to the required pressure for a steady extrusion of filaments via a pneumatic print head (Ultimus V, Nordson) at a deposition speed of about 4 mm s^{-1} . r_{gel} is calculated following equation 5.6. The gel and fluid fraction define the areal contribution of the respective flow type to the total cross-sectional area of the nozzle.

d (μm)	$r = d/2$ (μm)	L (mm)	ΔP (bar)	r_{gel} (μm)	gel (%)	fluid (%)
410	205	12.7	0.65-1.1	81-50	39-24	60-76
250	125	12.7	0.95-1.8	55-30	44-24	56-76

Additional Data Not Included in Publication

In chapter 5.6 we discussed that gravitational and capillary forces cause a deformation of the soft gel when the yield stress of the material is exceeded. Moreover, we observed the deformation of a pending filament with a diameter of $1540 \mu\text{m}$ although the yield stress of the material was higher than the estimated capillary pressure. We addressed this discrepancy to the observation that the tip of the filament was formed by a bended section and did not fully represent a simplified, straight fiber with a spherical end cap which was used to calculate the capillary pressure (Figure 5.10b). In a follow-up experiment we tried to create a better representation of a straight filament section. However, from these observation it seems that the end cap of a pending $1540 \mu\text{m}$ filament is better described by a rectangle with rounded corners where the edges have a higher curvature than the nozzle radius (Figure 5.21a-b). From the optical micrograph we approximate the radius of the corners as 0.2 mm which results in an capillary pressure of about 200 Pa according to equation 5.4 and exceeds the yield stress of 104 Pa . We assume that the rounded corners caused the deformation of the rectangularly shaped gel segment within 24 hours of extrusion (Figure 5.21c) in order to minimize the overall surface energy. This observation is still consistent with the hypothesis that capillary pressure is the main driving force of deformation. Regardless of which mechanism ultimately leads to a deformation, it should be noted that the ammonia assisted condensation process, which is the key component of the presented 3D printing method, prevents such drastic distortions by solidifying the gel before any shape changes can take place (Figure 5.21d-e).

Besides, we noticed that the visibility of the pending $250 \mu\text{m}$ filament in the heptane bath charged with Triton X-100 (Figure 5.10l-m) is worse in comparison to the other micrographs. Therefore, we present another dataset in Figure 5.22 with improved visibility. As for the previous

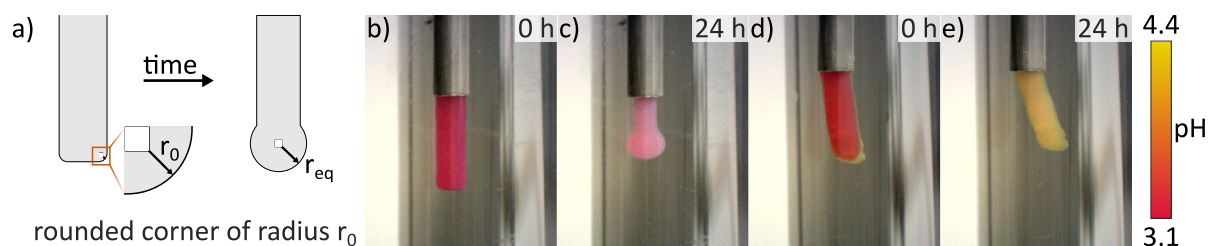


Figure 5.21: Deformation study of a straight, pending TiO_2 filament extruded through a nozzle with an inner diameter of $1540 \mu\text{m}$. a) The shape of the extruded filament can be approximated by a rectangle featuring rounded corners with a radius r_0 . The rounded corners locally cause a higher capillary pressure than expected for a filament with a spherical end cap and drives the deformation of the material. Optical micrographs of a pending TiO_2 filament 0 hours and 24 hours after extrusion from a nozzle with inner diameter of $1540 \mu\text{m}$ into b-c) a heptane bath d-e) an ammonia charged heptane bath, respectively. The filament is loaded with a pH indicator.

dataset, no droplet formed at the tip of the fiber which indicates that the surfactant reduces the interfacial tension. Moreover, we also observed the formation of an intermittent fibrous coating on the surface of the gel filament that started to form after about 1 hour, reached a maximum thickness after approximately 8 hours (Figure 5.22b), and subsequently started to disappear (Figure 5.22c-d). After 24 hours the fibrous coating only remained close to the exit of the nozzle (Figure 5.22e) and vanished after 89 hours (Figure 5.22f). The formation and dissolution of the fibrous coating remains unclear but seems to be related to the presence of Triton X-100 since no coating was observed for surfactant-free liquid baths.

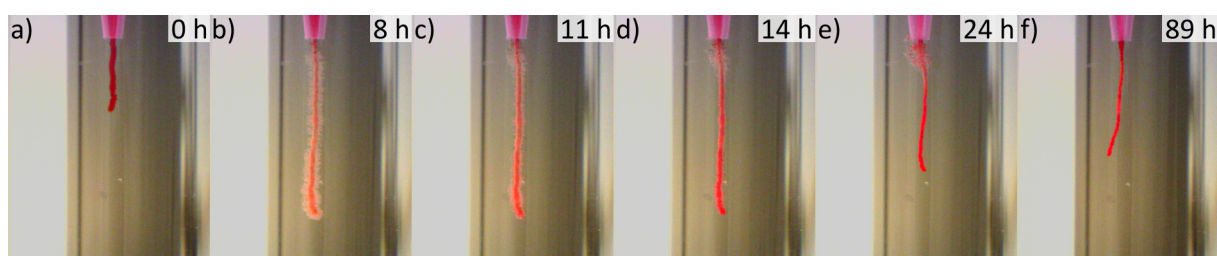


Figure 5.22: Optical micrographs of a pending TiO_2 filament a) 0 hours, b) 8 hours, c) 11 hours, d) 14 hours, e) 24 hours, and 89 hours after extrusion through a nozzle with an inner diameter of $250 \mu\text{m}$ into a heptane bath charged with Triton X-100.

In chapter 5.3 we derived a porosity of 95 % based on an apparent density of 0.20 g cm^{-3} for the TiO_2 aerogel and the density of 3.9 g cm^{-3} for bulk TiO_2 . In chapter 6.6 we followed the same protocol for the preparation of the aerogel, but calculated an apparent density of 0.25 g cm^{-3} which corresponds to a porosity of 94 %. We believe that the difference in porosity and density is caused by two effects. First, the processing route requires multiple steps from nanoparticle synthesis, ink formulation, 3D printing, solvent exchange and supercritical drying which are prone to human influence. Especially the extent by which the wet gel is cured in the ammonia charged liquid bath defines the shrinkage of the gel in the subsequent solvent exchange and supercritical drying. Since the amount of ammonia is controlled by manually exchanging the liquid bath during 3D printing, as described in chapter 5.5, the curing conditions potentially varied for both samples and resulted in aerogels of slightly different density. To avoid such an

effect in the future, a system which monitors and automatically adjusts the concentration of ammonia in the printing container is needed. Second, for the calculation of the apparent density the volume of the aerogel needed to be approximated. To this end, we measured the dimensions of the aerogel with a caliper in chapter 5.3. During the data collection for chapter 6.6 we learned that the measurements with a caliper depend on the user. Moreover, we noticed that the caliper is prone to overestimate the dimension of the aerogel because the sample cannot be tightly clamped with the measuring tips due to the brittle characteristic of the material. To obtain a better approximation of the aerogel dimension, we decided to define the outer dimension of the aerogel in chapter 6.6 from optical micrographs. If we assume that the caliper overestimated the dimension of the millimeter-sized aerogel in chapter 5.3 in each direction by $100\ \mu\text{m}$, which is less than the diameter of an individual filament in the printed object, we obtain a density and porosity of $0.23\ \text{g cm}^{-3}$ and 94 %, respectively. Independent of the measurement procedure, the porosity is still in line with other metal oxide aerogels, which typically feature values of 80 to 99.8 %, ^[12] and the main conclusion concerning the 3D printing method are not affected. To minimize the error for the determination of the apparent density, larger aerogel samples might be investigated in the future.

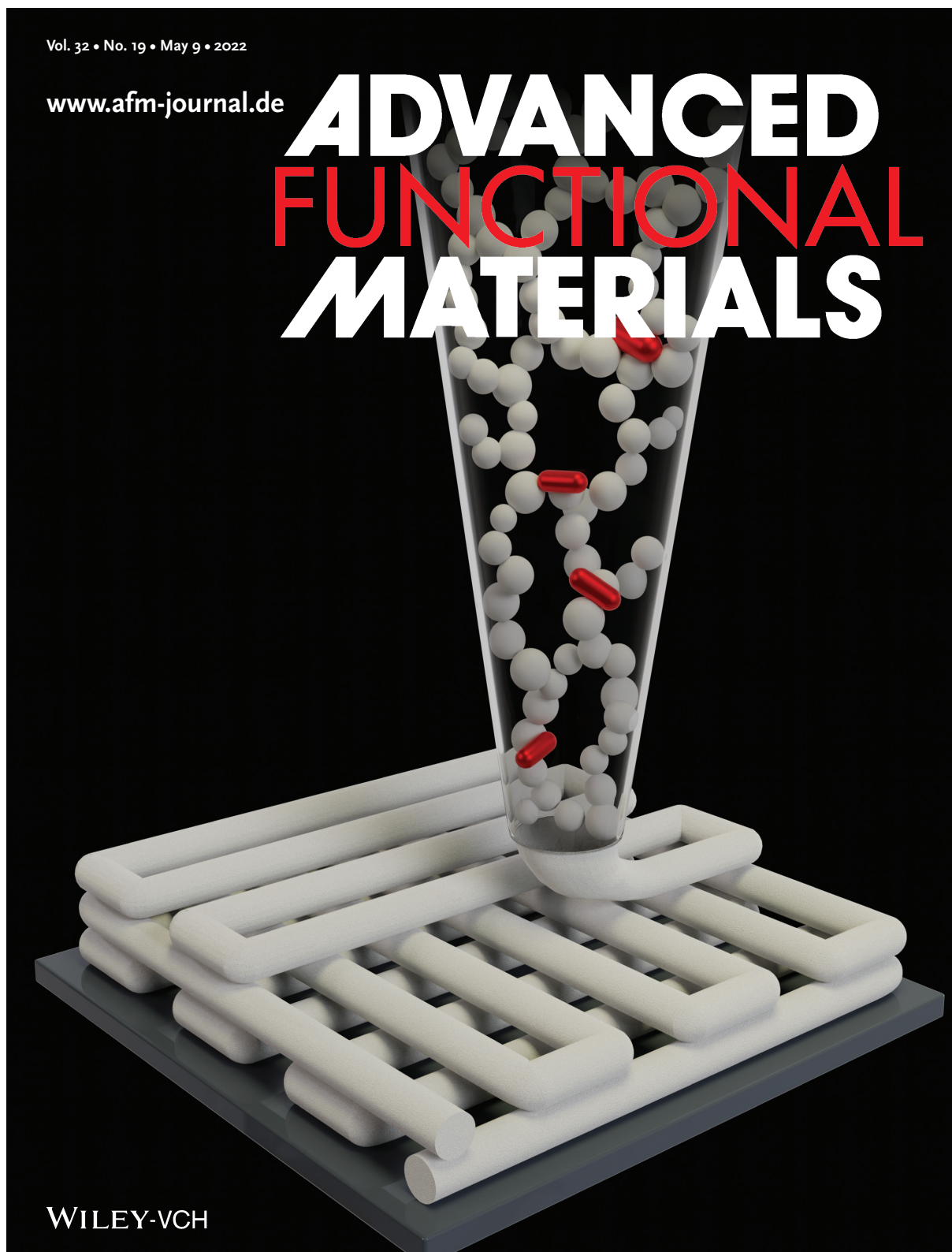


Figure 5.23: Inside front cover of *Adv. Funct. Mater.* **2022**, 32, 19. The cover shows TiO_2 nanoparticle-based gels as additive-free inks for 3D printing of structured aerogels. The TiO_2 gels are loaded with plasmonic AuNRs to facilitate photothermal heating of the aerogel. In general, diverse colloidal nanomaterials can be processed into inks and 3D printed, thus giving access to multifunctional aerogels with full control of the nano-, micro-, and macroscopic length scales.

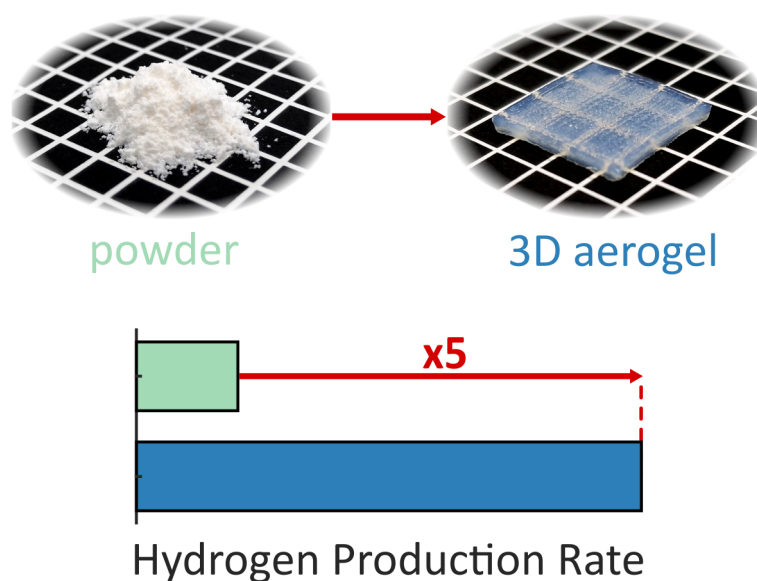
Bibliography

- [1] Z. Wu, S. Yang and W. Wu, *Nanoscale*, 2016, **8**, 1237–1259.
- [2] A. R. Tao, S. Habas and P. Yang, *Small*, 2008, **4**, 310–325.
- [3] J. Chang and E. R. Waclawik, *RSC Adv.*, 2014, **4**, 23505–23527.
- [4] M. A. Boles, M. Engel and D. V. Talapin, *Chem. Rev.*, 2016, **116**, 11220–11289.
- [5] M. Niederberger, *Adv. Funct. Mater.*, 2017, **27**, 1703647.
- [6] C. Ziegler, A. Wolf, W. Liu, A.-K. Herrmann, N. Gaponik and A. Eychmüller, *Angew. Chem. Int. Ed.*, 2017, **56**, 13200–13221.
- [7] F. J. Heiligtag, W. Cheng, V. R. de Mendonça, M. J. Süess, K. Hametner, D. Günther, C. Ribeiro and M. Niederberger, *Chem. Mater.*, 2014, **26**, 5576–5584.
- [8] P. Rusch, D. Zámbo and N. C. Bigall, *Acc. Chem. Res.*, 2020, **53**, 2414–2424.
- [9] F. Matter, A. L. Luna and M. Niederberger, *Nano Today*, 2020, **30**, 100827.
- [10] M. Schreck, N. Kleger, F. Matter, J. Kwon, E. Tervoort, K. Masania, A. R. Studart and M. Niederberger, *Small*, 2021, **17**, 2104089.
- [11] G. V. Franks, C. Tallon, A. R. Studart, M. L. Sesso and S. Leo, *J. Am. Ceram. Soc.*, 2017, **100**, 458–490.
- [12] N. Hüsing and U. Schubert, *Angew. Chem. Int. Ed.*, 1998, **37**, 22–45.
- [13] F. Rechberger and M. Niederberger, *Nanoscale Horiz.*, 2017, **2**, 6–30.
- [14] A. Krell, P. Blank, H. Ma, T. Hutzler and M. Nebelung, *J. Am. Ceram. Soc.*, 2003, **86**, 546–53.
- [15] J. Cesarano, *MRS Proc.*, 1998, **542**, 133.
- [16] E. Duoss, M. Twardowski and J. Lewis, *Adv. Mater.*, 2007, **19**, 3485–3489.
- [17] Q. Li and J. Lewis, *Adv. Mater.*, 2003, **15**, 1639–1643.
- [18] J. Smay, G. Gratson, R. Shepherd, J. Cesarano III and J. Lewis, *Adv. Mater.*, 2002, **14**, 1279–1283.
- [19] M. F. Bertino, *J. Sol-Gel Sci. Technol.*, 2018, **86**, 239–254.
- [20] S. Zhao, G. Siqueira, S. Drdova, D. Norris, C. Ubert, A. Bonnin, S. Galmarini, M. Ganobjak, Z. Pan, S. Brunner, G. Nyström, J. Wang, M. M. Koebel and W. J. Malfait, *Nature*, 2020, **584**, 387–392.
- [21] L. Wang, J. Feng, Y. Luo, Z. Zhou, Y. Jiang, X. Luo, L. Xu, L. Li and J. Feng, *ACS Appl. Mater. Interfaces*, 2021, **13**, 40964–40975.
- [22] H. Maleki, S. Montes, N. Hayati-Roodbari, F. Putz and N. Huesing, *ACS Appl. Mater. Interfaces*, 2018, **10**, 22718–22730.

- [23] T. Kotsokechagia, F. Cellési, A. Thomas, M. Niederberger and N. Tirelli, *Langmuir*, 2008, **24**, 6988–6997.
- [24] F. J. Heiligtag, M. D. Rossell, M. J. Süess and M. Niederberger, *J. Mater. Chem.*, 2011, **21**, 16893–16899.
- [25] A. L. Luna, F. Matter, M. Schreck, J. Wohlwend, E. Tervoort, C. Colbeau-Justin and M. Niederberger, *Appl. Catal., B*, 2020, **267**, 118660.
- [26] X. Tang, H. Zhou, Z. Cai, D. Cheng, P. He, P. Xie, D. Zhang and T. Fan, *ACS Nano*, 2018, **12**, 3502–3511.
- [27] S. S. Nadkarni and J. E. Smay, *J. Am. Ceram. Soc.*, 2006, **89**, 96–103.
- [28] S. Tagliaferri, A. Panagiotopoulos and C. Mattevi, *Materials Advances*, 2021, **2**, 540–563.
- [29] J. Lewis, *Adv. Funct. Mater.*, 2006, **16**, 2193–2204.
- [30] J. E. Smay, J. Cesarano and J. A. Lewis, *Langmuir*, 2002, **18**, 5429–5437.
- [31] N. Willenbacher and K. Georgieva, in *Rheology of Disperse Systems*, John Wiley & Sons, Ltd, 2013, book section 1, pp. 7–49.
- [32] J. C. Conrad, S. R. Ferreira, J. Yoshikawa, R. F. Shepherd, B. Y. Ahn and J. A. Lewis, *Current Opinion in Colloid & Interface Science*, 2011, **16**, 71–79.
- [33] A. Corker, H. C. H. Ng, R. J. Poole and E. García-Tuñón, *Soft Matter*, 2019, **15**, 1444–1456.
- [34] C. Zhu, T. Y.-J. Han, E. B. Duoss, A. M. Golobic, J. D. Kuntz, C. M. Spadaccini and M. A. Worsley, *Nat. Commun.*, 2015, **6**, 6962.
- [35] U. Schubert, in *Chemistry and Fundamentals of the Sol–Gel Process*, John Wiley & Sons, Ltd, 2015, book section 1, pp. 1–28.
- [36] J. Cihlář, *Colloids Surf., A*, 1993, **70**, 239–251.
- [37] K. D. Keefer, *MRS Online Proc. Libr.*, 2011, **32**, 15.
- [38] A. K. Grosskopf, R. L. Truby, H. Kim, A. Perazzo, J. A. Lewis and H. A. Stone, *ACS Appl. Mater. Interfaces*, 2018, **10**, 23353–23361.
- [39] Y. Jin, A. Compaan, W. Chai and Y. Huang, *ACS Appl. Mater. Interfaces*, 2017, **9**, 20057–20066.
- [40] T. J. Hinton, A. Hudson, K. Pusch, A. Lee and A. W. Feinberg, *ACS Biomater. Sci. Eng.*, 2016, **2**, 1781–1786.
- [41] M. K. Hausmann, P. A. Rühs, G. Siqueira, J. Läger, R. Libanori, T. Zimmermann and A. R. Studart, *ACS Nano*, 2018, **12**, 6926–6937.
- [42] S. Hæreid, J. Anderson, M. A. Einarsrud, D. W. Hua and D. M. Smith, *J. Non-Cryst. Solids*, 1995, **185**, 221–226.
- [43] B. Klemmed, L. V. Besteiro, A. Benad, M. Georgi, Z. Wang, A. Govorov and A. Eychmüller, *Angew. Chem. Int. Ed.*, 2020, **59**, 1696–1702.
- [44] O. Neumann, A. S. Urban, J. Day, S. Lal, P. Nordlander and N. J. Halas, *ACS Nano*, 2013, **7**, 42–49.
- [45] M. Gao, C. K. Peh, H. T. Phan, L. Zhu and G. W. Ho, *Adv. Energy Mater.*, 2018, **8**, 1800711.
- [46] Z. Wang, Y. Liu, P. Tao, Q. Shen, N. Yi, F. Zhang, Q. Liu, C. Song, D. Zhang, W. Shang

- and T. Deng, *Small*, 2014, **10**, 3234–3239.
- [47] M. Chen, Y. Wu, W. Song, Y. Mo, X. Lin, Q. He and B. Guo, *Nanoscale*, 2018, **10**, 6186–6193.
- [48] M. Zhu, Y. Li, F. Chen, X. Zhu, J. Dai, Y. Li, Z. Yang, X. Yan, J. Song, Y. Wang, E. Hitz, W. Luo, M. Lu, B. Yang and L. Hu, *Adv. Energy Mater.*, 2018, **8**, 1701028.
- [49] Y. Liu, S. Yu, R. Feng, A. Bernard, Y. Liu, Y. Zhang, H. Duan, W. Shang, P. Tao, C. Song and T. Deng, *Adv. Mater.*, 2015, **27**, 2768–2774.
- [50] T. Kong, C. Zhang, J. Lu, B. Kang, Z. Fu, J. Li, L. Yan, Z. Zhang, H. Zheng and H. Xu, *Nanoscale*, 2021, **13**, 4585–4591.
- [51] M. Gao, P. K. N. Connor and G. W. Ho, *Energy Environ. Sci.*, 2016, **9**, 3151–3160.
- [52] J. Kimling, M. Maier, B. Okenve, V. Kotaidis, H. Ballot and A. Plech, *J. Phys. Chem. B*, 2006, **110**, 15700–15707.
- [53] X. Ye, C. Zheng, J. Chen, Y. Gao and C. B. Murray, *Nano Lett.*, 2013, **13**, 765–771.
- [54] J. M. Feldkamp, C. G. Schroer, J. Patommel, B. Lengeler, T. F. Günzler, M. Schweitzer, C. Stenzel, M. Dieckmann and W. H. Schroeder, *Rev. Sci. Instrum.*, 2007, **78**, 073702.
- [55] W. van Aarle, W. J. Palenstijn, J. De Beenhouwer, T. Altantzis, S. Bals, K. J. Batenburg and J. Sijbers, *Ultramicroscopy*, 2015, **157**, 35–47.
- [56] W. van Aarle, W. J. Palenstijn, J. Cant, E. Janssens, F. Bleichrodt, A. Dabrovolski, J. De Beenhouwer, K. Joost Batenburg and J. Sijbers, *Opt. Express*, 2016, **24**, 25129–25147.
- [57] D. Kokkinis, M. Schaffner and A. R. Studart, *Nat. Commun.*, 2015, **6**, 8643.
- [58] A. M'Barki, L. Bocquet and A. Stevenson, *Sci. Rep.*, 2017, **7**, 6017.
- [59] M. Caggioni, A. V. Bayles, J. Lenis, E. M. Furst and P. T. Spicer, *Soft Matter*, 2014, **10**, 7647–7652.
- [60] M. Caggioni, J. Lenis, A. V. Bayles, E. M. Furst and P. T. Spicer, *Langmuir*, 2015, **31**, 8558–8565.
- [61] P. Nikitas and A. Pappa-Louisi, *J. Phys. Chem.*, 1990, **94**, 361–370.
- [62] M. Thommes, K. Kaneko, A. V. Neimark, J. P. Olivier, F. Rodriguez-Reinoso, J. Rouquerol and K. S. Sing, *Pure Appl. Chem.*, 2015, **87**, 1051–1069.

6 Nature-inspired 3D structuring of TiO_2 and Au/TiO_2 aerogels enables scalable photocatalytic hydrogen production



The content of this chapter provides a proof of concept for the rational design of a hierarchical, nature-inspired 3D aerogel photocatalyst geometry that reaches a fivefold improvement in the hydrogen production rate relative to the commonly utilized nanoparticle powder. The manuscript is co-authored by Hendrik Sannemüller, Michael Jaruszewski, Daniela Pfannkuche, and Atsushi Urakawa with Dorota Koziej as corresponding author. Paper submitted.

6.1 Abstract

Efficient mass transfer and light harvesting are essential for high photocatalytic production rates. Here, we present a hierarchical 3D printed aerogel photoreactor that unites both aspects by taking inspiration from the light scattering in clouds during photochemical processes and from mass transfer in leaves during photosynthesis. We combine the design-freedom of additive manufacturing with computational fluid dynamics and Monte Carlo simulations to guide the fabrication of a self-supported aerogel geometry. Here, periodic 3D microstructuring enhances the intrinsically low gas permeability of a monolithic aerogel by five orders of magnitude, while maintaining the high light harvesting efficiency of the nanoporous material. We match the macroscopic thickness with the UV light penetration depth and show that the 3D aerogel of 1.1 mm thickness improves photocatalytic hydrogen production rates relative to the powder counterpart by a factor of five from 1.3 to 6.6 $\mu\text{mol g}^{-1} \text{h}^{-1}$ for TiO_2 and from 30.0 to 142 $\mu\text{mol g}^{-1} \text{h}^{-1}$ for Au/TiO_2 , respectively. Thus, the relative photocatalytic improvement is not dependent on the materials composition, but foremost on the design of the mass- and light transport in the 3D structure. Ultimately, 3D printing guided by simulations enables the fabrication of upscaled photoreactors and provides a general tool to boost the photocatalytic performance of nanomaterials.

6.2 Introduction

Catalytic nanomaterials – especially for the photocatalytic conversion of solar energy into chemical fuels via CO_2 reduction or H_2 evolution – are considered as essential building blocks in the creation of a sustainable energy system.^[1–3] While big progress on the material side was achieved by doping,^[4,5] exposing reactive crystal facets,^[6,7] loading cocatalysts,^[4,6,8] or tuning selectivity in organic-inorganic hybrids,^[9] technological implementation of photocatalytic nanomaterials is still pending.^[10] One reason is that for an efficient photocatalyst the nanoscopic material properties not only need to be optimized but also be well integrated into a macroscopic photoreactor where chemical and geometrical control at multiple length scales is of great importance.^[11–13] In this regard, nature provides a blueprint for the synergy of elaborated structures and functional components to accelerate the solar energy conversion during photochemical processes.^[14] Particularly light-harvesting via multiple-scattering and efficient mass transfer in hierarchical architectures are two main characteristics commonly found in nature.^[15–19] Although catalyst designs advanced by replicating natural photocatalysts,^[14,20–22] most efforts only focused on the functional imitation of a single characteristic by tuning geometrical aspects of the photoactive material either at the nano- and microscopic length scale in controlled aggregates,^[23–26] and biotemplated films,^[14] or at the macroscale by processing nanomaterials into monolithic aerogels.^[27] Especially nanoparticle-based aerogels have huge potential as photocatalyst in the gas-phase because they fully maintain the photocatalytic properties of the nanoscale building blocks in a macroscopic body composed of an interconnected nanoporous network and a translucent, light harvesting characteristic.^[28,29]

Even tough aerogels provide a high number of catalytic active sites based on their large specific surface area, bulk nanoporous materials generally suffer from a poor gas permeability.^[30–33] Thus, to unlock the full potential of an aerogel photocatalyst the integration in a light and

mass transport optimized 3D geometry with deterministic control of the nano-, micro-, and macroscopic length scales is essential.^[12] A promising approach is the use of 3D printing which successfully boosted mass transfer rates in heterogeneous catalysis and energy storage, but so far has limited application for the production of solar fuels due to the opaque appearance of most photoactive inks which prevents a simultaneous interaction of light, reactant, and catalyst on the macroscopic scale of a 3D printed object.^[11,34–36] We overcome this limitation by 3D printing translucent TiO₂ nanoparticle-based aerogels, which combine a nature-inspired hierarchical mass transfer and light trapping characteristic in a single photocatalyst. We utilize computational fluid dynamics and the Monte Carlo method to derive an ideal photocatalyst geometry by modeling gas and photon transport in macroscopic simple-cubic (sc) and face-center cubic (fcc) 3D lattice structures. Based on our previously reported 3D printing procedure,^[37] we fabricate an ideal 3D aerogel geometry that maintains the light harvesting capabilities of a monolithic aerogel while offering a five orders of magnitude lower resistance to gas flow. We validate our approach by measuring the photocatalytic hydrogen evolution from a water/methanol mixture and show that 3D-structuring does not compromise the gas infiltration and photocatalytic performance, despite changing from a pressure-driven to a diffusion-driven mass transport regime. Moreover, by adjusting the thickness to the light penetration depth, we eliminate the poorly illuminated sections of the photocatalyst and demonstrate that 3D-structured TiO₂ and Au/TiO₂ aerogels outperform the powder counterpart by a factor of 5.2 and 4.7, respectively. Thus, our derived 3D aerogel geometry is not only an universal quantity to boost the photocatalytic performance independent of material composition, but more importantly achieves an effortless utilization of the nanoporous photocatalyst on a scalable 3D printing platform.

6.3 Results and Discussion

We create nature-inspired aerogels by 3D printing gelled TiO₂ and Au/TiO₂ nanoparticles according to the procedure we reported elsewhere.^[37] Here, the 3D printing process replicates the microscopic mass transfer highways in hierarchically architected leaves during photosynthesis,^[19] whereas the gelled nanoparticles act as scattering centers and trap UV light similar to water droplets in clouds during atmospheric photochemical processes for enhanced absorption efficiencies,^[17] as illustrated in Figures 6.1a-b. Figures 6.1c-e show an optical photograph and scanning electron microscopy images of a well-defined 3D printed TiO₂ aerogel that spans seven orders of magnitude, from the nanometer to centimeter length scale. The 3D printed aerogel appears cloudy but translucent and features lateral dimensions of 1.5 cm and a thickness of 2 mm. The filaments have diameter of about 200 μm and each consists of a nanoporous, finely branched network of nanoparticles that formed during the ink gelation process. Although a cloudy appearance and a hierarchical structuring can readily be imitated with our 3D printing process, we need to go one step further and engineer the macro- and microscopic geometry towards highest photocatalytic activity. We utilize a microstructuring approach based on sc and fcc unit cells to find a sweet spot between sufficient mass transport and maximum light utilization in a macroscopic aerogel.

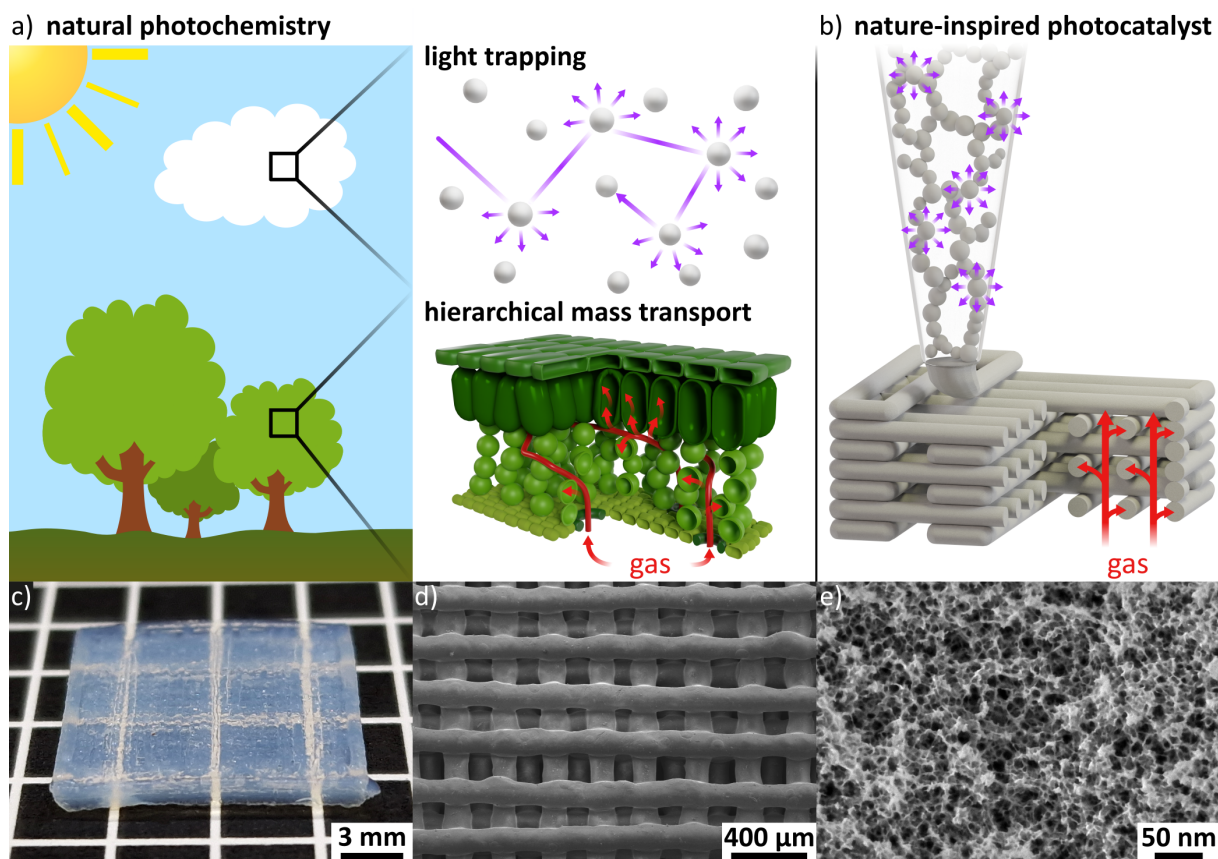


Figure 6.1: Nature-inspired photocatalyst for efficient light and mass transport. a) Schematic illustration of the natural photochemical design principles such as light trapping via scattering at cloud water droplets or facilitated mass transport via hierarchical architectures in leaves. b) Both natural design principles can be recreated in an artificial photocatalyst via 3D printing of gelled TiO_2 nanoinks. c) Optical micrograph of the translucent, cloudy 3D-printed TiO_2 aerogel with lateral dimensions of 1.5 cm. d-e) Scanning electron microscopy images reveal that the macroscopic aerogel consists of an array of nanoporous filaments with diameters of about 200 μm .

Figures 6.2a-b show 3D renderings of a sc-structured and fcc-structured aerogel, respectively. For both geometries, each layer consists of an array of parallel filaments where the center-to-center spacing is twice the filament diameter and alternating layers are orientated 90° to each other. Depending on the type of structuring, consecutive layers of same orientation are either aligned to yield a sc-geometry or shifted by one filament diameter for a fcc-geometry. Upon illumination several light-matter interactions such as refraction, specular reflection, scattering and absorption can occur. Refraction and specular reflection are neglected due to the low refractive index of the aerogel, as calculated in the Supporting Information. Thus, the light transport is purely defined by scattering and absorption processes in the 3D aerogel. We extract the scattering and absorption coefficients of the TiO_2 aerogel from experimental UV-vis data by solving the inverse problem of the radiative transfer equation (RTE) as described in section 6.6.1 of the Supporting Information.^[38] We identify Rayleigh scattering (Figure 6.2c) and electron excitation from the valance to the conduction band (Figure 6.2d) as the main light redirection and absorption mechanism in the TiO_2 aerogel, respectively. We use the derived optical coefficients and the Monte Carlo method to calculate the number of absorbed photons for unstructured, sc-, and fcc-structured aerogels with thicknesses in the range of 0 to 3.5 mm, as shown in Figure 6.2e. We see that the unstructured and fcc-structured aerogel reach similar absorption values with increasing sample thickness, whereas the maximum absorption for the sc unit cell is about 26 % lower. We address the lower light utilization of the sc structure to the direct line of sight which is a result of the filament stacking sequence and allows light to pass the aerogel without being absorbed. For the fcc structure we prevent a direct line of sight by shifting consecutive layers of same orientation by one filament diameter which results in similar levels of light utilization as for the unstructured sample.

With the microstructure in place, the macroscopic light propagation is purely defined by the nanoscopic optical characteristic of the ink. To reveal the impact of the Rayleigh scattering process on the light distribution, we performed time-resolved Monte Carlo simulations for a Rayleigh scattering and non-scattering sample shown in Figures 6.2f-g and 6.2h-i, respectively. In absence of any scattering, the infinitely thin pencil beam, which is launched at the top of the fcc-structured aerogel, just passes through the sample without any redirection of the photon path (Figures 6.2h-i). In contrast, Rayleigh scattering drastically spreads the incoming light and enables a more uniform light distribution on a macroscopic scale (Figures 6.2f-g). Moreover, when comparing the photon flux distribution after 1 ns in Figures 6.2g-i, a longer residence time of the photons becomes apparent in presence of scattering. Thus, the light is trapped in the aerogel in a similar fashion as in clouds during natural photochemical processes which enhances the probability of absorption.

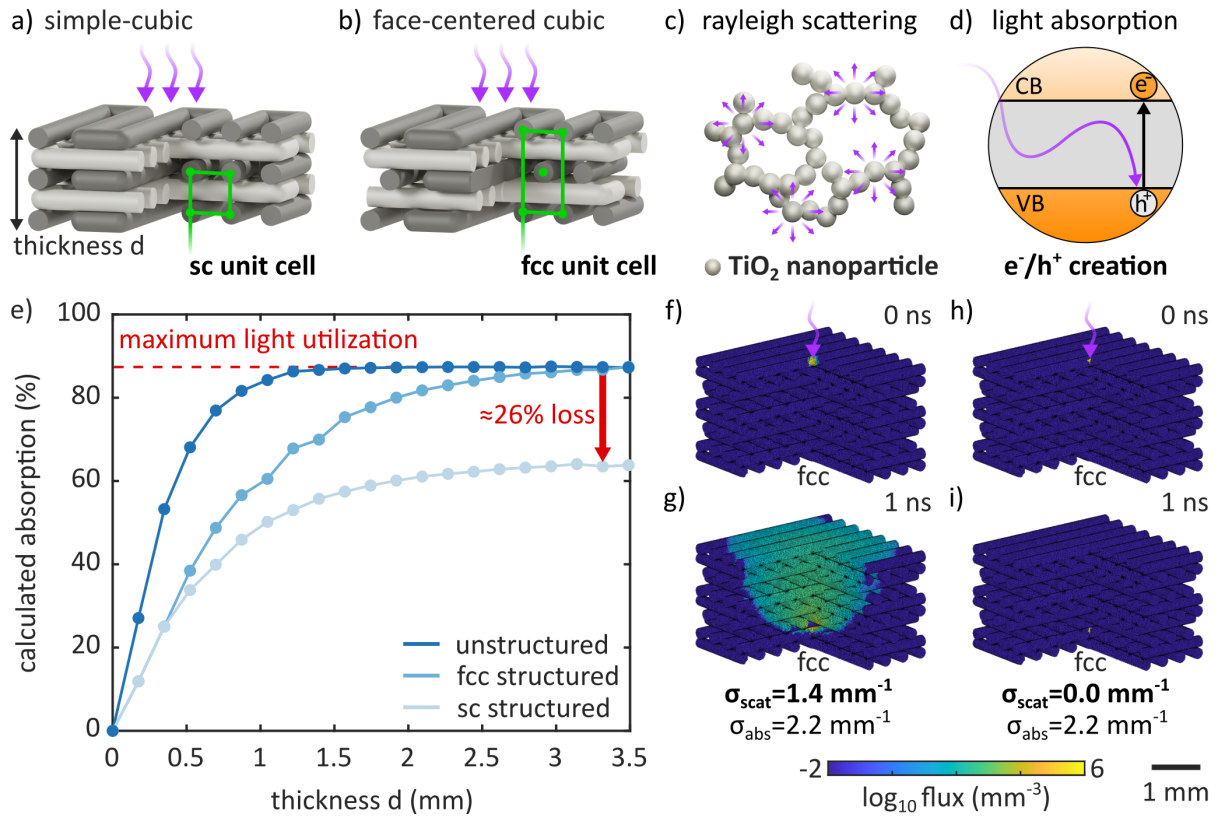


Figure 6.2: Light transport through a 3D printed TiO₂ aerogel is defined by light-matter interaction from the macro to the nanoscale. Schematic illustration of the macroscopic 3D printed aerogel where the microscopic filaments are arranged in a) a simple-cubic (sc) or b) a face-centered cubic (fcc) unit cell. Within the nanoporous TiO₂ network c) light scattering and d) light absorption processes take place. e) Calculated absorption for an unstructured, a fcc-structured, and a sc-structured TiO₂ aerogel microlattice with thicknesses in a range of 0 to 3.5 mm according to 3D mesh-based Monte Carlo simulations. Simulated photon flux in a fcc-structured aerogel 0 and 1 ns after launching a collimated, infinitely-thin pencil beam with a wavelength of 375 nm at the top of the geometry in f-g) presence and h-i) absence of scattering, respectively.

Photocatalytic processes not only require effective utilization of the incident light, but also efficient mass transport to the illuminated catalyst surface. To this end we take advantage of a leaf-type hierarchical architecture in sc- and fcc-structured aerogels, where the gas enters the macroscopic object through microchannels and then distributes into the nanoporous filaments to perform photocatalytic reactions. Computational fluid dynamics simulations in Figures 6.3a-b reveal that such a hierarchical flow characteristic can only be achieved by surrounding the microstructured aerogel geometry with continuous walls which can be easily added during the 3D printing process. Moreover, only with surrounding walls a pronounced interaction with the stronger illuminated section at the top of the photocatalyst becomes feasible. Besides, the multiscale hierarchical geometry of the sc- or fcc-structured aerogel facilitates the pressure driven mass transport compared to its unstructured counterpart. We evaluate the gas transport properties in a custom flow-through reactor by measuring the pressure drop of nitrogen gas across a fcc-structured sample in the flow range of 25 to 225 mL min⁻¹, as illustrated in Figure 6.4c. In Figure 6.4d we show that the fcc-structured aerogel exhibits a pressure drop of less than 1 Pa mm⁻¹ which agrees well with the predicted pressure drop obtained by computational fluid dynamics simulations. Calculations of an sc-structured aerogel forecast a similar pressure drop as for the fcc-pattern due to similar channel dimensions. In contrast, an unstructured sample, which represents the geometry of a conventionally casted aerogel, exceeds the upper pressure limit of 125 Pa for the used pressure sensor and calculations following Darcy's law predict a pressure drop of more than $1 \cdot 10^5$ Pa mm⁻¹. The reason for the five orders of magnitude higher pressure drop for the unstructured aerogel relies on the mean free path of the nitrogen gas molecule of about 59 nm which is higher than the aerogel's average pore size of 20 nm.^[39] Thus, the transport is dominated by molecule-wall interactions and high pressure differences are needed to squeeze the gas through the nanoporous network. In contrast, the sc- and fcc-structured sample offers 400 channels per cm² with dimensions of about 0.2 mm, which allows the gas molecules to flow freely and laminar through the 3D geometry, as derived in Section 6.6.3 of the Supporting Information. Nevertheless, squeezing the gas through the nanoporous network of an unstructured aerogel has the advantage that the reactants readily permeate the catalyst. However, this is only the case if the high pressure drop and resulting mechanical load do not lead to any cracking and gas channeling.^[12] For the 3D structured aerogel, reactants are no longer forced through the nanoporous network but need to diffuse from the channels into the aerogel to be converted during the photocatalytic process. Here, internal mass transfer limitations can occur if the reaction is much faster than the diffusion to the center of the filament. In section 6.6.2 of the Supporting Information we derive an estimation for the internal mass transfer and conclude that for a filament diameter of 200 μm no internal mass transfer limitations are present and that the whole catalyst participates in the reaction. Therefore, 3D printing not only allows us to adapt the gas flow to the reactor geometry, but also enables a reliable mass transfer, minimized energy consumption and a safer operation due to a lower pressure drop without compromising the gas permeation. We learned that the type of structuring is not as relevant for the pressure driven mass transport as for the light utilization and that a drastically lower flow resistance can be achieved as long as some type of structuring is present.

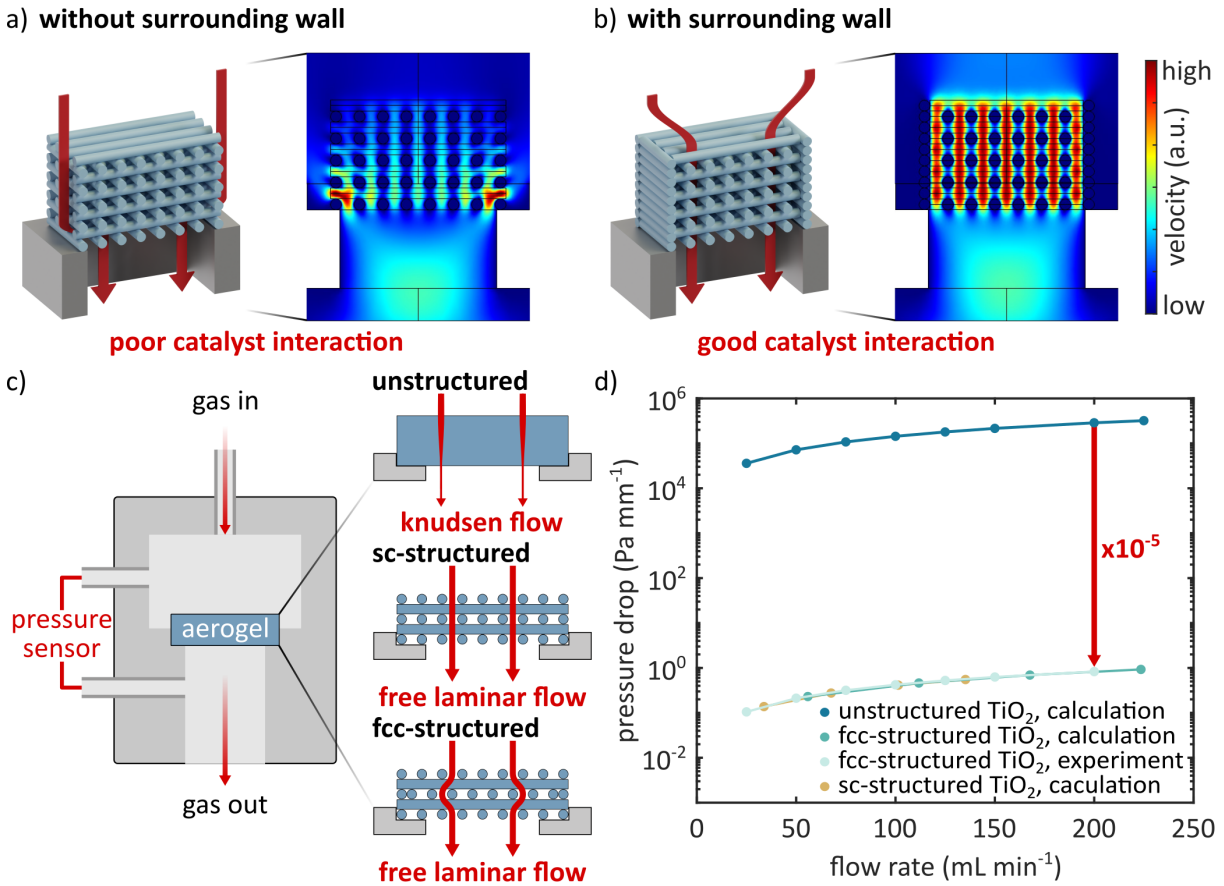


Figure 6.3: Effect of 3D-structuring on the mass transport characteristic of TiO₂ nanoparticle-based aerogels. Simulated velocity profiles of a sc-structured aerogel a) without and b) with a surrounding wall indicate that the geometry needs to be enclosed for a good interaction of the gas stream with the catalyst. c) Schematic drawing of a custom flow-through reactor that was utilized to evaluate the pressure drop of an unstructured and structured aerogel. For an unstructured and 3D-structured aerogel mass transport is dominated by Knudsen flow through the nanoporous medium and free, continuum flow through the microscopic channels of the 3D architecture, respectively. d) Measured and calculated pressure drops of unstructured and 3D-structured aerogels for flow rates in a range of 25 to 225 mL min⁻¹.

Combining the insights from the photon and mass transport simulation reveals that the fcc structure is most promising for a photocatalytic application, since we achieve similar levels of light utilization as an unstructured aerogel with a five order of magnitude lower resistance to gas flow. With a photon and mass transport optimized microstructure in place, we can now compare the performance of a fcc-structured, unstructured and powdery photocatalysts for the hydrogen formation from a helium gas stream saturated with a water/methanol mixture, as shown in Figure 6.4a. The reactor reflects the aspect ratio of the 3D printed aerogels and is designed in a way that the gas stream and photons penetrate the sample from the top. The evolved hydrogen is detected via gas chromatography every 29 min. Although the synthesis of TiO_2 nanoparticles is considered as ligand-free,^[40] solvents are involved during the processing of the 3D printed aerogels that remain attached to the surface of the nanoparticles after supercritical drying. These organic species may interfere with the photocatalytic hydrogen production process, where their decomposition during UV illumination result in misleading amounts of detected hydrogen or block catalytic active sites.^[41] We apply a UV pretreatment in air prior each measurement during which an online analysis via gas chromatography reveals that organic species decompose within 15 hours of illumination (Figure 6.5). Moreover, performing the catalytic reaction in absence of water and methanol subsequent to UV cleaning fails to produce any hydrogen. Thus, we conclude that the UV cleaning process effectively removes organic residues from the catalyst surface and that the hydrogen formation stems from the photocatalytic conversion of methanol and water on the TiO_2 aerogel. In presence of water/methanol we observe a strong formation of hydrogen, which declines within a couple of hours, before reaching a steady-state value (Figure 6.4b). This transient activity is a common effect for TiO_2 photocatalysts in the gas-phase and is generally attributed to the formation of intermediate surface species which are partly occupying the active sites.^[42–47] The transient activity recovers after performing a second UV cleaning process, as shown in Figure 6.6. We take the average of the steady-state values to evaluate the absolute amount of evolved hydrogen for fcc-structured TiO_2 aerogels with thicknesses in the range of 0.7 to 3.0 mm. In the inset of Figure 6.4b we see that the steady-state hydrogen evolution of the fcc-structured TiO_2 aerogel reaches 30 ppm for a thickness of 3.0 mm and follows a similar thickness dependence as the calculated light absorption from 3D mesh-based Monte Carlo simulations. Compared to an unstructured aerogel for a similar light absorption of 88 %, the absolute amount of evolved hydrogen is almost identical (Figure 6.7), which indicates that the gas infiltration and photocatalytic performance is not compromised despite changing from a pressure to a diffusion driven process which no longer squeezes the gas through the nanoporous aerogel.

Even though a thicker aerogel results in a higher absolute amount of evolved hydrogen (Figure 6.4b), the increase diminishes due to the exponential decrease of light intensity. Therefore, tripling the thickness of a fcc-structured TiO_2 aerogel from 1 to 3 mm, only rises the absolute amount of hydrogen by a factor of about 1.8. To enhance the utilization of the photocatalyst, an adjustment of the thickness for the most effective illumination is needed. We describe the effective use of the photocatalyst by calculating a mass-normalized hydrogen production rate for fcc-structured and unstructured aerogels, and a nanoparticle powder which is still one of the most employed approaches to benchmark a photocatalyst.^[12] We present the mass-normalized hydrogen production rates in Figure 6.4c. For identical outer dimensions and a thickness of

2.1 mm, the fcc-structured TiO_2 sample has a 25 % higher rate than the unstructured counterpart. We address this increase to the added porosity of the 3D printed microchannels which leads to an improved illumination along the catalyst thickness. Further, by varying the number of printed layers, we can optimally match the thickness of the fcc-structured aerogel to the light intensity distribution. In this way, decreasing the thickness from 2.1 to 1.1 mm enhances the hydrogen production rate by 41 % and we achieve a total improvement by a factor of 2.3 relative to the unstructured TiO_2 aerogel. Compared to same amount of TiO_2 nanoparticle powder the hydrogen production rate of the 1.1 mm thick fcc-structured aerogel is 5.2 times higher which highlights the benefits of 3D structuring and results from combining an efficient light utilization and a facile gas infiltration with the high surface area of a nanoporous solid.

Due to the modular ink design principle, pristine TiO_2 gels can also be loaded with other nanomaterials such as Au nanoparticles via cogelation. We show the hydrogen production rate of a fcc-structured Au/ TiO_2 aerogel of 1.1 mm thickness and Au/ TiO_2 powder in Figure 6.4d. Generally, we observe that the hydrogen production rates of Au decorated TiO_2 feature no transient activity and are about 20-times higher than pure TiO_2 due to less electron hole recombinations and a reduced activation barrier for hydrogen formation.^[8,48,49] Apart from the material-specific improvement, the mass normalized hydrogen production rate of the fcc-structured Au/ TiO_2 aerogel again rises nearly fivefold by a factor of 4.7. We address the slightly lower enhancement relative to the factor of 5.2 for pure TiO_2 to the reduced light penetration depth owing to the additional light absorption of Au nanoparticles. The similarity of both values indicates that our microstructuring approach is a universal, geometric tool and that comparable improvements can be expected for other photocatalytic materials than TiO_2 or Au/ TiO_2 when processed in the form of a fcc-structured aerogel. Such an optimized geometry can eventually be used for lateral upscaling of the photoreactor which maintains the mass-normalized production rates despite higher catalysts loadings. Nevertheless, for other materials with drastically different optical properties an adjustment of the 3D aerogel thickness is needed to compensate for the varying light penetration depths.

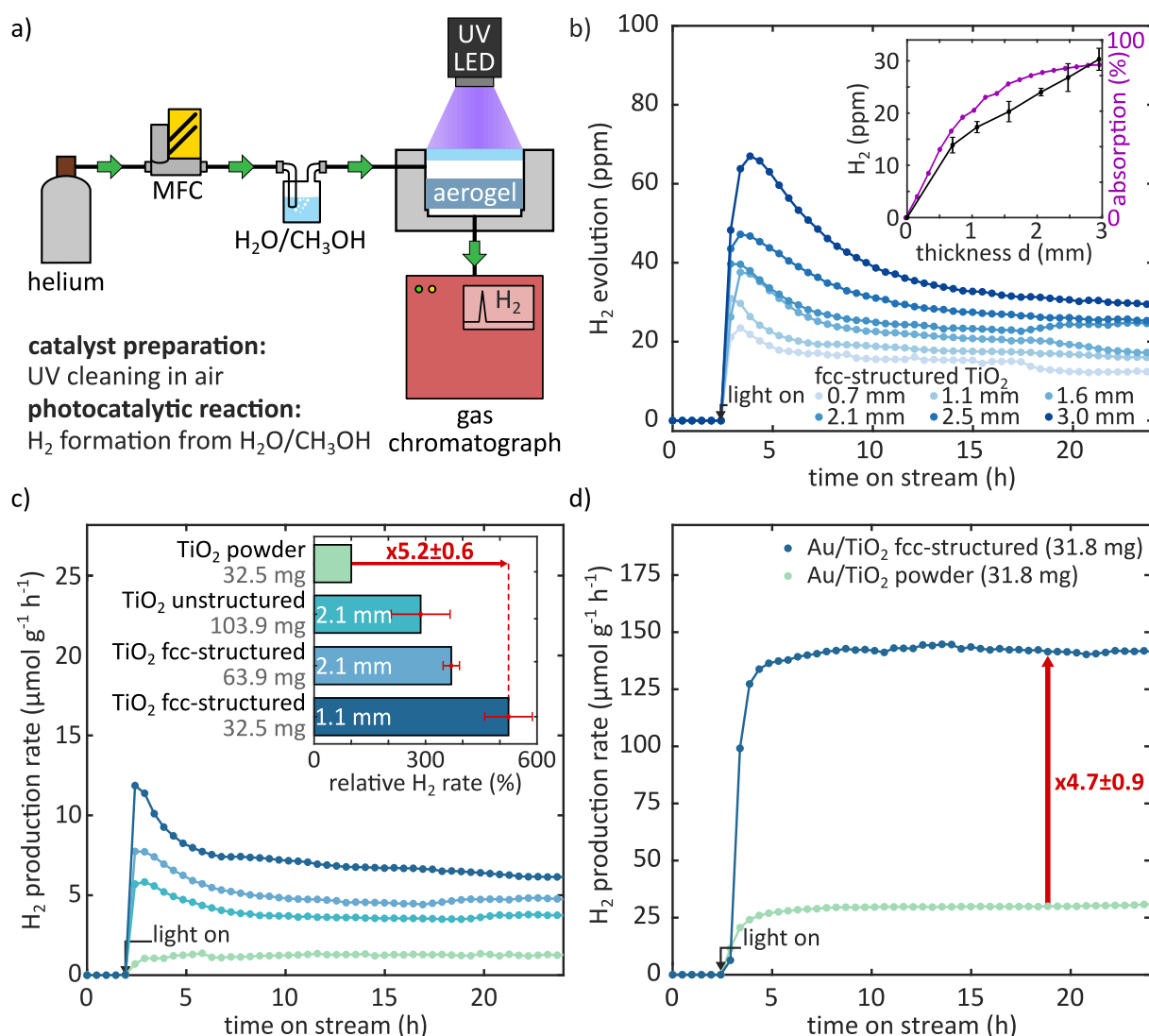


Figure 6.4: Effect of 3D-structuring on photocatalytic hydrogen evolution in the gas-phase. a) Schematic representation of the custom-made continuous-gas-flow reactor. Before each photocatalytic measurement, the samples are illuminated with UV light in a steady air stream to remove any organic residue from the catalyst surface. For the photocatalytic measurement, a helium gas stream is regulated with a mass flow controller and saturated with water and methanol vapor. The gas stream enters the reactor at the top and passes through the sample while being illuminated with a UV LED. Following that, the gas stream containing reactants and products of the photocatalytic reaction are directed to a gas chromatograph for the quantification of evolved hydrogen. b) Absolute hydrogen evolution versus time for fcc-structured TiO₂ aerogels with thicknesses in the range of 0.7 to 3.0 mm. The photocatalyst features a transient activity which declines within a couple of hours into a steady-state value. The inset shows the average and standard deviation of the steady-state region, and the calculated light absorption from 3D mesh-based Monte Carlo simulations plotted versus the sample thickness. c) Mass-normalized hydrogen production rate versus time for TiO₂ powder, an unstructured TiO₂ aerogel of 2.1 mm thickness, and fcc-structured TiO₂ aerogels of 2.1 and 1.1 mm thickness, respectively. The inset shows the hydrogen production rate relative to TiO₂ powder. d) Mass-normalized hydrogen production rate versus time for a fcc-structured Au/TiO₂ aerogel of 1.1 mm thickness and Au/TiO₂ powder. All samples feature lateral dimensions of about 1.5 cm to obtain a similarly illuminated surface area.

6.4 Conclusion

We demonstrate a versatile platform of 3D printing and computer-aided device engineering to design a TiO_2 nanoparticle-based aerogel photocatalyst with deterministic control along the nano-, micro-, and macroscopic length scales. We show that the nature-inspired light trapping and mass transfer characteristic of the 3D printed aerogels are effective tools to uniformly distribute photons and reactants throughout the macroscopic, microstructured sample. By computational fluid dynamics and Monte Carlo simulations we identify a fcc unit cell as the ideal photocatalyst microstructure since it maintains similar levels of light utilization as an unstructured aerogel combined with a five order of magnitude lower resistance to gas flow. We take the hydrogen evolution from a water/methanol saturated gas stream as an example and demonstrate that 3D printing permits a most effective use of the catalyst by tuning the macroscopic thickness for the light penetration depth. In this way, the mass normalized hydrogen evolution rate for the 3D TiO_2 aerogel raises by a factor of 5.2 in respect to TiO_2 powder. We indicate that the 3D printing approach is not limited to pure titania and that a similar five-folded improvement can be achieved by 3D structuring a Au/TiO_2 aerogel. Thus, we recognize the fcc aerogel architecture as an universal parameter which combines an effortless gas permeation and light harvesting with the high surface area of a nanoporous solid to boost the performance of any photocatalyst independent of material composition. Ultimately, the combination of a digital fabrication technique with a computer-aided design scheme creates a perspective for advanced aerogel photocatalysts architectures. We believe that such an interdisciplinary approach is essential and provides a great platform for engineers and scientists to design, optimize, and implement innovative aerogel photocatalysts for a variety of photochemical processes.

6.5 Experimental Section

Materials: Acetonitrile (99.95 %), diethyl ether (≥ 99.9 %), ethanol (EtOH, anhydrous, ≥ 99.97 %) were purchased from VWR. Ammonium hydroxide solution (28.0–30.0 % NH_3 basis), benzyl alcohol (anhydrous, 99.8 %), gold(III) chloride trihydrate (> 99.9 %), poly(methyl methacrylate) (PMMA, average $M_w = 120000$), poly(vinylpyrrolidone) (PVP, average $M_w = 40000$), sodium borohydride (NaBH_4 , 99 %), titanium(IV) tetrachloride (TiCl_4 , 99.9 % trace metal basis) were purchased from Sigma Aldrich. n-heptane (95 %) was purchased from Alfa Aesar. Liquid CO_2 , helium (purity 5.0) were purchased from Westfalen. Hydrogen (purity 5.0) was purchased from Linde. Nitrogen (purity 6.0) and synthetic air (hydrocarbon free) were purchased from SOL Deutschland GmbH. Calibration gases for quantification of hydrogen were purchased from Air Liquide Deutschland GmbH. All chemicals were used as received without further purification.

TiO_2 Synthesis: TiO_2 nanoparticle synthesis was adapted from a previously published protocol.^[40] In a argon-filled glovebox, 40 mL of benzyl alcohol were added to a 100 mL round bottom flask. Next, the flask was closed with a stopper, removed from the glovebox, and transferred to an oil bath set to 80°C while stirring and keeping the flask closed. In the meantime, 2 mL of TiCl_4 was dropwise added to a 50 mL round bottom flask containing 10 mL of EtOH while

stirring. After heating the benzyl alcohol for 10 min, the transparent yellow $\text{TiCl}_4/\text{EtOH}$ solution was swiftly added. The obtained solution was heated for 24 h while keeping the flask open. After that, the flask was immersed into an ambient water bath to quench the reaction. Next, the suspension was washed with diethyl ether (≈ 4.7 mL per mL dispersion) by three dispersion-centrifugation cycles (1160 RCF, 5 min, room temperature, Universal 320 centrifuge, Andreas Hettich GmbH & Co. KG). Afterwards, the supernatant was removed by decantation and the vial was loosely covered with its cap for slow evaporation of the remaining solvent. Finally, the dried precipitate was mortared to yield 1 g of a white powder.

Ink Formulation: Inks for 3D printing were formulated according to a previously reported procedure, but additionally filtered with a $0.2\ \mu\text{m}$ nylon syringe filter (KC92.1, Carl Roth) prior gelation.^[37] TiO_2 inks were loaded with Au by adapting a previously published protocol.^[50] HAuCl_4 (16 mM) and NaBH_4 (132 mM) stock solution were prepared by dissolving the salts in acetonitrile which was degassed beforehand by purging with nitrogen gas for 15 min. Next, 1 mL of an aqueous, degassed TiO_2 dispersion ($241\ \text{mg mL}^{-1}$) and $384\ \mu\text{L}$ of the HAuCl_4 stock solution were added to a vial. After 1 min, $116\ \mu\text{L}$ of freshly prepared NaBH_4 stock solution was quickly injected to the vigorously stirred solution. After 30 min of stirring at room temperature, the inks were stored in a refrigerator prior gelation. For gelation we applied the same procedure as described above for neat TiO_2 inks. We determined a Au loading of 0.9 wt. % for the Au/ TiO_2 aerogel by inductively coupled plasma mass spectrometry (ICP-MS, Agilent 7700 series).

3D Printing: For 3D printing tapered dispensing tips with an inner diameter of $250\ \mu\text{m}$ from Vieweg GmbH were used. The 3D printing process is described in more detail in a previously published protocol.^[37]

Photocatalysis: The photocatalytic hydrogen evolution from aerogels and powders was analyzed using a custom-made continuous gas flow reactor at room temperature and atmospheric pressure as shown in Figure 6.2a and Figure 6.8. The weights, absolute amounts of hydrogen, and the mass normalized hydrogen production rates of the catalysts are listed in Table 6.1. The self-supporting aerogels were fixed inside the reactor with grease to avoid bypass of the gas-stream. The loose powder was spread on a filter paper which was sealed in the same way as the aerogel. The powder was obtained by precipitating and drying a nanoparticle dispersion before inducing gelation. The viewport was sealed with a FPM75 O-ring. All connections were made with stainless steel tubing. Gas flows were adjusted using mass flow controllers (Bronkhorst). The outlet of the reactor was connected to a gas chromatograph (Agilent 8860) equipped with a deans-switch which directs the eluent from the PoraPLOT U ($25\ \text{m} \times 0.32\ \text{mm} \times 10\ \mu\text{m}$) column either to a series of thermal conductivity and flame ionization detector or to a series of a HP-Plot 5A ($30\ \text{m} \times 0.32\ \text{mm} \times 25\ \mu\text{m}$) column and a helium ionization detector. The hydrogen signal was calibrated with calibration gases containing defined amounts of hydrogen. The gas chromatograph enables sample acquisition every 29 min. Before each measurement, the samples were UV cleaned in the reactor for 24 h at room temperature in a continuous flow of synthetic air at a flow rate of $5\ \text{mL min}^{-1}$ and UV illumination with a 200 W Hg/Xe arc lamp (66984-200HX-r1, Newport) equipped with a water filter (61945, Newport) to remove Infrared (IR) light from the light source. Gas chromatograph measurements were performed to monitor the cleaning process. Next, helium was bubbled through a custom-made stainless-steel saturator filled with

water and methanol (1:1 v/v) to saturate the gas-stream with water and methanol vapor. Before light illumination, the flow rate was set to 20 mL min^{-1} to remove oxygen residues in the tubing and reactor. Next the flow rate was decreased to 5 mL min^{-1} and the sample was illuminated with a high-power LED (M375L4, Thorlabs) with an emission peak at 375 nm. The output of the LED was collimated with an aspheric condenser lens (ACL2520U-DG6-A, Thorlabs) and illuminated the whole sample area. The output power was measured with a photodiode power sensor (S120VC, Thorlabs). For this, the same distance between the light source and sensor as between the light source and sample was used. For the photocatalytic experiments the power of the LED was set to 116 mW cm^{-2} and was controlled via a custom-made electronic circuit consisting of a power supply, an LED driver (LDD-1500H, Mean Well), and an Arduino Nano. Each sample was measured twice for at least 24 hours to obtain statistically representative data. Control experiments were carried out with an empty reactor in a water/methanol saturated helium gas stream, and with an TiO_2 aerogel sample inside the reactor in a dry helium gas stream and no hydrogen evolution was observed.

Computational Modeling: For photon transport in 3D structured geometries tetrahedral meshes were generated using the MATLAB based program Iso2mesh.^[51] For computing reasons the mesh represents a small section of the periodic geometry. In detail, the number of filaments per layer were reduced from 39 to 8 for the structured samples. Moreover, the dimensions of the unstructured geometry were scaled to achieve a similar optical thickness in lateral direction than for the structured geometries. The generated meshes were used to perform 3D Monte Carlo light transport simulations with MMCLAB.^[52] The optical parameters were extracted from solving the inverse problem of the RTE and UV-vis integrating sphere measurements, as described in section 6.6.1 of the Supporting Information. The light source was either a pencil beam or a circular disk source with a diameter of twice the filament diameter. For each calculation at least 50000 photons were used. We verified mesh independence by calculating the absorption of a 3.5 mm thick fcc-structured aerogel for three different mesh sizes of 5.1, 8.7, and 14 million elements. The calculated absorption varied by less than 0.1 % and the mesh featured a mean Joe-Liu mesh quality metric of 0.8.^[53] Computational fluid dynamics simulations were performed with the 'Free and Porous Media Flow' Interface of COMSOL Multiphysics software (COMSOL 5.4). Computations were performed on a computing cluster (4xAMD EPYC 7302 processors, available RAM: 2060.17 GB). Mesh convergence was verified for three different mesh sizes with 2.1, 2.4, and 5.2 million elements, respectively. The pressure drop calculations for the three meshes varied by less than 1.3 %. For a more detailed description of the simulations, we refer to section 6.6.3 of the Supporting Information.

Characterization: The dimensions of the sample were determined from optical micrographs, and the mass was measured using a microbalance (LA 254i, VWR). The density of the samples was calculated from the measured mass and dimensions. Scanning electron microscopy images were taken with a Regulus 8220 (Hitachi High Technologies Corp., Japan). N_2 -Physisorption measurements are shown in Figure 6.10 and were performed at 77 K with a Quantachrome Autosorb 6-MP (Anton Paar QuantaTec Inc.). The specific surface area and pore size were determined via the Brunauer–Emmet–Teller (BET) method and density functional theory (DFT) analysis, respectively. For DFT analysis a Non Local DFT (NLDF) calculation model for nitrogen at

77 K using the equilibrium branch was applied and cylindrical pores in silica were assumed. Prior to measurement, samples were degassed at 100 °C for 24 h. Powder X-ray diffraction measurements are shown in Figure 6.8 and were performed on a Bruker D8 Discovery using Cu-K α X-ray radiation. UV-vis spectra were recorded using an Agilent Cary 5000 spectrophotometer equipped with a 150 mm integrating sphere. Pressure drop experiments were performed in a custom-designed flow cell, as shown in Figure 6.4a. The pressure drop was measured with a differential pressure sensor (SDP810-125Pa, Sensirion) with a detection range of 0 to 125 Pa. The edges of the 3D printed aerogel sample were sealed with grease, and flow rates between 0 to 200 mL min⁻¹ of nitrogen gas were used.

6.6 Supporting Information

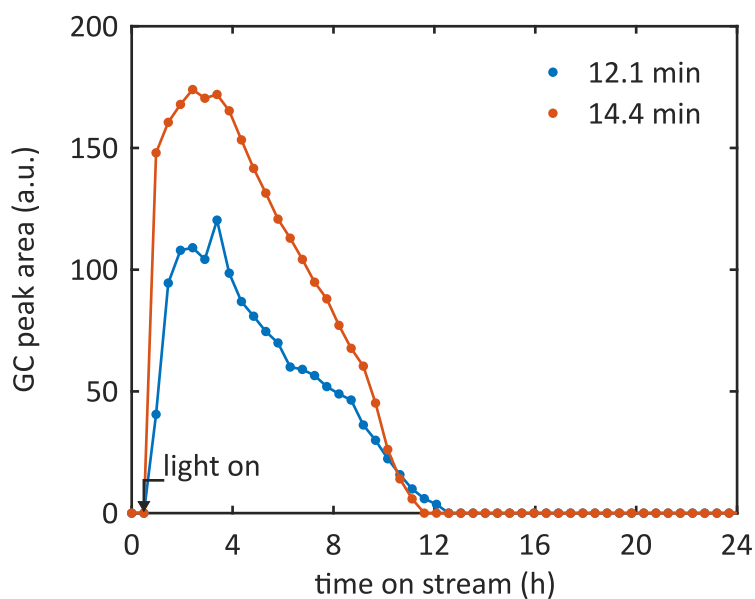


Figure 6.5: Peak areas at retention times of 12.1 and 14.4 min measured with the flame ionization detector of the gas chromatograph during UV cleaning. Since retention times are close to 14.2 min of pure ethanol, which is used as a solvent during sample preparation, we believe that detected compounds are some chemically related species that formed during the oxidative UV cleaning process.

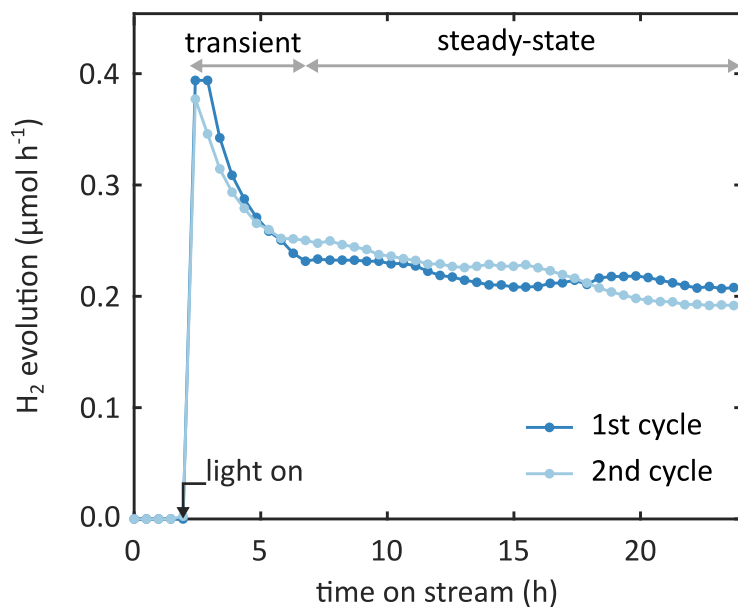


Figure 6.6: Hydrogen evolution over time during two photocatalytic cycles for an exemplary fcc-structured TiO₂ aerogel. Before each cycle, a UV cleaning procedure is applied by illuminating the sample with UV light in a continuous stream of synthetic air. We observe that the transient activity recovers after UV-cleaning. This underlines that the transient is caused by some surface species, which formed during the catalytic process and are removed during UV cleaning, and not by some irreversible structural degradation of the catalyst. This is further supported by the fact that the specific surface area and pore size distribution remain nearly unaffected by the catalytic process, as shown in Figure 6.10 and Table 6.2.

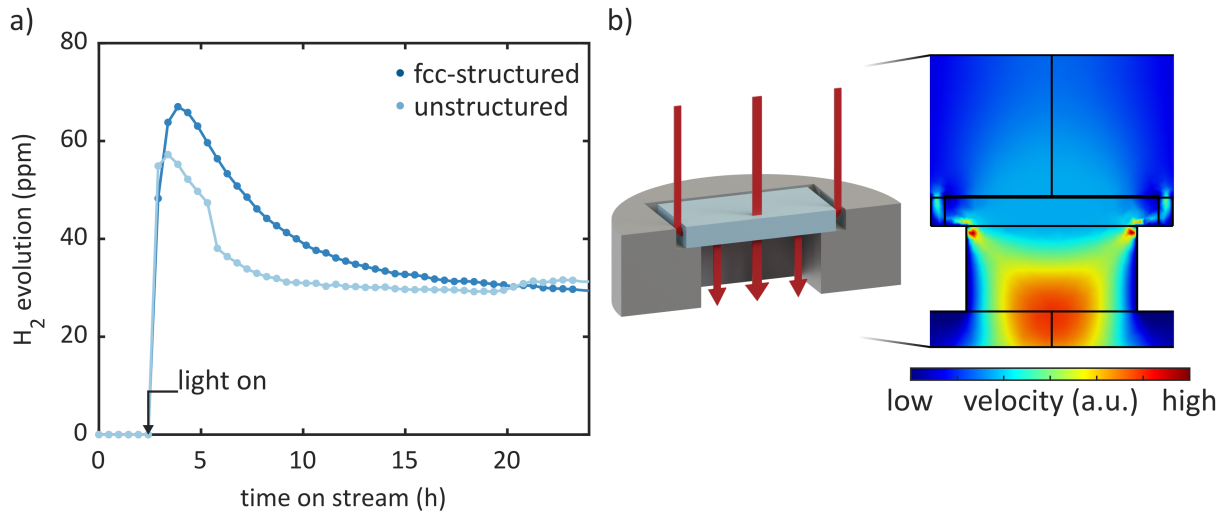


Figure 6.7: Absolute amount of evolving hydrogen over time for a fcc-structured and an unstructured TiO₂ aerogel of 3.0 and 2.1 mm thickness, respectively. The data of each sample show the average of two consecutive measurements. The samples feature different thicknesses to achieve a similar level of light absorption of 86 and 87 % for the fcc and unstructured TiO₂ aerogel, respectively (Figure 6.2e). We observe that the fcc and unstructured sample feature a similar hydrogen evolution of 30.0 ± 2.1 ppm and 30.0 ± 6.5 ppm, respectively. b) Simulated fluid velocity profile of an unstructured TiO₂ aerogel placed in the inlet of the reactor. The fluid tends to take the lowest path of resistance and because of the low permeability partly bypasses the better illuminated section of the unstructured aerogel at the top by flowing through the gap between the aerogel and the wall of the inlet and entering the aerogel at the side. This effect might lead to a slightly lower utilization of the catalyst for the unstructured TiO₂ aerogel, since no bypass of gas occurs for an fcc-structured aerogel (Figure 6.3b).

Table 6.1: Weight, absolute amount of evolved hydrogen, and calculated hydrogen production rate of various TiO₂ and Au/TiO₂ photocatalysts. The data for the hydrogen evolution and production rate of the TiO₂ powder were filtered as described in Figure 6.9.

sample	weight (mg)	hydrogen evolution (ppm)	hydrogen rate ($\mu\text{mol g}^{-1} \text{h}^{-1}$)
TiO ₂ powder	32.5	3.4 ± 0.2	1.30 ± 0.08
TiO ₂ fcc-structured aerogel (thickness: 0.7 mm)	23.8	14.0 ± 1.5	7.3 ± 0.8
TiO ₂ fcc-structured aerogel (thickness: 1.1 mm)	32.5	17.0 ± 1.1	6.6 ± 0.4
TiO ₂ fcc-structured aerogel (thickness: 1.6 mm)	52.9	20.0 ± 2.0	4.8 ± 0.5
TiO ₂ fcc-structured aerogel (thickness: 2.1 mm)	63.9	24.0 ± 0.8	4.7 ± 0.1
TiO ₂ fcc-structured aerogel (thickness: 2.5 mm)	83.1	27.0 ± 2.7	4.0 ± 0.2
TiO ₂ fcc-structured aerogel (thickness: 3.0 mm)	98.8	30.0 ± 2.1	3.8 ± 0.3
TiO ₂ unstructured aerogel (thickness: 2.1 mm)	103.9	30.0 ± 6.5	3.6 ± 0.8
Au/TiO ₂ powder	31.8	77.0 ± 8.7	30.0 ± 3.4
Au/TiO ₂ fcc-structured aerogel (thickness: 1.1 mm)	31.8	362 ± 26	142 ± 10

Table 6.2: Average specific surface area and pore size of three TiO₂ aerogels derived from N₂-Physisorption measurements before and after catalytic experiments. Exemplary nitrogen isotherms are shown in Figure 6.10.

sample	specific surface area ($\text{m}^2 \text{g}^{-1}$)	pore size (nm)
before catalysis	478 ± 45	21.6 ± 1.1
after catalysis	494 ± 22	17.0 ± 2.7

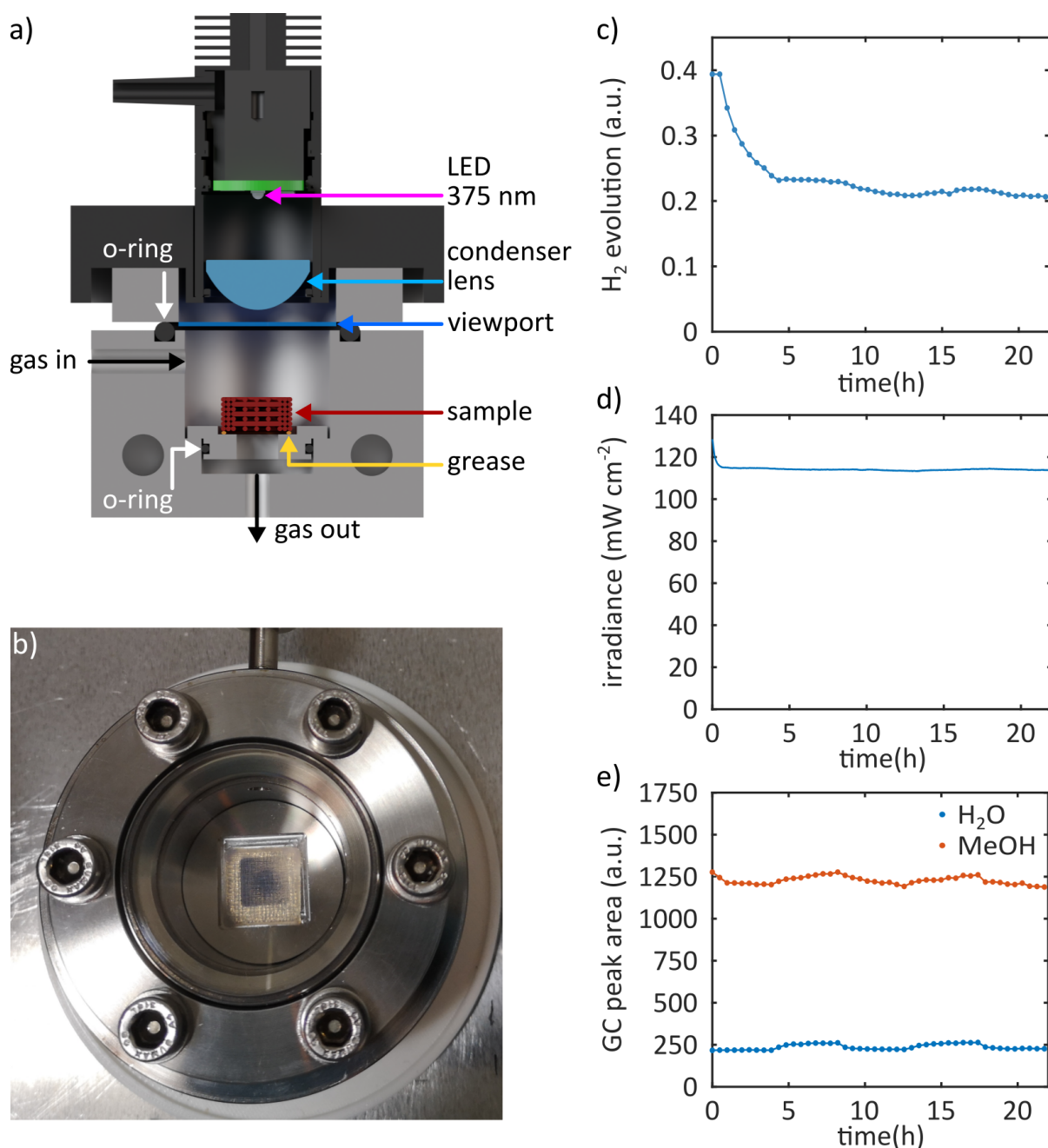


Figure 6.8: Custom-made gas flow photoreactor. a) Technical drawing of the photoreactor and b) photograph from the top showing a 3D printed aerogel mounted in the sample holder of the reactor. Exemplary time traces of c) the hydrogen evolution, d) the irradiance of the LED, and e) the detected amounts of water (H₂O) and methanol (MeOH). Since the quantities in d) and e) are nearly constant, the decrease of evolved hydrogen within the first five hours of illumination is not related to a potential change of light intensity or educt concentration in the gas stream. We address the transient hydrogen activity to the formation of some intermediate organic species on the TiO₂ surface, as discussed in chapter 6.3.

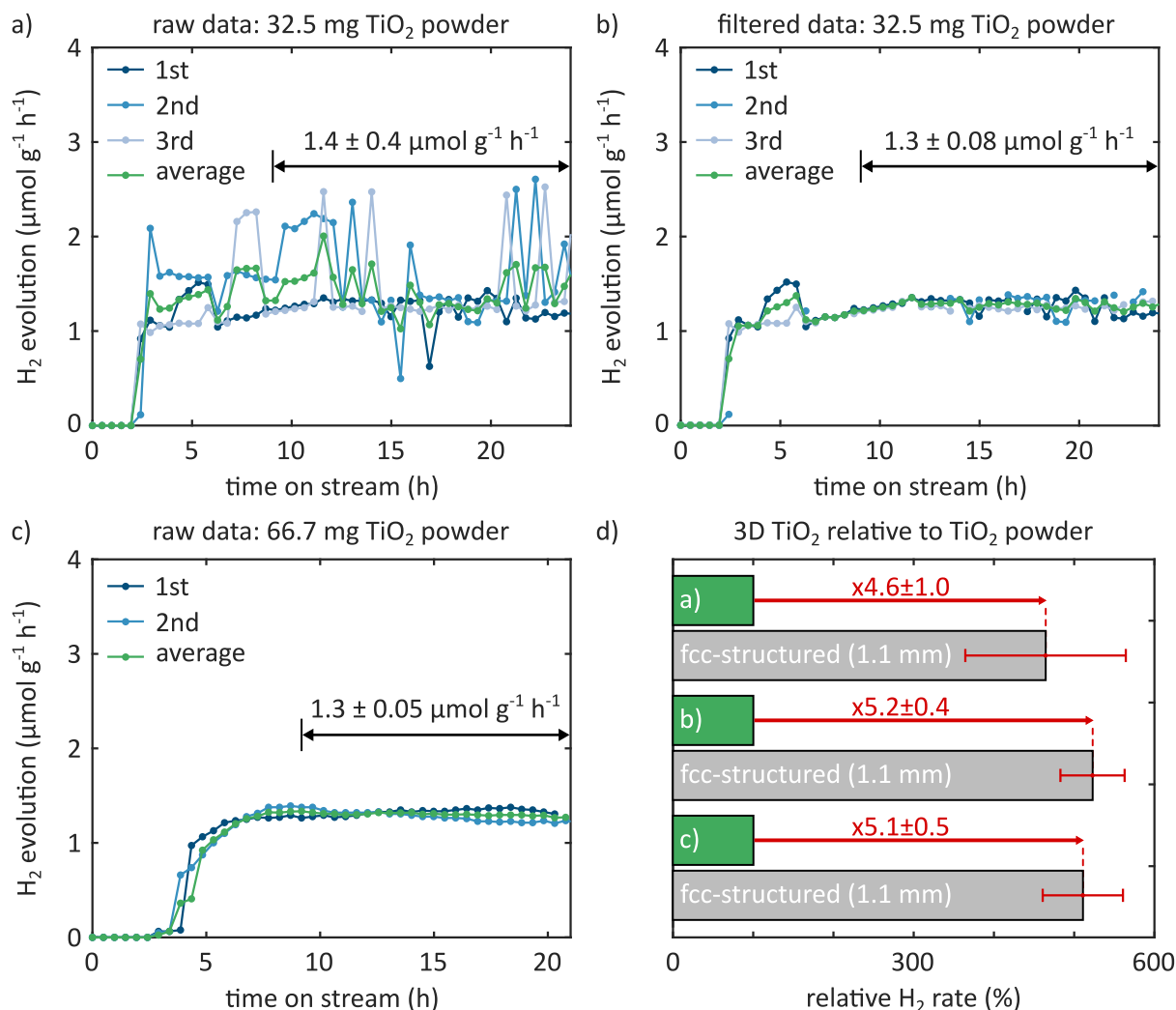


Figure 6.9: Hydrogen production rate versus time for 32.5 and 66.7 mg of TiO₂ nanoparticle powder and the calculation of a relative hydrogen production rate of an fcc-structured TiO₂ aerogel with respect to TiO₂ powder. a) shows the time trace for 3 measurements and the average which was measured for 32.5 mg of TiO₂ powder. Here, the data is superimposed with randomly appearing spikes. We believe that these artefacts are caused by the low absolute amounts of evolved hydrogen which is close to the detection limit of the gas chromatograph. Therefore, small fluctuations in the baseline signal of the detector cause an unreliable peak identification in the recorded chromatograph. In accordance with the analysis of the fcc-structured aerogels in Figure 6.4, we derive an average and standard deviation for the data from 9 hours onwards to rule out any contribution from a potential transient activity. For the raw data we calculate a rate of $1.4 \pm 0.4 \mu\text{mol g}^{-1} \text{h}^{-1}$. b) shows the time traces after manually removing the spikes from the dataset and we obtain a rate of $1.30 \pm 0.08 \mu\text{mol g}^{-1} \text{h}^{-1}$ for the filtered data. c) shows the time traces of 2 measurements and the average for 66.7 mg of TiO₂ nanoparticle powder. Here, the absolute amounts of hydrogen are well above the detection limit of the gas chromatograph due to the higher amount of catalyst and no spikes appear because of a more reliable peak identification. We derive a rate of $1.30 \pm 0.05 \mu\text{mol g}^{-1} \text{h}^{-1}$. Since the rate matches well with the filtered data in b), we believe that the rate of $1.3 \mu\text{mol g}^{-1} \text{h}^{-1}$ describes the actual rate of the TiO₂ nanoparticle powder. d) shows the relative rate of an fcc-structured TiO₂ aerogel with respect to the rates derived for TiO₂ powder in a-c). We observe a fivefold improvement for all the TiO₂ powder rates.

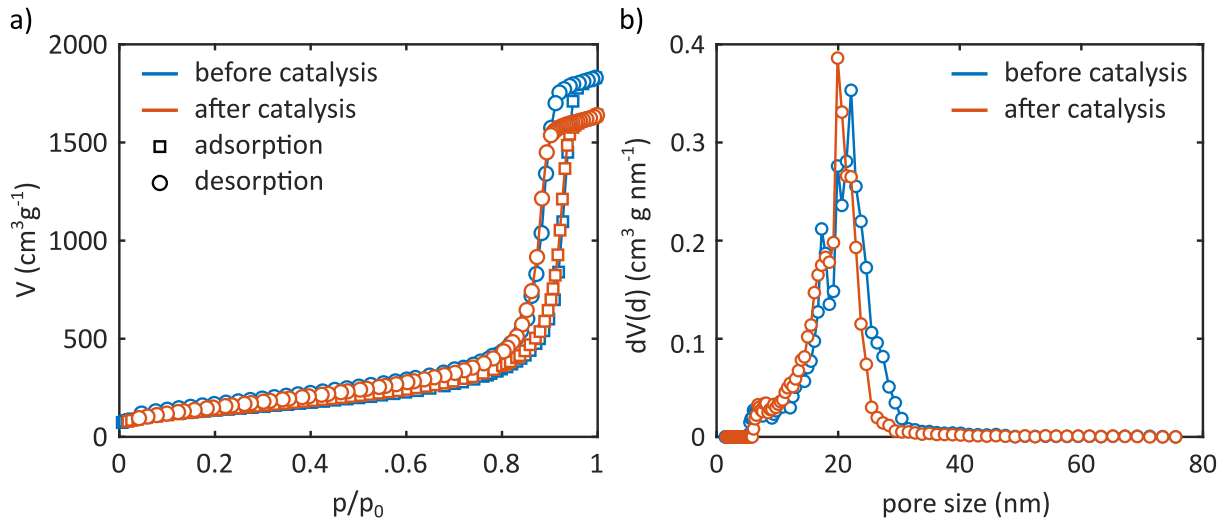


Figure 6.10: a) Exemplary nitrogen isotherm and b) derived pore size distribution for an TiO_2 aerogel before and after the catalytic experiment. The average specific surface area and pore size of three samples are listed in Table 6.2.

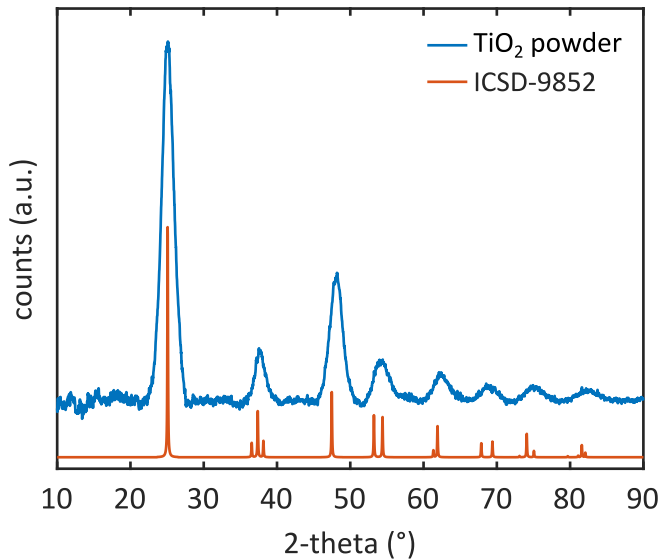


Figure 6.11: XRD measurement reveals that the 3D printed aerogels consist of crystalline anatase TiO_2 nanoparticles. For phase identification, a reference of TiO_2 anatase is shown (ICS-9852). The average crystallite size of the TiO_2 nanoparticles is about 4 nm, calculated from the full width at half maximum of the (101) reflex using the Scherrer equation.

Apparent Quantum Efficiency

We calculate the apparent quantum efficiency (AQE) according to the following equation:

$$\text{AQE} [\%] = \frac{2 \cdot n_{\text{H}_2}}{n_\lambda} \cdot 100 \quad (6.1)$$

where n_{H_2} and n_λ specify the rate of evolved hydrogen molecules and rate of incident photons per second, respectively. The rate of incident photons was calculated from the measured irradiance I ($\text{J s}^{-1} \text{cm}^{-2}$), the cross-sectional sample area A (cm^2), and the energy of a single photon E_λ (J) at 375 nm as:

$$n_\lambda = \frac{I \cdot A}{E_\lambda} \quad (6.2)$$

The photon energy E_λ was obtained from the Planck-Einstein relation:

$$E_\lambda = \frac{hc}{\lambda} \quad (6.3)$$

where h is Planck's constant, c is the speed of light in vacuum, and λ is the wavelength of the LED (375 nm).

Table 6.3: Rate of evolved hydrogen molecules n_{H_2} and AQE for TiO_2 powder, and TiO_2 and Au/TiO_2 aerogels. All samples were illuminated with a rate of $4.93 \cdot 10^{16}$ photons s^{-1} .

sample	n_{H_2} (s^{-1})	AQE (%)
TiO_2 powder	$1.44 \cdot 10^{13}$	0.0586
TiO_2 unstructured	$6.32 \cdot 10^{13}$	0.257
TiO_2 fcc-structured	$6.32 \cdot 10^{13}$	0.257
Au/TiO_2 fcc-structured	$1.12 \cdot 10^{15}$	4.54

6.6.1 Optical Characterization

We calculate the absorption and scattering coefficient of 3D printed TiO₂ aerogels by solving the inverse problem of the 1D RTE, as described previously.^[38] To this end, we first measure the UV-vis transmittance and reflectance spectra of an unstructured TiO₂ aerogel using an integrating sphere. In a second step, we extract the absorption and scattering coefficients by comparing the experimental spectra with calculated total transmittance and diffuse reflectance data predicted by the RTE. Figure 6.12 shows the measured total transmittance and diffuse reflectance spectra of a TiO₂ aerogel. The sample was illuminated with a collimated light beam.

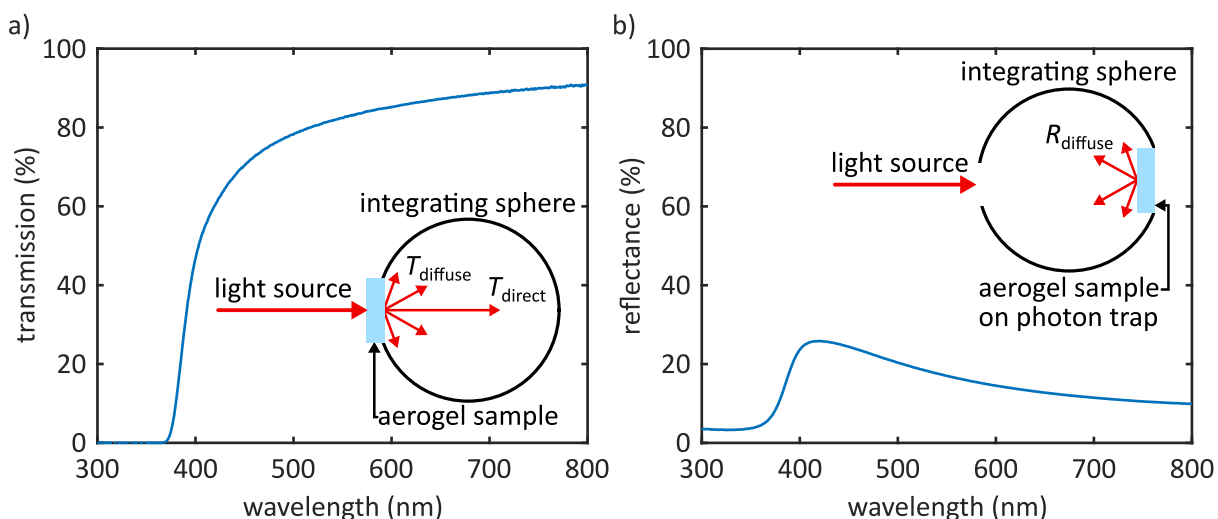


Figure 6.12: Measured total transmittance and reflectance spectra of a TiO₂ aerogel. The inset illustrates the experimental setup. For reflectance measurements the aerogel was mounted on a photon trap within the sphere.

We adapt the sample geometry of the experimental measurements for the RTE calculation, as illustrated in Figure 6.13. A collimated light beam hits the plane-parallel aerogel layer at $z = 0$ in normal direction ($\theta = 0^\circ$). As the light propagates through the aerogel, scattering and absorption processes can take place. Here, scattering changes the light propagation direction, whereas absorption diminishes its intensity. The light intensity I within the aerogel sample can be described by the 1D azimuthal RTE

$$\mu \frac{\partial I(\tau, \mu)}{\partial \tau} = -I(\tau, \mu) + \frac{\omega}{2} \int_{-1}^1 I(\tau, \mu') d\mu' \quad (6.4)$$

where $\mu = \cos(\theta)$ is the cosine of the polar angle θ , τ is the optical coordinate, and ω is the scattering albedo. The optical coordinate τ is defined via the extinction coefficient σ_{ext} as $\tau = \sigma_{\text{ext}} z$. The scattering albedo ω is defined via the absorption σ_{abs} and scattering coefficient σ_{scat} as

$$\omega = \frac{\sigma_{\text{scat}}}{\sigma_{\text{ext}}} = \frac{\sigma_{\text{scat}}}{\sigma_{\text{scat}} + \sigma_{\text{abs}}}. \quad (6.5)$$

We assumed isotropic scattering because TiO_2 particles within the aerogel are much smaller than the incident wavelength.^[54] Due to the high porosity of the aerogel, the refractive index is close to 1 and specular reflection at the air/aerogel interfaces can be neglected (equation 6.12-6.14). We solved equation 6.4 for the light intensity using the discrete ordinate method implemented in the DISORT algorithm.^[55] We calculate the total transmittance and diffuse reflectance by normalizing the directional sum of the light intensity at $z = L$ from $0 \leq \mu \leq 1$ and at $z = 0$ from $-1 \leq \mu \leq 0$ by the incident flux, respectively. In this way, the total transmittance and diffuse reflectance represents all light intensity that is leaving the sample at $z = L$ in the downward direction and at $z = 0$ in the upward direction, respectively.

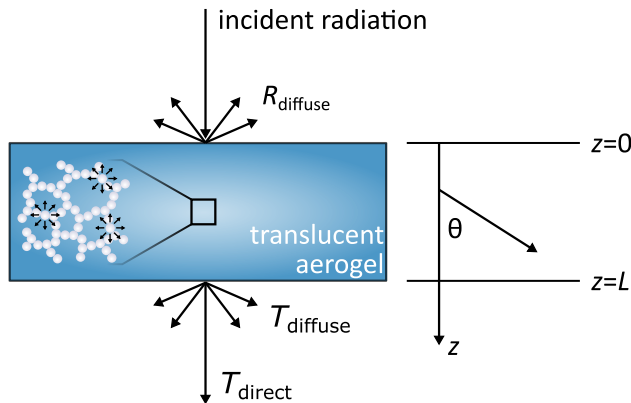


Figure 6.13: Schematic of the light propagation in a translucent aerogel of thickness L . We assume a plane-parallel geometry for the RTE model and approximate the incident radiation as a collimated light beam propagating in normal direction ($\theta = 0^\circ$). The light intensity distribution within the sample can be described with a z -coordinate and the polar angle θ .

We show the calculated transmittance and reflectance for scattering albedo of $0 \leq \omega \leq 1$ and optical thickness of $0 \leq \tau \leq 5$ in Figure 6.14. For a non-scattering sample ($\omega = 0$) the transmittance follows an exponential decrease with thickness according to Beer-Lambert law and diffuse reflectance is zero because of the absence of backscattering photons. For a purely scattering sample ($\omega = 1$) and high optical thickness, the sum of transmittance and reflectance is lower than 100 % due to light trapping within the sample.

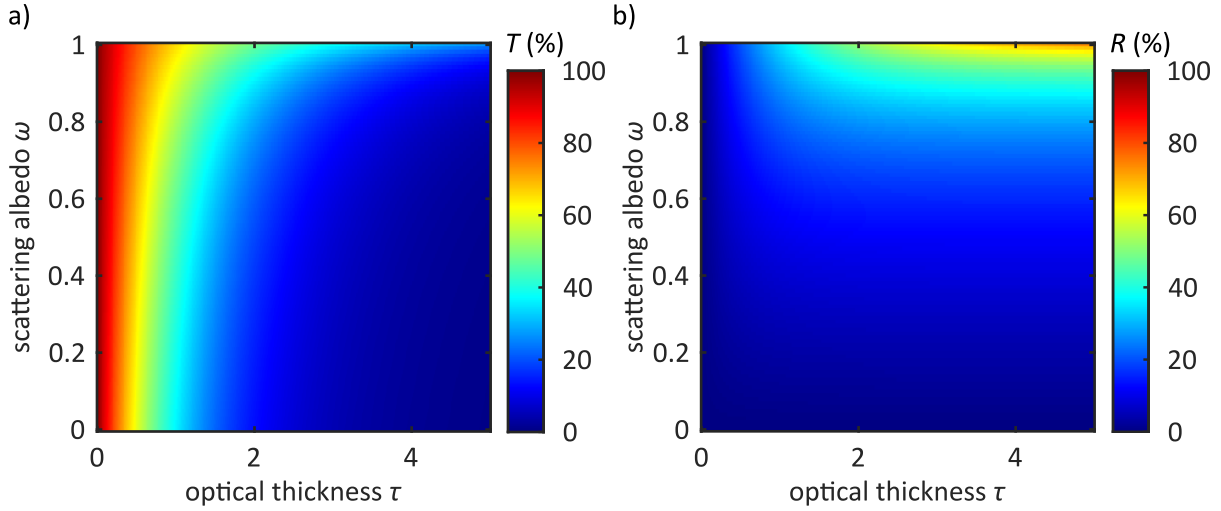


Figure 6.14: Calculated transmittance and reflectance as a function of the optical thickness τ and scattering albedo ω .

Combining the calculated transmittance and reflectance data in Figure 6.14 with the measured spectra in Figure 6.12 gives a unique solution for the scattering albedo ω and optical thickness τ for each wavelength. We illustrate this for a wavelength of 375 nm in Figure 6.15a-c. Figure 6.15a and b show the calculated transmittance and reflectance data including a contour of the measured transmittance and reflectance value, respectively. The intersect of both contours defines the scattering albedo ω and optical thickness τ that describes the measured transmittance and reflectance data (Figure 6.15c). Dividing τ by the physical thickness L yields the extinction coefficient of the sample σ_{ext} :

$$\sigma_{\text{ext}} = \frac{\tau}{L}. \quad (6.6)$$

Multiplying σ_{ext} with the scattering albedo ω yields the scattering coefficient σ_{scat} .

$$\sigma_{\text{ext}} \omega = (\sigma_{\text{abs}} + \sigma_{\text{scat}}) \left(\frac{\sigma_{\text{scat}}}{\sigma_{\text{abs}} + \sigma_{\text{scat}}} \right) = \sigma_{\text{scat}}. \quad (6.7)$$

We obtain the absorption coefficient σ_{abs} by subtracting the scattering coefficient from the extinction coefficient:

$$\sigma_{\text{ext}} - \sigma_{\text{scat}} = \sigma_{\text{abs}} \quad (6.8)$$

For a wavelength of 375 nm, we derive an absorption and scattering coefficient of 2.2 and 1.4 mm^{-1} , respectively. Applying this procedure to all wavelengths covered in the experiment yields a dataset of absorption and scattering coefficients as a function of wavelength, as shown in Figure 6.15d. The data in Figure 6.15d shows that the aerogel has an absorption onset at a wavelength slightly larger than the theoretical bandgap of 387 nm, which indicates the presence of oxygen vacancies in the TiO_2 aerogel. To verify whether Rayleigh scattering is the dominant mechanism in the UV range, we use the derived scattering coefficient to estimate an

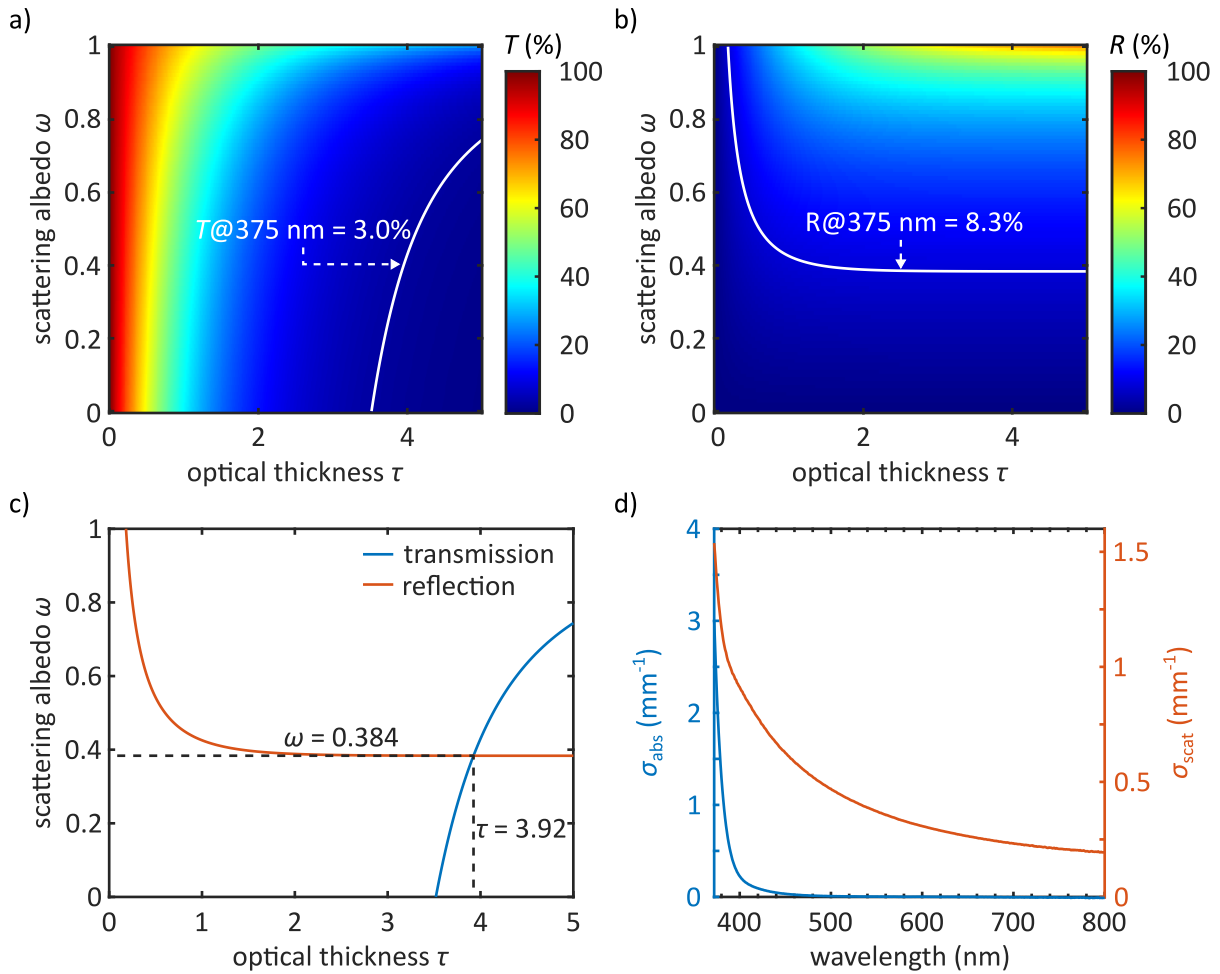


Figure 6.15: Illustration of the data processing routine. The white contour in a-b) shows the potential scattering albedo and optical thickness values for experimentally derived transmission and reflectance of 3.0 % and 8.3 % at a wavelength of 375 nm, respectively. c) The intercept of both contours yields a unique combination of $\omega = 0.384$ and $\tau = 3.92$ that describes the measured transmission and reflectance value at 375 nm. Combining these values with the physical thickness of 1.1 mm yields an absorption and scattering coefficient of 2.2 and 1.4 mm^{-1} , respectively, as derived in equations 6.6-6.8. d) Shows the absorption and scattering coefficients that were obtained following the ascribed procedure for a wavelength range of 372 to 800 nm.

effective scattering diameter. The Rayleigh scattering coefficient for spherical particles is defined as:^[38]

$$\sigma_{\text{scat}} = 4\pi^4 \frac{\rho_{\text{ag}}}{\rho_{\text{TiO}_2}} \frac{d_{\text{scat}}^3}{\lambda^4} \left(\frac{n^2 - 1}{n^2 + 2} \right)^2 \quad (6.9)$$

where ρ_{ag} is the apparent density of the TiO_2 aerogel sample (0.25 g cm^{-3}), ρ_{TiO_2} is the density of bulk TiO_2 (3.9 g cm^{-3}), d_{scat} is the mean diameter of the scattering center, λ is the wavelength of light, and n is the relative refractive index of bulk TiO_2 to air (2.5).^[56] For a wavelength of 375 nm we calculate a scattering diameter of 14 nm, which is in line with the dimension of the percolating network of nanoparticles and the pore size in the TiO_2 aerogel sample, as indicated by the TEM image in Figure 6.16a. Moreover, Rayleigh scattering is consistent with the scattering mechanism in SiO_2 aerogels of a similar nanoporous structure.^[38]

Based on equation 6.9 we expect a λ^{-4} dependence for the scattering coefficient. However, Figure 6.16b shows that a power law fit of the data reveals a $\lambda^{-2.2}$ relation, which rather indicates Mie instead of Rayleigh scattering.^[57–59] Moreover, we see that the fit does not represent the data well and especially fails to describe the scattering coefficients for wavelengths below 400 nm. We believe that the discrepancy is caused by two experimental limitations. First, for reflectance measurements the aerogel needed to be placed on a photon trap which features a finite reflectance of about 2 %. Therefore, photons that were reflected at the photon trap without being absorbed in the aerogel caused an overvalued reflectance. Second, the RTE assumes an aerogel with infinite side length, whereas the sample has a finite dimension of about 16 mm. Thus, diffusely scattered light may exit the aerogel at the side, as illustrated in Figure 6.16c, which leads to an overvalued reflectance during the integrating sphere measurement and an overestimated scattering coefficient in the subsequent data analysis. We believe that both artefacts are pronounced in the visible part of the spectrum because of strong light absorption in the UV range, which prevents that reflected or diffusely scattered UV light reaches the edge of the aerogel (Figure 6.16d). To verify, we estimate the optical thickness for a photon of 375 nm when traveling from the photon trap along the aerogel thickness or from the edge of the beam to the edge of the aerogel by taking the sample thickness of 1.1 mm, the spot size of 7 mm, the lateral sample dimension of 16 mm, and the extinction coefficient of 3.6 mm^{-1} into account. Based on the path length of 1.1 mm and the distance between the edge of the spot and the sample of $(16 \text{ mm} - 7 \text{ mm})/2 = 4.5 \text{ mm}$, we estimate an optical thickness of $1.1 \text{ mm} \cdot 3.6 \text{ mm}^{-1} = 4.0$ and $4.5 \text{ mm} \cdot 3.6 \text{ mm}^{-1} = 16$ which corresponds to $10^{-4} = 10^{-2} \%$ and $10^{-16} = 10^{-12} \%$ of the initial light intensity, respectively. Thus, the measured reflectance at 375 nm is not overvalued and the strong decay of the Rayleigh scattering coefficient only becomes apparent in the UV range as indicated by a slight kink in the data at about 390 nm (Figure 6.16b). To account for the escaped photons at the aerogel edges in the visible part of the spectrum, we correct the reflectance data by the absorption profile of the aerogel (Figure 6.16e) according to the following equation:

$$R_{\text{corrected}} = R - S \cdot \frac{100 - Abs}{100}. \quad (6.10)$$

Here, R and Abs are the recorded reflectance and absorption spectra, respectively, and S is a geometric scaling factor which depends on the aspect ratio of the sample. We use the corrected reflectance data as an input for the data processing routine shown in Figure 6.15 and present the corrected scattering coefficients and a power law fit in Figure 6.16f. We observe that the power law fit of the corrected data follows a $\lambda^{-4.1}$ dependence, which matches well with Rayleigh scattering. However, we would like to point out, that the applied data correction does not enable a quantitative description of the scattering coefficient in the visible range since the scaling factor of $S = 7.75$ was chosen for a best fit of the power law. Nevertheless, it indicates that the uncorrected data overestimates scattering in the visible part of the spectrum, and that Rayleigh scattering seems to be the actual scattering mechanism present in the sample, as expected from the structural characteristic of the aerogel discussed above. For a qualitative determination of the scattering coefficients in the visible range, a photon trap with a lower reflectance and samples with larger lateral dimensions are needed to avoid that light escapes at the edges of the aerogel. To estimate the required lateral dimension, we calculate a path length L_p to reduce the light intensity I to 1 % of the initial value I_0 according to Beer-Lambert law:

$$L_p = -\frac{\ln\left(\frac{I}{I_0}\right)}{\sigma_{\text{ext}}} \approx -\frac{\ln 0.01}{\sigma_{\text{scat}}} \quad (6.11)$$

Following equation 6.11, we obtain a path length of 98 mm for a scattering coefficient of 0.047 mm^{-1} at a wavelength of 800 nm. Thus, for a spot size of about 7 mm the sample should feature lateral dimensions of at least 203 mm (spot size + $2 \cdot L_p$) to eliminate excessive light loss for photons that are traveling from the edge of the beam to the edge of sample. The derived length greatly exceeds the maximum lateral dimension achievable with our current 3D printing setup.

Please note that the correction of the reflectance was only performed to illustrate the influence of an overvalued reflectance in the visible range. Since we investigated the light transport at 375 nm, which does not seem to be influenced by an overvalued reflectance as discussed above, we used the uncorrected raw data for all remaining optical simulations.

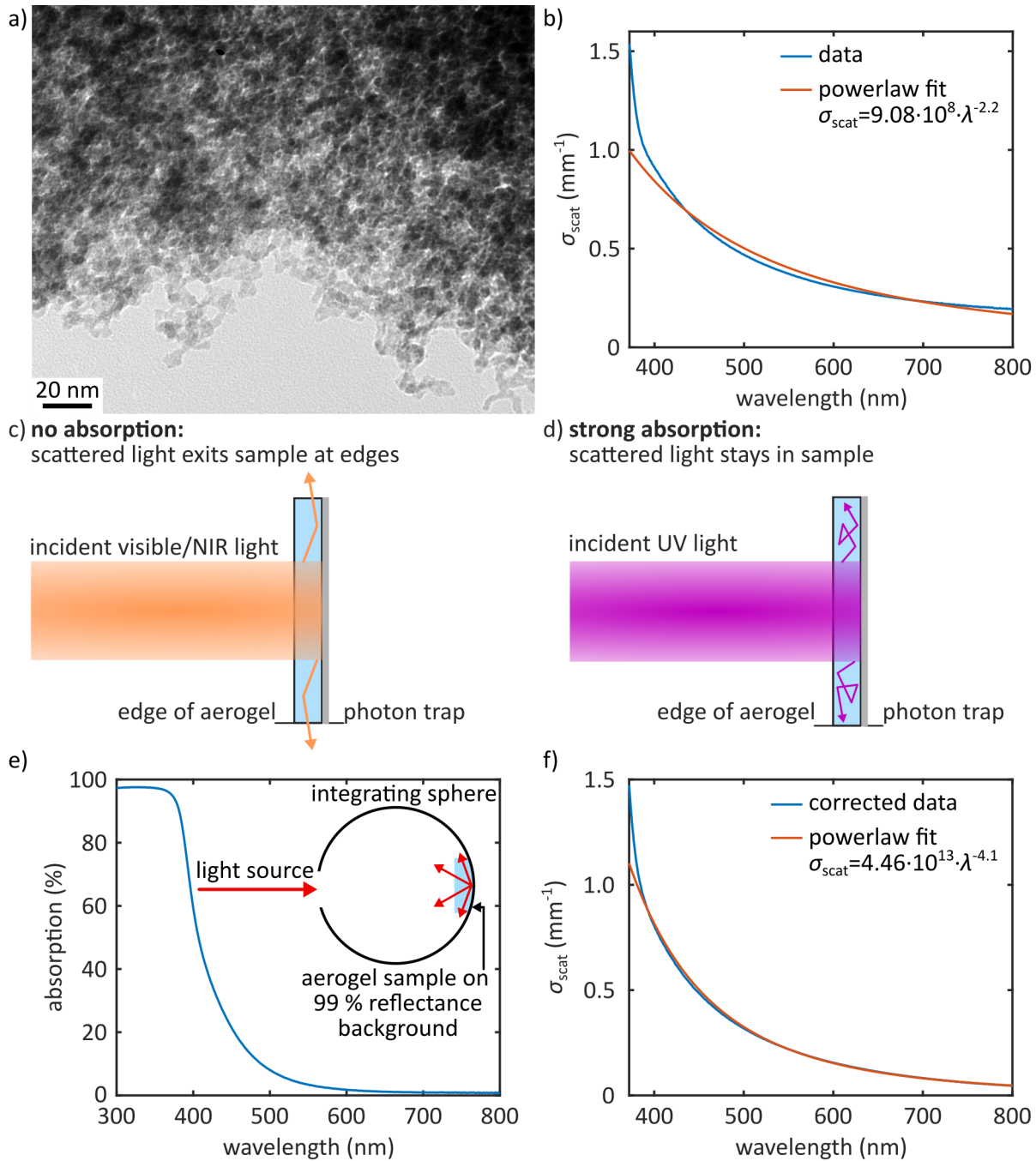


Figure 6.16: a) TEM image of a TiO_2 aerogel showing particle chains and pores with feature sizes in a range of 4 to 20 nm, which match well with the mean Rayleigh scattering center size of 14 nm according to equation 6.9. b) Scattering coefficient σ_{scat} plotted versus wavelength λ . Fitting the data with a power law yields a wavelength dependence of $\lambda^{-2.2}$ which rather indicates Mie than Rayleigh scattering. Besides, we see that the fit best describes the data in the visible range. We address the discrepancy with the expected λ^{-4} dependence to the 2 % reflectance of the photon trap, which is needed to mount the aerogel in the integrating sphere, and to the finite dimension of the sample, which allows light to exit the sample at the edges and leads to an overvalued reflectance. We believe that this artefact is pronounced in the visible part of the spectrum because of strong light absorption in the UV range, as indicated in c-d). e) Absorption spectrum of the TiO_2 aerogel. f) After correcting the reflectance by the absorption spectrum according to equation 6.10, the scattering coefficient shows a better agreement with a power law fit than the uncorrected data, and the $\lambda^{-4.1}$ relation indicates presence of Rayleigh scattering.

Refractive Index Approximation and Specular Reflectance

The aerogel's refractive index n_{aero} is approximated according to the Maxwell Garnett effective medium theory as

$$n_{\text{aero}} = n_{\text{TiO}_2} \left(1 + 3c_{\text{vol}} \frac{n_{\text{air}} - n_{\text{TiO}_2}}{n_{\text{air}} + 2n_{\text{TiO}_2} - c_{\text{vol}}(n_{\text{air}} - n_{\text{TiO}_2})} \right) \quad (6.12)$$

where the effective medium consists of air as a matrix medium with refractive index $n_{\text{air}} = 1.0$ and TiO_2 nanoparticles as inclusions with refractive index n_{TiO_2} in the range of 2.4 and 3.49 and a volume fraction of $c_{\text{vol}} = 0.05$.^[60,61] We derived the volume fraction c_{vol} from gravimetric density measurements. From these considerations and using the Maxwell Garnett mixing rule, we obtain an effective refractive index of $n_{\text{aero}} = 1.05$ to 1.07 .

The specular reflectance due to a change in refractive index can be described by Fresnel equations. The reflectance for s-polarized light is

$$R_s = \left| \frac{n_{\text{aero}} \cos \theta_i - n_{\text{air}} \sqrt{1 - \left(\frac{n_{\text{aero}}}{n_{\text{air}}} \sin \theta_i\right)^2}}{n_{\text{aero}} \cos \theta_i + n_{\text{air}} \sqrt{1 - \left(\frac{n_{\text{aero}}}{n_{\text{air}}} \sin \theta_i\right)^2}} \right|^2 \quad (6.13)$$

and the reflectance for p-polarized light is

$$R_p = \left| \frac{-n_{\text{air}} \cos \theta_i + n_{\text{aero}} \sqrt{1 - \left(\frac{n_{\text{aero}}}{n_{\text{air}}} \sin \theta_i\right)^2}}{n_{\text{air}} \cos \theta_i + n_{\text{aero}} \sqrt{1 - \left(\frac{n_{\text{aero}}}{n_{\text{air}}} \sin \theta_i\right)^2}} \right|^2 \quad (6.14)$$

where θ_i is the incident angle of light. Assuming an equal amount of power in the s and p polarizations, the effective reflectivity of the material is the average of both polarized reflectance $R_{\text{eff}} = \frac{1}{2}(R_s + R_p)$. For normal incident $\theta_i = 0^\circ$ there is no distinction between polarization and the reflectance simplifies to $R = \left| \frac{n_{\text{aero}} - n_{\text{air}}}{n_{\text{aero}} + n_{\text{air}}} \right|^2$. With an effective refractive index in the range of 1.05 to 1.07 we derive a negligible specular reflectance of 0.059% to 0.1%, which we approximate as 0% in all optical calculations.

6.6.2 Mass Transport Considerations

Aerogels are macroscopic, nanoporous objects with large specific surface areas that offer a huge number of catalytic active sites. In chapter 6.3 we showed that 3D structuring reduces the pressure drop by five orders of magnitude compared to an unstructured aerogel. Moreover, we discussed that the gas flow no longer penetrates the nanoporous aerogel, but rather flows around the filaments of the 3D microstructure. As a result, the gas needs to diffuse from the microscopic channels into the aerogel to interact with the catalyst. In the following section, we estimate whether the photocatalytic reaction within the aerogel is diffusion-limited and whether the full surface area of the aerogel still participates in the catalytic process.

Effective Use of Catalyst – Balance of Diffusion and Reaction Rate

Depending on reaction kinetics, reactants might not be able to reach the extensive number of catalytic active sites within the highly porous aerogel. If the chemical reactions proceed very rapidly, the concentration of reactants already diminishes close to the boundary layer and most of the internal catalyst surface area is unused. For slow kinetics, the concentration of reactants is high throughout the whole pore volume and the entire catalyst participates at the reaction with the same rate. The effective use of the catalytic active sites is described by the effectiveness factor η ranging from 0 to 1 and is defined as:

$$\eta = \frac{\text{actual rate of process}}{\text{rate of process if diffusion were infinitively fast}}. \quad (6.15)$$

The effectiveness factor η of a catalyst is generally measured by the Thiele modulus ϕ which accounts for the competition of chemical reactions at the surface of the nanoparticle and diffusive mass transport of the reactant through the porous catalyst. The exact mathematical expression of the Thiele modulus depends on the geometry of the catalyst but is typically computed by the ratio between the reaction and diffusion time scales.^[54] The equation for a cylindrical catalyst, which approximates the shape of an individual filament in our 3D printed aerogel, is given as:^[62]

$$\phi = \frac{d}{4} \sqrt{\frac{k_r}{D_{\text{eff}}}} \quad (6.16)$$

where d is the diameter of the cylinder, k_r is the 1st order reaction rate constant, and D_{eff} is the effective diffusion coefficient. The effectiveness factor η can be expressed as a function of the Thiele modulus ϕ , as shown in Figure 6.17.

In the following sections we derive an effective diffusion coefficient and estimate a 1st order reaction constant. Both quantities allow us to approximate the Thiele modulus according to equation 6.16 for a filament diameter of 200 μm . Comparing this value with the data in Figure 6.17 allows us to estimate the effectiveness of the 3D printed aerogel.

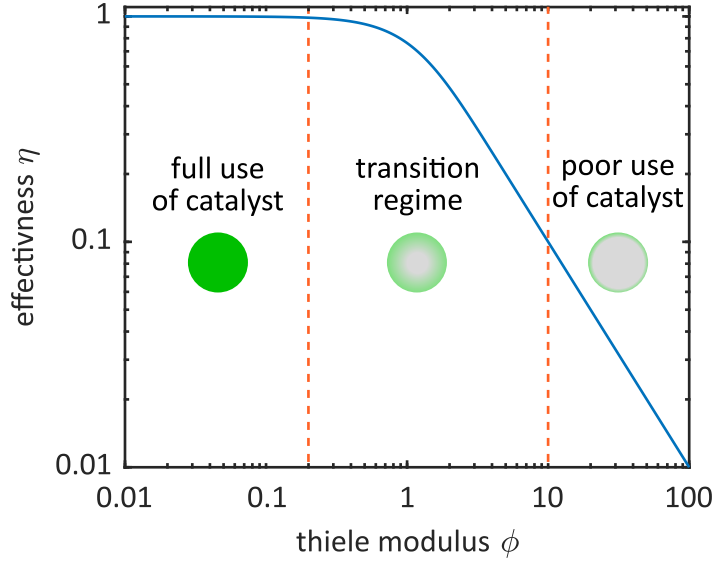


Figure 6.17: Effectiveness factor η as a function of Thiele modulus ϕ ($\eta = \tanh(\phi)/\phi$). For a Thiele modulus $\phi \gg 1$, the effectiveness factor decreases and only a small fraction of the catalyst is effectively used during the reaction. For a Thiele modulus $\phi \ll 1$, the effectiveness factor approaches 1, which indicates a full use of the catalyst.

Diffusion Coefficient

The type of diffusion is controlled via the pore size and can be estimated by the Knudsen number Kn which is given as:

$$Kn = \frac{\ell}{d_p} \quad (6.17)$$

where ℓ is the mean free path of the gas molecule and d_p is the pore diameter.

For $Kn \gg 1$ molecule-solid collisions occur much more frequently than molecule-molecule collisions. Thus, the diffusivity can be described by Knudsen diffusivity $D_{k,0}$ where gas molecules are confined within a straight cylindrical pore of diameter d_p :

$$D_{k,0} = \frac{1}{3} \bar{u}_t d_p. \quad (6.18)$$

Here, $\bar{u}_t = \sqrt{\frac{8RT}{\pi M}}$ is the mean thermal velocity at temperature T , R is the gas constant and M is the molar mass of the gas molecule. For $Kn \ll 1$ molecule-molecule collisions dominate and the diffusivity can be described by the molecular diffusivity in an unconstrained gas volume $D_{g,0}$. For $1 \leq Kn \leq 10$ both processes contribute to the diffusion process and the overall diffusivity D_0 can be approximated using the Bosanquet-formula:^[63]

$$\frac{1}{D_0} = \frac{1}{D_{k,0}} + \frac{1}{D_{g,0}}. \quad (6.19)$$

To correct for the increased molecular trajectories in the highly porous aerogel structure and for the fact that the geometric area normal to the direction of flux is partly occupied by nanoparticles, an effective diffusivity D_{eff} can be approximated by taking the tortuosity τ and porosity ϵ_p of the aerogel into account:^[64–66]

$$D_{\text{eff}} = \frac{\epsilon_p}{\tau} D_0. \quad (6.20)$$

For the TiO_2 aerogel with a mean pore diameter of 20 nm we estimate Kn following equation 6.17 as $Kn = 3.4$ which validates the use of equation 6.19 for the calculation of D_0 . We calculate D_{eff} according to equation 6.20 as $1.8 \cdot 10^{-6} \text{ m}^2 \text{ s}^{-1}$. We list all relevant parameters in Table 6.4.

Table 6.4: Used parameters for the estimation of H_2O vapor diffusion at 25°C .

parameter	value
effective diffusivity D_{eff}	$1.8 \cdot 10^{-6} \text{ m}^2 \text{ s}^{-1}$
reference diffusivity D_0	$3.8 \cdot 10^{-6} \text{ m}^2 \text{ s}^{-1}$
reference Knudsen diffusivity $D_{k,0}$	$3.9 \cdot 10^{-6} \text{ m}^2 \text{ s}^{-1}$
reference gas diffusivity $D_{g,0}$ ^[67]	$8.4 \cdot 10^{-5} \text{ m}^2 \text{ s}^{-1}$
tortuosity τ	2
porosity ϵ_p	0.95
pore diameter d_p	20 nm
mean free path of H_2O vapor ℓ	67 nm
temperature T	298 K
molar mass of H_2O $M_{\text{H}_2\text{O}}$	18 g mol^{-1}

Estimating the Effective Catalyst Use

To estimate the Thiele modulus in equation 6.16, we use the calculated diffusion coefficient of $1.8 \cdot 10^{-6} \text{ m}^2 \text{ s}^{-1}$ and reaction constants reported in literature and listed in Table 6.5. The kinetics of heterogenous photocatalysis are generally considered slow.^[34] Since photocatalytic activities are mainly reported as amount of detected hydrogen and apparent quantum efficiency, references for experimentally defined reaction constants on TiO_2 are scarce.^[68] As a result, we also use reaction constants for photocatalytic dissociation of individual methanol or water molecules on TiO_2 obtained by scanning tunneling microscopy, and reaction rates for hydrogen evolution from metal-loaded TiO_2 nanoparticles and for dye degradation to estimate the Thiele modulus of the TiO_2 aerogel. Since dye degradation has a thermodynamically much larger driving force and smaller kinetic barrier than hydrogen evolution reactions,^[69] they feature a good benchmark to estimate potential diffusion limitations due to the higher intrinsic reaction rate. Nevertheless, even for the highest reported constant of $2.0 \cdot 10^{-2} \text{ s}^{-1}$, we estimate a Thiele Modulus of $6.6 \cdot 10^{-3}$ for a filament diameter of 200 μm . Figure 6.17 illustrates that for such a Thiele Modulus an effectiveness of 1 is expected. Thus, we assume that the whole catalyst is utilized during the reaction and no internal diffusion limitations take place. We estimate that a drastically higher reaction constant of about $4.3 \cdot 10^4 \text{ s}^{-1}$ is needed to reach the diffusion-limited region in Figure 6.17. The estimation is in line with experimental observation where an fcc-

structured and unstructured TiO₂ aerogel of similar light absorption show comparable catalytic activity (Figure 6.7).

Table 6.5: Overview of reaction constant k_r reported in literature for water and methanol photodissociation, dye degradation on TiO₂ nanoparticles and H₂ evolution on Pt/TiO₂, Pd/TiO₂, and Rh/TiO₂ nanoparticles.

surface coverage θ	reaction constant k_r (s ⁻¹)	note
0.35	$5 \cdot 10^{-6}$	Water photodissociation on TiO ₂ (110) surface at 80 K in ultrahigh vacuum ^[70,71]
0.11 to 0.01	$6 \cdot 10^{-3}$ to $2.0 \cdot 10^{-2}$	Methanol photodissociation on TiO ₂ (110) surface at 80 K in ultrahigh vacuum ^[71]
not specified	$2 \cdot 10^{-5}$ to $3 \cdot 10^{-3}$	Photocatalytic H ₂ evolution in aqueous solutions containing amines as sacrificial agents on Pt/TiO ₂ nanoparticles ^[72]
not specified	$6.4 \cdot 10^{-5}$ to $14 \cdot 10^{-5}$	Photocatalytic H ₂ evolution in gas phase on NaOH-coated Pt/TiO ₂ ^[73]
not specified	$8.9 \cdot 10^{-5}$ to $50 \cdot 10^{-5}$	Photocatalytic H ₂ evolution in gas phase on NaOH-coated Pd/TiO ₂ ^[73]
not specified	$5.6 \cdot 10^{-5}$ to $8.3 \cdot 10^{-5}$	Photocatalytic H ₂ evolution in gas phase on NaOH-coated Rh/TiO ₂ ^[73]
not specified	$2.4 \cdot 10^{-4}$	Methyl orange dye degradation on TiO ₂ nanoparticles in solution ^[74]
not specified	$1.4 \cdot 10^{-4}$	Methyl blue dye degradation on TiO ₂ nanoparticles in solution ^[75]

6.6.3 Computational Fluid Dynamics

The flow through a nanoporous medium can either be laminar or turbulent. The type of flow can be estimated by Reynold's number

$$Re_{np} = \frac{d_p \rho v}{\eta} = \frac{d_p \rho Q}{\eta \epsilon_p A} \quad (6.21)$$

where d_p is the pore diameter, ρ is the fluid density, v is the fluid velocity, η is the dynamic fluid viscosity, Q is the volumetric flow rate, ϵ_p is the porosity, and A is the cross-sectional area of the sample. Since $Re_{np} \ll 1$ for all flow rates studied, the flow is laminar.^[76] As a result, the pressure drop ΔP through a nanoporous medium can be described by Darcy's law and the simplest form for laminar flow is given as

$$\frac{\Delta P}{t} = \eta \frac{v}{k} = \eta \frac{Q}{kA} \quad (6.22)$$

where t and k are the thickness and permeability of the sample, respectively. We estimate the permeability k from a universal law for aerogels

$$k = 1.32 \cdot 10^{-13} d_p^{1.41} \quad (6.23)$$

where d_p is the mean pore diameter in nm and k is given in cm^2 .^[31] All variables for the calculation of the pressure drop according to equation 6.22 are listed in Table 6.6.

For the 3D structured aerogel, the fluid exclusively flows through the microchannels of width w due to the large pressure drop through the nanoporous medium. We derive a Reynolds numbers $Re_{ch} = \rho v / \eta \ll 2000$ for the flow rates studied in our experiment. Thus, the flow in the microchannels is purely laminar. We use the '*Free and Porous Media*' interface in COMSOL to solve the laminar, incompressible, fluid flow in a small section of the structured aerogel. For computing reasons, we reduce the geometry from 1444 to 49 and 81 channels for the fcc- and sc-structured aerogel, respectively. The calculations were performed for volumetric flow rates of 2, 4, 6, and 8 mL min^{-1} to match with the flow rate per channel in the experimental conditions. We applied a zero-pressure boundary at the outlet and no-slip conditions at the walls. The pressure drop was determined by taking the average pressure in planes orthogonal to the flow direction at the inlet and outlet of the sample. Computations were performed for three different meshes with 2.1, 2.4, and 5.2 million elements, respectively. The pressure drop calculations on the three meshes varied by less than 1.3 %, which verifies mesh-independence of the computed solution. The experimental pressure drop of the fcc-structured aerogel can be best described with a sample of 240 μm channel width. This is in good agreement with the median channel width of 210 μm obtained from an optical microscope image shown in Figure 6.18, considering that the simulated structure is an idealized, simplified geometry of the actual sample.

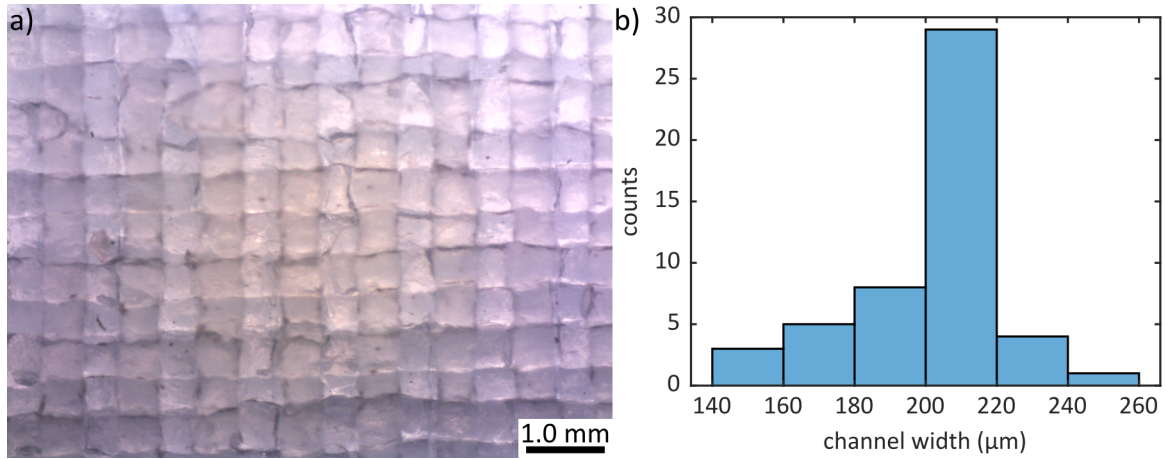


Figure 6.18: a) Optical micrograph and b) derived channel widths of the sample that was used to perform pressure drop measurements.

Table 6.6: List of variables used for the calculation of the Reynolds number Re_{np} , the pressure drop $\Delta P/t$, and the permeability k according to equations 6.21-6.23.

variable	quantity
pore diameter d_p	20 nm
fluid density ρ	1.25 kg m^{-3}
dynamic fluid viscosity η	$1.74 \cdot 10^{-5} \text{ Pa s}^{-1}$
volumetric flow rate Q	20 to 200 mL min^{-1}
porosity ϵ_p	0.95
cross-sectional area A	225 mm^2
sample thickness t	1 mm
permeability k	$9 \cdot 10^{12} \text{ cm}^2$

6.7 Acknowledgment

This work was supported by the Cluster of Excellence 'CUI: Advanced Imaging of Matter' of the Deutsche Forschungsgemeinschaft (DFG) – EXC 2056 – project ID 390715994, by GRK 2536 NANOHYBRID of the DFG, and by the Bundesministerium für Bildung und Forschung (BMBF) via project LUCENT (grant no. 05K19WMA). The authors thank Marvin Skiba for performing ICP-MS measurements, Sandra König for N₂ physisorption measurements, Sarah-Alexandra Hussak for support in scanning electron microscopy imaging, and the PHYSnet Computing Center for computing capacity. M.R. thanks Sönke Wengler-Rust for UV-vis training, Prof. Dr. Horst Weller for providing lab access, and Qianqian Fang for technical support during the MMCLAB implementation. M.J. thanks Martin Stieben and Bodo Krause-Kyora for technical support regarding calculations on the computing cluster.

6.8 Data Availability

The data that support the findings of this study are openly available in the zenodo repository at <http://doi.org/10.5281/zenodo.7018488>.^[77]

Bibliography

- [1] N. S. Lewis and D. G. Nocera, *Proc. Natl. Acad. Sci.*, 2006, **103**, 15729–15735.
- [2] F. E. Osterloh, *Chem. Mater.*, 2008, **20**, 35–54.
- [3] M. Hambourger, G. F. Moore, D. M. Kramer, D. Gust, A. L. Moore and T. A. Moore, *Chem. Soc. Rev.*, 2009, **38**, 25–35.
- [4] Y. Ma, X. Wang, Y. Jia, X. Chen, H. Han and C. Li, *Chem. Rev.*, 2014, **114**, 9987–10043.
- [5] R. Asahi, T. Morikawa, H. Irie and T. Ohwaki, *Chem. Rev.*, 2014, **114**, 9824–9852.
- [6] H. M. Chen, C. K. Chen, R.-S. Liu, L. Zhang, J. Zhang and D. P. Wilkinson, *Chem. Soc. Rev.*, 2012, **41**, 5654–5671.
- [7] J. Pan, G. Liu, G. Q. Lu and H.-M. Cheng, *Angew. Chem. Int. Ed.*, 2011, **50**, 2133–2137.
- [8] X. Chen, S. Shen, L. Guo and S. S. Mao, *Chem. Rev.*, 2010, **110**, 6503–6570.
- [9] M. Rebber, C. Willa and D. Koziej, *Nanoscale Horiz.*, 2020, **5**, 431–453.
- [10] G. Ozin and P. Kant, *Will industrial-scale photocatalysis see the light of day?*, 2021, <https://www.advancedsciencenews.com/will-industrial-scale-photocatalysis-see-the-light-of-day/>, accessed on 16.05.2022.
- [11] A. Zhakeyev, P. Wang, L. Zhang, W. Shu, H. Wang and J. Xuan, *Adv. Sci.*, 2017, **4**, 1700187.
- [12] F. Matter and M. Niederberger, *Adv. Sci.*, 2022, **9**, 2105363.
- [13] P. Wang, J. Xuan, R. Zhang, H. Zhang, Q. Wang, H. Wang, H. Liu and L. Zhang, *Adv. Mater. Technol.*, 2022, **7**, 2100672.
- [14] H. Zhou, X. Li, T. Fan, F. E. Osterloh, J. Ding, E. M. Sabio, D. Zhang and Q. Guo, *Adv. Mater.*, 2010, **22**, 951–956.
- [15] E. H. DeLucia, K. Nelson, T. C. Vogelmann and W. K. Smith, *Plant, Cell & Environment*, 1996, **19**, 159–170.
- [16] E. Shimoni, O. Rav-Hon, I. Ohad, V. Brumfeld and Z. Reich, *Plant Cell*, 2005, **17**, 2580–2586.
- [17] W. L. Chameides and D. D. Davis, *J. Geophys. Res. Oceans*, 1982, **87**, 4863–4877.
- [18] R. Pieruschka, A. Chavarría-Krauser, K. Cloos, H. Scharr, U. Schurr and S. Jahnke, *New Phytol*, 2008, **178**, 335–347.
- [19] D. F. Parkhurst, *New Phytol*, 1994, **126**, 449–479.
- [20] X. Li, T. Fan, H. Zhou, S.-K. Chow, W. Zhang, D. Zhang, Q. Guo and H. Ogawa, *Adv. Funct. Mater.*, 2009, **19**, 45–56.
- [21] Y. Li, Z.-Y. Fu and B.-L. Su, *Adv. Funct. Mater.*, 2012, **22**, 4634–4667.
- [22] D. Fattakhova-Rohlfing, A. Zaleska and T. Bein, *Chem. Rev.*, 2014, **114**, 9487–9558.

- [23] Q. Zhang, T. P. Chou, B. Russo, S. A. Jenekhe and G. Cao, *Adv. Funct. Mater.*, 2008, **18**, 1654–1660.
- [24] Q. Zhang, T. Chou, B. Russo, S. Jenekhe and G. Cao, *Angew. Chem. Int. Ed.*, 2008, **47**, 2402–2406.
- [25] J. Y. Y. Loh, A. Mohan, A. G. Flood, G. A. Ozin and N. P. Kherani, *Nat. Commun.*, 2021, **12**, 402.
- [26] Z. He and W. Que, *Phys. Chem. Chem. Phys.*, 2013, **15**, 16768–16773.
- [27] G. Prieto, H. Tüysüz, N. Duyckaerts, J. Knossalla, G.-H. Wang and F. Schüth, *Chem. Rev.*, 2016, **116**, 14056–14119.
- [28] W. Wan, R. Zhang, M. Ma and Y. Zhou, *J. Mater. Chem. A*, 2018, **6**, 754–775.
- [29] A. L. Luna, S. Papadopoulos, T. Kyburz, E. Tervoort, L. Novotny and M. Niederberger, *J. Mater. Chem. A*, 2021, **9**, 22380–22391.
- [30] J. Phalippou, G. W. Scherer, T. Woignier, D. Bourret and R. Sempéré, *Journal of Non-Crystalline Solids*, 1995, **186**, 64–72.
- [31] F. M. Kong, J. D. LeMay, S. S. Hulsey, C. T. Alviso and R. W. Pekala, *J. Mater. Res.*, 1993, **8**, 3100–3105.
- [32] S. Q. Zeng, A. Hunt and R. Greif, *Journal of Non-Crystalline Solids*, 1995, **186**, 264–270.
- [33] C. Zhu, Z. Qi, V. A. Beck, M. Luneau, J. Lattimer, W. Chen, M. A. Worsley, J. Ye, E. B. Duoss, C. M. Spadaccini, C. M. Friend and J. Biener, *Science Advances*, 2018, **4**, eaas9459.
- [34] D. Friedmann, A. F. Lee, K. Wilson, R. Jalili and R. A. Caruso, *J. Mater. Chem. A*, 2019, **7**, 10858–10878.
- [35] A. Elkoro, L. Soler, J. Llorca and I. Casanova, *Appl. Mater. Today*, 2019, **16**, 265–272.
- [36] L. Chen, X. Tang, P. Xie, J. Xu, Z. Chen, Z. Cai, P. He, H. Zhou, D. Zhang and T. Fan, *Chem. Mater.*, 2018, **30**, 799–806.
- [37] M. Rebber, M. Trommler, I. Lokteva, S. Ehteram, A. Schropp, S. König, M. Fröba and D. Koziej, *Adv. Funct. Mater.*, 2022, **32**, 2112914.
- [38] L. Zhao, S. Yang, B. Bhatia, E. Strobach and E. N. Wang, *AIP Adv.*, 2016, **6**, 025123.
- [39] K. S. F. W. Jousten, *Handbuch Vakuumtechnik*, Springer Fachmedien Wiesbaden, 2018.
- [40] T. Kotsokechagia, F. Cellési, A. Thomas, M. Niederberger and N. Tirelli, *Langmuir*, 2008, **24**, 6988–6997.
- [41] L. M. Rossi, J. L. Fiorio, M. A. S. Garcia and C. P. Ferraz, *Dalton Trans.*, 2018, **47**, 5889–5915.
- [42] A. Caravaca, H. Daly, M. Smith, A. Mills, S. Chansai and C. Hardacre, *React. Chem. Eng.*, 2016, **1**, 649–657.
- [43] C. A. Walenta, C. Courtois, S. L. Kollmannsberger, M. Eder, M. Tschurl and U. Heiz, *ACS Catal.*, 2020, **10**, 4080–4091.
- [44] K. R. Phillips, S. C. Jensen, M. Baron, S.-C. Li and C. M. Friend, *J. Am. Chem. Soc.*, 2013, **135**, 574–577.
- [45] M. Borges Ordoño and A. Urakawa, *J. Phys. Chem. C*, 2019, **123**, 4140–4147.
- [46] A. Bazzo and A. Urakawa, *ChemSusChem*, 2013, **6**, 2095–2102.

- [47] G. L. Chiarello, D. Ferri and E. Selli, *J. Catal.*, 2011, **280**, 168–177.
- [48] J. B. Joo, R. Dillon, I. Lee, Y. Yin, C. J. Bardeen and F. Zaera, *Proc. Natl. Acad. Sci.*, 2014, **111**, 7942–7947.
- [49] D. R. Rolison, J. J. Pietron, E. R. Glaser, T. H. Brintlinger, J. P. Yesinowski, P. A. DeSario, J. S. Melinger, A. D. Dunkelberger, J. B. Miller, C. L. Pitman, J. C. Owrutsky, R. M. Stroud and M. D. Johannes, *ACS Appl. Mater. Interfaces*, 2020, **12**, 41277–41287.
- [50] A. L. Luna, F. Matter, M. Schreck, J. Wohlwend, E. Tervoort, C. Colbeau-Justin and M. Niederberger, *Appl. Catal., B*, 2020, **267**, 118660.
- [51] Q. Fang and D. A. Boas, 2009 IEEE International Symposium on Biomedical Imaging: From Nano to Macro, 2009, pp. 1142–1145.
- [52] Q. Fang, *Biomed. Opt. Express*, 2010, **1**, 165–175.
- [53] A. Liu and B. Joe, *BIT Numerical Mathematics*, 1994, **34**, 268–287.
- [54] A. Visan, J. R. van Ommen, M. T. Kreutzer and R. G. H. Lammertink, *Ind. Eng. Chem. Res.*, 2019, **58**, 5349–5357.
- [55] K. Stamnes, S. C. Tsay, W. Wiscombe and K. Jayaweera, *Appl. Opt.*, 1988, **27**, 2502–2509.
- [56] T. Radhakrishnan, *Proceedings of the Indian Academy of Sciences - Section A*, 1952, **35**, 117.
- [57] D. J. Lockwood, in *Rayleigh and Mie Scattering*, ed. M. R. Luo, Springer New York, New York, NY, 2016, pp. 1097–1107.
- [58] Y. Du, X. Zhang, J. Wang, Z. Liu, K. Zhang, X. Ji, Y. You and X. Zhang, *ACS Nano*, 2020, **14**, 11919–11928.
- [59] H. C. Hulst and H. C. van de Hulst, *Light scattering by small particles*, Courier Corporation, 1981.
- [60] S. Sarkar, V. Gupta, M. Kumar, J. Schubert, P. T. Probst, J. Joseph and T. A. F. König, *ACS Appl. Mater. Interfaces*, 2019, **11**, 13752–13760.
- [61] M. W. Ribarsky, in *Titanium Dioxide (TiO₂) (Rutile)*, ed. E. D. Palik, Academic Press, Boston, 1985, pp. 795–804.
- [62] M. Hartmann, A. G. Machoke and W. Schwieger, *Chem. Soc. Rev.*, 2016, **45**, 3313–3330.
- [63] R. Mueller, S. Zhang, M. Klink, M. Bäumer and S. Vasenkov, *Phys. Chem. Chem. Phys.*, 2015, **17**, 27481–27487.
- [64] I. Sahin, Y. Ozbakir, Z. Inonu, Z. Ulker and C. Erkey, *Prog Coll Pol Sci S*, 2017, **4**, 3.
- [65] A. Visan, D. Rafeian, W. Ogieglo and R. G. H. Lammertink, *Appl. Catal., B*, 2014, **150–151**, 93–100.
- [66] G. F. Froment, *Chemical reactor analysis and design*, Wiley, 3rd edn., 2011.
- [67] C. V. Paganelli and F. K. Kurata, *Respiration Physiology*, 1977, **30**, 15–26.
- [68] T. Hisatomi, K. Takanabe and K. Domen, *Catal. Lett.*, 2015, **145**, 95–108.
- [69] T. Zhang and W. Lin, *Chem. Soc. Rev.*, 2014, **43**, 5982–5993.
- [70] S. Tan, H. Feng, Y. Ji, Y. Wang, J. Zhao, A. Zhao, B. Wang, Y. Luo, J. Yang and J. G. Hou, *J. Am. Chem. Soc.*, 2012, **134**, 9978–9985.
- [71] H. Feng, S. Tan, H. Tang, Q. Zheng, Y. Shi, X. Cui, X. Shao, A. Zhao, J. Zhao and B. Wang,

- J. Phys. Chem. C*, 2016, **120**, 5503–5514.
- [72] M. Yasuda, T. Tomo, S. Hirata, T. Shiragami and T. Matsumoto, *Catalysts*, 2014, **4**, 162–173.
- [73] K. Yamaguti and S. Sato, *Journal of the Chemical Society, Faraday Transactions 1: Physical Chemistry in Condensed Phases*, 1985, **81**, 1237–1246.
- [74] L. Xu, D. Zhang, L. Ming, Y. Jiao and F. Chen, *Phys. Chem. Chem. Phys.*, 2014, **16**, 19358–19364.
- [75] Z. Liu, H. Zheng, H. Yang, L. Hao, L. Wen, T. Xu and S. Wu, *RSC Adv.*, 2016, **6**, 54215–54225.
- [76] D. A. Nield and A. Bejan, *Convection in porous media*, Springer, 2013, vol. 4.
- [77] M. Rebber, H. Sannemüller, M. Jaruszewski, D. Pfannkuche, A. Urakawa and D. Koziej, Raw data for 'Nature-inspired 3D structuring of TiO₂ and Au/TiO₂ aerogels enables scalable photocatalytic hydrogen production', Zenodo <https://doi.org/10.5281/zenodo.7018488>, 2022.

7 Further Prospects of 3D Printed Aerogels

This chapter summarizes preliminary results of the 3D printing in a supportive gel, the alignment of AuNRs during extrusion, and the photocatalytic CO₂ reduction, and indicates their relevance for future applications.

7.1 3D Printing in a Supportive Gel

Even though complex geometries can be fabricated by 3D printing *gelled nanoinks* in a liquid bath charged with ammonia as presented in chapter 5, gravity still limits the extent of overhangs in the self-supporting printed structure. To increase the degree of complexity even further, the print can be physically supported by a strong, supportive gel matrix which allows the ink to be printed with the nozzle following a 3D trajectory, instead of being deposited in a layer-by-layer stacking sequence. The matrix material is based on Laponite, which is a layered lithium sodium magnesium silicate ($\text{Na}_{0.7}\text{Si}_8\text{Mg}_{5.5}\text{Li}_{0.3}\text{O}_{20}(\text{OH})_4$) with a layer thickness of approximately 1 nm and a particle diameter of 25 nm. In aqueous solutions, the disk-like Laponite particles gel by forming a stable house of card structure.^[1] The Laponite is dispersed in a water/acetonitrile (ACN) mixture of a 2 : 1 volumetric ratio to match the solvent composition of the ink and the pH value is adjusted to 11 to solidify the ink in a similar way as the ammonia charged liquid bath. Since the printed geometry is no longer limited to a layer-by-layer stacking, a direct contact to the build plate is no longer required and the printed TiO₂ gel floats in the Laponite matrix after extrusion (Figure 7.1a). The challenge of the embedded 3D printing approach is the removal of Laponite after the print has finished. After solidifying the TiO₂ gel at high pH, Laponite was dissolved by lowering the pH to a value of 2. Following solvent exchange and supercritical drying, we obtain a 3D printed TiO₂ aerogel as shown in Figure 7.1b, but the aerogel appears rather opaque and is not as translucent as an aerogel printed with the liquid bath approach. Further analysis with scanning electron microscopy reveals that the aerogel is coated with a rough, flake-like material (Figure 7.1.c) which we address to residues of Laponite due to the presence of magnesium and silicon lines at 1.25 and 1.74 keV in the energy dispersive X-ray spectrum, respectively (Figure 7.1.d). These residues persist despite extensive washing at low pH during the Laponite removal process. If the reduced transparency and the presence of Laponite residues on the aerogel are not detrimental for its application, highly sophisticated geometries could be fabricated following the embedded 3D printing approach. However, since aerogels are applied as a photocatalyst, a translucent characteristic and a clean aerogel surface are fundamental. As a result, the embedded printing approach was not further investigated in this thesis, but could still enable other applications besides sophisticated geometries such as the realization of a *printing-then-solidification* scheme, or the fabrication of *flexible aerogels* as

described below.

Printing-then-solidification: In a supportive gel matrix, solidification of the ink can take place much later than the actual printing process. Therefore, the yield stress of the ink does not need to fulfill a self-supporting characteristic and aerogel inks with much lower particle concentration and higher porosity could be formulated. Besides, external magnetic, electric, or acoustic fields could be applied to manipulate the position and orientation of nanomaterials incorporated in low-viscosity TiO₂ inks.^[2] With a subsequent solidification, which might be induced by a change of pH or temperature, 3D aerogels with structured nanomaterials and anisotropic properties could be obtained.

Flexible aerogels: For embedded 3D printing extrusion through thin nozzles becomes easier compared to layer-by-layer printing in a liquid bath, because a calibration with a build plate is no longer needed. Besides higher printing resolution, thin nozzles might enable the fabrication of flexible aerogels. Flexibility is an atypical mechanical property for metal oxide aerogels, since they exhibit high strength-to-weight ratios and a brittle characteristic with a low fracture toughness similar as glass. Although no flexibility was achieved for aerogel fiber diameters as low as 150 μm , flexibility might be induced and tuned by using nozzle sizes in the low micrometer or nanometer range.^[3] Thus, printing with different nozzle sizes could be used to program flexibility and rigidity in 3D to create aerogels with anisotropic mechanical properties. Moreover, elasticity of thin aerogel fibers could lead to aerogel 4D printing where the printed object deforms post-printing due to the exposure to an external stimulus.^[4]

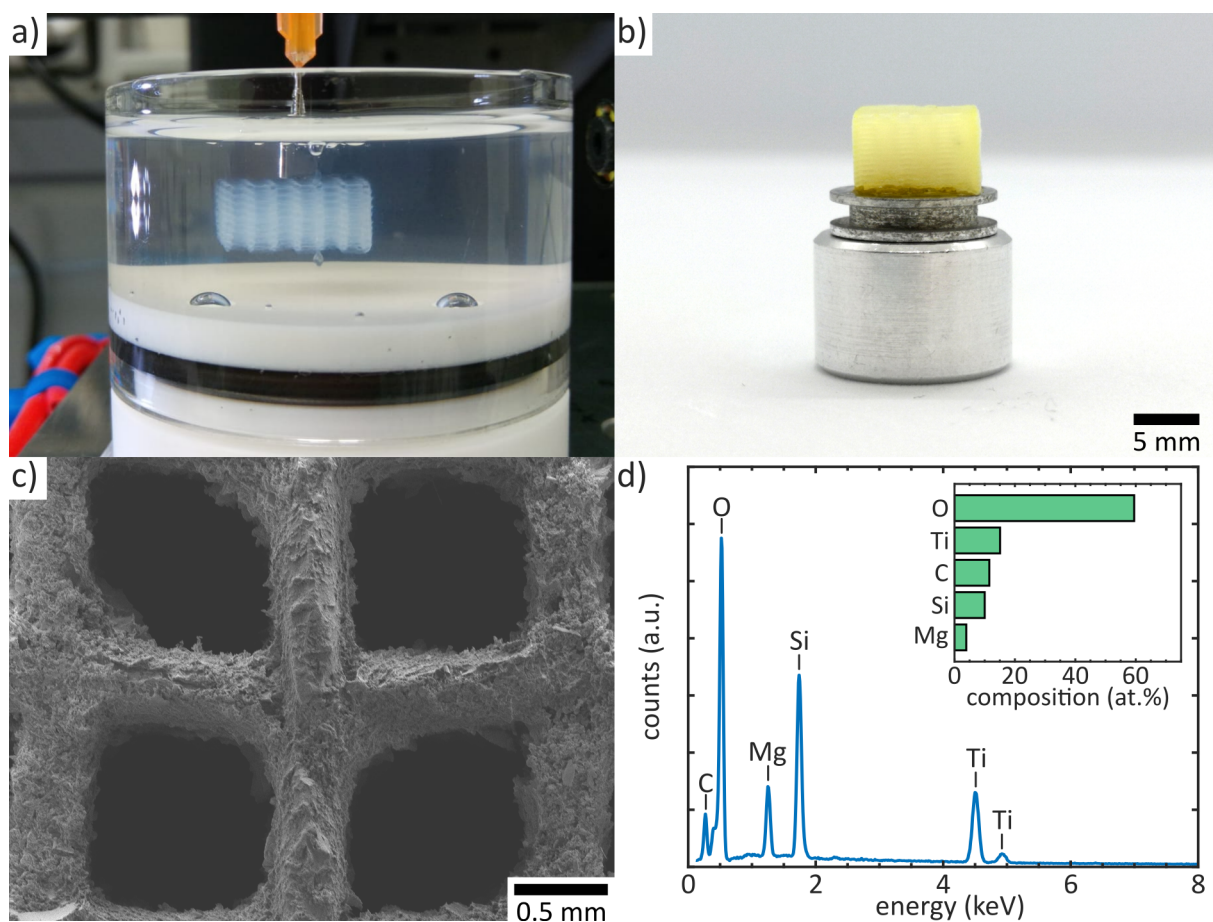


Figure 7.1: Embedded 3D printing of a TiO₂ nanoparticle-based aerogel. a) Photograph of the 3D printing process. The cylindrical container is charged with a Laponite gel, which was prepared by dispersing Laponite powder in a water/ACN mixture (2:1 volumetric ratio, pH=11). b) Photograph of the TiO₂ aerogel after removing Laponite in a HCl_(aq)/ACN mixture (2:1 volumetric ratio, pH=2) and supercritical drying. c) Scanning electron microscopy image of the aerogel showing that the filaments are coated with a rough, flake like material. d) Energy-dispersive X-ray spectroscopy identifies oxygen, titanium, carbon, silicon, and magnesium as main elements in the aerogel sample. We assign silicon and magnesium to Laponite ($\text{Na}_{0.7}\text{Si}_8\text{Mg}_{5.5}\text{Li}_{0.3}\text{O}_{20}(\text{OH})_4$) residues on the aerogel surface.

7.2 Alignment of Au Nanorods

In chapter 5, we harnessed the plasmonic optical characteristic of Au nanorods (AuNRs) to enable photothermal heating in AuNR/TiO₂ aerogels. The anisotropy of AuNRs causes two dominant plasmon resonances along the longitudinal and transverse direction which can be selectively excited with polarized light.^[5] By orientating the AuNRs within the TiO₂ aerogel matrix during the 3D printing process, photothermal heating could be structured depending on the polarization of the incident light. Alignment by shear or extensional flow is a particularly interesting approach since it is intrinsically present in extrusion-based 3D printing. Depending on the nozzle geometry, different stress profiles arise. For a straight nozzle, the shear stress is maximal at the wall and decreases linearly towards the center. For a conical nozzle, an additional velocity gradient in longitudinal direction exists due to a change in the nozzle cross-section. In both cases, flow induced alignment is only possible if the applied stress surpasses the flow stress of the ink.^[6] We tested AuNR alignment by measuring the transmission of light with polarization along and perpendicular to the printing direction of AuNR/TiO₂ aerogel plates that were printed with a straight and conical nozzle, respectively (Figure 7.2a-b). Since plasmonic excitation of AuNRs is polarization dependent, a reduced extinction of the misaligned plasmonic peak is expected. If we compare the polarization dependent UV-vis transmission spectra of AuNR/TiO₂ aerogels for a straight and conical nozzle in Figure 7.2c-d, we see that the extinction at the longitudinal plasmonic peak is nearly polarization independent for a straight nozzle, but decreases by about 18 % for the conical nozzle geometry. This indicates that with the conical nozzle, where shear and extensional flow are present, a partial alignment of the AuNRs is possible. However, it remains unclear whether the stress profile in the nozzle is insufficient to enable a full alignment of the AuNRs, or whether the alignment of the AuNRs in the nozzle is more complete but relaxes after extrusion and during curing of the AuNR/TiO₂ gel in the heptane/ammonia liquid bath. For clarification, in situ UV-vis spectroscopy in a glass capillary with a geometry comparable to the nozzle or in situ polarization rheology are relevant methods to study the alignment and relaxation of AuNRs as a function of the applied shear stress.^[6] Further analysis via X-ray photon correlation spectroscopy and small angle X-ray scattering could provide a more detailed picture of the dynamics within the surrounding TiO₂ gel network during 3D printing.^[7-9] Particularly, such measurement might disclose the breakdown behaviour of the colloidal gel structure upon flow and reveal whether the AuNRs remain embedded in nano- to microscopic TiO₂ gel fragments which hinder a shear-induced alignment of the AuNRs (Figure 7.2e), or whether the shear stress is sufficient to cause a complete disintegration of the gel (Figure 7.2f) in which the individual particles are susceptible for shear alignment. A thorough understanding of the extrusion process is fundamental to eventually gain control of the AuNR alignment by designing the 3D printing process and the nozzle geometry. Ultimately, this enables the realization of plasmonic metamaterials with a tunable extinction of the longitudinal plasmonic peak to facilitate more advanced heating applications, or optoelectronic devices such as polarization filters and optical orientation sensors.

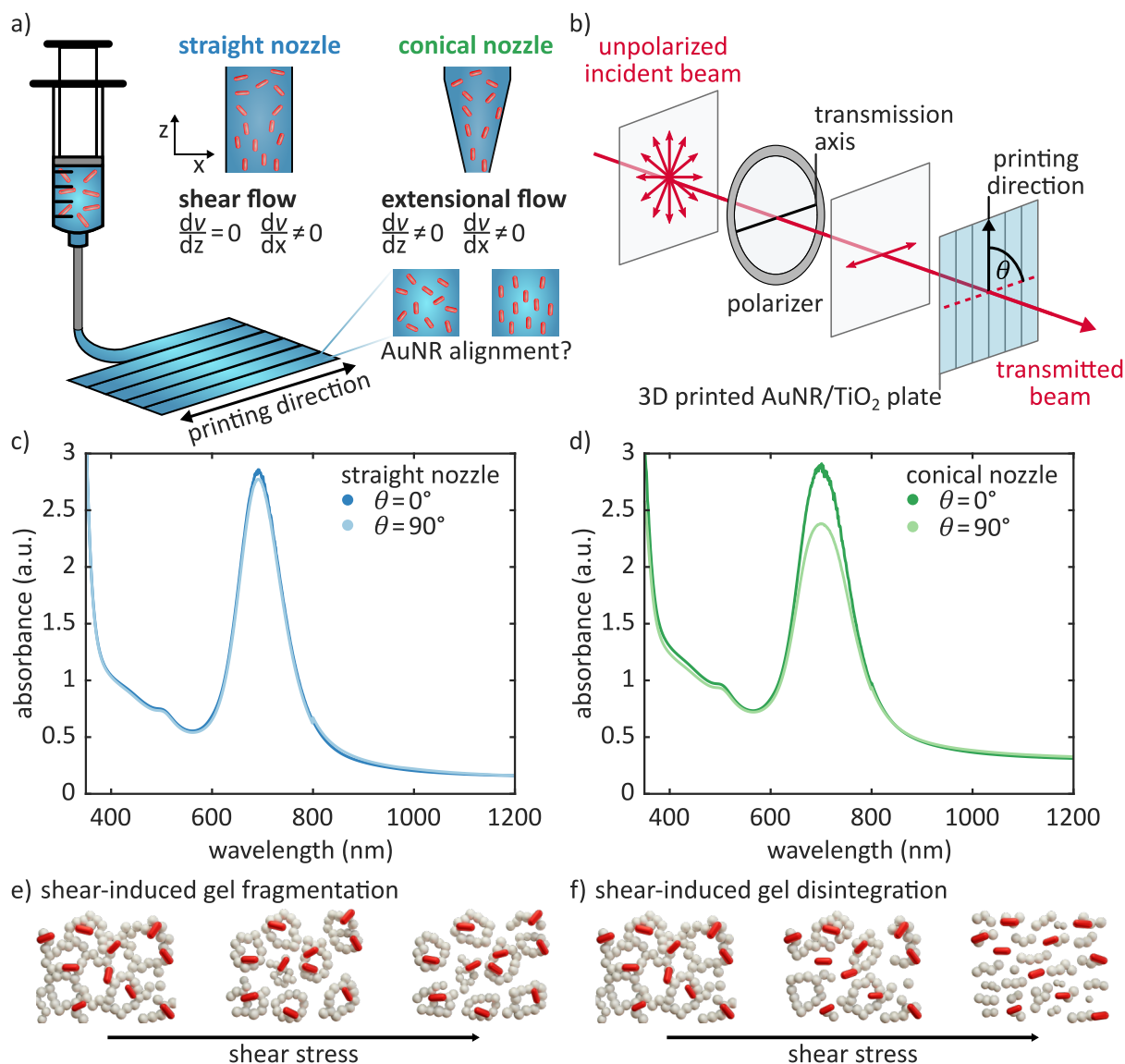


Figure 7.2: Alignment of AuNRs during 3D printing of a AuNR/TiO₂ gel. a) Illustration of the 3D printing process for the fabrication of AuNR/TiO₂ aerogel plates. The AuNR/TiO₂ ink is either extruded through a straight or conical nozzle and the printed plate consists of an array of parallel cylinders. The straight nozzle features a velocity gradient in radial direction, whereas the conical nozzle exhibits a gradient in radial direction and along the nozzle axis due to the changing nozzle cross-section. b) Schematic of the UV-vis experiment. A polarizer is used to change the polarization angle of the incident light θ relative to the printing direction of the AuNR/TiO₂ plate. c-d) Recorded UV-vis spectra with incident polarization along ($\theta = 0^\circ$) and perpendicular ($\theta = 90^\circ$) to the printing direction of a AuNR/TiO₂ aerogel plate printed with a straight 410 μm and conical 200 μm nozzle, respectively. The nano- and microscopic structural evolution of the AuNRs/TiO₂ gel at increasing level of shear stress might either result in e) a fragmentation of the network into smaller gel clusters in which the embedded AuNRs are hindered to change their orientation or f) a complete disintegration of the particle network in which the AuNRs align with the flow.

7.3 Photocatalytic CO₂ Reduction

In chapter 6, we used the photocatalytic activity of TiO₂ and Au/TiO₂ to produce hydrogen from a water/methanol saturated gas stream. Another appealing photocatalytic process is the reduction of CO₂ in a humidified gas stream, which can lead to a multitude of products depending on the number of transferred electrons and available hydrogen atoms. To evaluate the activity of a Au/TiO₂ photocatalyst for CO₂ reduction, we performed preliminary experiments on Au/TiO₂ powder in the group of Prof. Atsushi Urakawa situated in the Chemical Engineering Department of TU Delft. A flow scheme and photograph of the setup are shown in Figure 7.3a-b, respectively. Here, CO₂ is humidified by bubbling the gas stream through a water-filled saturator. Next, the gas passes over a photocatalyst spread on the bottom of a reactor and the composition of the exiting gas stream is analyzed with a mass spectrometer (MS). Upon illumination with a mercury (Hg) lamp, we observe a strong, transient formation of hydrogen and methane which declines into a steady value over time, as shown in Figure 7.3c. Since the MS was not calibrated, only an unbalanced reaction scheme can be proposed, as illustrated in Figure 7.3d. It is generally believed that a single methane molecule stems from the reduction of a single CO₂ molecule via the transfer of eight electrons where oxygen is the only byproduct and water acts as a source of hydrogen. Therefore, the detected hydrogen presumably results from water splitting which is a competing reaction of methane formation from CO₂ reduction, and requires only two instead of eight electrons to be transferred. However, further investigation comprising isotope labeling of ¹³CO₂ and D₂O are needed to clarify the origin of the catalytic reaction products.

Improvements of photocatalytic production rates due to 3D structuring as discussed in chapter 6 should directly translate to CO₂ photoreduction. However, to avoid the competing hydrogen evolution, the material composition needs to be tuned for higher methane selectivity. In chapter 9, we will discuss that organic-inorganic hybrids are effective materials to tune selectivity of the CO₂ reduction process – not only for methane but also to a multitude of products such as methanol, formic acid or carbon monoxide. Following that approach, various hybrid inks which are highly selective for a single compound can be formulated. Combined with 3D printing, modular and interchangeable photocatalytic reactors can be fabricated that are mounted on the gas stream depending on the desired product of the CO₂ photoreduction process. Alternatively, different photoreactors could be connected in series, where each reactor is responsible for a different CO₂ reduction pathway. Ultimately, inks that are highly selective for a single redox reaction could be formulated to separate the CO₂ reduction process into a CO₂ to CO and a dedicated CO to hydrocarbon step, as this circumvents the kinetically suppressed transfer of multiple electrons.

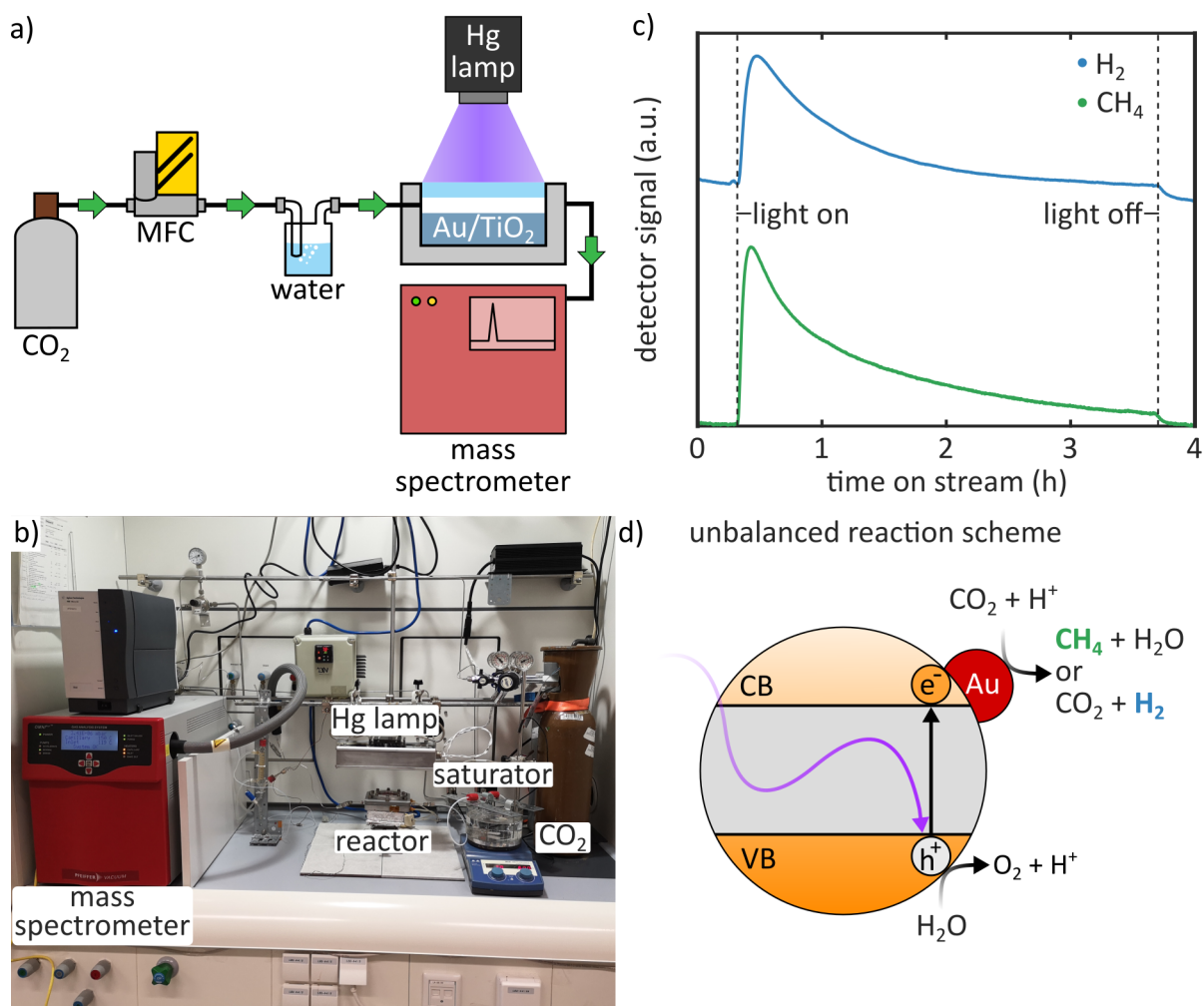


Figure 7.3: Photocatalytic CO₂ reduction on Au/TiO₂ powder. a) Scheme and b) photograph of the gas flow photoreactor in the catalysis engineering group of Prof. Atsushi Urakawa at TU Delft. A humidified CO₂ gas stream flows in a reactor, passes over a catalyst powder, and enters a mass spectrometer for product analysis. c) Time-trace profile of the raw signal of the mass spectrometer for methane (CH₄) and hydrogen (H₂) during the photocatalytic test. d) Schematic of an unbalanced reaction scheme for the conversion of a humidified CO₂ gas stream based on the detected products. UV light illumination creates an electron and a hole in the conduction and valence bands, respectively. The formation of CH₄ and H₂ are competing reactions during the reduction of the CO₂ from a humidified gas stream.

Bibliography

- [1] Y. Jin, A. Compaan, W. Chai and Y. Huang, *ACS Appl. Mater. Interfaces*, 2017, **9**, 20057–20066.
- [2] B. Elder, R. Neupane, E. Tokita, U. Ghosh, S. Hales and Y. L. Kong, *Adv. Mater.*, 2020, **32**, 1907142.
- [3] O. A. Tafreshi, S. G. Mosanenzadeh, S. Karamikamkar, Z. Saadatnia, C. B. Park and H. E. Naguib, *Mater. Today Chem.*, 2022, **23**, 100736.
- [4] M. A. S. R. Saadi, A. Maguire, N. T. Pottackal, M. S. H. Thakur, M. M. Ikram, A. J. Hart, P. M. Ajayan and M. M. Rahman, *Adv. Mater.*, 2022, **34**, 2108855.
- [5] J. Zheng, X. Cheng, H. Zhang, X. Bai, R. Ai, L. Shao and J. Wang, *Chem. Rev.*, 2021, **121**, 13342–13453.
- [6] M. K. Hausmann, P. A. Rühls, G. Siqueira, J. Läger, R. Libanori, T. Zimmermann and A. R. Studart, *ACS Nano*, 2018, **12**, 6926–6937.
- [7] N. Begam, A. Ragulskaya, A. Girelli, H. Rahmann, S. Chandran, F. Westermeier, M. Reiser, M. Sprung, F. Zhang, C. Gutt and F. Schreiber, *Phys. Rev. Lett.*, 2021, **126**, 098001.
- [8] A. Jain, F. Schulz, I. Lokteva, L. Frenzel, G. Grübel and F. Lehmkuhler, *Soft Matter*, 2020, **16**, 2864–2872.
- [9] C.-H. Lin, K. Dyro, O. Chen, D. Yen, B. Zheng, M. T. Arango, S. Bhatia, K. Sun, Q. Meng, L. Wiegart and Y.-c. K. Chen-Wiegart, *Appl. Mater. Today*, 2021, **24**, 101075.

8 Conclusion and Outlook

The excessive nanomaterial library permits a nearly unbound design space to realize atomically-defined, macroscopic, functional materials in a bottom-up approach. In this thesis, we introduced the concept of *gelled nanoinks* to enable 3D printing of colloidal nanomaterials in the form of hierarchically structured, macroscopic aerogels. We discussed that the scientific community working on aerogels developed a robust concept of controlled destabilization to induce the gelation for a broad range of nanomaterials. However, the tunability of the geometry of aerogels remained limited to a small size range that comes with traditional shaping methods such as gel casting. Although recent efforts demonstrated the feasibility of 3D printed aerogels, inks were either restricted to 2D nanomaterials such as graphene oxide, or required significant changes to the underlying gelation principles to enable printability which compromised the quality of the final aerogel. In contrast, we demonstrated that the well-established concepts of controlled destabilization can be translated to 3D printing by performing the print of TiO₂ nanoparticle based inks in a liquid bath charged with ammonia, which not only prevents solvent evaporation induced damage to the nanoporous gel network, but also solidified the weak gel to achieve a high shape fidelity. As a result, we maintained the structural nanoscopic characteristics of traditionally casted aerogels and added control of the micro- and macroscopic architecture by the 3D printing process. Moreover, we showed that the concepts of *gelled nanoinks* provides a modular platform to incorporate functional nanomaterials into the fabrication process. To illustrate the functional characteristic, we introduced a photothermal heating ability to the aerogel by cogelation of plasmonic Au nanorods and TiO₂ nanoparticles. We demonstrated that depending on the 3D microstructure a localized or homogeneous heat distribution can be achieved.

Next, we focused on the photocatalytic activity of the TiO₂ aerogel backbone. Here, we combined the geometric design freedom of 3D printing with computing methods to derive an ideal microstructure for photocatalytic hydrogen production in a water/methanol saturated gas stream. Bulk aerogels generally suffer from a low gas permeability and require high pressure differences to enforce a gas flow through the nanoporous medium. We showed that a 3D printed, microstructured aerogel decreased the flow resistance by five orders of magnitude compared to an unstructured aerogel, without compromising the gas infiltration and photocatalytic performance. Besides, we eliminated poorly illuminated sections of the photocatalyst by adjusting the thickness to the light penetration depth which lead to a fivefold improvement of the mass normalized hydrogen production rate relative to the respective catalyst powder counterpart. Combining an optimized 3D aerogel photocatalyst geometry with an energy efficient mass transport indicates great potential for technological upscaling.

The results on photothermal heating and the application as a tailor-made photocatalyst just rep-

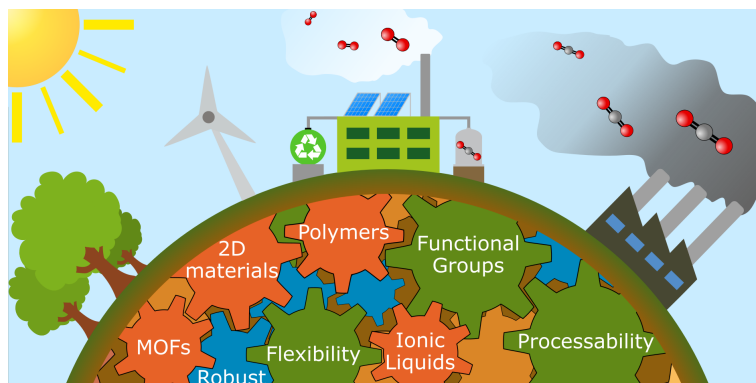
represent the tip of the iceberg for the 3D printing of gelled nanoinks. Besides TiO_2 and Au/TiO_2 , many more nanoparticle-based inks need to be formulated to induce new functional properties for novel applications and to improve the intrinsic efficiency of the presented 3D aerogel photocatalyst. Even though TiO_2 is by far the most studied photocatalyst, hydrogen production is still performed in the presence of hole scavengers with hydrogen evolution rates in the range of a few $\mu\text{mol h}^{-1}$. A promising alternative to TiO_2 are Ga_2O_3 based materials, which combine suitable energetic positions of the conduction and valence band for water splitting with a high charge carrier mobility.^[1–3] Photocatalytic activities of Ga_2O_3 exceed TiO_2 by multiple order of magnitudes and hydrogen evolution rates of several mmol h^{-1} were reported – even in the absence of sacrificial organic compounds.^[4] Thus, inks based on Ga_2O_3 nanoparticles could combine the advantages of 3D structuring with the high material-specific catalytic activity to enable photocatalytic hydrogen production from direct splitting of pure water. Moreover, such inks could be joined with photothermal nanomaterials presented in chapter 5, where plasmonic excitation harvest the broad solar spectrum and accelerate the catalytic process via heating.

Nevertheless, even for TiO_2 based nanoinks many intriguing applications are yet to be explored which include the fabrication of flexible aerogels enabled by an embedded 3D printing method (chapter 7.1), the alignment of anisotropic nanomaterials during ink extrusion (chapter 7.2), and photocatalytic processes such as CO_2 reduction (chapter 7.3). In the future other researchers might take advantage of the developed 3D printing process and follow their journey of innovation and discovery to formulate new ink compositions for more advanced 3D aerogel devices.

Bibliography

- [1] Y. Wang, P. Zhuang, H. Yue, H. Dong and X. Zhou, *J. Phys. Chem. C*, 2019, **123**, 8990–9000.
- [2] H. He, R. Orlando, M. A. Blanco, R. Pandey, E. Amzallag, I. Baraille and M. Rérat, *Phys. Rev. B*, 2006, **74**, 195123.
- [3] Y. Inoue, *Energy Environ. Sci.*, 2009, **2**, 364–386.
- [4] Y. Sakata, Y. Matsuda, T. Nakagawa, R. Yasunaga, H. Imamura and K. Teramura, *ChemSusChem*, 2011, **4**, 181–184.

9 Organic–Inorganic Hybrids for CO₂ Sensing, Separation, and Conversion



The content of this chapter envisions the creation of an artificial carbon cycle by combining individual building to organic-inorganic hybrid materials and was published in *Nanoscale Horizons*. The manuscript is co-authored by Christoph Willa, who contributed equally to this work, and Dorota Koziej as corresponding author.

9.1 Abstract

Motivated by the global air pollution that skyrocketed in numerous regions around the world, great effort was placed on discovering new classes of materials that separate, sense or convert CO₂ in order to minimize impact on human health. However, separation, sensing and conversion are not only closely intertwined due to the ultimate goal of improving human's well-being, but also because of similarities in material prerequisites – e.g. affinity to CO₂. Partly inspired by the unrivaled performance of complex natural materials, manifold inorganic-organic hybrids were developed. One of the most important characteristics of hybrids is their design flexibility, which results from the combination of individual constituents with specific functionality. In this review, we discuss commonly used organic, inorganic, and inherently hybrid building blocks for applications in separation, sensing and catalytic conversion and highlight inevitable benefits like durability, activity and low-cost and large scale fabrication. Moreover, we address obstacles and potential future developments of hybrid materials. This review should inspire young researchers in chemistry, physics and engineering to identify and overcome interdisciplinary research challenges by performing academic research but also – based on the ever-stricter emission regulations like carbon taxes – through exchanges between industry and science.

9.2 Introduction

The steadily rising level of CO₂ in the atmosphere and subsequent ocean acidification are environmental and health issues concerning everyone. Following the industrial revolution, human activities have significantly altered the global carbon cycle. Since the late 19th century, atmospheric CO₂ concentrations have increased from 275 ppm to more than 400 ppm with a record increase of 3.3 ppm between 2015 and 2016. There are both natural and anthropogenic sources of CO₂. Natural sources include animal and plant respiration or decomposition of organic matter, whereas anthropogenic sources include for example the combustion of fossil fuels, cement production, or power generation. Natural CO₂ sinks on the other hand include ocean- and terrestrial-based regions. In fact, oceans absorb roughly 40% of atmospheric CO₂.^[1] To decrease atmospheric CO₂ levels and to mitigate the adverse effects related to it, CO₂ needs to be efficiently separated and captured at its source, e.g. power plants or chemical factories, using for example amine scrubbers or gas separation membranes. CO₂ can then be recycled, e.g. in modified atmosphere packaging,^[2] as a supercritical solvent and heat transfer fluid,^[3,4] or in enhanced oil recovery. Alternatively, CO₂ can be converted to various reaction precursors or fuels such as carbon monoxide, methanol, ethanol, ethylene, formic acid, or formaldehyde. Indeed, solar irradiation can be utilized as an inexhaustible energy source to power electrocatalytic devices or to directly convert CO₂ in a photocatalytic approach. Importantly, separation and conversion processes need to be monitored accurately, thus requiring precise CO₂ sensors. Consequently, there is an ever-increasing need for functional materials that display application-specific interaction with CO₂. In this context, the use of organic-inorganic hybrids is a viable option because they combine typical properties related to organic materials (gas diffusivity, mass transport, flexibility, or chemical reactivity) and inorganic materials (surface area, mechanical stability, conductivity, or magnetic and optical properties), thus yielding new or enhanced properties

such as internal surface area, functionality, light harvesting, or mass transport. Additionally, the solution-processability of hybrids is a major advantage because it allows low-cost printing or roll-to-roll fabrication of flexible materials at industrial scales. Typical application areas include environmental gas sensors,^[5] solar cells,^[6] separation membranes,^[7] catalysts,^[8] proton conducting membranes,^[9] and supercapacitors.^[10] Various aspects of history, preparation, and design of hybrids have been covered previously.^[11–13] Here, we explicitly focus on current trends and novel ideas of how to take an advantage of synergistic interaction between organic and inorganic materials used for sensing, separation, and catalytic conversion of CO₂. To this end, we first briefly introduce the most frequently utilized components of hybrid structures and their properties that make them suitable for CO₂-based applications, as shown in Figure 9.1. We discuss specific figures of merit and highlight the most exciting examples of hybrid structures utilized in sensing (section 9.4), separation (section 9.5), and catalytic conversion (section 9.6) of CO₂, respectively. However, in these sections we refrain from comparing performance metrics because these highly depend on the experimental setup and are difficult to compare without effective benchmarking. Instead, we highlight common synergistic benefits of organic-inorganic hybrid materials across multiple material classes and identify experimental obstacles that limit their performance comparison. Finally, we give an outlook on future trends in the development of CO₂-active hybrid materials.

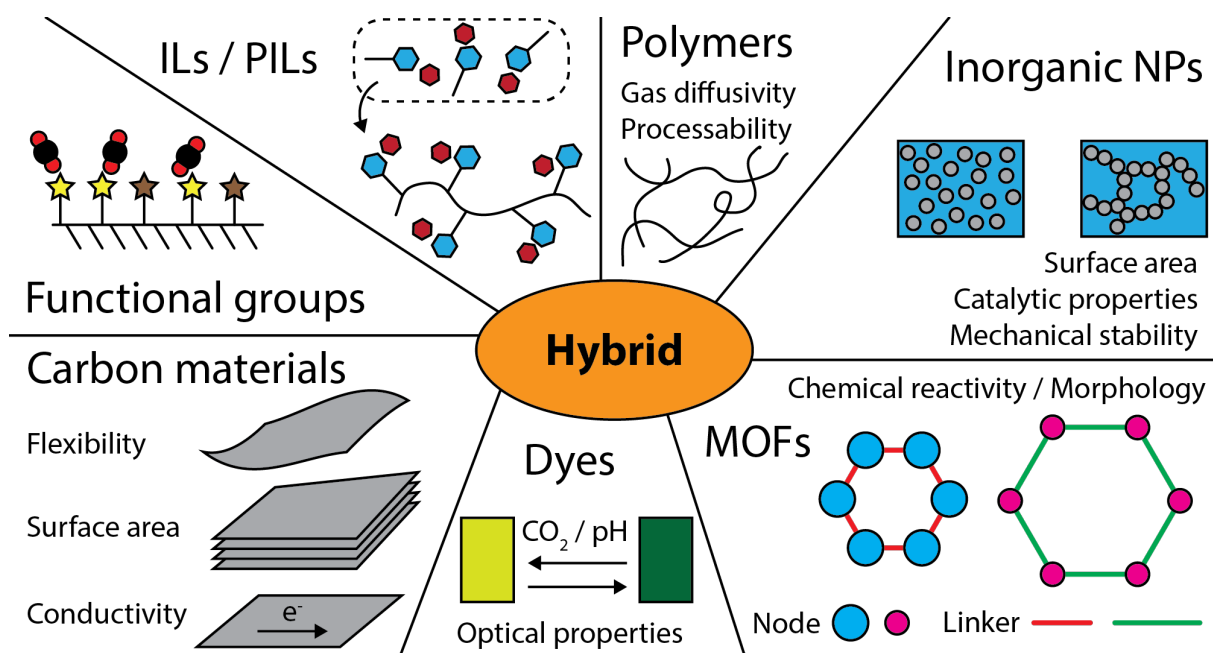
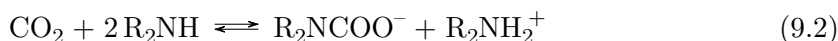
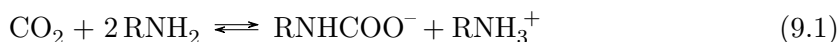


Figure 9.1: Most common building blocks used to design hybrid materials for CO₂ related applications. Reproduced from reference [14] with permission from the Royal Society of Chemistry.

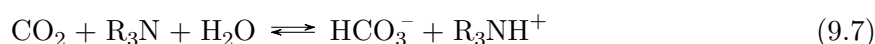
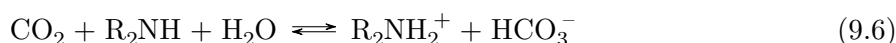
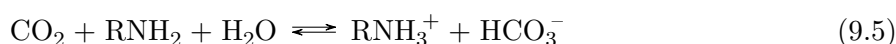
9.3 Individual Organic and Inorganic Building Blocks

Functional groups. Here, we discuss the chemical background behind the interaction of CO₂ with commonly used functional groups that can be bonded onto or incorporated into solid materi-

als in order to tune the chemical properties of otherwise unreactive surfaces. For example, amines interact with CO₂ based on the hard soft acid base (HSAB) concept and dipole-quadrupole interactions.^[15] Indeed, CO₂ (hard Lewis acid) has a strong affinity towards primary and secondary amines (hard Lewis base) under the formation of alkylammonium carbamate complexes:

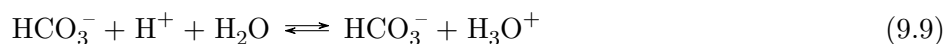


The anhydrous carbamation reaction (equation 9.1-9.4) cannot occur for tertiary amines. Instead, in the presence of humidity hydrogen carbonate forms:



Note that primary amines (Equation 9.1) are typically more reactive than secondary amines (Equation 9.2). Compared to primary and secondary amines, tertiary amines (Equation 9.7) are not as reactive, but can be regenerated at moderate temperatures.^[16] Further, CO₂ loading is limited to 0.5 mol of CO₂ per mol of primary or secondary amines, compared to 1 mol of CO₂ per mol of tertiary amines.

At room temperature, the equilibrium of these reactions is typically on the right side of the reaction formula, while elevated temperatures promote desorption and evaporation of CO₂, thus pushing it to the left side. Examples of chemicals with high primary and secondary amine loading include diethylenetriamine (DETA), triethylenetetramine (TETA), and tetraethylenepentamine (TEPA). Alternatively, CO₂ also interacts with water (Equation 9.8-9.9).



The formation of protons and hydronium ions is utilized for instance in colorimetric CO₂ sensors based on pH indicators^[17,18] or tunable ion conductors.^[19]

However, the presence of amines and/or water may lead to corrosion which not only triggers catalytic degradation of amine functional groups but also causes degradation of equipment.^[20,21] Therefore, corrosion inhibitors or alternatives to amines like ionic liquids are of major interest. Ionic liquids (ILs) are salts that have melting points below 100 °C. In particular, room temperature ILs (RTILs) are liquid at room temperature. Besides their negligible vapor pressure, ILs display good chemical and thermal stability. Generally, ILs are composed of organic cations such as imidazolium, pyridinium or ammonium ions and of anions ranging from halides, to polyatomic inorganic anions such as tetrafluoroborate [BF₄]⁻ and hexafluorophosphate [PF₆]⁻ or

to large organic anions like bistriflimide $[\text{Tf}_2\text{N}]^-$. Owing to the large variety of ions available, physicochemical properties and affinity towards CO_2 can be readily adjusted.^[22–24] For example, ILs with high CO_2 solubility were synthesized by using ammonium, imidazolium, or pyridinium cations.^[22,25–31] Besides minor interactions with the cation, CO_2 (hard Lewis acid) primarily interact with $[\text{BF}_4]^-$, $[\text{PF}_6]^-$, or $[\text{Tf}_2\text{N}]^-$ anions (hard Lewis base) by accepting partial electric charges from the electronegative fluorine atoms.^[22,32] Although the affinity of CO_2 towards the respective cations seems to be marginal, the side chain length of a cation can control free volume to accommodate CO_2 .^[22]

Polymers. The affinity of solid substrates towards CO_2 can be increased through functionalization with amines or ionic liquids. However, as prepared materials are typically limited to silicas due to presence of surface hydroxyl groups and suffer from relatively low number of functional groups and insufficient efficiency.^[33] Therefore, polymers that directly interact with CO_2 are interesting for uses requiring functional films with good gas selectivity and permeability, e.g. in gas sensing, separation or conversion. Many polymers show high amine loading and are used to selectively absorb CO_2 . Examples include amidine and guanidine-based polymers,^[34,35] poly(ether imide),^[36] or poly(ethylene-imine).^[37] Alternatively, by polymerizing ILs, so-called polymerized ionic liquids or poly(ionic liquid)s (PILs) are obtained. Unlike their IL precursor, PILs are usually solid at room temperature. Several PILs have been shown to selectively and reversibly absorb CO_2 .^[27,38,39] The use of PILs in capture and separation was recently reviewed elsewhere.^[40]

Also, the polymer nanostructure, i.e. nanopores or segregated microphases can affect the diffusion of gases or reactants, thus proving useful in gas separation and catalysis. For example, polymers such as polystyrene (PS), polysulfone (PSf), or poly(ether-b-amide-6) (PEBA) are used owing to their controllable porosity as well as their good CO_2 permeability and selectivity.^[41] PEBA is a block-copolymer composed of amorphous and permeable polyethylene oxide (PEO) units interacting with CO_2 via dipole-quadrupole interaction^[42] as well as crystalline polyamide (PA) segments giving mechanical stability.^[23] Alternatively, porous organic polymers synthesized from individual multidentate organic building blocks can be used for nanostructuring. Depending on polymerization conditions, cross-linking of polymer can be influenced to obtain micro (<2nm), meso (2-50 nm), and macroporous (>50 nm) materials.^[43] Due to high surface area, large pore volume and wide range of building blocks, porous organic polymers display a huge potential as CO_2 adsorbent and as a catalytic platform. Diverse synthetic routes and challenges related to the pore size distribution have been covered previously.^[44,45] Through thermal decomposition of polymeric structures with a well-defined porous structure, microporous carbon materials with precisely tuned structure can be obtained. Indeed, the pyrolysis of nitrogen-containing polymers, such as polypyrrole,^[46] melamine formaldehyde resin,^[47] polyacrylonitrile^[48] and polyaniline^[49] results in N-doped porous carbon materials, thus improving CO_2 adsorption capabilities when compared to pure carbon frameworks. It is however still under debate whether the increased CO_2 adsorption by N-doping is a result of facilitated CO_2 adsorption by acid-base interaction, improved hydrogen-bonding capability or by residual ions.^[50,51] Owing to their low cost, high thermal and chemical stability, controllable pore structure, high surface area and abundant nitrogen surface atoms, N-doped carbon materials are gaining signif-

icant attention for CO₂ capture and separation.^[52,53]

Moreover, by incorporating inorganic building blocks within the polymer matrix inherent properties of inorganic nanomaterials or additional features of the formed polymer-nanoparticle-interface can be observed while maintaining flexibility and processability of polymeric materials.^[54] However, weak interfacial bonding is still an obstacle for obtaining uniform dispersions of nanomaterials in polymer matrices. For instance, functional groups that interact with the surface of particles can be integrated for steric stabilization of inorganic building blocks to avoid loss of functionality as a result of agglomeration – which is currently one of the major challenges for practical application.^[55]

Dyes. Even though dyes usually do not interact directly with CO₂, their pH-sensitivity can be used to detect and respond to proton concentration changes occurring upon the interaction of CO₂ with water or humidity (see Equation 9.7-9.8). This effect is utilized in various optical CO₂ sensors. pH-sensitive dyes include thymol blue (TB),^[56–58] bromothymol blue (BTB),^[57] phenol red (PSP),^[56,58] methyl red,^[58] cresol red,^[56] or luminescent 1-hydroxypyrene-3,6,8-trisulfonate (HPTS).^[59] Finally, porphyrine-based dyes can be used to promote the absorption of visible light in photocatalytic conversion of CO₂.^[60]

Carbon materials. Graphene exhibits exceptional mechanical, optical, thermal, and electrical properties while having a low density and it has become a real game changer in material science.^[61] It is a zero band gap semiconductor with symmetric band structure showing high electron mobility.^[62,63] Moreover, graphene displays a 2-dimensional nanosheet morphology resulting in high specific surface area and its π -conjugated structure supports the interaction with π -bonds in CO₂.^[64] Therefore, graphene and its derivatives such as graphene oxide (GO) or reduced graphene oxide (rGO) are now utilized in sensing, separation, and catalytic conversion.^[65–68] Graphene oxide (GO) can be synthesized by chemical oxidation and exfoliation of graphite using strongly oxidizing agents. In contrast to graphene, the surface of GO is heavily decorated with electron-rich, oxygen-containing, and highly reactive polar groups such as hydroxyls, epoxides, or carboxyls, thus exhibiting oxygen contents of up to 40 at %.^[69] The electron-donating nature of these moieties leads to preferential adsorption of CO₂ through dipole-quadrupole interaction.^[70] Furthermore, the interlayer spacing of GO can be adjusted, thus making it interesting for membrane applications.^[70–75] Moreover, exfoliated GO nanosheets are hydrophilic and thus stable in water. Therefore, organic solvents are not necessary and the environmental friendliness of industrial scale production and processing is enhanced. By reducing GO, it is possible to partially restore the properties of graphene.^[76] The reduced graphene oxide (rGO) shows good electrical conductivity, dominated by positively charged carriers (holes).^[77] Consequently, when CO₂ interacts with functional groups at the rGO surface by transferring an electron to rGO, the hole concentration decreases and the resistance increases. This effect is a chemical foundation for CO₂ sensing.^[78,79]

Graphitic carbon nitride (g-C₃N₄) is closely related to graphene, GO, and rGO. It is a 2-dimensional, semiconducting material with a band gap of about 2.7 eV and is composed of tri-s-triazine units that are interconnected by planar tertiary amino groups. It can be prepared

from low-cost nitrogen- and carbon-rich precursors such as cyanamide, dicyandiamide, melamine, and urea.^[80–82] By altering the precursor and through chemical functionalization following the synthesis, the electronic band structure of the material and its light absorption properties can be tuned,^[83] thus making it attractive for various catalytic applications.^[84]

Metal-organic frameworks. Metal organic frameworks (MOF) are an emerging class of crystalline hybrid materials consisting of metal containing nodes, also called secondary building units (SBU), that are interconnected by organic linkers forming a 1-, 2-, or 3-dimensional porous network. MOF crystals typically display large internal cavities that are interconnected by small channels.^[85] Owing to their highly ordered nanoporosity of up to 90 %, MOFs provide correspondingly large internal surface area.^[19,86] Moreover, the molecular building blocks can be varied systematically, which is a major reason for the exceptionally high chemical and functional versatility as well as adjustable internal surface properties. Consequently, and in contrast to other porous materials such as zeolites or aerogels, MOFs show precisely tunable pore size in a typical range of 2–100 Å.^[87–91] For example it is possible to fit the size of molecular guests, thus even enabling H₂/D₂ isotope separation by quantum sieving.^[91] Furthermore, enzyme-like selectivity was demonstrated after postsynthetic modification with molecular recognition groups. Additionally, the incorporation of MOFs as fillers in polymeric matrices is facilitated by their partially organic nature that yields good compatibility. Therefore, MOFs are interesting for numerous applications including molecular sieving,^[92,93] CO₂ separation,^[94,95] catalysis,^[96] sequestration,^[97,98] and chemical sensing.^[93,99–102] Owing to their tunability, it is possible to design MOFs specifically interacting with CO₂.^[89,103,104] For example, zeolitic imidazole frameworks (ZIF) (Zn/Co SBUs, imidazole-based linkers) are interesting because of their good CO₂ capture and sieving properties. For instance, ZIF-8 displays large cages (11.6 Å) and narrow pore apertures (3.4 Å),^[105,106] which can be tuned such that the large cages contain CO₂ absorbing ILs while the narrow pores allow molecular sieving of CO₂.^[107,108] Similarly, MFU-4 (Zn₅C₁₄ SBUs, benzobistriazolone linkers) displays alternating small (3.88 Å) and large cages (11.94 Å) connected by narrow apertures (2.52 Å).^[109] Alternatively, MIL-101 (Cr SBUs, terephthalic acid linkers) can easily be functionalized with CO₂ sensitive molecules owing to numerous unsaturated chromium sites within the structure. Also, CuBDC (Cu SBUs, 2-hydroxyterephthalic acid linkers) and MIL-53 (Al SBUs, terephthalic acid linkers) display good CO₂/CH₄ selectivity.^[36,110,111] Moreover, by incorporating catalytic centers and photosensitizers in MIL-125 (Ti SBUs, 2-aminoterephthalate linkers), it was possible to combine the photocatalytic CO₂ reduction activity with large surface area and open porosity of MOFs for improved mass transport.^[112] This list is by far not exhaustive, but it hints at the versatility of MOFs for application in CO₂ separation and conversion. Nevertheless, certain MOFs are water sensitive, thus limiting stability in process environments. Water adsorption concepts, water stability of several MOFs and experimental characterization procedures have been discussed previously.^[113]

Inorganic nanomaterials. Depending on the application, inorganic materials are generally selected based on their morphology or their surface and bulk properties. For instance, in applications that require high specific surface area or short charge carrier diffusion lengths, nano-sized

building blocks are employed. Regarding the morphology, structures with various dimensionality such as spherical nanoparticles, nanowires or -chains, nanosheets, and nanocubes that show dimension- and shape-dependent optical and electrical properties can be distinguished.^[114,115] Moreover, given that different morphologies exhibit different crystallographic surfaces and surface energies, they also display different affinities to CO₂. For example, nanoparticles of various shapes show varying activities and selectivities for identical catalytic reactions due to the exposure of different crystal facets.^[116,117] In addition, catalytic activity also depends on chemical composition. For electrocatalytic reduction of CO₂, copper and noble metals like gold, silver and palladium showed to be most effective. However, based on varying ability to stabilize reaction intermediates, copper is uniquely active for reduction of CO₂ to hydrocarbons, while gold, silver and palladium form CO as major product.^[118] For photocatalytic reduction, metal oxides like TiO₂, Cu₂O, WO₃ and Bi₂WO₆ or metal sulfides as CdS, ZnS were intensively investigated due to their suitable band gap.^[119] Among these various semiconductor photocatalysts capable of driving CO₂ reduction, perovskite oxides (ABO₃) emerged as a promising class of materials because band structure, charge transfer and adsorption of CO₂ can easily be manipulated and optimized by varying A- and B-site cation composition.^[120] Besides, more advanced synthesis protocols allow precise fabrication of colloidal semiconductor quantum dots or lead-halide perovskites that can be utilized for CO₂ reduction due to the size-dependent band structure.^[121] These inorganic building blocks can be assembled to macroscopic objects e.g. by formation of aerogels which increases the dwell time of CO₂ molecules in the confined space and enables interparticle charge transfer such that lifetime of photoexcited charge carriers is extended.^[122] Additionally, aerogels can be functionalized with organic groups, thus providing high reactive site densities. Moreover, by tuning the pore size in mesoporous silica materials, good sieving properties can be obtained.

9.4 Organic-Inorganic Hybrids for Sensing of CO₂

In the past years, the evolution of the internet of things (IoT) has yielded a steadily growing interest for different types of sensors and actuators.^[123] In particular, CO₂ sensors that are technologically relevant in exhaust gas analysis, in breath analysis for medical diagnosis, or in indoor air quality monitoring for intelligent ventilation systems are attracting a lot of attention. Gaseous and dissolved CO₂ is commonly detected and quantified using the non-dispersive infrared (NDIR) and the potentiometric Severinghaus techniques,^[124] respectively. The NDIR method is based on the Beer-Lambert law of absorption of infrared radiation by CO₂ molecules and shows high selectivity, sensitivity, and cyclability in a large concentration range. In contrast, Severinghaus sensors measure the pH-change of a bicarbonate buffer solution induced by the CO₂/H₂O interaction. However, both sensor types have limited miniaturization potential, which impedes their use in portable devices. Consequently, considerable efforts were made to develop innovative CO₂ sensors based on the resistive and capacitive read-out. The main advantage of this technology lies within its applicability in flexible and printed electronics as well as in battery-driven devices. For example, polymeric materials with tuned functionality were developed and have shown improved gas-sensing performance.^[125] However, despite many efforts in material design and morphology control, problems of long-term stability, moisture sensitivity

and conductivity remain unsolved. Alternatively, inorganic metal-oxide semiconductors show pronounced CO₂ sensitivity at operating temperatures of 250-350°C.^[126-128] However, because of the high energy demand related to the elevated operating temperatures they are unsuited for applications in battery-driven devices. Moreover, heated sensors could act as ignition sources under flammable condition. Nevertheless, the issues related to organic and inorganic materials can be overcome by utilizing hybrids thereof.^[5,129,130] We discuss the main figures of merit used to characterize CO₂ sensors and present a selection of hybrid CO₂ sensors pooled by their respective transducing technology including electrical, optical, and acoustic sensors. Figure 9.2 gives an overview of different sensors discussed herein. We finally summarize the main limitations of these sensors and how they can be tackled.

Figures of Merit

Depending on sensor type, different properties of the active material such as resistance, capacitance (electrical sensors), absorption, transmission, wavelength shift, luminescence (optical sensors), or resonance frequency (resonant sensors) are monitored as a function of CO₂ concentration. The extent of the measured signal change determines the sensitivity that is typically given as an absolute or relative change with respect to the baseline signal. Sensor kinetics are commonly characterized by the response and recovery times of sensors. For instance, t_{90} is the time needed to reach 90 % of the absolute change measured at equilibrium condition. Slower sensors are sometimes defined by their t_{50} value. The sensor kinetics strongly depend on CO₂ adsorption and desorption rates of the active layer. Moreover, desorption substantially influences the cyclability of a sensor, which is a crucial property for industrial applications. Furthermore, the limit of detection as well as the dynamic range determine the lower and upper bound of the concentration range in which the sensor can be operated, respectively. It is worth mentioning that the necessitated dynamic range depends on the field of application and has therefore to be adjusted accordingly. For example, when controlling air quality, CO₂ concentrations below 0.5 % have to be detected whereas in food packaging, CO₂ concentrations above 80 % are usual.^[131] Finally, the cross-sensitivity of a CO₂ sensor towards humidity and other gases as well as environmental effects including temperature and pressure is a key characteristic. For the sensors discussed next, some of these parameters are given in Table 9.1. We refrain from listing response and recovery times because these values strongly depend on gas flow and sample chamber volume, which are not directly comparable from one study to another.

Resistive and Capacitive Sensors

A resistive or capacitive CO₂ sensor monitors changes of resistance or capacitance of a transducing material as a function of CO₂ concentration as depicted in Figure 9.2a. Most organic-inorganic hybrid gas sensors combine the chemical activity of a low-conducting organic material with the transducing functionality of a conductive inorganic constituent. The chemical interaction of CO₂ with the organic material has a direct impact on charge carrier density or mobility in the transducer or causes relative permittivity variations in the dielectric layer, thus yielding resistance or capacitance changes. Unsurprisingly, carbon-based materials turn out to be

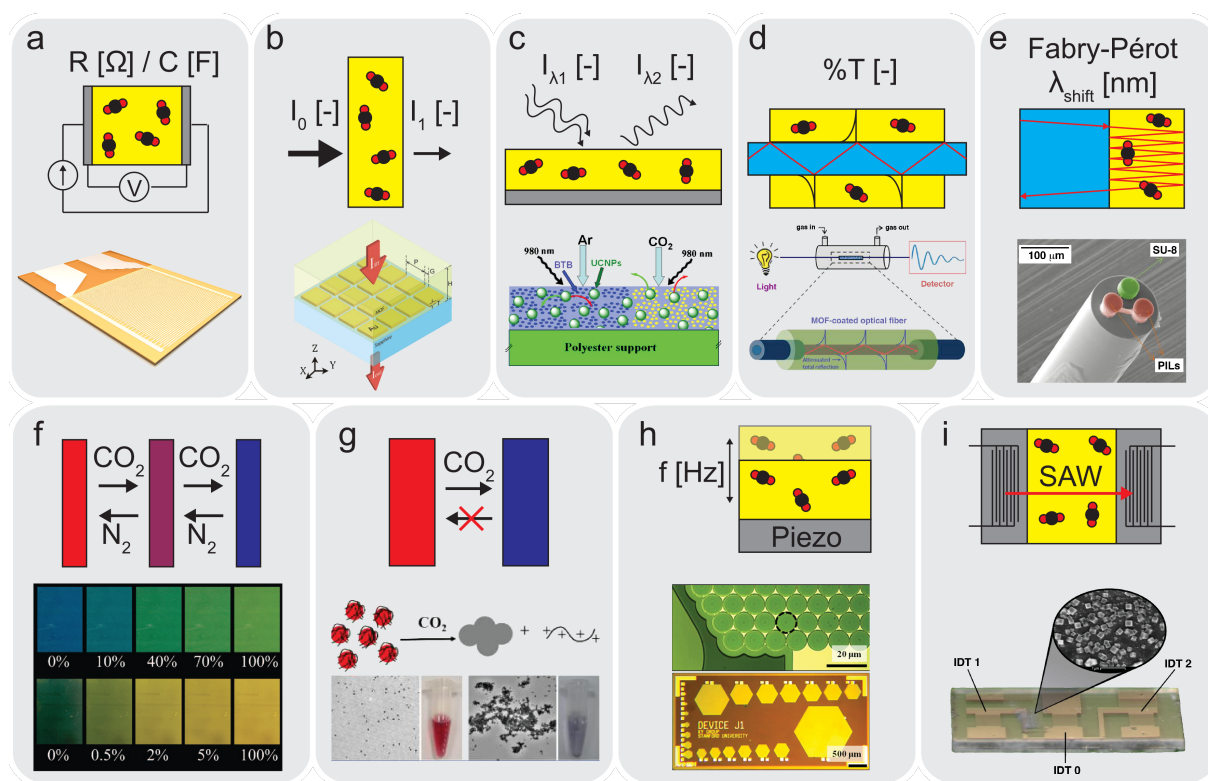


Figure 9.2: Schematics of operating principles for different sensors with examples from literature. a) Resistive or capacitive-type sensor, b) IR-type sensor with enhanced CO₂ absorption layer,^[143] c) optical sensor utilizing upconverting particles,^[41] d) optical fibre cladded with CO₂ sensitive MOF layer,^[137] e) optical sensor based on Fabry-Pérot interferometer,^[138] f) colorimetric sensor utilizing pH-sensitive dye,^[57] g) unidirectional CO₂ indicator,^[142] h-i) CMUT^[35] and SAW^[141] sensors measuring resonance frequency changes upon CO₂ absorption. Reproduced from reference [14] with permission from the Royal Society of Chemistry.

ideal transducers.^[78,132,133,140] For example, PEI-modified carbon nanotube field-effect transistors (NTFETs) were designed for CO₂ sensing.^[132] The selective interaction of CO₂ with the primary and secondary amines of PEI leads to the formation of carbamates, which in turn lowers the pH of the polymer layer and reduces the electron-donating effect of PEI to the carbon nanotube channel. In addition, starch was used to improve the PEI/carbon nanotube interaction and because of its hygroscopic nature, permits higher CO₂ absorption and results in a stronger protonation of the amino groups of PEI. Similarly, single-walled carbon nanotubes (SWCNT) can be functionalized with percolating networks of ammonium-based P[VBTMA][BF₄].^[140] Owing to the strong interaction of P[VBTMA][BF₄] with SWCNT through cation- π and π - π interactions, the polymer chains wrap around the SWCNTs while agglomeration of particles is prevented by repulsive forces among imidazolium cations. As CO₂ interacts with [BF₄]⁻, charge transfer from [BF₄]⁻ to CO₂ will diminish electron donating-effect of [BF₄]⁻ to SWCNT, thus increasing the hole concentration and eventually lowering the electrical resistance. An important drawback is that the recovery has to be triggered by an UV illumination step, which decreases the CO₂ desorption energy barrier. Others chemically modify 3-dimensional reduced graphene oxide (rGO) with hydroquinone, thus introducing doping and defect sites on the surface of rGO.^[133] In fact,

charge transfer from CO₂ to rGO leads to enriched hole concentration in rGO and lower resistance.

In our own research, we disperse inorganic filler particles in polymeric films to increase gas permeability. Even though it might seem counter-intuitive, the addition of nanoparticles leads to increased voids by hindering crystallization of polymers. We synthesize P[VBTMA][PF₆]/La₂O₂CO₃^[134] as well as P[VBTMA][PF₆]/Al₂O₃^[135] hybrids for CO₂ sensing. In the first study, La₂O₂CO₃, which is inherently sensitive towards CO₂ at elevated temperatures,^[126,144] was combined with P[VBTMA][PF₆] that is able to reversibly absorb large amounts of CO₂, eventually acting as a preconcentrator. In the follow-up study, the same principle was demonstrated, but we replace La₂O₂CO₃ by Al₂O₃ particles because of recyclability, environmental, and ecological reasons and because of their inertness to other gases. We find that the role of particles mainly consists in increasing gas permeability and allowing fast and reversible sensing, while CO₂ influences the electric and ionic conductivities of the polymer measured via DC resistance and AC impedance. Impedance studies highlight the importance of protons during CO₂ sensing, supported by the fact that a minimum relative humidity around 40 % RH is needed so that its interaction with CO₂ yields protons and hydrogen carbonate (Equation 9.8). A similar behavior was observed in highly porous, γ -cyclodextrin-based CDMOF-2.^[19] The noncovalent bonding of CO₂ with readily available free hydroxyl groups forms alkyl carbonic acid, which leads to a decrease of proton conductivity. CDMOF-2 is highly sensitive in the low CO₂ concentration regime and displays good reproducibility over several cycles. Besides measuring electrical resistance or ionic conductivity changes upon exposure to CO₂, it is also possible to track the capacitance of a sensor as a function of time. For instance, silica nanoparticles that are combined with PEI by wet-impregnation display linear capacitance changes as a function of CO₂ and humidity.^[136,145] The measurements show good reproducibility even after ageing for several weeks at ambient conditions.

Because sensors based on the electrical principle transduce a chemical signal that is induced by a certain number of adsorption sites into an electrical signal, the sensor operability is usually limited to low CO₂ concentrations (<10%), while it saturates at higher concentrations. This is one of the reasons driving the search for alternative detection principles such as via optical read-out, which enables measurements also at high concentration (10-100 %).

Optical Sensors

Optical gas sensors typically measure either the infrared radiation absorption or colorimetric and fluorescence intensity changes of a sensing layer as illustrated in Figure 9.2b-g.^[146] The main benefits of optical sensors are their large dynamic range, their high selectivity, and their usability for remote or electrically isolated sensing. Furthermore, they are applicable for the detection of dissolved CO₂, which is needed for CO₂ monitoring in blood or seawater and which makes them serious competitors to current Severinghaus detectors. Many efforts are made to find smaller alternatives to conventional NDIR sensors. Some studies focus on improving NDIR sensors e.g. by using enhanced thermal IR emitters^[147] or by using amine-functionalized structures to increase IR absorption, eventually reducing the light path length needed to reach a given sensi-

tivity.^[143,148] For example, porous Al₂O₃ substrates were functionalized with a glutaraldehyde-interlinked PEI film that acts as an enrichment layer.^[148] Likewise, metal-organic frameworks can be combined with plasmonic gold nanopatch arrays, thus increasing the absorption path of on-chip sensors.^[143]

Alternatively, CO₂ sensors monitoring the color or the fluorescence of the sensing layer take advantage of the pH changes induced by the CO₂/H₂O interaction. Through adding a dye that changes its color upon protonation, the color is indicative of CO₂ content. Additionally, the sensitivity can be adjusted by tuning the pK_a value of the pH indicator, thus allowing precise CO₂ measurement in a well-defined concentration range. As an example, the usability of silicone-encapsulated room temperature ILs was demonstrated.^[57] As CO₂ dissolves in the buffer and reacts with [BMIM][TOS], the pH increases leading to a colorimetric change of the dye. The fluorescence intensity decreases exponentially with CO₂ concentration and the sensitivity can be tuned by the choice of the room temperature ionic liquid (RTIL) counteranion. However, photobleaching in the presence of oxygen is a possible reason for fluorescence intensity decrease over time.

The use of optical fibers is attractive owing to their mechanical flexibility and in situ/in vivo operability.^[149,150] For example, the cladding can be removed by etching to enable subsequent surface functionalization with a sensitive coating. Since CO₂ alters the refractive index of the sensing layer, the evanescent waves propagating into the layer as well as the transmission through the fiber will be affected.^[151] For instance, porous ZIF-8 films can be deposited on the surface of an optical fibre.^[137] CO₂ molecules selectively interact with the MOF material, influencing pore filling and refractive index. As the refractive index of the MOF-film draws closer to the refractive index of the fiber, a larger portion of light propagates into the film causing a linear decrease of transmittance, which is in direct correlation with CO₂ concentration. The challenge of this method lies in the detection of extremely small variations in refractive index induced by CO₂. Others have used hybrids containing thymol blue (TB) dye and found logarithmic dependence of sensor signal with CO₂ concentration.^[18] Alternatively, the sensitive layer can be deposited onto the fiber tip, giving rise to a Fabry-Pérot interferometer (FPI)^[152] for example by direct μ -printing of poly(allyl-3-vinylimidazolium bromide) (PAVB) on the fiber tip.^[138] Indeed, the reversible CO₂ absorption of PAVB induces refractive index changes measurable by a shift of the interference peak. Interestingly, because a multi-cored optical fiber can be employed, it is possible to simultaneously measure temperature using SU-8 epoxy control sample. This points towards the possibility to detect and monitor multiple parameters in parallel which is important for signal calibration in electronic noses.

Another interesting approach consists in mixing NaYF₄:Yb,Er upconverting nanoparticles together with longwave absorbing and pH-sensitive BTB dye in a PS matrix.^[41] Upconversion takes advantage of a nonlinear optical process involving the absorption of two or more low-energy photons in long-living energy states with subsequent emission of a single higher-energy photon. The composite film is excited using a NIR-laser, and the dye-induced luminescence can be recorded as a measure of CO₂ concentration.

In most applications, reversibility of CO₂ sensors is highly desired. However, unidirectional optical CO₂ indicators that switch color upon onetime exposure are conceivable, e.g. as an alert sign similar to mechanical shock indicators. For instance, gold NPs were functionalized

with CO₂-responsive poly(N-(3-amidino)-aniline) (PNAAN).^[142,153] Because the amidine groups from PNAAN capture protons generated by the CO₂/H₂O interaction, the polymer becomes hydrophilic, swells and detaches from the gold surface. The subsequent irreversible aggregation of gold NPs leads to a unidirectional color change from red to blue.

Resonant Sensors

The resonant gas sensors take advantage of the mass-loading mechanism (see Figure 9.2h-i). This effect exploits the fact that whenever a resonant oscillator absorbs CO₂, its mass increases, thus leading to a decrease of resonance frequency. For this method to work, high mass sensitivity has to be achieved. This is possible with surface acoustic wave (SAW),^[154] quartz crystal microbalance (QCM), or capacitive micromachined ultrasound transducers (CMUT).^[35,155] A major advantage of these transducers lies within their good CMOS compatibility making them interesting, cost-effective candidates for miniaturized gas sensors. For example, an APTES-functionalized mesoporous silica and guanidine-based polymer layer was deposited onto a CMUT substrate.^[35] The device is operated at its mechanical resonance frequency and shows linear dependence of frequency shift with CO₂ concentration without saturating. Alternatively, SAW-based acoustic transducers monitor the propagation of SAWs in terms of amplitude, phase, and wave velocity. Any mass, conductivity, or stiffness change of the sensitive layer will affect these parameters.^[156] SAW-based sensors have already been utilized for the detection of humidity and organic analytes.^[157,158] More recently, porous MFU-4 films were directly grown from solution onto SAW substrates for the adsorption and detection of CO₂.^[141] However, because CO₂ interacts with MOFs solely by physisorption, the differentiation between CO₂ and other adsorbates remains a major issue. Nevertheless, owing to the fast response time and picogram accuracy, it is possible to differentiate absorbed gases by their uptake rate. Furthermore, temperature-dependent measurements allow the evaluation of the activation energy of CO₂ uptake and show that at low temperatures, the phase shift increases due to a higher mass loading. In another study, ZIF-8 is deposited onto SAW and QCM transducers and used as the CO₂ sensitive material with SAW sensors outperforming QCM devices.^[139]

Common Limitations of Sensors

A notable issue of many sensors is the cross-sensitivity towards interfering gases. Therefore, it is necessary to design sensors depending on their application field. Conceivable approaches include the use of coordinated sensor arrays that enable calibration procedures or sensor filters and coatings for the encapsulation of the sensing material. Alternatively, environmental effects can be compensated by specially designed circuitry, e.g. Wheatstone bridges. In addition, sensors should ideally be reversible and recover rapidly under mild conditions. Sensors that display high selectivity typically interact chemically with the analyte resulting in high activation energy for CO₂ desorption. As a consequence, pulsed or continuous heating as well as UV illumination are still required for many sensors.^[133] Possible solutions include the optimization of sensing layer morphology as well as the use of physisorbing materials showing enhanced reversibility but with the drawback of lower selectivity. Regarding the response and recovery times of sensors, direct

comparison of these characteristics from different studies is difficult because they are strongly dependent on gas flow as well as the volume of the respective flow chambers. Apart from this, an interesting approach using magnetic nanostirrers for enhanced response in gas sensors has been demonstrated recently.^[159] Cyclability and long-term stability are usually tested on a small number of pulses within a relatively short time scale, i.e. hours and days. However, it is necessary to test the sensors in a longer time scale to prove their usability in real-life applications. This is particularly important for sensors working in aggressive environments that are detrimental to the service life of the sensing layer. An alternative approach consists in protecting the sensor layers by employing coatings with selective gas permeability. Finally, because of the temperature and pressure-dependence of sensitivity, particularly for absorption-based sensors, it is necessary to calibrate both temperature and pressure using reference sensors. Moreover, there is a traditional trade-off between slow desorption at low temperatures and low sensitivity at high temperatures.

Table 9.1: Sensor characteristics of hybrid CO₂ sensors and indicators discussed within this section.

material	carrier	dynamic range	temperature/humidity	reference
	Air	500 ppm - 10 %	RT/80 % RH	[132]
PEI Starch@CNT	Syn. air	100 - 1000 ppm	RT-80 °C/-	[133]
Hydroquinone @3D-rGO	Syn. air	150 - 2400 ppm	RT/50 % RH	[134]
La ₂ O ₂ CO ₃ + P[VBTMA][PF ₆]	Syn. air	600 - 3200 ppm	RT/30-70 % RH	[135]
Al ₂ O ₃ + P[VBTMA][PF ₆]	Syn. air	400 - 3000 ppm	RT/24-78 % RH	[136]
PEI+SiO ₂	N ₂	0 - 100 %	10-50 °C/100 % RH	[57]
[BMIM][TOS]+ Silicone	N ₂	0 - 100 %	RT/-	[137]
ZIF-8@ SAW	N ₂	0 - 75 %	RT-50 °C/-	[138]
PAVB@ Optical fiber	N ₂	0 - 100 %	RT/-	[19]
CDMOF-2	N ₂	0 - 2 %	RT, regeneration at 120 °C/0-80 % RH	[35]
APTES@+ Mesoporous layer	N ₂	5 - 100 %	RT/-	[139]
ZIF-8@SAW	N ₂	500 ppt - 50 ppm	RT/42 % RH	[140]
PIL@SWCNT	N ₂ /He	1 ppm - 100 %	-63-28 °C/-	[141]
MFU-4@SAW	Ar	1 - 3 %	RT/100 % RH	[41]
NaYF ₄ :Yb:Er+ BTB+PS	-	-	RT/-	[142]
PNAAN@AuNP				

9.5 Organic–Inorganic Hybrids for Separation of CO₂

The efficient separation of CO₂ from gas mixtures is important e.g. in flue gas treatment (CO₂/N₂), natural gas sweetening (CO₂/CH₄), or syngas cleaning (CO₂/H₂).^[160–164] Conventional separation processes include amine scrubbing by aqueous alkanolamine solutions, pressure swing absorption, or cryogenic distillation.^[165–167] However, these processes are costly and/or energy intensive during regeneration, thus lowering plant efficiency and impeding the use in large-scale industrial applications. Furthermore, amine-based processes suffer from the volatility and corrosivity of amine solutions. A promising alternative is the use of solid separation membranes, which are characterized by simple operation, low energy consumption, and environmental friendliness.^[113,168–170] For instance, dense polymeric membranes show reasonable selectivity but an inherent permeability-selectivity trade off limits their use.^[171–173] Alternatively, inorganic membranes show enhanced permeability-selectivity,^[92] but these membranes are difficult to fabricate, expensive, and brittle. In fact, the low mechanical strength makes them particularly vulnerable to the high transmembrane pressure drop that is required for efficient separation. Recently, mixed matrix membranes (MMM), which are fabricated by incorporating filler particles such as zeolites, MOFs, carbon-based materials, or mesoporous silica into polymeric matrices, have been demonstrated to overcome permeability and stability issues.^[162,174,175] Here, we present the key parameters used to characterize gas separation membranes and describe recent advances in the development of hybrid materials for CO₂ separation. Finally, we discuss common limitations and solutions thereto.

Figures of Merit

Permeability and selectivity are the most important parameters utilized to characterize gas separation membranes:

$$\text{Permeability}_i = \text{Diffusivity}_i \cdot \text{Solubility}_i \quad (9.10)$$

$$\text{Selectivity}_{ij} = \text{Permeability}_i / \text{Permeability}_j \quad (9.11)$$

While selectivity is unitless, permeability is measured in barrer with 1 barrer = 10⁻¹⁰ cm³ (STP) cm cm⁻² s⁻¹ cm Hg which is related to the flow rate (cm³ (STP) s⁻¹), membrane thickness (cm) and area (cm²), as well as pressure difference across the membrane (cmHg). Note that one cm³ (STP) is not a volume but the amount of gas in one cm³ at standard temperature and pressure (STP). Importantly, there is a traditional permeability-selectivity trade-off exemplified by Robeson's upper bound^[176,177] restricting gas separation performance (see Figure 9.3). Because the permeability of a gas through a membrane is determined by its diffusivity as well as its solubility (see Equation 9.9), membranes based on size exclusion and solution-diffusion can be utilized taking advantage of physical and chemical differences between the gases, respectively. This is schematically shown in Figure 9.4. Moreover, because permeation is a thermally activated process following the Arrhenius equation, the temperature during the separation process needs to be controlled. Table 9.2 shows key properties of hybrid separation membranes.

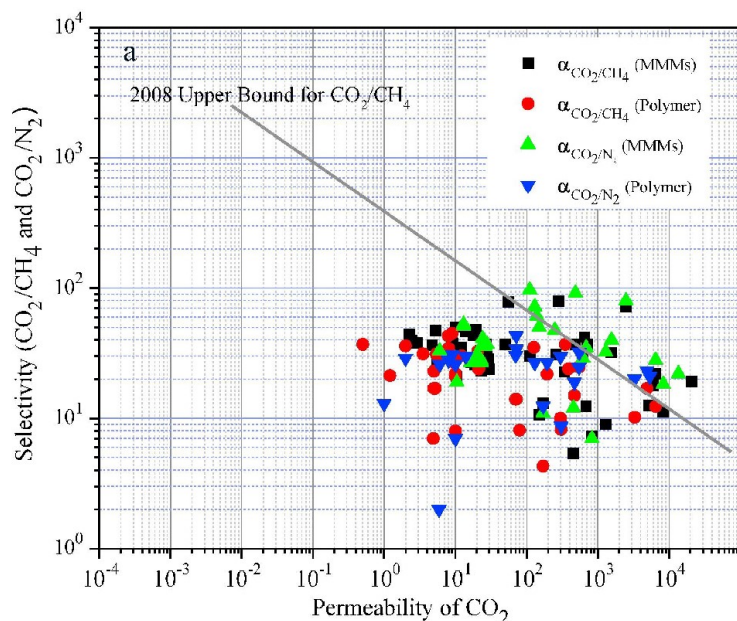


Figure 9.3: Selectivity versus permeability for the separation of CO₂ from CH₄ and N₂. It appears that MMMs (black squares, green triangles pointing up) generally perform better than the respective neat polymeric matrices (red circles, blue triangles pointing down). The straight line corresponds to Robeson's upper bound, which shows the experimentally defined permeability-selectivity limit. Note that both permeability and selectivity are plotted on a logarithmic axis. Reproduced from reference [14] with permission from the Royal Society of Chemistry.

Size Exclusion Mechanism

The size exclusion mechanism is based on the size-dependence of permeability. In fact, when CO₂ is separated using molecular sieves, a smart balance of pore size has to be found such that pores are small enough to efficiently separate the different gases and large enough to allow reasonable gas flow. Pore sizes of 5-10 Å were found to be suitable for separation of CO₂ whose kinetic diameter is smaller than many light gases, CO₂ (330 pm) < N₂ (364 pm) < CO (376 pm) < CH₄ (380 pm).^[188]

In particular, MOFs play an important role in molecular sieving and they are often used as filler material in hybrid membranes owing to their precisely tunable pore size. It is also possible to incorporate ILs into MOFs to fine-tune the effective aperture size. For instance [bmim][Tf₂N] was incorporated into ZIF-8 particles via in situ ionothermal synthesis.^[185] The [bmim]⁺ cation is used because of its size, which enables efficient cavity occupancy, whereas the [Tf₂N]⁻ anion promotes CO₂ absorption. Because 1-2 IL molecules are confined in each sodalite cage of ZIF-8, they lead to a strong decrease of surface area of the MOF host. By incorporating as prepared IL-modified ZIF-8 particles into a PSf matrix, CO₂ permeability as well as CO₂/CH₄ and CO₂/N₂ selectivities was remarkably increased. This example shows that it is possible to achieve a target-oriented alteration of MOF cut-off size through choosing ILs with proper chain length and by controlling the confinement ratios.

Alternatively, dual-channel pore engineering, i.e. the utilization of two different pore sizes in a single composite material, is an attractive method that combines precise separation with high

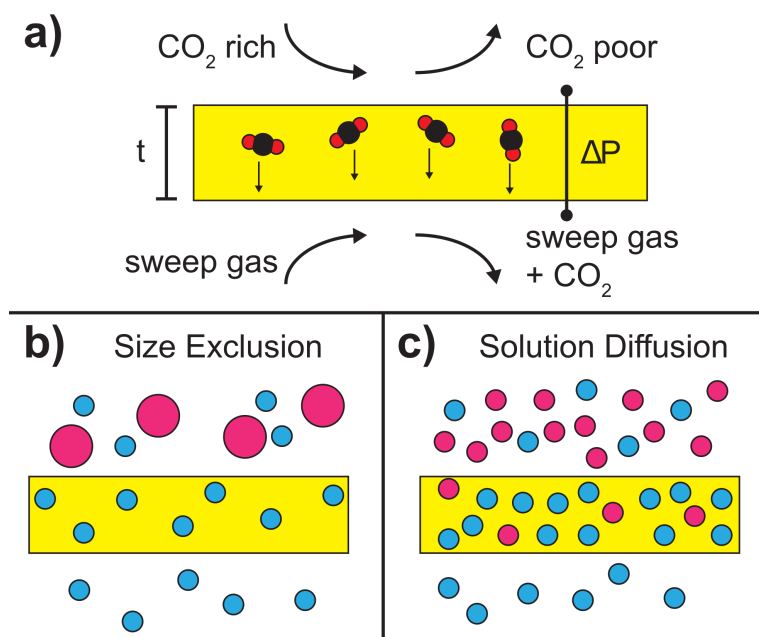


Figure 9.4: a) Schematic drawing of the gas separation process. On the top, a CO_2 rich gas reaches the membrane surface while on the bottom, the CO_2 that permeated through the membrane is removed using a sweep gas. The permeation is enhanced for small membrane thickness t and high transmembrane pressure drop ΔP . b) Separation via size exclusion. In contrast to gas molecules with a small kinetic diameter (blue circles), gas molecules with a large kinetic diameter (pink circles) do not permeate through the membrane. c) Separation via solution-diffusion. The membrane preferentially absorbs a particular gas (blue circles). The resulting concentration gradient with respect to the permeate side leads to higher permeability. Reproduced from reference [14] with permission from the Royal Society of Chemistry.

permeability. For example, particles composed of a UiO-66-NH₂ core with large pores surrounded by a ZIF-8 shell with small pores were fabricated and embedded in a PSf matrix as shown in Figure 9.5a.^[178] The advantage of such core/shell particles is that the large pores of the MOF provide facilitated transport pathways whereas the smaller pores of the ZIF as well as incommensurately overlapping pores at the MOF/ZIF interface act as the sieving layer. Furthermore, it is possible to optimize permeability and selectivity by adjusting the shell thickness. Similar observations were made utilizing porous liquids as dual-channel molecular sieves where hollow silica spheres coated with a microporous shell were used for gas separation.^[179] As obtained core/shell particles can further be functionalized with organosilane moieties that react with hydroxy groups on the shell surface. Eventually, a poly(ethylene glycol)-tailed sulfone canopy is added. Such organic-inorganic particles, which remain liquid even under vacuum condition, can be embedded in a polymeric matrix to obtain solid membranes. In these materials, two effects are actively taking part in the separation process: the acid/base interaction of CO_2 with ether groups in the canopy and the diffusion process through the cavities of the porous liquid that provide free volume.

A useful strategy to increase membrane selectivity involves the decrease of permeability of larger gas molecules by homogeneously incorporating exfoliated nanosheets or layered materials into the gas separation layer. Moreover, the layered structure forces the CO_2 molecules to diffuse

along 2-dimensional voids, thus free diffusion pathways are efficiently eliminated. For instance, MoS₂, montmorillonite, Mg-Al hydrotalcite, or CuBDC MOF were dispersed in various polymers such as PSf or PI.^[114,162,180] Note that a main disadvantage of this approach is the strong filler orientation-dependence of overall gas permeability.

Finally, many efforts are made targeting at the enhancement of CO₂ permeability by tuning the geometry of membranes, especially by reducing the membrane thickness. This leads to less tortuosity for the diffusing species and diminution of gas diffusion resistance. For example, ultrathin asymmetric MMM layers have been created.^[36] Alternatively, it has been shown that capillary-based structures can be chemically modified in a way that only a small fraction of the capillary is filled by the gas separation medium, yielding μm thin membranes (see Figure 9.5b).^[189]

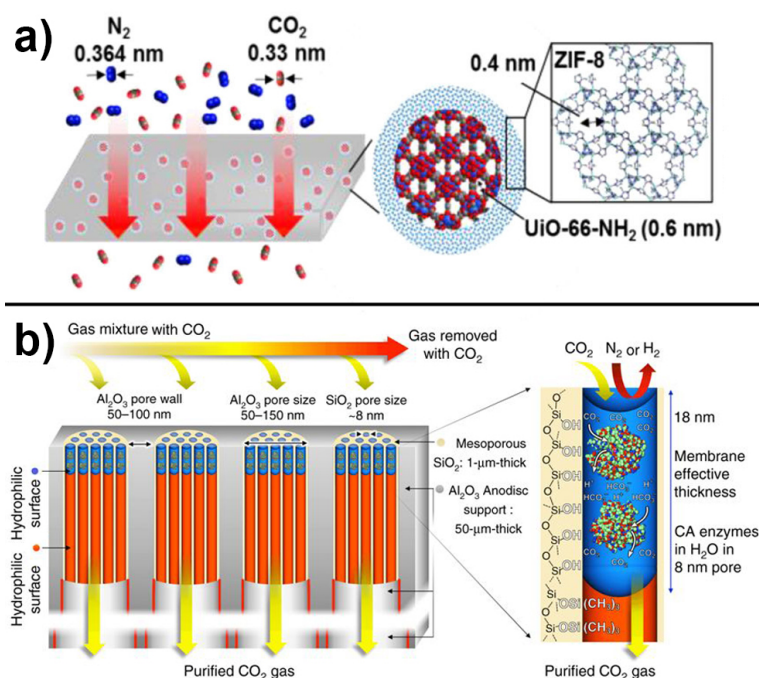


Figure 9.5: a) Dual channel pore engineering. The gases are separated according to their kinetic size using ZIF/MOF core-shell structures embedded in a polymeric matrix. From reference [178]. b) Approach to decrease layer thickness, tortuosity, and thus increase permeability. Reproduced from reference [14] with permission from the Royal Society of Chemistry.

Solution-Diffusion Mechanism

Separation via solution-diffusion utilizes the high and selective CO₂ solubility of the organic matrices in hybrids that is often related to the comparably high quadrupolar moment of CO₂ with respect to other light gases such as N₂ or CH₄. For example, CO₂/N₂ selectivity can be adjusted by focusing on CO₂-philicity or N₂-phobicity of the membrane material. It is important to note that in membranes based on the solution-diffusion mechanism, the permeance is not necessarily following the kinetic diameter of gases. Many ILs have inherent CO₂/N₂ permeability-selectivity and can be inserted into polymeric network membranes for separation applications.^[22,190] However, a common issue with such supported ionic liquid membranes (SILM) is the leakage of ILs and blow-out effect occurring at high transmembrane pressure drops. Consequently, membranes

with chemically bound functional groups are considered more durable than their counterparts with mobile carriers. A possible approach is the fabrication of ion gel membranes combining RTIL and a 3D network of inorganic nanoparticles in a stabilizing polymeric matrix, thus forming so-called double network gels where inorganic nanoparticles lead to toughening of the membranes.^[191–194] For instance, [C2mim][Tf₂N]^[182] and [C2mim][B(CN)₄]^[181] ILs were combined with silica and incorporated into a polymeric matrix. It turns out that the ionic liquid promotes CO₂ solubility and enhances the adhesion between the silica particles and the polymeric matrix. Concurrently, the fragile inorganic network can easily be ruptured, thus dissipating the energy loaded upon the ion gel, which in turn leads to increased toughness. Furthermore, as prepared membranes show good compression stress behavior and are able to withstand high pressure difference over several days, suggesting good IL holding property. The observed effects are in strong contrast with standard SILMs, thus underlining the utility of double network gels. Common issues observed when filler particles are dispersed in an organic matrix include the aggregation and poor particle dispersion as well as voids between the filler and the matrix material. All of these effects are detrimental to efficient separation. Nevertheless, these issues can be tackled by chemically modifying the filler particles. For instance, MIL-53 particles were functionalized with aminosilanes and blended into poly(ether imide).^[184] MIL-53 increases the permeance while the aminosilanes act as interfacial bridges to the polymer and enhance adhesion. This prevents nonselective transport through defects in the skin layer at the MOF/matrix interface. On the other hand, the poly(ether imide) provides mechanical, thermal, and chemical stability together with high selectivity. Furthermore, CO₂ accumulates at adsorption sites and thus leads to a crowding out effect by the formation of a large concentration gradient that accelerates the diffusion of CO₂. Alternatively, MOF structures can be decorated with IL moieties and incorporated into polymeric matrices. In the case of [bmim][Tf₂N]/ZIF-8/PEBA composites, the addition of ZIF-8 particles results in both a stiffening of the PEBA matrix as well as an increase of CO₂ permeability by the formation of narrow voids.^[183] Furthermore, the addition of IL improves the compatibility of ZIF-8 with the polymeric matrix, thus lowering the crystallinity and yielding higher free volume that in turn is beneficial for gas diffusion. Moreover, by employing [BF₄][−] and [DCA][−] anions, the importance of the anion choice is demonstrated. Indeed, the use of [Tf₂N][−] yields highest permeability, whereas [BF₄][−] yields best CO₂/CH₄ selectivity and [DCA][−] yields best CO₂/N₂ selectivity. Interestingly, the composites show relative diffusivities CO₂ > N₂ > CH₄ which is in accordance with their kinetic diameter. Also, GO can be utilized to tune the CO₂ selectivity, solubility, and permeability. For example, [emim][BF₄]/GO/PEBA thin film membranes are suitable for CO₂/N₂ and CO₂/CH₄ separation.^[186] Indeed, CO₂ binds to oxygen-containing functional groups on the GO surface whereas diffusion of other gases is impeded by increased tortuosity as a result of the insertion of GO nanosheets. With increasing humidity and temperature, the overall permeance increases, but at a higher rate for N₂ than CO₂, thus decreasing the selectivity of the hybrid. Regarding long-term operability, it is noteworthy to mention that even though the permeance decreases over time, the selectivity is retained for at least half a year. Furthermore, it is believed that the use of a PDMS matrix is a possible solution to avoid increased transport resistance after ageing. Similarly, separation membranes made from GO embedded in PEO-PBT copolymer were tested.^[187] However, it appears that if the content of GO is too high, the nanosheets begin to stack, eventually hindering the efficient diffusion of

CO₂.

Common Limitations of Sorbents and Separation Membranes

Humidity has a strong influence on separation performance and many membranes need the CO₂-carrying gas stream to be humidified in order to avoid drying-out. Furthermore, because high pressure drops across the membrane are required for efficient separation, mechanical strength of membranes is important. Due to the trade-off between mechanical strength and diffusivity, practical solutions such as the use of strong polymer networks and dual-network structures need to be utilized. In addition, the performance stability over time is a major issue in hybrid separation membranes. This is particularly important for membranes based on ILs. Furthermore, it will be necessary to develop new regeneration methods in order to optimize long-term stability. Also, the large majority of hybrid membranes are being used for CO₂/N₂ separation. However, gas purification processes usually contain gas mixtures and impurities as SO₂, H₂S, CO, H₂. Therefore, it will be important to study selectivity of CO₂ compared to diverse gas components and to focus on other separation processes such as CO₂/CO, CO₂/CH₄ or CO₂/H₂ as well. Finally, an enormous potential lies within the utilization of computational methods to predict the CO₂ separation characteristics of potential MMMs.^[195]

Table 9.2: Key characteristics of different hybrid materials used for CO₂ separation.

material	carrier gas/ selectivity	CO ₂ permeability	ΔP	reference
ZIF-8 @ UiO-66-NH ₂ in PSf	N ₂ /39	45.2 barrer	-	[178]
PEG+organosilane @ SiO ₂	N ₂ /10	158 barrer	-	[179]
MoS ₂ + PEBA+ PDMS in PSf	N ₂ /93	64 barrer	-	[180]
poly(PEA-Montmoril- lonite-TMC) in PSf	N ₂ /37	16 barrer	1 bar	[114]
poly(PEA-Hydro- talcite-TMC) in PSf	N ₂ /40	15 barrer	1 bar	[114]
[C ₂ mim][B(CN) ₄] + SiO ₂ in PDMAAm	N ₂ /38	2600 barrer	6 bar	[181]
[C ₂ mim][Tf ₂ N] + SiO ₂ in PIL	N ₂ /24	500 barrer	6 bar	[182]
[bmim][Tf ₂ N] + ZIF-8 in PEBA	N ₂ /42	231 barrer	1 bar	[183]
MIL-53 + Amino- silane in poly(ether imide)	N ₂ /41	24 GPU	6 bar	[184]
CuBDC + polyimide	CH ₄ /85	3-6 barrer	7.5 bar	[162]
[bmim][Tf ₂ N] @ZIF-8 in PSf	N ₂ /152 CH ₄ /66	310 barrer	10 bar 20 bar	[185]
[emim][BF ₄] + GO in PEBA	N ₂ /44 CH ₄ /11	981 GPU	-	[186]
GO in PEO-PBT	N ₂ /73 CH ₄ /21 H ₂ /12	143 GPU	-	[187]

9.6 Organic-Inorganic Hybrids for Catalytic Conversion of CO₂

Nature has established a dynamic equilibrium between generation and recovery of carbon dioxide. Indeed, CO₂ is emitted e.g. by decomposition of organic matter or by respiration^[196] while plants and algae capture gaseous or dissolved CO₂ and photosynthetically convert it back to carbohydrates. However, there is a man-made imbalance between emission and recovery that should be reverted by considering CO₂ as a renewable carbon feedstock. In fact, by combining CO₂ capture and storage technology with CO₂ conversion on industrial scale, an artificial, carbon-neutral life cycle can be mimicked. Chemical fuels obtained from the conversion of CO₂ are attractive in terms of energy storage owing to their 10 to 100-fold higher energy density as compared to batteries.^[197,198]

After the first attempts to catalytically reduce CO₂ in 1870,^[199] it took nearly one century until research in this field intensified between the 1970s and 1980s where photo- and electrocatalytic reduction of CO₂ to methane,^[200,201] ethylene,^[200] formic acid,^[201,202] methanol,^[201,202] and formaldehyde^[201,202] were demonstrated. Among various photocatalytically active semiconductor materials, TiO₂ has been investigated most extensively owing to its high availability, low cost, and high chemical stability.^[203] However, photocatalytic efficiency for CO₂ conversion is often limited by high electron-hole recombination rates and low visible light absorption that is related to the wide-bandgap of TiO₂. Consequently, several strategies were developed to enhance visible light absorption including doping, deposition of metal co-catalysts that act as electron sinks and suppress electron-hole recombination, or formation of heterostructures where two semiconductor materials are coupled to promote charge carrier separation.^[119,204–210] Furthermore, the role of surface reactions,^[205,211] morphology and crystal phase of semiconductors,^[206] inorganic-inorganic hybrid materials,^[212] metal oxides,^[119,207] or size dependency of metal catalysts^[209] were studied. Alternatively, organic-inorganic hybrid materials can be utilized because the organic part allows introduction of functional groups like amines or ionic liquids, which act as mediators for the electro- and photochemical reduction of CO₂. Recently, imidazolium-based ionic liquids were used as additives in electrolytes to enhance electrocatalytic reduction of CO₂ due to increased solubility of CO₂ and significantly lower energy barrier for electron-transfer processes.^[209,213,214] Additionally, amine functionalization of titania nanoparticles,^[215] zinc oxide,^[216] or titanate nanosheets^[217] substantially improved CO₂ adsorption - thus enhancing photocatalytic activity.^[215]

In this section, we briefly present the theoretical background of CO₂ conversion by electro- and photocatalytic processes and discuss different hybrids based on MOFs, g-C₃N₄, carbon materials and organically doped metals. We then present and discuss future perspectives of organic-inorganic hybrid materials for CO₂ reduction.

Thermodynamics and Kinetics of CO₂ Conversion

CO₂ is a product of the combustion (oxidation) process of organic matter and its carbon atom displays an oxidation state of +IV. Because the bonding energy of a C=O double bond is 750 kJ mol⁻¹, which is considerably larger than C-C (336 kJ mol⁻¹), C-O (327 kJ mol⁻¹) or C-H bonds (411 kJ mol⁻¹), the photo- or electrocatalytic reduction of CO₂ (see Figure 9.6) is challenging from a thermodynamic point of view. Typical products of the CO₂ reduction process display

oxidation states of carbon ranging from +II (CO) to -IV (CH₄) and can be formed by different pathways involving the transfer of multiple electrons. One-electron reduction is complicated by big structural differences between the linear CO₂ and the bent CO₂-molecule (Equation 11) in Table 9.3).^[218] On the contrary, proton-assisted multi-electron transfer processes exhibit significantly lower redox potentials and yield manifold reaction products like CO, HCOOH (Equation 12), MeOH (Eq. 16), or CH₄ (Eq. 17). The redox potential limits the products that are obtained since reactions with more positive redox potential are more likely to happen. On the other hand, the number of electrons dictates the reduction kinetics. For example, the reduction of CO₂ to CH₄ is thermodynamically favoured but kinetically suppressed because eight electrons need to be transferred simultaneously. Consequently, it is hard to achieve high selectivity in electro- or photocatalytic reduction of CO₂.^[219] Because CO₂ is inert under UV-vis and at RT, semiconduc-

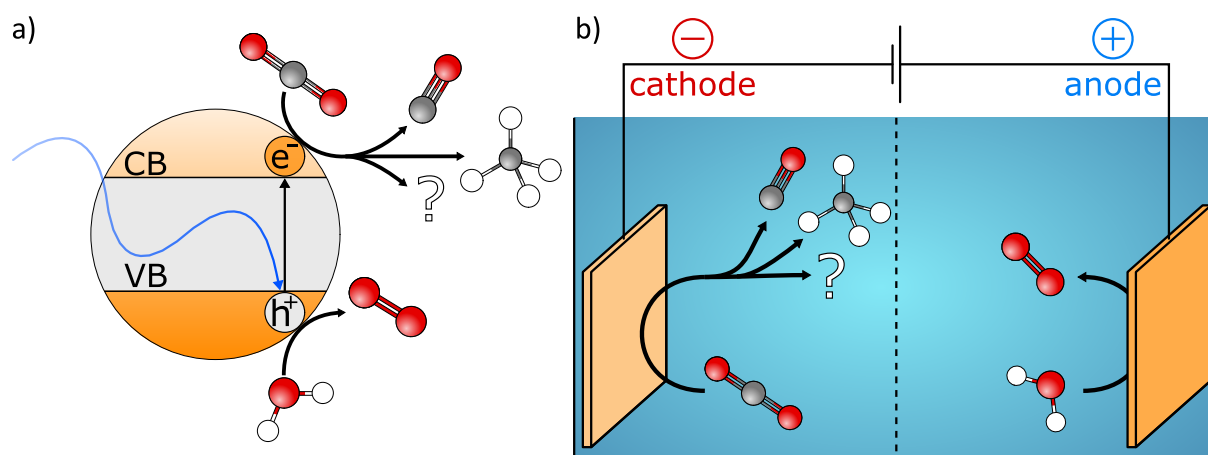


Figure 9.6: Schematic representation of a) the photo- and b) the electrocatalytic reduction of CO₂. During photocatalytic reduction, a photon is absorbed by a semiconductor under the formation of an electron-hole pair. While the electron in the conduction band (CB) can be utilized to reduce CO₂, the hole in the valence band (VB) commonly drives the oxidation of water. Similar reactions take place during the electrocatalytic reduction of CO₂. However, in this case, electrons and holes are provided by an external power supply and the cathodic reduction and anodic oxidation processes are spatially separated by a membrane. Reproduced from reference [14] with permission from the Royal Society of Chemistry.

tor catalysts are required for its photocatalytic reduction. The bandgap of the catalyst affects the portion of the absorbed solar spectrum, and the respective positions of the valence band (VB) and conduction band (CB) determine the photocatalytic performance. Consequently, band structure engineering enables the enhancement of photon efficiency. For instance, if the CB is at more negative potential than the redox potential of the corresponding CO₂ reduction reaction, the transfer of photogenerated electrons to surface-adsorbed CO₂ molecules is facilitated. On the other hand, if the VB is at more positive potential than the H₂O oxidation reaction (Eq. 18), the consumption of photogenerated holes is enabled. Although H₂O seems well suited for the neutralization of photogenerated holes (Eq. 18) and for providing protons for the reduction reactions, protons also compete with electrons in the CB for the generation of hydrogen (Eq. 15).^[220] This dual behaviour of H₂O is one of the major challenges in electrocatalytic reduction of CO₂. While the extent of the photocatalytic reduction is determined by the position of the

CB, it additionally depends on the applied bias in the case of the electrocatalytic reduction. Consequently, the selectivity of the reduction reaction can be influenced by the applied potential^[221] and in order to increase electrocatalytic conversion efficiency the inherent charge carrier mobility has to be optimized. Both approaches require facile transfer of multiple electrons from the catalyst to the CO₂ molecule. Furthermore, the surface of the catalyst should facilitate adsorption of reactants, while efficient desorption of reaction products avoids catalyst poisoning. Moreover, the nature of the products and their purity are determined by the chemical properties of the catalyst material like CO₂ binding affinity and redox behaviour. However, combining selectivity, activity, and efficiency into a single catalyst material is very challenging. Nevertheless, organic-inorganic hybrids were shown to enhance the electro- and photocatalytic activity by optimizing light harvesting, charge separation as well as mass transport and CO₂ affinity.

Table 9.3: Redox potentials of CO₂ reduction and side reactions ordered by their redox potential. Redox potentials are tabulated versus normal hydrogen electrode (NHE) under standard conditions in aqueous solution (pH 7, 25 °C, 1 atm).^[222]

reaction		redox potential vs. NHE, pH 7.0	equation
CO ₂ + e ⁻	⇌ CO ₂ ⁻	E = -1.90 V	(8.12)
CO ₂ + 2 e ⁻ + 2 H ⁺	⇌ HCOOH	E = -0.61 V	(8.13)
CO ₂ + 2 e ⁻ + 2 H ⁺	⇌ CO + H ₂ O	E = -0.53 V	(8.14)
CO ₂ + 4 e ⁻ + 4 H ⁺	⇌ HCHO + H ₂ O	E = -0.48 V	(8.15)
2 H ⁺ + 2 e ⁻	⇌ H ₂	E = -0.41 V	(8.16)
CO ₂ + 6 e ⁻ + 6 H ⁺	⇌ CH ₃ OH + H ₂ O	E = -0.38 V	(8.17)
CO ₂ + 8 e ⁻ + 8 H ⁺	⇌ CH ₄ + 2 H ₂ O	E = -0.24 V	(8.18)
2 H ₂ O + 4 h ⁺	⇌ O ₂ + 4 H ⁺	E = 0.82 V	(8.19)

Figures of Merit

The photo- or electrocatalytic reduction of CO₂ is a complicated, multi-step process in which different aspects as light absorption, charge carrier separation and movement to surface reaction sites or adsorption and desorption of molecules determine the overall efficiency. Besides these multi-step processes, also sample geometry and experimental parameters such as temperature, illumination, gas flow and composition play a decisive role.^[211,223–225] However, currently there is no single quantity which considers this complexity and allows distinct comparison of several catalyst materials. Instead, there are measures which relate the performance to either amount of catalyst, illumination power or amount of catalytic active sites. For electrocatalytic reduction, turnover frequency (TOF) and faradaic efficiency are commonly used as performance metrics to evaluate CO₂ reduction electrocatalysts. TOF is defined as rate of electrochemical conversions per number of catalytic active sites and illustrates its activity. In order to reflect selectivity of

electrocatalysts, the faradaic efficiency of a certain product is defined as the ratio of transferred charges to obtain the product relative to the number of total charges. The faradaic efficiency is often restricted by H₂ formation. Therefore, faradaic efficiencies >80 % are considered for good CO₂ reduction electrocatalysts.^[226]

For photocatalytic reduction, the most often used quantity is the rate-per-weight of a product that is usually given in mol of product per hour of illumination and per gram of catalysts (mol h⁻¹ g⁻¹). However, the rate-per-weight data is specific for the material and experimental setup and does not reflect the intrinsic catalytic activity. Moreover, TOF values can be calculated based on the specific area of the photocatalysts obtained by Brunauer–Emmett–Teller (BET) measurements. Nevertheless, due to internal shading not the complete surface area is uniformly illuminated, which means that the surface area may not accurately describe the number of available catalytic active sites. Additionally, even if the number of catalytic sites can be accurately described, it is unclear how many are actually active throughout the entire experiment. At present there is no straight-forward quantity which can be used to compare the catalytic performance of different materials obtained by different experimental setups. To avoid misleading interpretations of experimental data and to allow better comparison within the CO₂ reduction community, rigorous testing protocols including advanced scientific techniques like ¹³CO₂ isotope labelling are mandatory when studying CO₂ reduction.^[227] Since the discussion of merits is beyond the scope of this review we would like to refer to publications which exclusively deal with objective evaluation of catalyst's performance.^[228–234]

By choosing adequate building blocks of MOFs, it is possible to incorporate photosensitizers or catalytic centres directly in the MOF structure. For example, it was demonstrated that CO₂ is reduced to formate anions under visible light irradiation using MIL-125.^[112] The amine functional group within the structure led to improved CO₂ adsorption capability and extended the upper bound of visible light absorption from 350 to 550 nm. More recently, it was demonstrated that photocatalytic properties of MOFs can be tuned by small variations of the backbone. Indeed, a series of MIL-125 materials whose organic linker feature N-alkyl substituents with increasing chain length and varying connectivity (primary or secondary amines) were prepared.^[235] In fact, inductive electron donating ability depends on chain length and reduces the optical band gap from 2.56 to 2.29 eV, whereas the utilization of secondary amines enhances the lifetime of excited states. In particular, MIL-125-NH-cyclopentyl shows optimum activity due to its long-living excited state and narrow band gap. These observations demonstrate that small variations in the MOF backbone strongly influence photocatalytic properties for CO₂ reduction.

Also MOF-based hybrids are fabricated to boost selectivity, activity, and efficiency of CO₂ reduction catalysts.^[236] For example, Re3-UiO-67 was deposited onto Ag nanocubes (see Figure 9.7a) to confine photoactive Re centres to the plasmon-intensified electric field at the surface of Ag nanocubes, resulting in a 7-fold enhancement of CO₂ to CO conversion under visible light as compared to bare Re3-UiO-67.^[237] To enable plasmon-enhanced reduction, the localized surface plasmon resonance (LSPR) peak of the metallic nanoparticle has to overlap with the absorption range of the linker molecule of the MOF. Due to the material- and size-dependency of the LSPR, plasmon-enhanced photocatalytic activity should be transferable to different MOF materials that show enhanced selectivity to higher-valued hydrocarbons.

Another attractive alternative used to improve light absorption is the combination of MOFs

with semiconductor materials. For example, ZIF-8 nanoparticles were grown onto semiconducting Zn₂GeO₄ nanorods or HKUST-1 was coated with a porous TiO₂ shell, thus resulting in a strong enhancement of photocatalytic CO₂ to CH₃OH or CO₂ to CH₄ conversion as compared to bare Zn₂GeO₄ and TiO₂, respectively.^[238,239] These observations are explained by the successful combination of the CO₂ adsorption property of ZIF-8 and HKUST-1 and the light harvesting ability of Zn₂GeO₄ and TiO₂ (Figure 9.7c), respectively.

Noble metal nanoparticles can also be used to tune the CO₂ conversion selectivity of catalysts (see Figure 9.7b).^[240] First, by replacing rigid linker molecules of a Ni-based MOF with softer molecules, a spongy, disordered, and defective metal-organic material with high selectivity in photocatalytic CO₂ to CO conversion can be obtained. Second, the selectivity can be tuned by decorating the spongy material with Ag or Rh nanoparticles resulting in the formation of formic acid or acetic acid as a major product, respectively. These observations were attributed to further reduction of the intermediate CO molecules, as depicted in Figure 9.7b.

Metal-Organic Frameworks and Their Hybrids

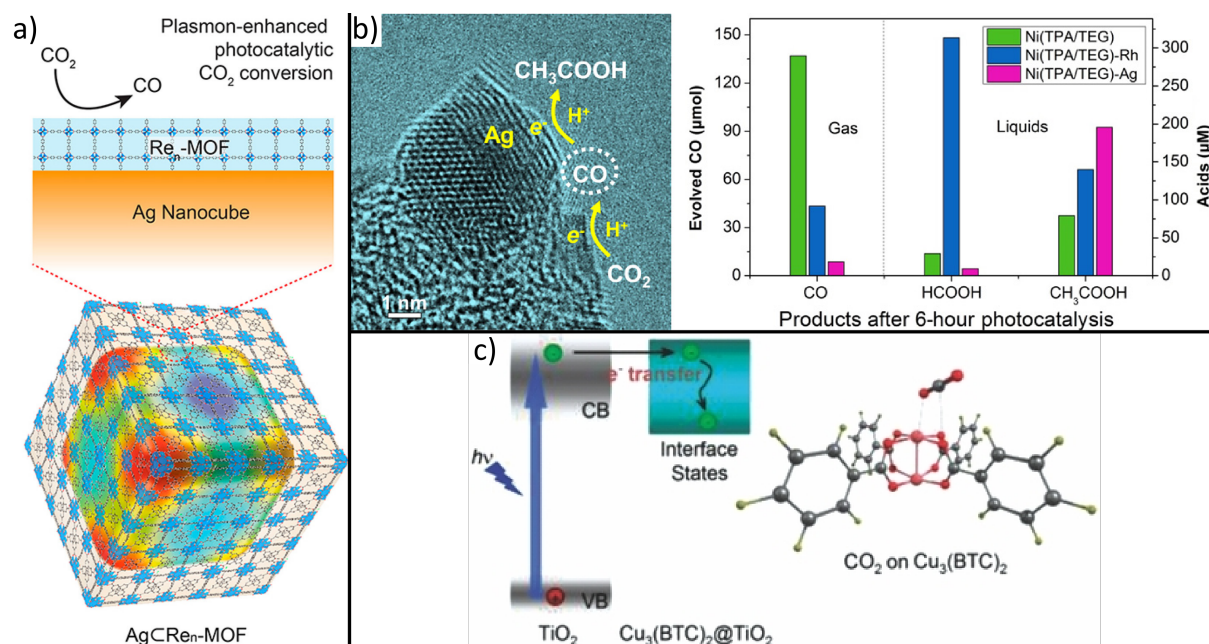


Figure 9.7: MOF-based hybrids synthesized to boost activity, selectivity and efficiency of CO₂ photoreduction. Integration of metal nanoparticles, (a) incorporates a plasmon-intensified electric field leading to higher photonic efficiency within the MOF building block or (b) controls selectivity by loading different type of metals.^[237,240] Moreover, (c) superior CO₂ adsorption on Cu sites of HKUST-1 causes dramatically improved performance and selectivity compared to bare TiO₂.^[239] Reproduced from reference [14] with permission from the Royal Society of Chemistry.

Carbon Materials

Due to their intrinsic advantages such as abundant natural resources, low cost and variety of dimensions, carbon-based materials like fullerenes (0D), carbon nanotubes (1D) and graphene (2D) have attracted great attention as alternatives to costly noble metal based electrocatalysts in recent years.^[241–243] Although carbon catalysts show excellent activity for electrocatalytic conversion of CO₂, effect of heteroatom doping and structural defects as an origin for its activity are currently under debate and not fully understood.^[243] Moreover, quality of commercial graphene flakes is rather poor and irregular as they contain different type of impurities, thus hindering comparison between different studies and real-world applications of final products.^[244] Nevertheless, the $\pi - pi$ interaction between graphene and CO₂ can cause destabilization and activation of CO₂ for facilitated reduction reactions.^[245] Moreover, through its 2-dimensional structure with high specific surface area and conductivity, graphene has been widely used to promote electron-hole separation during photocatalytic reduction of CO₂.^[210,246–250] For example, graphene-TiO₂ hybrid thin films yield strong enhancement in the photo-reduction.^[248]

Besides graphene, GO was demonstrated to significantly enhance CO₂ photoreduction. Recently, it was shown that the band gap of GO can be tuned by the carbon to oxygen ratio, an effect that can be exploited to optimize CO₂ to MeOH conversion.^[251] Although pristine GO shows six-fold enhancement of CO₂ to MeOH conversion efficiency as compared to commercial TiO₂ nanoparticles, even higher conversion rates are required for practical applications. For this, GO was decorated with Cu nanoparticles, thus yielding high and tuneable methanol and acetaldehyde production rates.^[252] This tendency was attributed to enhanced electron-hole separation and to a change in the GO CB position with increasing Cu loading as shown in Figure 9.8a.

However, graphene hybrids are not only prominent for high electron mobility which relieves charge transfer of photogenerated electrons, but also for prevention of catalyst degradation. In detail, attack of active species like OH radicals on photoactive CdS NPs can be avoided by wrapping GO around positively charged CdS NPs as shown in Figure 9.8b.^[253] By subsequent grafting of ethylenediamine via coupling reaction between one amine group and the carboxylic acid group of GO, CO₂ adsorption capacity was several times higher than in rGO/CdS, thus resulting in an enhanced photocatalytic activity. There is a strong need for alternatives to typical II–VI semiconductors like CdS since their toxicity often prevents practical use. In fact, perovskite materials have attracted great interest in the field of optoelectronic devices such as LEDs or photovoltaic cells owing to high extinction coefficients, wide absorption ranges, and long charge carrier diffusion lengths.^[254,255] These outstanding optical properties ensue perovskites as interesting candidates for efficient photocatalytic CO₂ reduction. Recently, GO was decorated with CsPbBr₃ quantum dots (QD).^[256] Compared to individual CsPbBr₃ QDs, photocatalytic activity of CsPbBr₃/GO composites was increased mainly because of fast separation and suppressed recombination of photogenerated electron-hole pairs. Nevertheless, insufficient stability and toxicity of CsPbBr₃ also limits their practical application. Therefore, the development of lead-free halide perovskites where Pb is replaced by less toxic Sn, Sb or Bi is of significant academic and industrial interest.^[257]

As an alternative to noble metals or toxic semiconductor materials, transition metal disulfides such as tungsten disulfide (WS₂) or molybdenum disulfide (MoS₂) are increasingly attracting attention due to low price and outstanding electrocatalytic performance. The latter is commonly

attributed to the metallic character and high d-electron density at Mo-terminated edges.^[258] For example, graphene/MoS₂/TiO₂ hybrids with hierarchical porosity were prepared by self-assembly in a simple one-pot hydrothermal synthesis and applied for photocatalytic reduction of CO₂.^[259] The 3-dimensional, graphene-based aerogel decreases the electron-hole recombination by creating an electron-conduction channel from TiO₂ to MoS₂, while the macroporous structure offers efficient mass transport, large surface area, mechanical stability, and enhanced light harvesting via multiple reflections. This noble metal-free approach offers a high CO selectivity and higher production yield than bare TiO₂ by integrating structural and functional merits of TiO₂, MoS₂ and graphene into a 3-dimensional material, as shown in Figure 9.8d. In another inspiring approach, the catalytic performance of a hierarchical N-doped carbon/NiCo₂O₄ double-shell nanobox benefits from a unique composition and structure.^[260] For this, sacrificial Fe₂O₃ nanocubes were coated with a thin layer of polydopamine, which was subsequently pyrolyzed under N₂ atmosphere to create an N-doped carbon shell. In a further step, the oxide core was selectively etched to generate hollow nanoboxes while in a last step, NiCo₂O₄ nanosheets were grown on the nanoboxes via a hydrothermal reaction (Figure 9.8c). Regarding photoreduction of CO₂, such hollow nanoboxes combine structural and functional features like catalytic activity of NiCo₂O₄, high electrical conductivity of the carbon-based inner layer, large active surface area, and enhanced light absorption by multiple light scattering events within the hollow structure.

Graphitic Carbon Nitride

g-C₃N₄ shows increased absorbance in the visible-light range as compared to commonly used catalysts such as TiO₂. However, the photocatalytic efficiency is limited by fast electron-hole pair recombination.^[82,261] Therefore, many attempts were made to overcome this challenge by combining g-C₃N₄ with inorganic materials.^[212] For example, charge carrier separation is facilitated by utilizing noble metals or other semiconductors.^[212] Moreover, the deposition of Pt nanoparticles on g-C₃N₄ not only boosts CO₂ reduction activity, but also affects the selectivity for CO₂ conversion to methane, methanol, and formaldehyde.^[262] In detail, Pt acts as a sink for photogenerated electrons and therefore prevents the electron-hole recombination. By investigating the role of single Pd or Pt atoms deposited on g-C₃N₄ using DFT calculations, it turns out that during the reduction reaction, the noble metal atoms act as active sites while the g-C₃N₄ provides hydrogen from hydrogen evolution reaction.^[263] Furthermore, it appears that HCOOH and CH₄ are preferentially produced by Pd/g-C₃N₄ and Pt/g-C₃N₄, respectively. In another study, Ag-decorated g-C₃N₄ shows direct generation of syngas during electrocatalytic reduction of CO₂ in water.^[264] Furthermore, the H₂/CO ratio can be adjusted by varying the applied potential and the Ag particle loading. Moreover, no significant loss of selectivity or activity was observed, thus demonstrating high stability of g-C₃N₄ in electrocatalytic conditions. Note that the produced syngas can directly be reacted to industrially relevant chemical fuels via Fischer-Tropsch process or MeOH synthesis.

Alternatively, g-C₃N₄ can be decorated with semiconducting materials, which facilitate electron-hole pair separation. For instance, Ag₃PO₄/g-C₃N₄ hybrids efficiently separate electron-hole pairs based on a z-scheme mechanism, where holes from the VB of g-C₃N₄ combine with elec-

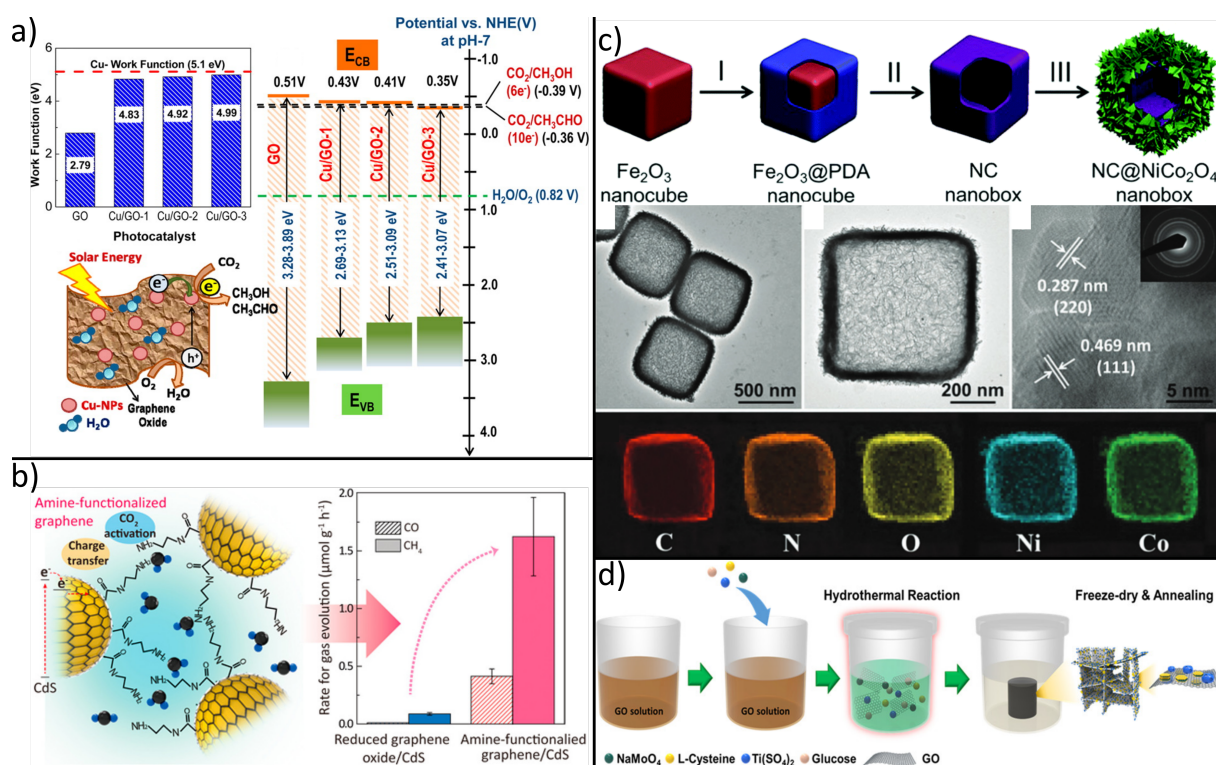


Figure 9.8: Carbon-based hybrids synthesized for improved CO₂ conversion by tuning (a) selectivity, (b) affinity and (c+d) by creating hierarchical architectures. (a) Decoration of GO with increasing amounts of Cu nanoparticles leads to a decrease of CB position and eventually to different products. (b) Grafting of ethylenediamine leads to higher CO₂ adsorption capacity and photocatalytic activity.^[253] Synthesis of hierarchical (c) graphene/MoS₂/TiO₂^[259] and (d) N-doped carbon/NiCo₂O₄ double-shell nanoboxes^[260] enable improved CO₂ reduction capabilities by enhanced mass transport and light harvesting. Reproduced from reference [14] with permission from the Royal Society of Chemistry.

trons from the CB of Ag₃PO₄, resulting in the generation of electrons and holes in the CB of g-C₃N₄ and VB of Ag₃PO₄, respectively. Consequently, the recombination of photocatalytically active electrons is strongly suppressed.^[265] The same mechanism is observed in hierarchical structures that combine 3D urchin-like α-Fe₂O₃ and g-C₃N₄.^[266] Such hybrids display facilitated electron-hole pair separation, increased binding energy, and increased CO₂ adsorption capacity, thus demonstrating the utility of z-scheme g-C₃N₄ based photocatalysts. Moreover, many other materials were combined with g-C₃N₄ including CdS,^[267] ZnO,^[268] CeO₂,^[269] TiO₂,^[270] WO₃,^[271] In₂O₃,^[272] BiOI,^[273] LaPO₄,^[274] CdMoO₄,^[275] and Bi₂WO₆.^[276]

Because the electron transfer from catalytic active site to CO₂ requires an intimate contact, adsorption of CO₂ on the catalyst surface is essential for efficient CO₂ reduction. For this, g-C₃N₄ was combined with ZIF-9^[277] and UiO-66^[278] cocatalysts that enhance the adsorption of CO₂ and separation of photogenerated charge carriers. Furthermore, besides exploiting the high specific surface area of MOFs, CO₂ adsorption of g-C₃N₄ can be facilitated by chemical functionalisation. Recently, amino-rich g-C₃N₄ containing carbon defects and intercalated [K]⁺ ions was synthesized.^[279] Amino-groups on the surface of g-C₃N₄ strongly enhance CO₂ adsorption and conversion, and activate the CO₂ molecule for subsequent reduction processes,^[280] while K⁺

and carbon defects enhance the separation and transfer of photogenerated charge carriers.

Organically Doped Metals

The research field of organically doped metals is relatively new and their application for CO₂ electroreduction is still in its infancy. For example, pyridine-functionalized Pd electrodes have been used to electrochemically reduce CO₂.^[281] Others entrap pyridine derivatives within Pd^[282] or Cu-Pd alloy cages^[283] in order to combine the catalytic activity for CO₂ to MeOH conversion of pyridine with the large surface area of the porous and electrically conductive metal cage. This approach prevents the use of large amounts of pyridine that are commonly needed for the reduction of CO₂ to MeOH.^[282] Besides showing constant current density for several hours, such hybrids can easily be recycled after washing with water. It appears that Pd and Cu catalysts facilitate the generation of MeOH and EtOH, respectively. Consequently, the Cu-Pd alloy combines two catalytically active sites within one material, thus allowing electrochemical reduction of CO₂ to MeOH or EtOH depending on the applied potential. To conclude, the entrapment of pyridine derivatives within metallic nanoparticles allows effective electrochemical reduction of CO₂ with high stability, reusability, and tuneable selectivity.

Common Limitations of Catalysts

Established concepts used to enhance CO₂ reduction performance of purely inorganic materials such as semiconductor/semiconductor or semiconductor/metal combinations are also applicable to different classes of organic-inorganic hybrids. To date, research mainly focussed on improving the electro- and photocatalytic activity by optical or electronic efficiency optimisation including bandgap engineering, plasmonic enhancement, or facilitated charge carrier mobility. However, the process of catalytic conversion starts with adsorption of CO₂ on the catalysts surface and is completed with desorption of the product molecule. These intermediate steps of the overall conversion process can be tackled by the appropriate choice of an organic component of organic-inorganic hybrids allowing chemical functionalization that results in significantly increased CO₂ affinity, suppressed competitive hydrogen evolution reactions, and enhanced selectivity towards higher-valued hydrocarbons. Nevertheless, the organic components can act as catalysts on their own, block reagents from reaching catalytic centres, or suppress charge transfer. Moreover, the origin of catalytic reaction products need further attention, e.g. through investigations comprising isotope labelling of ¹³CO₂ to avoid misleading interpretations of the detected products.^[220,227,284] Consequently, the organic component harbours many opportunities but also extra complexity for catalytic applications.

Because CO₂ reduction is closely associated with water oxidation, which is the second half reaction of the redox process, further investigations in this field need to be promoted. In detail, insufficient oxidation diminishes hydrogen formation and causes hole accumulation, both of which negatively affect the product yield. Finally, an enormous potential still lies within biological/inorganic hybrids that have recently demonstrated CO₂ reduction efficiencies exceeding natural photosynthetic systems.^[285–287]

Ultimately, to enable real-world application of organic-inorganic hybrid materials for CO₂ con-

version, catalysts have to exhibit a long term stability over thousands of hours, cyclability, non-toxicity, and economic feasibility besides showing good catalytic activity. Consequently, better understanding of the catalyst degradation mechanism is crucial to improve future catalysts. Recently, the general degradation mechanism of metallic CO₂ electrocatalysts was revealed and correlated to the catalytic performance by monitoring structural changes of different sized copper nanocubes and performing density functional theory calculations.^[288]

Furthermore, to promote cost-effective real-world applications, CO₂ conversion to higher valued hydrocarbons can be broken into a CO₂ to CO and a separate CO to hydrocarbon reduction step as this circumvents the kinetically suppressed transfer of multiple electrons and allows usage of different catalysts which are highly selective for a single redox reaction and tailor-made for its specific environmental conditions.

9.7 Conclusion

This review discusses the most common components of state-of-the-art organic-inorganic hybrid materials designed for sensing, separation, and catalytic conversion of CO₂. In fact, organic-inorganic hybrids are generating a strong excitement in the field of materials science and new building blocks are constantly synthesized at high-rate, thus yielding an ever-growing toolbox of materials. Nevertheless, many challenges have yet to be overcome to enable the breakthrough of hybrid materials for the production at industrial scale and utilization in real-world applications. For instance, the loss of functionality during long-time exposure to detrimental operating conditions and subsequent durability and stability issues need to be addressed. Additionally, conventional synthesis routes need to be optimized and extended in order to yield superior control over composition, morphology, and intermixing of organic and inorganic phases down to the nanometer scale.^[289]

In the future, computational methods that are currently still in their infancy, will become a promising tool to simulate and predict material properties and electrical or chemical interaction of hybrids with CO₂.^[195,221,290] Moreover, in operando characterization of working devices will yield more detailed knowledge of working mechanisms.^[128] Furthermore, researchers will have to take environmental compatibility, renewability, and sustainability of new organic-inorganic hybrids into account. It is quite certain that such efforts will in turn lead to their industrial viability and accelerate their utilization in CO₂-related applications, ultimately enabling to close the artificial carbon cycle. For instance, owing to steadily advancing fabrication techniques, one can imagine fabrication of multifunctional devices that combine multiple hybrid materials into a single unit. For example, CO₂ can be separated from flue gas and reduced to CO and higher valued hydrocarbons using multiple catalyst materials which are highly selective for a specific reduction process. Those catalysts can easily be combined with CO₂/CO or CO/CH₄ separation materials to enable recirculation of unreacted educts and storage of products with very high purity. It is self-evident that all these processes have to be controlled with accurate sensors. Consequently, this topic holds many challenges and opportunities and constitutes a versatile playground for chemists, physicists, and material scientists.

9.8 Acknowledgment

This work is supported by University of Hamburg and the Cluster of Excellence 'Advanced Imaging of Matter' of the Deutsche Forschungsgemeinschaft (DFG) - EXC 2056 - project ID 390715994.

Bibliography

- [1] T. DeVries, M. Holzer and F. Primeau, *Nature*, 2017, **542**, 215–215.
- [2] P. Singh, A. Wani Ali, A. A. Karim and H. Langowski, *Int. J. Dairy Technol.*, 2011, **65**, 161–177.
- [3] X. Zhang, S. Heinonen and E. Levanen, *RSC Adv.*, 2014, **4**, 61137–61152.
- [4] L. F. Cabeza, A. de Gracia, A. I. Fernández and M. M. Farid, *Appl. Therm. Eng.*, 2017, **125**, 799–810.
- [5] A. Kaushik, R. Kumar, S. K. Arya, M. Nair, B. D. Malhotra and S. Bhansali, *Chem. Rev.*, 2015, **115**, 4571–4606.
- [6] M. Wright and A. Uddin, *Sol. Energy Mater. Sol. Cells*, 2012, **107**, 87–111.
- [7] F. Peng, L. Lu, H. Sun, Y. Wang, J. Liu and Z. Jiang, *Chem. Mater.*, 2005, **17**, 6790–6796.
- [8] N. Hüsing and S. Hartmann, in *Inorganic-Organic Hybrid Porous Materials*, ed. L. Merhari, Springer US, Boston, MA, 2009, pp. 131–171.
- [9] M. Aparicio and A. Durán, *J. Sol-Gel Sci. Technol.*, 2004, **31**, 103–107.
- [10] J. Tao, N. Liu, W. Ma, L. Ding, L. Li, J. Su and Y. Gao, *Sci. Rep.*, 2013, **3**, 2286.
- [11] C. Sanchez, P. Belleville, M. Popall and L. Nicole, *Chem. Soc. Rev.*, 2011, **40**, 696–753.
- [12] L. Nicole, C. Laberty-Robert, L. Rozes and C. Sanchez, *Nanoscale*, 2014, **6**, 6267–6292.
- [13] M. Faustini, L. Nicole, E. Ruiz-Hitzky and C. Sanchez, *Adv. Funct. Mater.*, 2018, **0**, 1704158.
- [14] M. Rebber, C. Willa and D. Koziej, *Nanoscale Horiz.*, 2020, **5**, 431–453.
- [15] K. D. Vogiatzis, A. Mavrandonakis, W. Klopper and G. E. Froudakis, *ChemPhysChem*, 2009, **10**, 374–383.
- [16] P. D. Vaidya and E. Y. Kenig, *Chem. Eng. Technol.*, 2007, **30**, 1467–1474.
- [17] R. N. Dansby-Sparks, J. Jin, S. J. Mechery, U. Sampathkumaran, T. W. Owen, B. D. Yu, K. Goswami, K. Hong, J. Grant and Z.-L. Xue, *Anal. Chem.*, 2010, **82**, 593–600.
- [18] H. Segawa, E. Ohnishi, Y. Arai and K. Yoshida, *Sens. Actuators, B*, 2003, **94**, 276–281.
- [19] J. J. Gassensmith, J. Y. Kim, J. M. Holcroft, O. K. Farha, J. F. Stoddart, J. T. Hupp and N. C. Jeong, *J. Am. Chem. Soc.*, 2014, **136**, 8277–8282.
- [20] F. L. Bernard, B. B. Polesso, F. W. Cobalchini, A. J. Donato, M. Seferin, R. Ligabue, V. V. Chaban, J. F. do Nascimento, F. Dalla Vecchia and S. Einloft, *Polymer*, 2016, **102**, 199–208.
- [21] I. R. Soosaiprakasam and A. Veawab, *Int. J. Greenhouse Gas Control*, 2008, **2**, 553–562.
- [22] Z. Dai, R. D. Noble, D. L. Gin, X. Zhang and L. Deng, *J. Membr. Sci.*, 2016, **497**, 1–20.

- [23] J. Lilleparg, P. Georgopoulos, T. Emmeler and S. Shishatskiy, *RSC Adv.*, 2016, **6**, 11763–11772.
- [24] N. M. Yunus, M. I. A. Mutalib, Z. Man, M. A. Bustam and T. Murugesan, *Chem. Eng. J.*, 2012, **189-190**, 94–100.
- [25] L. A. Blanchard, D. Hancu, E. J. Beckman and J. F. Brennecke, *Nature*, 1999, **399**, 28.
- [26] Z. Lei, C. Dai and B. Chen, *Chem. Rev.*, 2014, **114**, 1289–1326.
- [27] J. Tang, H. Tang, W. Sun, M. Radosz and Y. Shen, *J. Polym. Sci., Part A: Polym. Chem.*, 2005, **43**, 5477–5489.
- [28] P. G. Mineo, L. Livoti, M. Giannetto, A. Gulino, S. Lo Schiavo and P. Cardiano, *J. Mater. Chem.*, 2009, **19**, 8861–8870.
- [29] J. Yuan and M. Antonietti, *Polymer*, 2011, **52**, 1469–1482.
- [30] J. Yuan, D. Mecerreyes and M. Antonietti, *Prog. Polym. Sci.*, 2013, **38**, 1009–1036.
- [31] W. Fang, Z. Luo and J. Jiang, *Phys. Chem. Chem. Phys.*, 2013, **15**, 651–658.
- [32] S. G. Kazarian, B. J. Briscoe and T. Welton, *Chem. Commun.*, 2000, 2047–2048.
- [33] G. Qi, L. Fu and E. P. Giannelis, *Nat. Commun.*, 2014, **5**, 5796.
- [34] T. Endo, D. Nagai, T. Monma, H. Yamaguchi and B. Ochiai, *Macromolecules*, 2004, **37**, 2007–2009.
- [35] H. J. Lee, K. K. Park, M. Kupnik and B. T. Khuri-Yakub, *Sens. Actuators, B*, 2012, **174**, 87–93.
- [36] H. Zhu, L. Wang, X. Jie, D. Liu and Y. Cao, *ACS Appl. Mater. Interfaces*, 2016, **8**, 22696–22704.
- [37] X. Wang, V. Schwartz, J. C. Clark, X. Ma, S. H. Overbury, X. Xu and C. Song, *J. Phys. Chem. C*, 2009, **113**, 7260–7268.
- [38] S. Supasitmongkol and P. Styring, *Energy Environ. Sci.*, 2010, **3**, 1961–1972.
- [39] E. I. Privalova, E. Karjalainen, M. Nurmi, P. Mäki-Arvela, K. Eränen, H. Tenhu, Y. Murzin Dmitry and J. Mikkola, *ChemSusChem*, 2013, **6**, 1500–1509.
- [40] S. Zulfiqar, M. I. Sarwar and D. Mecerreyes, *Polym. Chem.*, 2015, **6**, 6435–6451.
- [41] R. Ali, S. M. Saleh, R. J. Meier, H. A. Azab, I. I. Abdelgawad and O. S. Wolfbeis, *Sens. Actuators, B*, 2010, **150**, 126–131.
- [42] A. Car, C. Stropnik, W. Yave and K. Peinemann, *Adv. Funct. Mater.*, 2008, **18**, 2815–2823.
- [43] D. Wu, F. Xu, B. Sun, R. Fu, H. He and K. Matyjaszewski, *Chem. Rev.*, 2012, **112**, 3959–4015.
- [44] P. Bhanja, A. Modak and A. Bhaumik, *ChemCatChem*, 2019, **11**, 244–257.
- [45] P. Kaur, J. T. Hupp and S. T. Nguyen, *ACS Catal.*, 2011, **1**, 819–835.
- [46] M. Sevilla, P. Valle-Vigón and A. B. Fuertes, *Adv. Funct. Mater.*, 2011, **21**, 2781–2787.
- [47] Y. Wu, Y. Li, L. Qin, F. Yang and D. Wu, *J. Mater. Chem. B*, 2013, **1**, 204–212.
- [48] M. Zhong, E. K. Kim, J. P. McGann, S.-E. Chun, J. F. Whitacre, M. Jaroniec, K. Matyjaszewski and T. Kowalewski, *J. Am. Chem. Soc.*, 2012, **134**, 14846–14857.
- [49] A. Silvestre-Albero, J. Silvestre-Albero, M. Martínez-Escandell and F. Rodríguez-Reinoso, *Ind. Eng. Chem. Res.*, 2014, **53**, 15398–15405.

- [50] Y. Zhao, X. Liu and Y. Han, *RSC Adv.*, 2015, **5**, 30310–30330.
- [51] G.-P. Hao, W.-C. Li, D. Qian and A.-H. Lu, *Adv. Mater.*, 2010, **22**, 853–857.
- [52] A. Alabadi, H. A. Abbood, Q. Li, N. Jing and B. Tan, *Sci. Rep.*, 2016, **6**, 38614.
- [53] A. Rehman and S.-J. Park, *Chem. Eng. J.*, 2018, **352**, 539–548.
- [54] L. S. Schadler, L. C. Brinson and W. G. Sawyer, *JOM*, 2007, **59**, 53–60.
- [55] G. Dong, H. Li and V. Chen, *J. Mater. Chem. A*, 2013, **1**, 4610–4630.
- [56] N. Nakamura and Y. Amao, *Sens. Actuators, B*, 2003, **92**, 98–101.
- [57] S. M. Borisov, M. C. Waldhier, I. Klimant and O. S. Wolfbeis, *Chem. Mater.*, 2007, **19**, 6187–6194.
- [58] K. Wysokiński, M. Napierała, T. Stańczyk, S. Lipiński and T. Nasilowski, *Sens.*, 2015, **15**, 31888–31903.
- [59] O. Oter, K. Ertekin, D. Topkaya and S. Alp, *Anal. Bioanal. Chem.*, 2006, **386**, 1225–1234.
- [60] D.-I. Won, J.-S. Lee, Q. Ba, Y.-J. Cho, H.-Y. Cheong, S. Choi, C. H. Kim, H.-J. Son, C. Pac and S. O. Kang, *ACS Catal.*, 2018, **8**, 1018–1030.
- [61] K. S. Novoselov, A. K. Geim, S. V. Morozov, D. Jiang, Y. Zhang, S. V. Dubonos, I. V. Grigorieva and A. A. Firsov, *Science*, 2004, **306**, 666 LP–669.
- [62] H. Hirai, H. Tsuchiya, Y. Kamakura, N. Mori and M. Ogawa, *J. Appl. Phys.*, 2014, **116**, 083703.
- [63] K. M. Borysenko, J. T. Mullen, E. A. Barry, S. Paul, Y. G. Semenov, J. M. Zavada, M. B. Nardelli and K. W. Kim, *Phys. Rev. B*, 2010, **81**, 121412.
- [64] A. D. Smith, K. Elgammal, X. Fan, M. C. Lemme, A. Delin, M. Räsander, L. Bergqvist, S. Schröder, A. C. Fischer, F. Niklaus and M. Östling, *RSC Adv.*, 2017, **7**, 22329–22339.
- [65] F. Schedin, A. K. Geim, S. V. Morozov, E. W. Hill, P. Blake, M. I. Katsnelson and K. S. Novoselov, *Nat. Mater.*, 2007, **6**, 652.
- [66] E. Singh, M. Meyyappan and H. S. Nalwa, *ACS Appl. Mater. Interfaces*, 2017, **9**, 34544–34586.
- [67] G. Liu, W. Jin and N. Xu, *Chem. Soc. Rev.*, 2015, **44**, 5016–5030.
- [68] F. Perreault, A. Fonseca de Faria and M. Elimelech, *Chem. Soc. Rev.*, 2015, **44**, 5861–5896.
- [69] D. R. Dreyer, S. Park, C. W. Bielawski and R. S. Ruoff, *Chem. Soc. Rev.*, 2010, **39**, 228–240.
- [70] J. H. Lee, H. J. Lee and J. W. Choi, *Phys. Chem. Chem. Phys.*, 2017, **19**, 22743–22748.
- [71] R. R. Nair, H. A. Wu, P. N. Jayaram, I. V. Grigorieva and A. K. Geim, *Science*, 2012, **335**, 442.
- [72] P. Sun, M. Zhu, K. Wang, M. Zhong, J. Wei, D. Wu, Z. Xu and H. Zhu, *ACS Nano*, 2013, **7**, 428–437.
- [73] H. W. Kim, H. W. Yoon, S.-M. Yoon, B. M. Yoo, B. K. Ahn, Y. H. Cho, H. J. Shin, H. Yang, U. Paik, S. Kwon, J.-Y. Choi and H. B. Park, *Science*, 2013, **342**, 91.
- [74] H. Huang, Y. Ying and X. Peng, *J. Mater. Chem. A*, 2014, **2**, 13772–13782.
- [75] B. Mi, *Science*, 2014, **343**, 740.
- [76] S. Pei and H.-M. Cheng, *Carbon*, 2012, **50**, 3210–3228.

- [77] C. Gómez-Navarro, R. T. Weitz, A. M. Bittner, M. Scolari, A. Mews, M. Burghard and K. Kern, *Nano Lett.*, 2007, **7**, 3499–3503.
- [78] H. Kim Jung, S. Chang Won, D. Kim, R. Yang Jong, T. Han Joong, G. Lee, T. Kim Ji and K. Seol Seung, *Adv. Mater.*, 2015, **27**, 157–161.
- [79] L. Ganhua, E. O. Leonidas and C. Junhong, *Nanotechnology*, 2009, **20**, 445502.
- [80] X. Wang, K. Maeda, A. Thomas, K. Takanabe, G. Xin, J. M. Carlsson, K. Domen and M. Antonietti, *Nat. Mater.*, 2008, **8**, 76.
- [81] S. C. Yan, Z. S. Li and Z. G. Zou, *Langmuir*, 2009, **25**, 10397–10401.
- [82] F. Dong, L. Wu, Y. Sun, M. Fu, Z. Wu and S. C. Lee, *J. Mater. Chem.*, 2011, **21**, 15171–15174.
- [83] K. Wang, Q. Li, B. Liu, B. Cheng, W. Ho and J. Yu, *Appl. Catal., B*, 2015, **176-177**, 44–52.
- [84] F. Goettmann, A. Fischer, M. Antonietti and A. Thomas, *Angew. Chem. Int. Ed.*, 2006, **45**, 4467–4471.
- [85] A. Bétard and R. A. Fischer, *Chem. Rev.*, 2012, **112**, 1055–1083.
- [86] H.-C. Zhou, J. R. Long and O. M. Yaghi, *Chem. Rev.*, 2012, **112**, 673–674.
- [87] M. Eddaoudi, J. Kim, N. Rosi, D. Vodak, J. Wachter, M. Keeffe and O. M. Yaghi, *Science*, 2002, **295**, 469.
- [88] Y.-S. Bae, O. K. Farha, J. T. Hupp and R. Q. Snurr, *J. Mater. Chem.*, 2009, **19**, 2131–2134.
- [89] J. A. Thompson, N. A. Brunelli, R. P. Lively, J. R. Johnson, C. W. Jones and S. Nair, *J. Phys. Chem. C*, 2013, **117**, 8198–8207.
- [90] M. S. Denny Jr, J. C. Moreton, L. Benz and S. M. Cohen, *Nat. Rev. Mater.*, 2016, **1**, 16078.
- [91] J. Teufel, H. Oh, M. Hirscher, M. Wahiduzzaman, L. Zhechkov, A. Kuc, T. Heine, D. Denysenko and D. Volkmer, *Adv. Mater.*, 2012, **25**, 635–639.
- [92] Z. Kang, Y. Peng, Y. Qian, D. Yuan, M. A. Addicoat, T. Heine, Z. Hu, L. Tee, Z. Guo and D. Zhao, *Chem. Mater.*, 2016, **28**, 1277–1285.
- [93] J.-R. Li, R. J. Kuppler and H.-C. Zhou, *Chem. Soc. Rev.*, 2009, **38**, 1477–1504.
- [94] A. O. Yazaydin, R. Q. Snurr, T.-H. Park, K. Koh, J. Liu, M. D. LeVan, A. I. Benin, P. Jakubczak, M. Lanuza, D. B. Galloway, J. J. Low and R. R. Willis, *J. Am. Chem. Soc.*, 2009, **131**, 18198–18199.
- [95] L. Cao, K. Tao, A. Huang, C. Kong and L. Chen, *Chem. Commun.*, 2013, **49**, 8513–8515.
- [96] Y.-B. Huang, J. Liang, X.-S. Wang and R. Cao, *Chem. Soc. Rev.*, 2017, **46**, 126–157.
- [97] K. Sumida, D. L. Rogow, J. A. Mason, T. M. McDonald, E. D. Bloch, Z. R. Herm, T.-H. Bae and J. R. Long, *Chem. Rev.*, 2012, **112**, 724–781.
- [98] Y. Lin, C. Kong, Q. Zhang and L. Chen, *Adv. Energy Mater.*, 2016, **7**, 1601296.
- [99] K. Li, D. H. Olson, J. Seidel, T. J. Emge, H. Gong, H. Zeng and J. Li, *J. Am. Chem. Soc.*, 2009, **131**, 10368–10369.
- [100] L. E. Kreno, K. Leong, O. K. Farha, M. Allendorf, R. P. Van Duyne and J. T. Hupp,

- Chem. Rev.*, 2012, **112**, 1105–1125.
- [101] D. J. Wales, J. Grand, V. P. Ting, R. D. Burke, K. J. Edler, C. R. Bowen, S. Mintova and A. D. Burrows, *Chem. Soc. Rev.*, 2015, **44**, 4290–4321.
- [102] I. Stassen, N. Burtch, A. Talin, P. Falcaro, M. Allendorf and R. Ameloot, *Chem. Soc. Rev.*, 2017, **46**, 3185–3241.
- [103] S. M. Cohen, *Chem. Sci.*, 2010, **1**, 32–36.
- [104] S. M. Cohen, *Chem. Rev.*, 2012, **112**, 970–1000.
- [105] K. S. Park, Z. Ni, A. P. Côté, J. Y. Choi, R. Huang, F. J. Uribe-Romo, H. K. Chae, M. O’Keeffe and O. M. Yaghi, *Proc. Natl. Acad. Sci. U.S.A.*, 2006, **103**, 10186.
- [106] G. Lu and J. T. Hupp, *J. Am. Chem. Soc.*, 2010, **132**, 7832–7833.
- [107] K. Fujie, T. Yamada, R. Ikeda and H. Kitagawa, *Angew. Chem. Int. Ed.*, 2014, **53**, 11302–11305.
- [108] S. Shahid, K. Nijmeijer, S. Nehache, I. Vankelecom, A. Deratani and D. Quemener, *J. Membr. Sci.*, 2015, **492**, 21–31.
- [109] S. Biswas, M. Grzywa, H. P. Nayek, S. Dehnen, I. Senkowska, S. Kaskel and D. Volkmer, *Dalton Trans.*, 2009, 6487–6495.
- [110] X. Y. Chen, V.-T. Hoang, D. Rodrigue and S. Kaliaguine, *RSC Adv.*, 2013, **3**, 24266–24279.
- [111] R. Adams, C. Carson, J. Ward, R. Tannenbaum and W. Koros, *Microporous Mesoporous Mater.*, 2010, **131**, 13–20.
- [112] Y. Fu, D. Sun, Y. Chen, R. Huang, Z. Ding, X. Fu and Z. Li, *Angew. Chem. Int. Ed.*, 2012, **51**, 3364–3367.
- [113] M. Zhou, D. Korelskiy, P. Ye, M. Grahn and J. Hedlund, *Angew. Chem. Int. Ed.*, 2014, **53**, 3492–3495.
- [114] Y. Zhang, H. Wang, Y. Zhang, X. Ding and J. Liu, *Sep. Purif. Technol.*, 2017, **189**, 128–137.
- [115] X. Peng, L. Manna, W. Yang, J. Wickham, E. Scher, A. Kadavanich and A. P. Alivisatos, *Nature*, 2000, **404**, 59–61.
- [116] S. Cao, F. Tao, Y. Tang, Y. Li and J. Yu, *Chem. Soc. Rev.*, 2016, **45**, 4747–4765.
- [117] A. Loiudice, P. Lobaccaro, E. A. Kamali, T. Thao, B. H. Huang, J. W. Ager and R. Buonsanti, *Angew. Chem. Int. Ed.*, 2016, **55**, 5789–5792.
- [118] D. Raciti and C. Wang, *ACS Energy Lett.*, 2018, **3**, 1545–1556.
- [119] S. N. Habisreutinger, L. Schmidt-Mende and J. K. Stolarczyk, *Angew. Chem. Int. Ed.*, 2013, **52**, 7372–7408.
- [120] R. Shi, G. I. Waterhouse and T. Zhang, *Sol. RRL*, 2017, **1**, 1700126.
- [121] J. Hou, S. Cao, Y. Wu, Z. Gao, F. Liang, Y. Sun, Z. Lin and L. Sun, *Chem. Eur. J.*, 2017, **23**, 9481–9485.
- [122] L. He, T. E. Wood, B. Wu, Y. Dong, L. B. Hoch, L. M. Reyes, D. Wang, C. Kübel, C. Qian, J. Jia, K. Liao, P. G. O’Brien, A. Sandhel, J. Y. Y. Loh, P. Szymanski, N. P. Kherani, T. C. Sum, C. A. Mims and G. A. Ozin, *ACS Nano*, 2016, **10**, 5578–5586.
- [123] M. Benammar, A. Abdaoui, S. H. M. Ahmad, F. Touati and A. Kadri, *Sens.*, 2018, **18**,

- 581.
- [124] J. W. Severinghaus and A. F. Bradley, *J. Appl. Physiol.*, 1958, **13**, 515–520.
- [125] H. Liu, S. Lin, Y. Feng and P. Theato, *Polym. Chem.*, 2017, **8**, 12–23.
- [126] I. Djerdj, A. Haensch, D. Koziej, S. Pokhrel, N. Barsan, U. Weimar and M. Niederberger, *Chem. Mater.*, 2009, **21**, 5375–5381.
- [127] D. R. Miller, S. A. Akbar and P. A. Morris, *Sens. Actuators, B*, 2014, **204**, 250–272.
- [128] O. Hirsch, K. O. Kvashnina, L. Luo, M. J. Süess, P. Glatzel and D. Koziej, *Proc. Natl. Acad. Sci. U.S.A.*, 2015, **112**, 15803–15808.
- [129] R. A. Potyrailo, C. Surman, N. Nagraj and A. Burns, *Chem. Rev.*, 2011, **111**, 7315–7354.
- [130] C. M. Hangarter, N. Chartuprayoon, S. C. Hernández, Y. Choa and N. V. Myung, *Nano Today*, 2013, **8**, 39–55.
- [131] P. Puligundla, J. Jung and S. Ko, *Food Control*, 2012, **25**, 328–333.
- [132] A. Star, T. R. Han, V. Joshi, J. C. P. Gabriel and G. Gruener, *Adv. Mater.*, 2004, **16**, 2049–2052.
- [133] J. Wu, K. Tao, J. Zhang, Y. Guo, J. Miao and L. K. Norford, *J. Mater. Chem. A*, 2016, **4**, 8130–8140.
- [134] C. Willa, J. Yuan, M. Niederberger and D. Koziej, *Adv. Funct. Mater.*, 2015, **25**, 2537–2542.
- [135] C. Willa, A. Schmid, D. Briand, J. Yuan and D. Koziej, *ACS Appl. Mater. Interfaces*, 2017, **9**, 25553–25558.
- [136] J. Boudaden, A. Klumpp, H.-E. Endres and I. Eisele, *Proceedings*, 2017, **1**, 472.
- [137] K.-J. Kim, P. Lu, J. T. Culp and P. R. Ohodnicki, *ACS Sens.*, 2018, **3**, 386–394.
- [138] J. Wu, M.-j. Yin, K. Seefeldt, A. Dani, R. Guterman, J. Yuan, A. P. Zhang and H.-Y. Tam, *Sens. Actuators, B*, 2018, **259**, 833–839.
- [139] J. Devkota, K.-J. Kim, P. R. Ohodnicki, J. T. Culp, D. W. Greve and J. W. Lekse, *Nanoscale*, 2018, **10**, 8075–8087.
- [140] Y. Li, G. Li, X. Wang, Z. Zhu, H. Ma, T. Zhang and J. Jin, *Chem. Commun.*, 2012, **48**, 8222–8224.
- [141] B. Paschke, A. Wixforth, D. Denysenko and D. Volkmer, *ACS Sens.*, 2017, **2**, 740–747.
- [142] Y. Ma, K. Promthaveepong and N. Li, *Anal. Chem.*, 2016, **88**, 8289–8293.
- [143] X. Chong, K.-J. Kim, Y. Zhang, E. Li, P. R. Ohodnicki, C.-H. Chang and A. X. Wang, *Nanotechnology*, 2017, **28**, 26LT01.
- [144] A. Haensch, D. Koziej, M. Niederberger, N. Barsan and U. Weimar, *Procedia Eng.*, 2010, **5**, 139–142.
- [145] J. Boudaden, A. Klumpp, H.-E. Endres and I. Eisele, *Nanomaterials*, 2019, **9**, 1097.
- [146] J. Hodgkinson and R. P. Tatam, *Meas. Sci. Technol.*, 2013, **24**, 012004.
- [147] A. Pusch, A. De Luca, S. S. Oh, S. Wuestner, T. Roschuk, Y. Chen, S. Boual, Z. Ali, C. C. Phillips, M. Hong, S. A. Maier, F. Udrea, R. H. Hopper and O. Hess, *Sci. Rep.*, 2015, **5**, 17451.
- [148] S. Moumen, I. Raible, A. Krauß and J. Wöllenstein, *Sens. Actuators, B*, 2016, **236**, 1083–

- 1090.
- [149] C. Caucheteur, T. Guo, F. Liu, B.-O. Guan and J. Albert, *Nat. Commun.*, 2016, **7**, 13371.
- [150] X.-d. Wang and O. S. Wolfbeis, *Anal. Chem.*, 2016, **88**, 203–227.
- [151] X. Chong, K.-J. Kim, E. Li, Y. Zhang, P. R. Ohodnicki, C.-H. Chang and A. X. Wang, *Sens. Actuators, B*, 2016, **232**, 43–51.
- [152] M. Nazari, M. A. Forouzandeh, C. M. Divarathne, F. Sidiroglou, M. R. Martinez, K. Konstantas, B. W. Muir, A. J. Hill, M. C. Duke, M. R. Hill and S. F. Collins, *Opt. Lett.*, 2016, **41**, 1696–1699.
- [153] Y. Ma and L.-Y. L. Yung, *Anal. Chem.*, 2014, **86**, 2429–2435.
- [154] S. Sivaramakrishnan, R. Rajamani, C. S. Smith, K. A. McGee, K. R. Mann and N. Yamashita, *Sens. Actuators, B*, 2008, **132**, 296–304.
- [155] H. J. Lee, K. K. Park, M. Kupnik, N. A. Melosh and B. T. Khuri-Yakub, *Anal. Chem.*, 2012, **84**, 3063–3066.
- [156] J. Devkota, R. P. Ohodnicki and W. D. Greve, *Sens.*, 2017, **17**, 801.
- [157] A. L. Robinson, V. Stavila, T. R. Zeitler, M. I. White, S. M. Thornberg, J. A. Greathouse and M. D. Allendorf, *Anal. Chem.*, 2012, **84**, 7043–7051.
- [158] P. Davydovskaya, A. Ranft, B. V. Lotsch and R. Pohle, *Anal. Chem.*, 2014, **86**, 6948–6958.
- [159] R. Gondosiswanto, D. B. Hibbert, Y. Fang and C. Zhao, *ACS Appl. Mater. Interfaces*, 2017, **9**, 43377–43385.
- [160] D. Aaron and C. Tsouris, *Sep. Sci. Technol.*, 2005, **40**, 321–348.
- [161] T. E. Rufford, S. Smart, G. C. Y. Watson, B. F. Graham, J. Boxall, J. C. Diniz da Costa and E. F. May, *J. Pet. Sci. Technol.*, 2012, **94-95**, 123–154.
- [162] T. Rodenas, I. Luz, G. Prieto, B. Seoane, H. Miro, A. Corma, F. Kapteijn, F. X. Llabrés i Xamena and J. Gascon, *Nat. Mater.*, 2014, **14**, 48.
- [163] A. Kılıç, C. Atalay-Oral, A. Sirkecioğlu, S. B. Tantekin-Ersolmaz and M. G. Ahunbay, *J. Membr. Sci.*, 2015, **489**, 81–89.
- [164] T. Pröll and H. Hofbauer, *Fuel Process. Technol.*, 2008, **89**, 1207–1217.
- [165] E. Favre, *J. Membr. Sci.*, 2007, **294**, 50–59.
- [166] G. T. Rochelle, *Science*, 2009, **325**, 1652.
- [167] M. Tagliabue, D. Farrusseng, S. Valencia, S. Aguado, U. Ravon, C. Rizzo, A. Corma and C. Mirodatos, *Chem. Eng. J.*, 2009, **155**, 553–566.
- [168] S. Basu, A. L. Khan, A. Cano-Odena, C. Liu and I. F. J. Vankelecom, *Chem. Soc. Rev.*, 2010, **39**, 750–768.
- [169] T. C. Merkel, H. Lin, X. Wei and R. Baker, *J. Membr. Sci.*, 2010, **359**, 126–139.
- [170] D. L. Gin and R. D. Noble, *Science*, 2011, **332**, 674.
- [171] S. D. Kenarsari, D. Yang, G. Jiang, S. Zhang, J. Wang, A. G. Russell, Q. Wei and M. Fan, *RSC Adv.*, 2013, **3**, 22739–22773.
- [172] D. F. Sanders, Z. P. Smith, R. Guo, L. M. Robeson, J. E. McGrath, D. R. Paul and B. D. Freeman, *Polymer*, 2013, **54**, 4729–4761.
- [173] M. Carta, R. Malpass-Evans, M. Croad, Y. Rogan, J. C. Jansen, P. Bernardo, F. Bazzarelli

- and N. B. McKeown, *Science*, 2013, **339**, 303.
- [174] A. F. Bushell, P. M. Budd, M. P. Attfield, J. T. A. Jones, T. Hasell, A. I. Cooper, P. Bernardo, F. Bazzarelli, G. Clarizia and J. C. Jansen, *Angew. Chem. Int. Ed.*, 2012, **52**, 1253–1256.
- [175] B. Seoane, J. Coronas, I. Gascon, M. E. Benavides, O. Karvan, J. Caro, F. Kapteijn and J. Gascon, *Chem. Soc. Rev.*, 2015, **44**, 2421–2454.
- [176] L. M. Robeson, *J. Membr. Sci.*, 1991, **62**, 165–185.
- [177] L. M. Robeson, *J. Membr. Sci.*, 2008, **320**, 390–400.
- [178] Z. Song, F. Qiu, E. W. Zaia, Z. Wang, M. Kunz, J. Guo, M. Brady, B. Mi and J. J. Urban, *Nano Lett.*, 2017, **17**, 6752–6758.
- [179] J. Zhang, S. Chai, Z. Qiao, S. M. Mahurin, J. Chen, Y. Fang, S. Wan, K. Nelson, P. Zhang and S. Dai, *Angew. Chem. Int. Ed.*, 2015, **127**, 946–950.
- [180] Y. Shen, H. Wang, X. Zhang and Y. Zhang, *ACS Appl. Mater. Interfaces*, 2016, **8**, 23371–23378.
- [181] F. Ranjbaran, E. Kamio and H. Matsuyama, *J. Membr. Sci.*, 2017, **544**, 252–260.
- [182] M. G. Cowan, D. L. Gin and R. D. Noble, *Acc. Chem. Res.*, 2016, **49**, 724–732.
- [183] M. Li, X. Zhang, S. Zeng, L. bai, H. Gao, J. Deng, Q. Yang and S. Zhang, *RSC Adv.*, 2017, **7**, 6422–6431.
- [184] H. Zhu, X. Jie, L. Wang, G. Kang, D. Liu and Y. Cao, *RSC Adv.*, 2016, **6**, 69124–69134.
- [185] Y. Ban, Z. Li, Y. Li, Y. Peng, H. Jin, W. Jiao, A. Guo, P. Wang, Q. Yang, C. Zhong and W. Yang, *Angew. Chem. Int. Ed.*, 2015, **54**, 15483–15487.
- [186] W. Fam, J. Mansouri, H. Li, J. Hou and V. Chen, *ACS Appl. Mater. Interfaces*, 2018, **10**, 7389–7400.
- [187] M. Karunakaran, R. Shevate, M. Kumar and K. V. Peinemann, *Chem. Commun.*, 2015, **51**, 14187–14190.
- [188] J.-R. Li, Y. Ma, M. C. McCarthy, J. Sculley, J. Yu, H.-K. Jeong, P. B. Balbuena and H.-C. Zhou, *Coord. Chem. Rev.*, 2011, **255**, 1791–1823.
- [189] Y. Fu, Y.-B. Jiang, D. Dunphy, H. Xiong, E. Coker, S. Chou, H. Zhang, J. M. Vanegas, J. G. Croissant, J. L. Cecchi, S. B. Rempe and C. J. Brinker, *Nat. Commun.*, 2018, **9**, 990.
- [190] J. Deng, L. Bai, S. Zeng, X. Zhang, Y. Nie, L. Deng and S. Zhang, *RSC Adv.*, 2016, **6**, 45184–45192.
- [191] K. Ueno, S. Imaizumi, K. Hata and M. Watanabe, *Langmuir*, 2009, **25**, 825–831.
- [192] J. P. Gong, *Soft Matter*, 2010, **6**, 2583–2590.
- [193] L. Viau, M.-A. Néouze, C. Biolley, S. Volland, D. Brevet, P. Gaveau, P. Dieudonné, A. Galarneau and A. Vioux, *Chem. Mater.*, 2012, **24**, 3128–3134.
- [194] Q. Chen, H. Chen, L. Zhu and J. Zheng, *J. Mater. Chem. B*, 2015, **3**, 3654–3676.
- [195] C. Altintas, G. Avci, H. Daglar, A. Nemati Vesali Azar, S. Velioglu, I. Erucar and S. Keskin, *ACS Appl. Mater. Interfaces*, 2018, **10**, 17257–17268.
- [196] P. Falkowski, R. J. Scholes, E. Boyle, J. Canadell, D. Canfield, J. Elser, N. Gruber, K. Hi-

- bbard, P. Högberg, S. Linder, F. T. Mackenzie, B. Moore Iii, T. Pedersen, Y. Rosenthal, S. Seitzinger, V. Smetacek and W. Steffen, *Science*, 2000, **290**, 291 LP–296.
- [197] M. Aresta, A. Dibenedetto and A. Angelini, *Chem. Rev.*, 2014, **114**, 1709–1742.
- [198] H. Büttner, L. Longwitz, J. Steinbauer, C. Wulf and T. Werner, *Top. Curr. Chem.*, 2017, **375**, 50–50.
- [199] M. E. Royer, *Compt. Rend.*, 1870, 731–732.
- [200] Y. Hori, K. Kikuchi, A. Murata and S. Suzuki, *Chem. Lett.*, 1986, **15**, 897–898.
- [201] T. Inoue, A. Fujishima, S. Konishi and K. Honda, *Nature*, 1979, **277**, 637–637.
- [202] M. Halmann, *Nature*, 1978, **275**, 115–115.
- [203] H. Abdullah, M. M. R. Khan, H. R. Ong and Z. Yaakob, *J. CO₂ Util.*, 2017, **22**, 15–32.
- [204] J. L. White, M. F. Baruch, J. E. Pander, Y. Hu, I. C. Fortmeyer, J. E. Park, T. Zhang, K. Liao, J. Gu, Y. Yan, T. W. Shaw, E. Abelev and A. B. Bocarsly, *Chem. Rev.*, 2015, **115**, 12888–12935.
- [205] X. Chang, T. Wang and J. Gong, *Energy Environ. Sci.*, 2016, **9**, 2177–2196.
- [206] S. Xie, Q. Zhang, G. Liu and Y. Wang, *Chem. Commun.*, 2016, **52**, 35–59.
- [207] Y. Ma, X. Wang, Y. Jia, X. Chen, H. Han and C. Li, *Chem. Rev.*, 2014, **114**, 9987–10043.
- [208] M. B. Gawande, A. Goswami, F.-X. Felpin, T. Asefa, X. Huang, R. Silva, X. Zou, R. Zboril and R. S. Varma, *Chem. Rev.*, 2016, **116**, 3722–3811.
- [209] L. Liu and A. Corma, *Chem. Rev.*, 2018, **118**, 4981–5079.
- [210] W. Tu, Y. Zhou and Z. Zou, *Adv. Mater.*, 2014, **26**, 4607–4626.
- [211] L. B. Hoch, T. E. Wood, P. G. O’Brien, K. Liao, L. M. Reyes, C. A. Mims and G. A. Ozin, *Adv. Sci.*, 2014, **1**, 1400013.
- [212] J. K. Stolarczyk, S. Bhattacharyya, L. Polavarapu and J. Feldmann, *ACS Catal.*, 2018, **8**, 3602–3635.
- [213] T. Benedetti, S. Naficy, A. Walker, D. L. Officer, G. G. Wallace and F. Dehghani, *Energy Technology*, 2018, **6**, 702–709.
- [214] A. Weilhard, M. I. Qadir, V. Sans and J. Dupont, *ACS Catal.*, 2018, **8**, 1628–1634.
- [215] Y. Liao, S.-W. Cao, Y. Yuan, Q. Gu, Z. Zhang and C. Xue, *Chem. Eur. J.*, 2014, **20**, 10220–10222.
- [216] Y. Liao, Z. Hu, Q. Gu and C. Xue, *Molecules*, 2015, **20**, 18847.
- [217] S. Liu, J. Xia and J. Yu, *ACS Appl. Mater. Interfaces*, 2015, **7**, 8166–8175.
- [218] J. Mao, K. Li and T. Peng, *Catal. Sci. Technol.*, 2013, **3**, 2481–2498.
- [219] L. Yuan and Y.-J. Xu, *Appl. Surf. Sci.*, 2015, **342**, 154–167.
- [220] K. Li, B. Peng and T. Peng, *ACS Catal.*, 2016, **6**, 7485–7527.
- [221] Z. D. Dong, L. J. Long and Q. S. Zhang, *Adv. Mater.*, 2016, **28**, 3423–3452.
- [222] P. D. Tran, L. H. Wong, J. Barber and J. S. C. Loo, *Energy Environ. Sci.*, 2012, **5**, 5902–5918.
- [223] M. Schreck and M. Niederberger, *Chem. Mater.*, 2019, **31**, 597–618.
- [224] W. Sun, C. Qian, L. He, K. K. Ghuman, A. P. Y. Wong, J. Jia, A. A. Jelle, P. G. O’Brien, L. M. Reyes, T. E. Wood, A. S. Helmy, C. A. Mims, C. V. Singh and G. A. Ozin, *Nat.*

- Commun.*, 2016, **7**, 12553.
- [225] K. K. Ghuman, T. E. Wood, L. B. Hoch, C. A. Mims, G. A. Ozin and C. V. Singh, *Phys. Chem. Chem. Phys.*, 2015, **17**, 14623–14635.
- [226] J. Wu, Y. Huang, W. Ye and Y. Li, *Adv. Sci.*, 2017, **4**, 1700194.
- [227] C.-C. Yang, Y.-H. Yu, B. van der Linden, J. C. S. Wu and G. Mul, *J. Am. Chem. Soc.*, 2010, **132**, 8398–8406.
- [228] H. Kisch, *Angew. Chem. Int. Ed.*, 2010, **122**, 9782–9783.
- [229] H. Kisch and D. Bahnemann, *J. Phys. Chem. Lett.*, 2015, **6**, 1907–1910.
- [230] T. Maschmeyer and M. Che, *Angew. Chem. Int. Ed.*, 2010, **49**, 1536–1539.
- [231] J. M. Buriak, P. V. Kamat and K. S. Schanze, *ACS Appl. Mater. Interfaces*, 2014, **6**, 11815–11816.
- [232] M. Qureshi and K. Takanabe, *Chem. Mater.*, 2017, **29**, 158–167.
- [233] J. G. Chen, C. W. Jones, S. Linic and V. R. Stamenkovic, *ACS Catal.*, 2017, **7**, 6392–6393.
- [234] E. L. Clark, J. Resasco, A. Landers, J. Lin, L.-T. Chung, A. Walton, C. Hahn, T. F. Jaramillo and A. T. Bell, *ACS Catal.*, 2018, **8**, 6560–6570.
- [235] M. W. Logan, S. Ayad, J. D. Adamson, T. Dilbeck, K. Hanson and F. J. Uribe-Romo, *J. Mater. Chem. A*, 2017, **5**, 11854–11863.
- [236] C. S. Diercks, Y. Liu, K. E. Cordova and O. M. Yaghi, *Nat. Mater.*, 2018, **17**, 301–307.
- [237] K. M. Choi, D. Kim, B. Rungtaweivoranit, C. A. Trickett, J. T. D. Barmanbek, A. S. Alshammari, P. Yang and O. M. Yaghi, *J. Am. Chem. Soc.*, 2017, **139**, 356–362.
- [238] Q. Liu, Z.-X. Low, L. Li, A. Razmjou, K. Wang, J. Yao and H. Wang, *J. Mater. Chem. A*, 2013, **1**, 11563–11569.
- [239] R. Li, J. Hu, M. Deng, H. Wang, X. Wang, Y. Hu, H.-L. Jiang, J. Jiang, Q. Zhang, Y. Xie and Y. Xiong, *Adv. Mater.*, 2014, **26**, 4783–4788.
- [240] K. Niu, Y. Xu, H. Wang, R. Ye, H. L. Xin, F. Lin, C. Tian, Y. Lum, K. C. Bustillo, M. M. Doeff, M. T. M. Koper, J. Ager, R. Xu and H. Zheng, *Sci. Adv.*, 2017, **3**, 1–9.
- [241] X. Duan, J. Xu, Z. Wei, J. Ma, S. Guo, S. Wang, H. Liu and S. Dou, *Adv. Mater.*, 2017, **29**, 1701784.
- [242] S. Zhao, D.-W. Wang, R. Amal and L. Dai, *Adv. Mater.*, 2019, **31**, 1801526.
- [243] R. Paul, F. Du, L. Dai, Y. Ding, Z. L. Wang, F. Wei and A. Roy, *Adv. Mater.*, 2019, **31**, 1805598.
- [244] A. P. Kauling, A. T. Seefeldt, D. P. Pisoni, R. C. Pradeep, R. Bentini, R. V. B. Oliveira, K. S. Novoselov and A. H. Castro Neto, *Adv. Mater.*, 2018, **30**, 1803784.
- [245] W.-J. Ong, L.-L. Tan, S.-P. Chai and S.-T. Yong, *Chem. Commun.*, 2015, **51**, 858–861.
- [246] W. Tu, Y. Zhou and Z. Zou, *Adv. Funct. Mater.*, 2013, **23**, 4996–5008.
- [247] W. Tu, Y. Zhou, Q. Liu, S. Yan, S. Bao, X. Wang, M. Xiao and Z. Zou, *Adv. Funct. Mater.*, 2012, **23**, 1743–1749.
- [248] Y. T. Liang, B. K. Vijayan, K. A. Gray and M. C. Hersam, *Nano Lett.*, 2011, **11**, 2865–2870.
- [249] Y. T. Liang, B. K. Vijayan, O. Lyandres, K. A. Gray and M. C. Hersam, *J. Phys. Chem.*

- Lett.*, 2012, **3**, 1760–1765.
- [250] L.-L. Tan, W.-J. Ong, S.-P. Chai and A. R. Mohamed, *Nanoscale Res. Lett.*, 2013, **8**, 465.
- [251] H.-C. Hsu, I. Shown, H.-Y. Wei, Y.-C. Chang, H.-Y. Du, Y.-G. Lin, C.-A. Tseng, C.-H. Wang, L.-C. Chen, Y.-C. Lin and K.-H. Chen, *Nanoscale*, 2013, **5**, 262–268.
- [252] I. Shown, H.-C. Hsu, Y.-C. Chang, C.-H. Lin, P. K. Roy, A. Ganguly, C.-H. Wang, J.-K. Chang, C.-I. Wu, L.-C. Chen and K.-H. Chen, *Nano Lett.*, 2014, **14**, 6097–6103.
- [253] K. M. Cho, K. H. Kim, K. Park, C. Kim, S. Kim, A. Al-Saggaf, I. Gereige and H.-T. Jung, *ACS Catal.*, 2017, **7**, 7064–7069.
- [254] Y. Wang, X. Li, J. Song, L. Xiao, H. Zeng and H. Sun, *Adv. Mater.*, 2015, **27**, 7101–7108.
- [255] S. A. Veldhuis, Y. K. E. Tay, A. Bruno, S. S. H. Dintakurti, S. Bhaumik, S. K. Muduli, M. Li, N. Mathews, T. C. Sum and S. G. Mhaisalkar, *Nano Lett.*, 2017, **17**, 7424–7432.
- [256] Y.-F. Xu, M.-Z. Yang, B.-X. Chen, X.-D. Wang, H.-Y. Chen, D.-B. Kuang and C.-Y. Su, *J. Am. Chem. Soc.*, 2017, **139**, 5660–5663.
- [257] J. Sun, J. Yang, J. I. Lee, J. H. Cho and M. S. Kang, *J. Phys. Chem. Lett.*, 2018, **9**, 1573–1583.
- [258] M. Asadi, B. Kumar, A. Behranginia, B. A. Rosen, A. Baskin, N. Reppin, D. Pisasale, P. Phillips, W. Zhu, R. Haasch, R. F. Klie, P. Král, J. Abiade and A. Salehi-Khojin, *Nat. Commun.*, 2014, **5**, 4470–4470.
- [259] H. Jung, K. M. Cho, K. H. Kim, H.-W. Yoo, A. Al-Saggaf, I. Gereige and H.-T. Jung, *ACS Sustainable Chem. Eng.*, 2018, **6**, 5718–5724.
- [260] S. Wang, B. Y. Guan and X. W. Lou, *Energy Environ. Sci.*, 2018, **11**, 306–310.
- [261] H. Shi, G. Chen, C. Zhang and Z. Zou, *ACS Catal.*, 2014, **4**, 3637–3643.
- [262] J. Yu, K. Wang, W. Xiao and B. Cheng, *Phys. Chem. Chem. Phys.*, 2014, **16**, 11492–11501.
- [263] G. Gao, Y. Jiao, E. R. Waclawik and A. Du, *J. Am. Chem. Soc.*, 2016, **138**, 6292–6297.
- [264] F. Sastre, M. J. Muñoz-Batista, A. Kubacka, M. Fernández-García, W. A. Smith, F. Kapteijn, M. Makkee and J. Gascon, *ChemElectroChem*, 2016, **3**, 1497–1502.
- [265] Y. He, L. Zhang, B. Teng and M. Fan, *Environ. Sci. Technol.*, 2015, **49**, 649–656.
- [266] M. Jiang, B. Li, X. Cui, Q. Yang, Z. Bao, Y. Yang, H. Wu, W. Zhou, B. Chen and H. Xing, *ACS Appl. Mater. Interfaces*, 2018, **10**, 16628–16635.
- [267] X. Yang, W. Xin, X. Yin and X. Shao, *Chem. Phys. Lett.*, 2016, **651**, 127–132.
- [268] W. Yu, D. Xu and T. Peng, *J. Mater. Chem. A*, 2015, **3**, 19936–19947.
- [269] M. Li, L. Zhang, M. Wu, Y. Du, X. Fan, M. Wang, L. Zhang, Q. Kong and J. Shi, *Nano Energy*, 2016, **19**, 145–155.
- [270] M. Reli, P. Huo, M. Šihor, N. Ambrožová, I. Troppová, L. Matějová, J. Lang, L. Svoboda, P. Kuśtrowski, M. Ritz, P. Praus and K. Kočí, *J. Phys. Chem. A*, 2016, **120**, 8564–8573.
- [271] T. Ohno, N. Murakami, T. Koyanagi and Y. Yang, *J. CO₂ Util.*, 2014, **6**, 17–25.
- [272] S.-W. Cao, X.-F. Liu, Y.-P. Yuan, Z.-Y. Zhang, Y.-S. Liao, J. Fang, S. C. J. Loo, T. C. Sum and C. Xue, *Appl. Catal., B*, 2014, **147**, 940–946.
- [273] J.-C. Wang, H.-C. Yao, Z.-Y. Fan, L. Zhang, J.-S. Wang, S.-Q. Zang and Z.-J. Li, *ACS Appl. Mater. Interfaces*, 2016, **8**, 3765–3775.

- [274] M. Li, L. Zhang, X. Fan, M. Wu, M. Wang, R. Cheng, L. Zhang, H. Yao and J. Shi, *Appl. Catal., B*, 2017, **201**, 629–635.
- [275] L. Zhao, L. Zhang, H. Lin, Q. Nong, M. Cui, Y. Wu and Y. He, *J. Hazard. Mater.*, 2015, **299**, 333–342.
- [276] M. Li, L. Zhang, X. Fan, Y. Zhou, M. Wu and J. Shi, *J. Mater. Chem. A*, 2015, **3**, 5189–5196.
- [277] S. Wang, J. Lin and X. Wang, *Phys. Chem. Chem. Phys.*, 2014, **16**, 14656–14660.
- [278] L. Shi, T. Wang, H. Zhang, K. Chang and J. Ye, *Adv. Funct. Mater.*, 2015, **25**, 5360–5367.
- [279] Z. Sun, S. Wang, Q. Li, M. Lyu, T. Butburee, B. Luo, H. Wang, J. M. T. A. Fischer, C. Zhang, Z. Wu and L. Wang, *Advanced Sustainable Systems*, 2017, **1**, 1700003–1700003.
- [280] H. Wang, Z. Sun, Q. Li, Q. Tang and Z. Wu, *J. CO₂ Util.*, 2016, **14**, 143–151.
- [281] G. Seshadri, C. Lin and A. B. Bocarsly, *J. Electroanal. Chem.*, 1994, **372**, 145–150.
- [282] H.-P. Yang, S. Qin, H. Wang and J.-X. Lu, *Green Chem.*, 2015, **17**, 5144–5148.
- [283] H.-P. Yang, S. Qin, Y. N. Yue, L. Liu, H. Wang and J.-X. Lu, *Catal. Sci. Technol.*, 2016, **6**, 6490–6494.
- [284] T. Yui, A. Kan, C. Saitoh, K. Koike, T. Ibusuki and O. Ishitani, *ACS Appl. Mater. Interfaces*, 2011, **3**, 2594–2600.
- [285] C. Liu, B. C. Colón, M. Ziesack, P. A. Silver and D. G. Nocera, *Science*, 2016, **352**, 1210–1213.
- [286] K. K. Sakimoto, A. B. Wong and P. Yang, *Science*, 2016, **351**, 74 LP–77.
- [287] E. M. Nichols, J. J. Gallagher, C. Liu, Y. Su, J. Resasco, Y. Yu, Y. Sun, P. Yang, M. C. Y. Chang and C. J. Chang, *Proc. Natl. Acad. Sci. U.S.A.*, 2015, **112**, 11461–11466.
- [288] J. Huang, N. Hörmann, E. Oveisi, A. Loiudice, G. L. De Gregorio, O. Andreussi, N. Marzari and R. Buonsanti, *Nat. Commun.*, 2018, **9**, 3117.
- [289] L. Chen, X. Tang, P. Xie, J. Xu, Z. Chen, Z. Cai, P. He, H. Zhou, D. Zhang and T. Fan, *Chem. Mater.*, 2018, **30**, 799–806.
- [290] G. Sastre, J. van den Bergh, F. Kapteijn, D. Denysenko and D. Volkmer, *Dalton Trans.*, 2014, **43**, 9612–9619.

List of Figures

2.1	General aerogel processing scheme.	8
2.2	Energy diagram of nanoparticle stabilization.	9
2.3	Overview of nanoparticle gelation strategies.	10
2.4	Phase diagram of the gel drying process.	12
2.5	Literature overview of nanoparticle-based aerogels.	13
3.1	Covered length scales during aerogel processing.	18
3.2	Overview of common 3D printing methods.	19
3.3	Literature overview of 3D printed nanoparticle-based aerogels.	23
3.4	Literature overview of 3D printed molecular-based aerogels.	24
4.1	Photographs of the 3D printing setup.	32
4.2	Schematic of standard rheological performance tests.	33
4.3	Overview of the photocatalysis setup.	35
4.4	Photographs of the custom-made flow-through reactor.	36
4.5	Flow scheme of the gas chromatograph.	37
4.6	Simplified decision scheme for Monte Carlo photon transport simulations.	41
5.1	Modular 3D printing approach of TiO ₂ nanoparticle-based aerogels.	49
5.2	Rheological properties of TiO ₂ inks.	51
5.3	Experimental obstacles for DIW of TiO ₂ nanoparticle-based aerogels.	53
5.4	Illustration of the shear-induced fluid-shell formation.	54
5.5	Covered length scales of a 3D printed TiO ₂ aerogel.	55
5.6	Photothermal heating of neat TiO ₂ and AuNR/TiO ₂ hybrid aerogels.	57
5.7	Effect of microstructuring on temperature and light distribution in 3D printed AuNR/TiO ₂ aerogels.	58
5.8	Ink stability for increasing ACN contents and different nanomaterial compositions.	64
5.9	Rheologic characterization of TiO ₂ , AuNP/TiO ₂ and AuNR/TiO ₂ inks.	65
5.10	Stress estimation for a 3D printed grid geometry and a pending gel filament.	68
5.11	Photograph of the 3D printing setup.	71
5.12	Mechanical compression test of AuNR/TiO ₂ aerogels.	73
5.13	Exfoliation test of an unstructured AuNR/TiO ₂ aerogel.	73
5.14	Porosity characterization of 3D printed and casted aerogel.	74
5.15	TEM and HAADF-STEM images of a AuNR/TiO ₂ aerogel.	75
5.16	Photothermal heating ability of TiO ₂ and AuNR/TiO ₂ aerogels.	76
5.17	TiO ₂ characterization via DLS and XRD.	77
5.18	Attenuated total reflection infrared spectra of dried TiO ₂ particles.	77

5.19	Structural and optical characterization of AuNPs and AuNRs.	78
5.20	Corrected version of Figure 5.7.	81
5.21	Deformation study of a pending filament with a diameter of 1540 μm	83
5.22	Deformation study of a pending filament in heptane charged with Triton X-100.	83
5.23	Inside front cover of <i>Adv. Funct. Mater.</i> 2022 , 32, 19.	85
6.1	Nature-inspired aerogel photocatalysts.	94
6.2	Light transport in aerogels.	96
6.3	Mass transport in aerogels.	98
6.4	Photocatalytic hydrogen evolution from aerogels and powders.	101
6.5	Compounds detected via gas chromatography during UV cleaning.	106
6.6	Hydrogen evolution during two photocatalytic cycles.	107
6.7	Hydrogen evolution for an unstructured and fcc-structured TiO_2 aerogel.	108
6.8	Overview of the custom-made gas flow photoreactor.	110
6.9	Illustration of the data analysis for the hydrogen evolution of a TiO_2 powder sample.	111
6.10	N_2 isotherms of aerogels before and after a photocatalytic experiment.	112
6.11	XRD pattern of a 3D printed TiO_2 aerogel.	112
6.12	Measured total transmittance and reflectance spectra of a TiO_2 aerogel.	114
6.13	Schematic of the light propagation in a translucent aerogel.	115
6.14	Plots of the calculated transmittance and reflectance.	116
6.15	Illustration of the data processing routine for the determination of scattering and absorption coefficients.	117
6.16	Effect of escaped photons during reflectance measurements.	120
6.17	Effectiveness factor η as a function of Thiele modulus ϕ	123
6.18	Histogram of the channel width in an fcc-structured TiO_2 aerogel.	127
7.1	Embedded 3D printing of a TiO_2 nanoparticle-based aerogel.	135
7.2	Alignment of AuNRs during 3D printing of a AuNR/ TiO_2 gel.	137
7.3	Photocatalytic CO_2 reduction on Au/ TiO_2 powder.	139
9.1	Overview of common building blocks to design hybrid materials for CO_2 related applications.	149
9.2	Schematic drawings of different CO_2 sensing principles.	156
9.3	Robeson plot for CO_2/CH_4 and CO_2/N_2 separation.	163
9.4	Schematic drawing describing available gas separation mechanisms.	164
9.5	Dual pore and thickness engineering for CO_2 separation membranes.	165
9.6	Schematic drawings of photo- and electrocatalytic reduction processes.	170
9.7	MOF-based hybrids for CO_2 conversion.	173
9.8	Carbon-based hybrids for CO_2 conversion.	176

List of Tables

3.1	Overview of ink compositions for DIW of aerogels.	22
4.1	List of events during a single run of the gas chromatograph.	38
5.1	Yield stress τ_y and flow stress τ_f of TiO ₂ inks.	64
5.2	Physical description of 3D printed grid geometries.	69
5.3	Fluid-shell estimation during DIW of TiO ₂ gels.	72
5.4	Specific surface area and mean pore size of TiO ₂ , AuNP/TiO ₂ , and AuNR/TiO ₂ aerogels.	74
5.5	Updated version of Table 5.5	82
6.1	List of investigated photocatalyst samples.	109
6.2	Average specific surface area and pore size of three TiO ₂ aerogels before and after photocatalytic experiments.	109
6.3	List of calculated apparent quantum efficiencies.	113
6.4	List of parameters for the estimation of H ₂ O vapor diffusion.	124
6.5	Overview of reaction constant k_r for various photochemical processes.	125
6.6	List of variables used for the calculation of the Reynolds number Re_{np} , the pressure drop $\Delta P/t$, and the permeability k according to equations 6.21-6.23.	127
9.1	CO ₂ sensing characteristics of hybrid materials.	161
9.2	CO ₂ separation characteristics of hybrid materials.	168
9.3	Redox potentials for CO ₂ reduction and side reactions.	171

List of Abbreviations

ACN	Acetonitrile
AQE	Apparent Quantum Efficiency
AuNP	Au Nanoparticle
AuNR	Au Nanorod
BET	Brunauer-Emmet-Teller
DC	Direct Current
DFT	Density Functional Theory
DIW	Direct Ink Writing
DLP	Digital Light Processing
DLS	Dynamic Light Scattering
EtOH	Ethanol
fcc	Face-Center Cubic
FDM	Fused Deposition Modeling
FID	Flame Ionization Detector
HID	Helium Pulsed Discharge Ionization Detector
IR	Infrared
MeOH	Methanol
MFC	Mass Flow Controller
MS	Mass Spectrometer
NIR	Near-Infrared
NLDFT	Non Local DFT
PDMS	Polydimethylsiloxan
PMMA	Poly(methyl methacrylate)
PVP	Polyvinylpyrrolidone
RTE	Radiative Transfer Equation
sc	Simple-Cubic
SEM	Scanning Electron Microscopy
SLA	Stereolithography
SLS	Selective Laser Sintering
TCD	Thermal Conductivity Detector
TEM	Transmission Electron Microscopy
UV	Ultraviolet
vis	Visible

Declaration

The findings presented within this thesis are the result of strong collaborations with researchers. For clarity, their contributions are listed below:

Andrea Köppen and Stefan Werner are employees at electron microscopy service unit at the Institute of Physical Chemistry, University of Hamburg. Stefan and Andrea recorded transmission electron microscopy images in chapters 5 and 6.

Dr. Andreas Schropp and Samanehalsadat Ehteram are senior scientist and Ph.D. student in X-ray Nanoscience and X-Ray Optics Group lead by Prof. Christian Schroer at DESY, respectively. Andreas and Samaneh performed tomographic measurements and data reconstruction of TiO₂ aerogels in chapter 5. Visualization of the reconstructed data was performed by myself.

Prof. Atsushi Urakawa is a leading scientist for catalysis engineering at TU Delft. Atsushi hosted my visiting research stay in his group, introduced me into photocatalysis and reactor design, and influenced my understanding of catalytic processes.

Charline Becker is a Ph.D. student in the Biophotonic Group lead by Prof. Wolfgang Parak at the Institute for Nanostructures and Solid State Physics, University of Hamburg. Charline assisted in dynamic light scattering measurements in chapter 5.

Prof. Christian Schroer is the head of the X-ray Nanoscience and X-Ray Optics group at DESY. Christian is the 2nd supervisor of this thesis, and provided lab access for tomographic measurements.

Prof. Daniela Pfannkuche is head of the Dynamics in Correlated Systems group at the I. Institute of Theoretical Physics, University of Hamburg. Daniela assisted me in solving the radiative transfer equation in chapter 6 and influenced my understanding on numerical computation.

Dr. Dirk Eifler and Nuray Eroglu are head and technical assistant of the central elemental analysis at Department of Chemistry, University of Hamburg. Dirk and Nuray performed elemental analysis in chapter 5.

Prof. Dorota Koziej is the head of the Hybrid Nanostructures group at the Institute for Nanostructures and Solid State Physics, University of Hamburg. Dorota is the 1st supervisor of this thesis.

Ferdinand Otto is a Ph.D. student in the Biophotonic Group lead by Prof. Wolfgang Parak at the Institute for Nanostructures and Solid State Physics, University of Hamburg. Ferdinand

introduced me to the interfacial tension measurements. All experiments were performed and analyzed by myself.

Hendrik Sannemüller is a former master student in the Hybrid Nanostructures Group lead by Prof. Dorota Koziej at the Institute for Nanostructures and Solid State Physics, University of Hamburg. Hendrik prepared most of the samples and conducted most of the photocatalytic measurements in chapter 6.

Dr. Irina Loketeva was a senior scientist in Coherent X-ray Scattering Group lead by Prof. Gerhard Grübel at DESY. Irina provided AuNRs and introduced me to UV-vis spectrometer setup in chapter 5.

Malte Trommler is a former master student in the Hybrid Nanostructures Group lead by Prof. Dorota Koziej at the Institute for Nanostructures and Solid State Physics, University of Hamburg. Malte contributed to the sample preparation and performed photothermal measurements in chapter 5.

Marvin Skiba is a Ph.D. student in the Biophotonic Group lead by Prof. Wolfgang Parak at the Institute for Nanostructures and Solid State Physics, University of Hamburg. Marvin performed and analyzed the inductively coupled plasma mass spectrometry measurements for quantification of gold in Au/TiO₂ aerogels in chapter 6.

Merlina Thiessen is a Ph.D. Student in group lead by Prof. Volker Abetz at the Institute of Physical Chemistry, University of Hamburg. Merlina introduced me into rheology measurements. Prof. Michael Fröba is the head of a research group at the Institute of Applied and Inorganic Chemistry, University of Hamburg. Michael provided resources for N₂-physisorption measurements.

Michael Jaruzewski is a former master student in the Hybrid Nanostructures Group lead by Prof. Dorota Koziej at the Institute for Nanostructures and Solid State Physics, University of Hamburg. Michael performed all computational fluid dynamics simulations and pressure drop measurements in chapter 6.

Prof. Qianqian Fang leads the Computational Optics and Translational Imaging group at the Northeastern University. Qianqian is the author of MMCLAB and answered technical questions regarding the implementation of Monte Carlo simulations in chapter 6.

Sandra König is a technical assistant at the Institute of Applied and Inorganic Chemistry at the University of Hamburg and associated to the group of Prof. Michael Fröba. Sandra performed and analyzed all N₂-Physisorption measurements in chapters 5 and 6.

Sarah-Alexandra Hussak is a master student in the Hybrid Nanostructures group lead by Prof. Dorota Koziej at the Institute for Nanostructures and Solid State Physics, University of Hamburg. Sarah recorded the scanning electron microscopy image in Figure 6.1g.

Sönke Wengler-Rust is a Ph.D. Student in the Nanochemistry group lead by Prof. Dr. Horst

Weller at the Institute of Physical Chemistry, University of Hamburg. Sönke introduced me to the UV-vis integrating sphere setup in chapter 6.

Dr. Christoph Willa is a former Ph.D. Student in the Hybrid Nanostructures Group lead by Prof. Dorota Koziej at the Institute for Nanostructures and Solid State Physics, University of Hamburg. Christoph contributed to chapter 9 by reviewing current trends in organic/inorganic materials for the sensing and separation of CO₂.

Acknowledgments

Prof. Dorota Koziej. Thank you for allowing me to work creatively, for letting me open so many doors along my journey, but also for reminding me not to open too many. Your positive spirit and the challenge to build a lab and a project from scratch initially made me join your group. Although the task has been extremely demanding, your relentless support and your trust in my skills strengthened my resilience, and my determination to reach one goal after another. It was a great pleasure to work with you.

Prof. Andreas Stierle. Thank you for being the second examiner of this thesis and the interest in my work.

Prof. Daniela Pfannkuche. Thank you for being so patient and for the multiple ZOOM sessions to implement the DISORT algorithm. Although it is only a small part of the Ph.D. project it is one that still fulfills me with so much joy since it was so far out of my comfort zone. Without your support I would not have conquered this scientific obstacle.

Prof. Arwen Pearson and Dr. Robert Zierold. Thank you for being part of the examination committee and for your interest in my work.

Prof. Christian Schroer. Thank you for co-supervising the progress of my Ph.D project, for your feedback in our annual meetings and for providing access to your laboratory for X-ray microtomography measurements.

Prof. Atsushi Urakawa. Thank you for being such a great host and for introducing me into the beauty and challenges of photocatalysis during my research stay in your laboratories. Also, big thank you to **Bart, Els, Liliana, Sorin, Lingjun, Donato** and **Nat** who either assisted me in the lab or just helped me to have a great time in Delft.

Samanehalsadat Ehteram and Dr. Andreas Schropp. Thank you for the pleasant collaboration and performing the X-ray microtomography measurements.

Sandra König. Thank you for performing endless physisorption measurements throughout my Ph.D project. I highly value our straightforward cooperation, your explanation of technical details and the data analysis.

Prof. Michael Fröba. Thank you for dedicating resources to the physisorption measurements and your interest in my work during presentations within the GRK NANOHYBRID seminars or the CUI Annual Meeting.

Dr. Irina Lokteva. Thank you unlocking the lab whenever I needed to use the UV-vis, and more importantly thank you for providing the Au nanorods which eventually led to a publication. Collaboration can be so easy!

Merlina Thiessen, Charline Becker, Ferdinand Otto, Marvin Skiba, and Sönke-Wengler Rust. Thank you for your expertise and your interest in my work. Many measurements and resulting conclusions would have been impossible without your help.

The mechanical workshop. Thank you for all the discussions and for machining new devices. Without your help the 3D printing and photocatalysis setup would not exist.

Matthias Hein. Thank you for your generous support when I needed to install the stainless steel tubings, fittings, and the pressure reducers for the gas chromatograph. I never imagined that I would learn to do orbital welding during my Ph.D.

Raphael, Malte, Michael, Hendrik. Thank you for joining my Ph.D. project with your bachelor or master project. It was great fun to tackle the technical boundaries of 3D printing and I highly value your expertise and opinion. Thank you for your efforts in the lab, for new ideas, and for fruitful discussions.

GRK 2536 NANOHYBRID and the Cluster of Excellence 'CUI: Advanced Imaging of Matter'. Thank you for providing such a great platform of scientific exchange and for the financial support.

All current and former members of the Hybrid Nanostructures Group. Thank you for such a pleasant working atmosphere and for the good company during lunch breaks. Although COVID hindered us from having more social activities, we still created many nice moments. Let's hope that we'll create many more whenever we reconvene in the future.

Dear friends and family. Thank you for being part of my life and for distracting me from work. Thank you for your continuous support and for asking not too many questions about my research which really helped me to recharge my batteries.

Curriculum Vitae

Personal Data

Name: Matthias Rebber
Date of Birth: November 23, 1993
Place of Birth: Aurich, Germany

Education

JAN 2018 - CURRENT Ph.D. Candidate in Physics
Hybrid Nanostructures Group
Department of Physics, University of Hamburg, Germany

SEP 2019 - OCT 2019 Research Visit
Group of Prof. Atsushi Urakawa
Department of Chemical Engineering, TU Delft, Netherlands

OCT 2015 - JAN 2018 M.Sc. in Nanoscience
Department of Chemistry, University of Hamburg, Germany
Thesis: 'Cross-Linked Gold Nanoparticle Membranes:
Resistive Pressure Sensors and Electromechanical
Characterization'

OCT 2012 - JAN 2016 B.Sc. in Nanoscience
Department of Chemistry, University of Hamburg, Germany
Thesis: 'Freestanding Dithiol-Cross-Linked Gold Nanoparticle
Membranes: Materials for a Novel Class of Pressure Sensors'

List of Talks

Seventh International Conference on Multifunctional, Hybrid and Nanomaterials,
October 19-22, 2022 in Genoa, Italy.

NANOHYBRID - Hamburg Conference on Complex Nanostructures, October 4-7,
2022 in Hamburg, Germany.

6th International Seminar on Aerogels, September 28-30, 2022 in Hamburg, Germany.

List of Scientific Publications

Matthias Rebber, Hendrik Sannemüller, Michael Jaruszewski, Daniela Pfannkuche, Atsushi Urakawa, and Dorota Koziej. Nature-inspired 3D structuring of TiO₂ aerogels enables scalable photocatalytic hydrogen production. Paper submitted.

Matthias Rebber, Malte Trommler, Irina Lokteva, Samanehsadat Ehteram, Andreas Schropp, Sandra König, Michael Fröba, and Dorota Koziej. Additive-Free, Gelled Nanoinks as a 3D Printing Toolbox for Hierarchically Structured Bulk Aerogels. *Advanced Functional Materials* **2022**, 32, 2112914.

Lukas Grote, Cecilia A. Zito, Kilian Frank, Ann-Christin Dippel, Patrick Reisbeck, Krzysztof Pitala, Kristina O. Kvashnina, Stephen Bauters, Blanka Detlefs, Oleh Ivashko, Pallavi Pandit, Matthias Rebber, Sani Y. Harouna-Mayer, Bert Nickel, and Dorota Koziej. X-ray studies bridge the molecular and macro length scales during the emergence of CoO assemblies. *Nature Communications* **2021**, 12, 4429.

Matthias Rebber, Christoph Willa, and Dorota Koziej. Organic–inorganic hybrids for CO₂ sensing, separation and conversion. *Nanoscale Horizons* **2020**, 5, 431-453.

Hendrik Schlicke, Svenja Kunze, Matthias Rebber, Norbert Schulz, Svenja Riekeberg, Hoc Khiem Trieu, and Tobias Vossmeier. Cross-Linked Gold Nanoparticle Composite Membranes as Highly Sensitive Pressure Sensors. *Advanced Functional Materials* **2020**, 30, 2003381.

Hendrik Schlicke, Matthias Rebber, Svenja Kunze, and Tobias Vossmeier. Resistive pressure sensors based on freestanding membranes of gold nanoparticles. *Nanoscale* **2016**, 8, 183-186.

Eidesstattliche Versicherung / Declaration on oath

Hiermit versichere ich an Eides statt, die vorliegende Dissertationsschrift selbst verfasst und keine anderen als die angegebenen Hilfsmittel und Quellen benutzt zu haben. Ich versichere, dass das gebundene Exemplar der Dissertation und das in elektronischer Form eingereichte Dissertationsexemplar (über den Docata-Upload) und das bei der Fakultät (zuständiges Studienbüro bzw. Promotionsbüro Physik) zur Archivierung eingereichte gedruckte gebundene Exemplar der Dissertationsschrift identisch sind.

I hereby declare upon oath that I have written the present dissertation independently and have not used further resources and aids than those stated in the dissertation. I, the undersigned, declare that the bound copy of the dissertation and the dissertation submitted in electronic form (via the Docata upload) and the printed bound copy of the dissertation submitted to the faculty (responsible Academic Office or the Doctoral Office Physics) for archiving are identical.

Hamburg, den 14.09.2022

Matthias Nils Rebber